Laser trapping of sodium isotopes for a high-precision β-decay experiment

Kruithof, Wilbert Lucas

Laser trapping of sodium isotopes for a high-precision β-decay experiment

COVER: *Sodium streetlamps along the Eesveenseweg, where the author grew up. Photo Jan Kruithof.*

This work is part of the research programme of the Foundation for Fundamental Research on Matter (FOM), which is part of the Netherlands Organisation for Scientific Research (NWO).

PRINTED BY: Ipskamp Drukkers, Enschede, July 2012

RIJKSUNIVERSITEIT GRONINGEN

Laser trapping of sodium isotopes for a high-precision β-decay experiment

Proefschrift

ter verkrijging van het doctoraat in de
Wiskunde en Natuurwetenschappen
aan de Rijksuniversiteit Groningen
op gezag van de
Rector Magnificus, dr. E. Sterken,
in het openbaar te verdedigen op
vrijdag 14 september 2012
om 16.15 uur

door

Wilbert Lucas Kruithof

geboren op 10 januari 1983
te Steenwijk

Promotor:	Prof. dr. H.W.E.M. Wilschut
Copromotor:	Dr. S. Hoekstra
Beoordelingscommissie:	Prof. dr. ir. R.A. Hoekstra
	Prof. dr. L. Moi
	Prof. dr. C. Weinheimer

ISBN: 978-90-367-5586-3 Printed version
ISBN: 978-90-367-5585-6 Electronic version

Contents

Chapter 1

Introduction

The forces and particles in nature are described by the Standard Model (SM) of particle physics and General Relativity (GR) [1, 2]. Although especially the SM withstood many high-precision tests and is able to explain a wide variety of observations [3], the SM and GR have some shortcomings. The first is that they fail at the Planck energy scale of 10^{19} GeV. This was the energy scale in the very early universe [4]. Furthermore, to explain for instance the rotation velocities of galaxies, dark matter is needed [5]. Additionally, the accelerating expansion of the universe is best explained by dark energy [6]. Dark matter (22.7%) and energy (72.8%) even make up 96% of all energy and matter in the universe [7]. Only 4.6% can be accounted for by the SM and GR and therefore most probably new particles and interactions are required. Also the dominance of matter over anti-matter in the universe is not explained by the current SM [8], since the prediction of CP violation in the SM is several orders of magnitude too small to explain the observed asymmetry [9]. This provides evidence that new sources of CP violation are required that are not part of the SM[1]. Presently, the only experimental evidence for physics beyond the SM is through the observation of neutrino oscillations [11]. These oscillations can be explained by assuming non-zero neutrino masses, which cannot be accounted for in the SM.

Therefore, there is no doubt that the current description of nature by the SM and GR alone is incomplete and that there are more forces or elementary particles in nature than we currently know of. Numerous quantum gravity models claim that they offer a successor to the combination of SM and GR, among which are supersymmetric extensions of the SM [12], quantum loop gravity [13] and higher dimensional (noncommutative geometry based) theories like superstring and M-theory [14, 15].

Two strategies are being followed to constrain the number of possible successors of the SM. At the Large Hadron Collider (LHC) facility at CERN new particles can be created directly in collider experiments at very high energy, typically at the TeV energy scale [16]. The second approach utilizes high-precision experiments at low(er)

[1] Within the SM also a cold electroweak baryogenesis might be a viable scenario [10].

energies. Within the SM fundamental symmetries are related to the mediators of forces. Measuring a violation, or an excess of a violation of a symmetry therefore reveals new forces. Bounds from these experiments can also be translated to an equivalent high-energy scale and constrain new physics. This also allows for complementary research, *i.e.* searches at high and low energy are sensitive to different (combinations of) parameters of the proposed models.

An example of searches at low energies probing such new physics is the precise measurement of properties of β-decay [17]. Crucial in these experiments are, besides sensitivity to the symmetry of interest, a high precision (statistical significance) and a high accuracy (small systematic errors).

This thesis describes two steps towards a high-precision β-decay correlations experiment using the radioactive ^{21}Na isotope produced by the TRIμP facility at KVI[2]. The first step is to select and collect the radioactive particles, that are produced by an accelerator, with laser light in an atom trap. This has to be done efficiently to achieve the required precision in the final experiment. To minimize the background due to the decay of untrapped particles, the second step is to transport the trapped atoms over about 1 m towards a shielded setup. There precise and accurate decay measurements can take place [18].

In section 1.1 we briefly review the different types of interactions which can be studied in β-decay. The different particle traps which are used for precision β-decay experiments are discussed in section 1.2. Some completed and current β-decay experiments testing the SM are discussed in section 1.3. Our motivation to perform with ^{21}Na a high-precision β-decay experiment can be found in section 1.4. We end with the outline of this thesis in section 1.5.

1.1 Observables in β-decay

One possibility to study physics beyond the SM in β-decay is by measuring correlations between the decay products from the β-decay. The distribution in the electron and neutrino directions and electron energy for an allowed transition from an oriented nucleus is given by

$$\omega(\langle J\rangle|E_e,\Omega_e,\Omega_\nu)\,dE_e\,d\Omega_e\,d\Omega_\nu = \frac{1}{(2\pi)^5}p_eE_e(Q+m_e-E_e)^2\,dE_e\,d\Omega_e\,d\Omega_\nu\,\xi \qquad (1.1)$$
$$\times\left[1+a\frac{\vec{p}_e\cdot\vec{p}_\nu}{E_eE_\nu}+b\frac{m_e}{E_e}+c\left(\frac{1}{3}\frac{\vec{p}_e\cdot\vec{p}_\nu}{E_eE_\nu}-\frac{(\vec{p}_e\cdot\vec{j})(\vec{p}_\nu\cdot\vec{j})}{E_eE_\nu}\right)\left(\frac{J(J+1)-3\langle(\vec{J}\cdot\vec{j})^2\rangle}{J(2J-1)}\right)\right.$$
$$\left.+\frac{\vec{J}}{J}\cdot\left(A\frac{\vec{p}_e}{E_e}+B\frac{\vec{p}_\nu}{E_\nu}+D\frac{\vec{p}_e\times\vec{p}_\nu}{E_eE_\nu}\right)\right],$$

where $E_{e(\nu)}$ is the total relativistic energy of the electron (neutrino), $\vec{p}_{e(\nu)}$ the momentum of the electron (neutrino), Q the available kinetic energy in the decay, $\vec{J}$ the

[2]TRIμP stands for Trapped Radioactive Isotopes: μlaboratories for Fundamental Physics, KVI for Kernfysisch Versneller Instituut.

spin of the nucleus and $\vec{j}$ a unit vector parallel to it [19]. The influence of the non-zero neutrino masses can be considered negliglible for our purposes. The coefficients a, b, c, A, B and D are the correlation parameters. These as well as ξ are defined in terms of the coupling coefficients C_i and C_i' of the various interactions in the β-decay Hamiltonian [20]. We do not include in this equation other correlations which involve for example the observation of the polarization of the emitted β particle. We refer to [17] for a complete review of tests of the SM in β decay.

With β detectors the momentum vector of the β particle can be determined, but a measurement of the neutrino momentum is practically impossible. Instead the recoil momentum of the daughter nucleus is measured. This technique requires a substrate free sample because of the low recoil energy of about 100 eV. One possibility, described in this thesis, is to laser cool the radioactive atoms to low temperatures and trap them in a small volume under vacuum conditions. In this way $\vec{p}_\nu$ can be determined indirectly.

We now briefly discuss the physics behind equation 1.1. The first line of equation 1.1 is the phase space factor, except for the constant ξ, the strength of the decay. In the second line three coefficients appear, a, b and c. To measure the $\beta - \nu$ correlation parameter a and the Fierz interference term b, no nuclear-spin polarization is required (the c term contribution vanishes for an unpolarized sample and for $J = 1/2$). The third line contains the nuclear spin related correlation coefficients. A is the parity violating coefficient which was first measured by Wu *et al.* using polarized ^{60}Co [21]. Depending on the sign of A the β particles are primarily emitted (anti-)parallel to the spin axis. The neutrino asymmetry parameter is given by B.

Inspection of the term $\vec{J} \cdot \vec{p}_e \times \vec{p}_\nu$, associated with the D coefficient, shows that this term contributes to violation of time-reversal symmetry. By the CPT theorem [22], CP violation is equivalent to T violation (a violation of the CPT symmetry necessarily violates Lorentz invariance [23]). With CPT symmetry, a bound on D gives thus also a constraint on CP violation. As under a parity transformation D is even, measuring D also constraints C violation alone.

All correlation coefficients can be expressed in terms of coupling coefficients of vector (V), axial-vector (A), scalar (S) and tensor (T) couplings. These correlations coefficients depend on electro-magnetic final state interactions (FSI) that need to be taken into account. For example, FSI lead to a non-zero value of D and its precise value is needed to obtain the true value of the SM.

In the SM β-decay is described with left-handed vector and axial-vector interactions (V−A theory). The angular momentum state of a nucleus is usually denoted with J^π, where J is the spin of the nucleus and π indicates its parity: $+$ (even) or $-$ (odd). We consider here only allowed transitions, where no orbital angular momentum is carried away by the pair of outgoing leptons and total parity is not changed. If the outgoing pair of leptons has a total spin $S = 0$, it is called a Fermi (F) transition (vector coupling). For $S = 1$ it is called a Gamow-Teller (GT) transition (axial-vector coupling). For a decay where $0^+ \rightarrow 0^+$, a GT transition cannot occur because of angular momentum considerations.

Various deviations of the SM are predicted by leptoquark models, left-right sym-

metric models, supersymmetric models and models with charged Higgs exchange [24]. These differ from the standard V−A coupling: V+A (right handed), scalar, tensor and imaginary parts of all types of couplings[3]. Three typical experiments can be distinguished according to the type of the transition in the decay process:

- Fermi transitions: in pure F decay $a < 1$ indicates scalar or right-handed couplings. The strength of superallowed Fermi transitions ($\mathcal{F}t$ values) is sensitive to scalar interactions via the Fierz interference term b. A, B and D are necessarily 0.
- Gamow-Teller transitions: Here the SM values for A, B are $\neq 0$. In a pure GT transition, $a > -1/3$ implies tensor or right-handed couplings. Here, b, A and B also primarily constrain tensor couplings.
- Mixed F-GT transitions: a, A and D are $\neq 0$, the precise values depend on the nuclear structure. The SM value for $D \approx 10^{-12}$ [25], a larger value indicates imaginary couplings of the V−A theory and implies a larger time-reversal violation than the SM predicts.

A possible source of scalar-type interactions are charged Higgs-boson exchanges, for tensor interactions these can be leptoquarks [24]. Left-right symmetric models, exotic fermions and leptoquark models can provide sources for time-reversal violation [24]. In experiments usually only the shape of the correlation distribution is assessed experimentally and not the full expression of equation 1.1. Therefore it is convenient to introduce

$$\tilde{x} = \frac{x}{1 + b\langle \frac{m_e}{E_e} \rangle} \,. \tag{1.2}$$

Although not mentioned by all authors reporting on measurements of the correlations coefficients, this is the value that is measured in most experiments. Within the β-decay ^{21}Na experiment in TRIμP, we aim to measure first $\tilde{a}$ and then $\tilde{D}$. This will be discussed in more detail in section 1.4.

1.2 Particle traps suited for a β-decay correlation experiment

To measure β-decay correlations requires radioactive particles for which the decay correlations can be measured. An accelerator based facility is able to produce the particles on demand. The research described in this thesis has been performed with the TRIμP facility, which is an example of such a facility. It offers a wide range of low-energy radio-active isotopes and due to its design a variety of experiments can make use of it.

As we focus in this thesis on the efficient collecting of particles in an atom trap, we discuss here the various traps used in β-decay experiments. Open, shallow particle traps are well suited for precision β-decay experiments as most of the solid angle can be used for particle detectors. Due to the low temperature (for laser cooled samples)

[3] Pseudo-scalar couplings are not relevant at low energies [20].

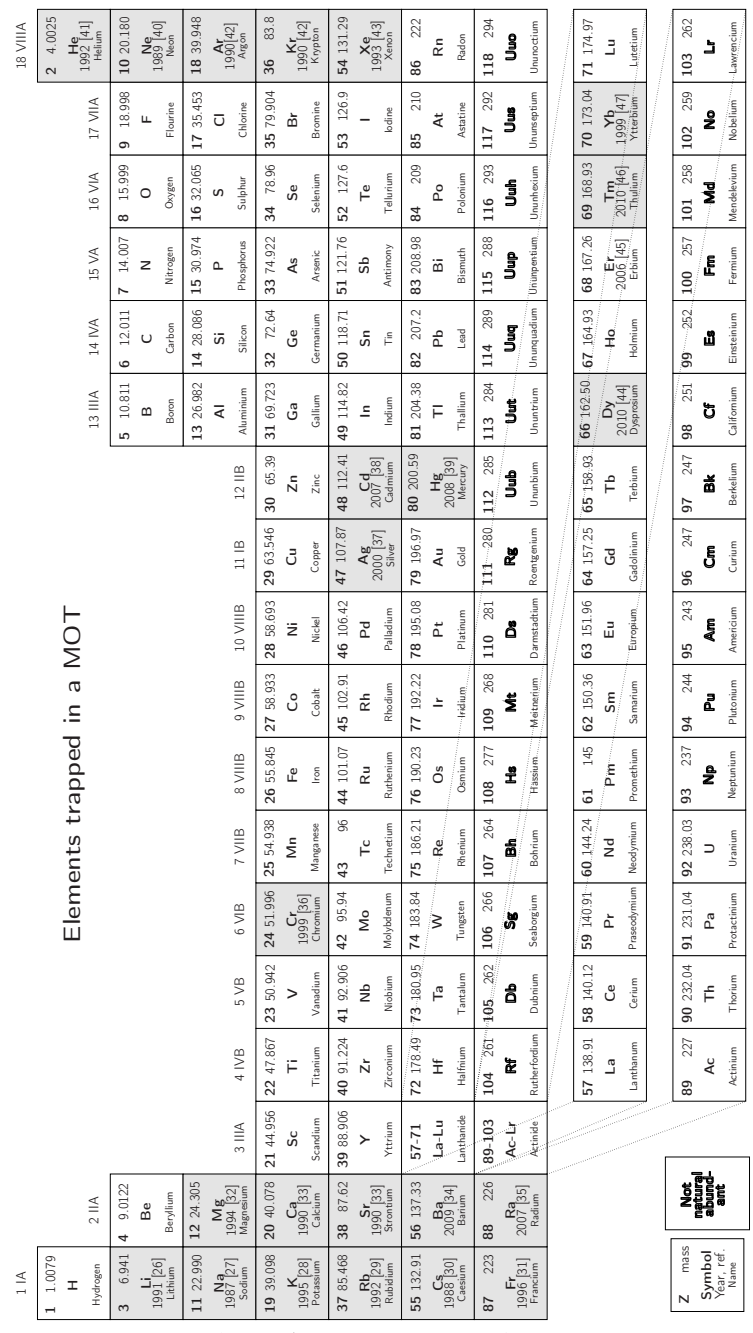

Figure 1.1: *The elements of the periodic table. The year and reference when one of the isotopes was trapped in a Magneto-Optical Trap (MOT) for the first time is indicated.*

the uncertainty on the initial momenta can be neglected. For neutral particles three types of traps can be distinguished: a magneto-optical trap which uses near resonant laser light and a quadrupole magnetic field, a purely magnetic trap and traps based on the interaction of off-resonant laser light with the atoms [48, 49].

The first atom trap, which uses on-resonance laser light, is a dissipative radiation-pressure trap. It utilizes near-resonant laser light with a wavelength typically in the range of 400 nm to 900 nm with a quadrupole magnetic field (Magneto-Optical Trap, MOT), with a typical trap depth of a Kelvin. The MOT was demonstrated experimentally for the first time in 1987 by Raab *et al.* [27] using sodium atoms. A MOT produces an unpolarized atom cloud[4] with a sample temperature of typically 100 μK. Spin polarization of the atoms trapped in a MOT can be achieved by temporarily turning off the trapping beams and magnetic field[5] and optically pumping the cloud [52]. Also by misaligning the MOT trapping beams spin polarization can be achieved in a MOT system[6] [53].

As can be seen in figure 1.1, most of the alkali(-earth) elements have been trapped in a MOT, notably Ba was trapped first at KVI [34, 54]. Due to the large energy separation between the ground state and the first excited states, noble gas atoms are trapped using metastable states. Whether an atom can be trapped in a MOT depends on two points: the availability of a reasonably closed cooling cycle and sufficient laser power at the required laser frequency for such a scheme.

The second atom trap type, first demonstrated in 1985 by Migdall *et al.* using sodium atoms, is the magnetic trap [55]. The magnetic trap provides a conservative potential, the force on the magnetic dipole moment of the atom depends on the magnetic substate. This type of trap is ideally suited to generate a spin-polarized sample. The trap depth is typically about 10 mK, the cloud temperature is a fraction of the trap depth. To enhance the number of trapped particles in a magnetic trap, it is usually loaded from a MOT.

The third trap type is a dipole laser trap (Far Off-Resonant Trap, FORT), first demonstrated for sodium atoms by Chu *et al.* in 1986. The FORT offers a typical trap depth of 1 mK, the cloud temperature is a fraction of the trap depth. The conservative potential is provided by the interaction of the induced electric dipole moment with the electric field of the laser light, which is far detuned from the atomic transition (as used in a MOT). As the detuning is typically several hundreds of nm, the trap is versatile. With this trap type highly polarized samples have been produced [56–58], also a precise determination of the spin polarization of the trapped atoms has been demonstrated [59].

We now consider the traps for charged particles. Ions are conveniently trapped by a combination of static and alternating (radio frequency, RF) electric fields of typically a MHz (Paul trap), or a combination of a static magnetic field and a static electric field (Penning Trap). The achievable ion cloud temperature is with buffer gas cooling

[4] An upper limit on the sample polarization of 0.2% was measured for ^{23}Na [50].

[5] A MOT using an AC magnetic field, reducing the switching time, has also been demonstrated [51].

[6] Flipping the spin polarization is not easy in this scheme.

about 1000 K (or 0.1 eV) [60]. For β-decay experiments this might be too high, but additional (indirect) cooling is possible with lasers. For laser cooling, a single laser beam is sufficient and the temperatures reached are about the same as can be achieved in a MOT.

Laser cooling of ions also depends on having a suitable energy level scheme, only a handful of ions can directly be laser cooled: all hydrogen like elements (group 2 IIA in figure 1.1) and additionally Yb^+ and Hg^+ [61]. As in a MOT, a reasonably closed cooling scheme has to be present, as well as sufficient laser power. The latter requirement is often easier to fulfill for an ion trap than for a MOT system, as the ion is initially trapped by the ion trap and the cooling light only needs to be present in a relatively small volume compared to a MOT system. Sympathetic cooling provides an alternative. One ion species is laser-cooled, the other ions are only trapped by the electric field but are cooled through the Coulomb interaction with the laser cooled ions. This enables cooling of any other ion [61, 62].

For β-decay experiments the atom and ion traps are surrounded by a combination of an ion detector (typically a Multi Channel Plate (MCP)), which detects the recoiling daughter ion, and β detectors. In the case of an atom trap, the recoiling ions, because of their low energies, can be collected efficiently by applying a static electric field. By using the fast β particle as a trigger, the energy of the recoil ion can be determined from its time of flight. In the decay process, also electrons are shaken off. The same electric field guides the shake-off electrons to the opposite direction, where they can be detected and serve as a trigger. When the electron time of flight is short compared to the time of flight of the recoiling ion and when the β momentum reconstruction is not needed this is much more efficient than detecting the β particle. The shake-off detection procedure has been applied to measure ^{21}Na recoil spectra [63, 64]. However, this method cannot be used to measure A or D.

1.3 Completed and current β-decay experiments

To get an impression of the activities, we present two tables which summarize completed and ongoing experiments testing the SM via β-decay. We divide the experiments in two categories: experiments which use particle traps and those that do not. For both we do not go into the details of the possible production methods or the detector schemes and associated sources of systematic errors to reconstruct the β-decay decay. We focus on acquiring sufficient decay data.

In table 1.1 we give an overview of β-decay correlation measurements performed in particle traps. We list values relevant for this thesis: typical production rates for the radioactive particles as well as the trapping efficiency (the fraction from the produced particles which ends up trapped) and detection efficiency. The ratio of the typical (coincidence) rate to the production rate gives an indication of the combined trapping and detection efficiencies, in case these are not known. For most of the experiments we combined information from several references to arrive at these values, therefore they should be considered as indicative. Where experiments progressed over time, we

mention the highest values reported. The Cs and both Fr experiments are not β-decay experiments, but we include them in this overview as they use also MOT systems for the efficient collection of radioactive isotopes.

For a precision at the level of 1%, statistically at least 10^4 events are required. This is the minimal number of events; due to a non-zero background and systematic studies generally a larger number of events is required. We observe that the detected (coincidence) event rate (called 'science rate' in the table) is a fraction of the order of 10^{-7} of the source rate. The source rates (table 1.1) are in the range $10^7 - 2 \cdot 10^9$ /s.

Now we look in more detail at the entries from table 1.1. We first discuss the ^{21}Na experiment from Laurence Berkeley National Laboratories (LBNL) separately. The other experiments using atom traps use the same technique, we therefore discuss them together. The $^6He^+$ experiment from Laboratoire de Physique Corpusculaire (LPC) we also discuss in more detail, as they are making the transition from an ion trap experiment to an atom trap experiment.

The ^{21}Na experiment performed at LBNL is particularly interesting, as we use the same isotope. Therefore we discuss their strategy to achieve a high collection efficiency in more detail. The ^{21}Na experiment at Berkeley uses a 1.2 m long Zeeman slower to capture the ^{21}Na atoms which are evaporated from an oven after online production (proton beam on a MgO target) [65]. Before the atoms enter the slowing stage, they are cooled in optical molasses[7] to reduce the transverse velocity of the atomic beam. For an oven temperature of 1000 °C and the used slowing laser intensity, maximally 13.6% of atoms can be slowed down by the Zeeman slower. Of the atoms that enter the MOT setup, which uses 3.5 cm large trapping beams, about 25% are trapped. From the Zeeman slowed beam, instead of 25% initially only 1% was captured by the MOT. To reduce the background in the correlations measurements from these untrapped atoms, a double MOT system was set up. A transfer efficiency of 40 ± 20% was demonstrated.

Except the ^{21}Na experiment done at Berkeley, which uses a Zeeman slower, all the other experiments in table 1.1 using an atom trap are based on the same principle. The ions are neutralized by implanting the ion beam in a neutralizer foil. This foil is (periodically) heated to evaporate the atoms. The atoms thermalize during the first collision with the cell wall. Because the wall is coated with a non-stick, transparent thin layer of a paraffin like material, the atoms bounce up to a thousand times. The geometry of the cell is such that the atoms pass the laser trap volume often before they are lost through one of the tubes, which connects the cell to the ion beam line. To maximize the capture efficiency per trap passage and minimize the loss through the exits, a large (cubic) cell is used together with large laser trapping beams.

For the $^6He^+$ experiment the uncertainty in the ion cloud size dominates with 90% the systematic error, which itself is half of the total error. An atom trap solves the problem of the sample size, as in a MOT the spatial distribution can be monitored more easily than in an ion trap[8].

[7] A molasses is a MOT without the magnetic quadrupole field.

[8] In an ion trap, the temperature and size of the ion cloud are linked by the trapping effective potential.

Table 1.1: *Overview of completed and current β-decay experiments using traps testing the Standard Model at low energy. The entries for the ^{21}Na KVI experiment are expected values. The source rate is number of produced particles/s. The science rate is the coincidence count rate of off-line accepted events. The trapping efficiency includes transfer for double-Magneto Optical Trap (MOT) systems. Decay type: Fermi (F), Gamow-Teller (GT) and mixed F-GT transition (M). DM stands for double-MOT system, OP for optical pumping. The two experiments, shown between the dashed lines, are not β-decay experiment, but use similar techniques to produce laser trapped samples of radioactive atoms.*

Atom trap	Decay type	Correlation parameter	Source rate (/s)	Science rate (/s)	Trapping efficiency	Detection efficiency	Remarks	Reference(s)
^{21}Na, LBNL	M	$a = 0.553(2)$	$3 \cdot 10^8$	15	$2 \cdot 10^{-4}$	$9 \cdot 10^{-2}$	Zeeman slower[1]	[65, 68]
^{21}Na, KVI	M	a, D	$3 \cdot 10^8$	10^3	$3 \cdot 10^{-3}$	$1 \cdot 10^{-2}$	DM	[69]
^{37}K, TRIUMF	M	$B_\nu = -0.76(2), A_\beta$	$6 \cdot 10^7$	0.14	-	-	DM, OP[2]	[70, 71]
^{38m}K, TRIUMF	F	$a = 0.998(5)$	10^7	-	10^{-3}	-	DM	[70, 72, 73]
^{80}Rb, TRIUMF	GT	$A = 0.02(4)$	$2 \cdot 10^9$	100	-	-	DM, OP	[74]
^{82}Rb, LANL	GT	A	$3 \cdot 10^8$	5	$3 \cdot 10^{-5}$	-	DM+TOP trap[3]	[75–77]
^{209,210}Fr, LNL	-	-	10^6	-	$3 \cdot 10^{-4}$	-	PNC exp.	[78]
^{210}Fr, SUNY	-	-	10^6	-	$6 \cdot 10^{-3}$	-	PNC exp. [79]	[80, 81]
Ion trap								
^{6}He$^+$, GANIL	GT	$a = -0.33(1)$	$3.2 \cdot 10^8$	-	$2 \cdot 10^{-4}$	$1.5 \cdot 10^{-3}$	Paul trap[4]	[66, 82–84]
^{35}Ar$^+$, WITCH	M	a	10^7	150	0.8	0.15	Expected[5]	[85, 86]

[1] The trapping efficiency estimation is based on $8 \cdot 10^5$ trapped atoms in the MOT and a lifetime of 12 s [65]. The science rate is based on the same lifetime and the values from [64]. The coincidence detection efficiency estimation assumes 15% detection efficiency for the e^- and 60% for the ion. The β^+ detection is about 3% of the efficiency of the shake-off method [63–65].

[2] Beside measuring A_β, an improvement to a precision of 0.5% on B_ν is planned as well [87]. Improvement on the current value for $D = (-3 \pm 35)10^{-3}$ [71] can then also be expected.

[3] Off-line source. The 20% transfer efficiency and 50% loss when loading from the MOT into the Time Orbiting Potential (TOP) is included in the trapping efficiency. Science rate estimated from 10^5 events in 6 hr [76]. Polarization in an optical dipole trap has been demonstrated as well [57–59].

[4] The given value for $a_{\beta\nu}$ is for 10^5 coincidence events. An statistical precision of 0.5% is expected, considering the off-line cuts that will be done on the $4 \cdot 10^6$ detected coincidence events. An atom version of this experiment is considered as well, see text.

[5] The recoil is detected in a retardation spectrometer and thus has to be scanned. Among other things, therefore there is an additional factor 10^4 between the number of ions in the derived recoil spectrum and the number of decayed ions [85].

The ion cloud has a diameter of a few mm [66] and the thermal energy is typically 0.1 eV [106], achieved through buffer gas cooling. For a MOT the cloud size is sub mm and the temperature typically achieved is in the (sub) mK regime [107]. Therefore an efficient atom trap with a transverse cooling stage and a Zeeman slower aiming for a collection efficiency of $2 \cdot 10^{-6}$ is under construction [108]. At GANIL ^{6}He ($t_{1/2}$=807 ms) and ^{8}He ($t_{1/2}$=119 ms) were trapped in a MOT with a total capture efficiency of 10^{-7}[109, 110].

In table 1.2 some experiments that do not use a trap are listed. Three types of experiments can be distinguished: beam experiments (neutron), cell experiments where the spin-polarized atoms bounce off the walls and hardly depolarize (^{19}Ne) and sample experiments. In sample experiments, the particles are implanted in a foil which is kept at cryogenic temperatures and strong magnetic fields are used to polarize the nuclei. In the ^{32,33}Ar experiments the recoil distribution is observed indirectly from the Doppler-shifted particle decay of the daughter nucleus. Table 1.2 is not complete, but serves to show some characteristic examples. For example, a range of experiments aims to measure correlation parameters in neutron decay with a precision of 0.1% [111].

Comparing table 1.2 to table 1.1 shows that except for the Ar experiments, the source rates for the non-trap experiments are similar or higher than those for the trap experiments. The neutron experiment by Mumm *et al.* is particularly interesting because of its high precision they achieved. The D coefficient for the neutron has been measured for the first time in 1974 by Steinberg *et al.* [112], they found $D = -(1.1 \pm 1.7) \times 10^{-3}$. At the end of 2011 Mumm *et al.* published the result of the data they took at the end of 2003 [88]. The analysis of the data of such a beam experiment is very challenging. The systematic error is about the size of the statistical error, $D = (-0.96 \pm 1.89(\text{stat}) \pm 1.01(\text{sys})) \times 10^{-4}$. For the neutron experiment only a fraction of about $2 \cdot 10^{-7}$ of all the neutrons decays in the fiducial detector volume. This fraction is comparable to the overall trapped particle efficiency in MOT experiments.

Summarizing, trap experiments are conceptually easier because they provide a point-like and substrate free source of decay. Non-trap experiments are ultimately limited in the final precision by systematic effects. In trap experiments these can be better controlled as more diagnostic tools are available. In ion traps, the temperature of the cloud can be limiting at some point, in which case (sympathetic) laser cooling is required. For the trap experiments there is the challenge to acquire sufficient statistics. Conceptually β-decay experiments using traps have ultimately the most potential to perform measurements in β-decay with high precision when recoil detection is required.

Other observables also constrain non-SM physics: for example bounds on the permanent Electric Dipole Moments (EDM) [54] and the neutrino mass [113, 114]. These bounds in turn constrain possible values of correlation coefficients in β-decay decay. Upper limits on the neutrino mass appear to constrain the scalar and tensor

Since they are correlated, Fléchard *et al.* [66] usually speak about the temperature. If one could decouple size and temperature, the dominant source of systematic error would be the size [67].

Table 1.2: *Some completed and current β-decay experiments, which do not use traps, testing the Standard Model at low energy. The table gives an impression the several types of experiments. There are many more experiments [17], for example for the neutron [100, 101]. The science count rate is the coincidence rate of off-line accepted events. Correlation type: Fermi (F), Gamow-Teller (GT) and a mixed F-GT transition (M).*

Experiment	Decay type	Correlation parameter	Source rate (/s)	Remarks	Reference(s)
n, NCNR	M	$D = -1(2) \cdot 10^{-4}$	$3 \cdot 10^9$	Cold beam, $5 \cdot 10^2$ decays/s, science rate 15/s.[1]	[88, 89]
^{6}He	GT	$a = -0.334(3)$	$7 \cdot 10^{11}$	Magnetic/electric spectrometer.	[90, 91]
^{8}Li	GT	$R = 0.9(2) \cdot 10^{-3}$	$1.2 \cdot 10^9$	Polarized d on helium temperature ^{7}Li target.[2]	[92, 93]
^{19}Ne, Berkeley	M	$D = 2(4) \cdot 10^{-3}$	$3 \cdot 10^{11}$	10^4 decays/s in cell, $4 \cdot 10^6$ D events in 125 hr.[3]	[94]
^{32}Ar, ISOLDE	F	$a = 0.999(7)$	94	60 keV implanted in a C foil, 3.5 T magnetic field,	[95]
^{33}Ar, ISOLDE	M	$a = 0.944(4)$	$3.9 \cdot 10^3$	delayed p detection instead of recoil.	[96]
^{60}Co, Leuven	GT	$A = -1.01(2)$	-	Implantation in a Cu foil, 13 T magnetic field.	[97, 98]
^{114}In, Leuven	GT	$A = -0.994(14)$	-	70 keV implanted in Fe foil, 0.1 T magnetic field.[4]	[98, 99]

[1] Estimated value, using an effective detector length of 30 cm, a free neutron lifetime of 880 s [102] and $v_0 = 2200$ m/s (40 K cold beam) [88].
[2] Fermi admixture is of the order of $|M_F/M_{GT}|^2 = 0.001$ only, source rate estimated using decay rate from [92]. An experiment is underway at TRIUMF aiming for a 0.1% precision [103].
[3] The average value for ^{19}Ne is $D = (1 \pm 6) \cdot 10^{-4}$ [104]. The R coefficient has also been measured for this system [105].
[4] Dose was 10^{12} ^{114m}In/cm^2 [99].

components of the β-decay [113, 114]. The KATRIN experiment [115], which aims to achieve a sensitivity of 0.2 eV for the electron neutrino mass, will further sharpen this constraint. In the framework of a R-parity conserving minimal supersymmetric extension of the SM (MSSM) a bound of $|D| \leq 10^{-7}$ is set by EDM measurements [116]. For leptoquark models it was believed that EDM limits would not constrain D: D could be as large as the present experimental limits [117]. However, recent work by Ng *et al.* [118] shows that for some of these models EDM measurements also provide stronger constraints on D (about $10 - 10^3$ stronger) than β-decay does currently. The precision that currently running β-decay experiments can be expected to achieve is still away from these bounds.

However, these alternative routes to bound non-SM physics depend on unknown model parameters and might fail under certain circumstances, see *e.g.* [117]. Furthermore EDM measurements provide little model-discriminating power and for example limits on D might still play an important role in untangling the nature of CP violation [118]. In addition, transitions in mirror nuclei (with a $N = Z$ core and a single valence nucleon) provide an alternative way (to superallowed Fermi transitions) to determine the Cabibbo-Kobayashi-Maskawa (CKM) $|V_{ud}|$ matrix element [119]. For these nuclei a correlation experiment is required in addition to the lifetime measurement. Therefore β-decay experiments remain powerful.

1.4 The ^{21}Na experiment at the KVI

Measuring the time-reversal violating term D requires a nucleus which decays by a mixed Gamow-Teller Fermi transition and has a moderate lifetime. ^{21}Na has these properties, see figure 1.2: it decays to its mirror nucleus, ^{21}Ne by positron emission and has a lifetime of 22.5 s. The structure of such nuclei is rather simple, allowing accurate determinations of the relative matrix elements. This is important for the interpretation of the correlation coefficients. ^{21}Na was already trapped in a MOT at Berkeley by Lu *et al.* in 1993 [120, 121], it was actually the first radioactive atom for which this was demonstrated[9]. ^{21}Na has nearly identical properties for laser cooling and trapping as stable ^{23}Na, which is routinely trapped in MOT systems. In principle the knowledge obtained with ^{23}Na in off-line measurements can thus be translated directly to ^{21}Na.

Some experience has thus already been built up with ^{21}Na: at Berkeley precision measurements of the correlation parameter a in ^{21}Na have been made [50, 63, 64, 122, 123]. The mixed transition in ^{21}Na allows to investigate all possibilities for non-SM searches in β-decay. To precisely determine the correlations of the decay products a sufficiently large number of point source like, substrate free and nuclear spin polarized ^{21}Na particles has to be obtained. The experiments presented in this thesis work towards this goal.

[9] The first radioactive atom trapped in a MOT is ^{87}Rb, but its long half-life of $5 \cdot 10^{10}$ years results in a natural abundance of 28%.

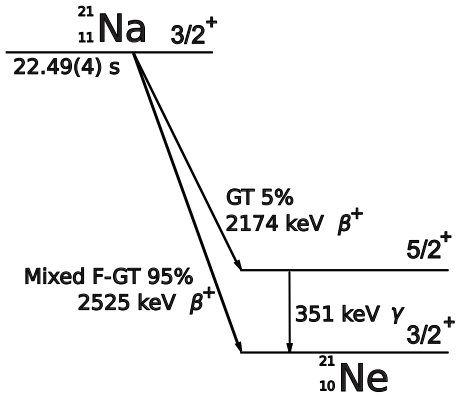

Figure 1.2: *The decay scheme of ^{21}Na [124]. The Q value of the decay is 3548 keV [119]. Because of its small branching ratio of $4{\cdot}10^{-4}$%, the decay to the $1/2^+$ state at 2794 keV is not shown.*

At the KVI the TRIμP facility has been set up to provide experiments, in a versatile way, with high intensity and high purity ion beams of short-lived isotopes. Using the AGOR cyclotron and a gas target a high-energy ^{21}Na ion beam is produced. It is separated from the primary beam by a dual magnetic separator [125–127]. The challenge is to efficiently convert this high-energy (MeV) ion beam into a low-energy (μeV) trapped atomic sample: a decrease in kinetic energy of 12 orders of magnitude.

The first stage after the production and separation is the ion catcher [128, 129]. In TRIμP the ion catcher is a thermal ionizer. It stops the ion beam in a stack of thin foils. Heating the stack allows one to extract the ^{21}Na particles as a low-energy (keV) ion beam. This ion beam is guided towards a dual Magneto-Optical Trap (MOT) system. In the first MOT cell (called the collector MOT) the ions are neutralized using a heated metal foil. After diffusing out and evaporating from the foil the atoms are then trapped with the combination of a magnetic field and laser cooling forces.

To provide a good environment for a high-precision study of the β-decay correlation parameters the trapped atoms are optically transported over a distance of about 1 meter into a second MOT chamber (referred to as the science MOT). ^{21}Na decays into ^{21}Ne, a positron and an anti-neutrino. In the second vacuum chamber the kinematics of this decay can be reconstructed by measuring the momenta of the emerging high-energy (MeV) positron and low-energy (maximally 229 eV) recoiling daughter ion. Therefore the trap center is viewed by a β detector and an ion spectrometer for the recoiling daughter ion. The anti-neutrino momentum can be reconstructed from the β and daughter ion momenta. The initial momentum of the point source like cloud of laser trapped atoms is extremely small compared to the outgoing momenta. From the reconstructed momenta the β-decay correlation parameters can be extracted. Details on this can be found in [69] and in [18].

The strategy for ^{21}Na is to first measure a and then D. Both A and a can be used

for a determination of $|V_{ud}|$. The value for the D parameter within the SM is negliglible small, $\sim 10^{-12}$. As already mentioned before, a systematic effect in D are QED final state interactions (FSI) between the daughter ion and the β particle, which mimics the D correlation [130]. In neutron decay $D_{\mathrm{FSI}} = 10^{-5}$ [131]. Veenhuizen [132] estimated for the neutron D_{FSI} to be of order 10^{-5} as well, for ^{19}Ne and ^{21}Na the FSI was found to be about 10^{-4}. By measuring the β momentum dependence of the FSI, it can be distinguished from the contribution from the true D [132].

When the required precision has to be achieved in a measurement of a day and under the assumption of a certain (coincidence) detection efficiency an efficiency budget for the experiment emerges [69].

To measure a correlation parameter with a relative precision of 10^{-4}, purely statistically about 10^8 coincidence events have to be detected in a single day. With the planned production rate and coincidence detection efficiency, a collection efficiency of 1% in the collection MOT and an atom transfer efficiency of 50% is required. In these considerations it was taken into account that not all ^{21}Na decays result in ions. A measurement of the charge-state distribution in ^{21}Na shows that about 20% of the decays shake off ≥ 2 electrons, leading to positive ions (no negative ions were detected) [122]. Only the ions are extracted by the electric field, also the MCP detector is much more efficient for ions than for neutrals. Both effects together make that maximally 20% of the recoils can potentially be detected efficiently.

In this thesis we report on our research that focuses on two crucial steps that are necessary to perform a measurement of the a and D correlation coefficients in ^{21}Na at the level of 10^{-4}. The first step is the neutralization of the low-energy ion beam and the subsequent capture of these neutral atoms in the collector MOT. The second step is the transfer to the science MOT.

1.5 Outline of this thesis

Chapter 2 introduces first the concepts of laser cooling and trapping of atoms in an atom trap (MOT). To put the results for Na in context we consider also for all other alkaline metal atoms the trapping efficiency of MOT systems loaded from a vapor. Furthermore we discuss the properties of the neutralization of the low energy ion beam and the problem of atoms sticking to the cell wall. We also consider the different approaches that can be taken to transfer the trapped atoms to a second atom trap. In chapter 3 the TRIμP production and separation facility and the double MOT β-decay setup is described. The demonstration of optical trapping of both sodium isotopes using the collector MOT setup is described in chapter 4. After extracting and discussing the various efficiencies the possible improvements are identified. Chapter 5 presents the double MOT transfer measurements done with an on-resonance push beam and the first enhancement of the transfer efficiency obtained by using an optical funnel. Finally, in chapter 6 the status of the ^{21}Na β-decay experiment is summarized and an outlook is given.

Chapter 2

Laser trapping of atoms from a neutralized ion beam

This chapter describes the neutralization of a low-energy ion beam and, after evaporation, the subsequent capturing of the atoms with a Magneto-Optical Trap (MOT). A MOT can slow down and confine atoms through a combination of three pairs of counterpropagating laser beams and a magnetic field. We transfer the atoms from the "collector cell" (CC) MOT to a second "science cell" (SC) MOT. The vacuum chamber, containing the SC MOT system, provides a low-background environment. Here a high precision measurement of the β-decay correlation parameters of ^{21}Na can be performed (see chapter 1).

In MOTs usually stable atoms are trapped. As the β-decay experiment will be done with radioactive ^{21}Na atoms, the key ingredients in are the efficiencies of the neutralization, collection and transfer process. The number of radioactive atoms available for trapping is very small due to the nature of the possible production mechanisms.

We could produce online, by colliding a high energy beam with a target, about 10^7 ^{21}Na/s. For a day of measurement and a typical detection efficiency, reaching the required precision of 10^{-4}, the CC MOT has to collect about 10^5 ^{21}Na/s. This implies that a collection efficiency of 1% has to be achieved for the CC MOT system.

A standard MOT system has a capture efficiency from a vapor of about 10^{-5}, which is a factor of a thousand lower than we need. For stable isotopes usually the source rate which can be achieved is typically 10^{12} /s, compared to 10^8 /s typically for radioactive atoms. Therefore a low capture efficiency is not an issue for experiments using stable atoms. In this chapter we focus, therefore, on maximizing the single-pass capture efficiency of a MOT and how to let the atoms pass as often as possible the laser trap volume (multi-pass capture efficiency).

We introduce the concept of the MOT in section 2.1. In section 2.2 we discuss a MOT which is loaded from a background vapor. For such a MOT the number of trapped atoms depends on the loading rate and the loss rate of the atoms into the trap.

The loading rate is related to the maximal velocity of the atoms for which a MOT can still slow the atoms and capture them: the capture velocity. A study of the literature shows that the capture velocity is rarely measured. Therefore we are interested in determining the capture velocity from a few simple observables of the MOT. To do so, the loss rate has to be calculated. To validate our calculation, we compare the prediction from an simple atom-atom loss rate model with experimental values.

In deriving the loading rate in section 2.2 we simplify the loading rate process by assuming that all atoms below the capture velocity entering the MOT volume will be trapped. This overestimates the capture efficiency, as the path through the trapping volume may be shorter than the diameter we assume. Therefore we consider in section 2.3 the loading rate in more detail by introducing the description of a 1D and 3D simulation of the capture process. In section 2.4 we compare the results from these simulations with experimental values.

In section 2.5 we calculate the capture velocity for a large variety of experiments where alkaline isotopes are trapped in a vapor MOT system. This overview allows us to compare the trapping of Na with the other alkaline elements.

The process of stopping a low-energy beam and the subsequent release of neutral atoms is described in section 2.6. In section 2.7 we review the literature for measurements related to adsorption energies and discuss studies of wall coatings which reduce the adsorption energy. Through simulations, introduced in section 2.8, we determine the number of times the atoms bounce in a cell and pass the laser trap volume. Together with the capture efficiency of the MOT and the release efficiency of the neutralizer this results in an overall trapping efficiency of atoms originating from neutralized ions.

After the ^{21}Na are trapped in the CC MOT, they need to be transferred to the SC MOT system which provides a background free environment. In section 2.9 we introduce five different strategies to transfer cold atoms between two MOT setups. We give an overview of the typical achieved transfer efficiencies of each method. After investigating the (dis)advantages of each type we conclude which approach fits our purposes best to achieve a transfer efficiency of 50%.

In section 2.10 we summarize how to achieve an overall ion to trapped atom conversion of 1% and how to transfer atoms between two MOT systems with 50% efficiency.

2.1 Laser cooling and trapping of atoms

The simplest system for laser cooling and trapping is a two level system: a ground state and an excited state. An atomic transition in such a two-level system can be made by photons with a wavelength λ corresponding to the energy difference of the levels. Alkaline atoms, which can be found in the left column of the periodic system (figure 1.1), have a single valence electron and provide such a simple level scheme.

The scattering rate of photons is the decay rate, Γ, from the excited state times

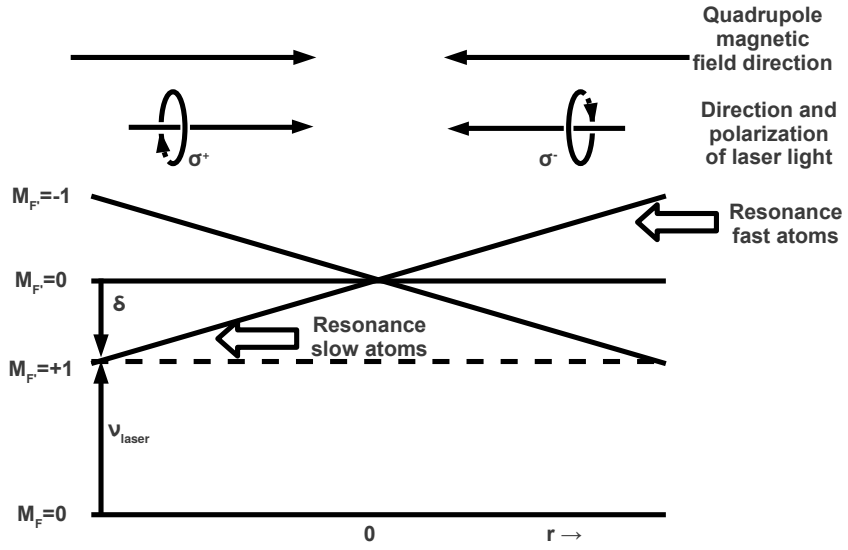

Figure 2.1: *The dependence of the force in a MOT on the velocity and position. We assume a $F = 0$ ground state and a $F = 1$ excited state. The Zeeman magnetic substate energy levels are labeled by m_F and shift up and down as function of the magnetic field strength. The σ^+ laser beam from the left can excite the $m_F = 0 \rightarrow m_{F'} = +1$ transition, the σ^- laser beam from the right can make the $m_F = 0 \rightarrow m_{F'} = -1$ transition.*

the fraction, in which it is in the excited state and is given by [48]

$$\gamma_{\mathrm{p}} = \frac{\Gamma}{2} \frac{s_0}{1 + s_0 + 4(\delta/\Gamma)^2} \,, \tag{2.1}$$

for a total detuning δ from the atomic transition and the saturation parameter s_0 in units of the saturation intensity

$$s_0 \equiv 2 \left(\frac{\Omega}{\Gamma} \right)^2 = \frac{I}{I_{\mathrm{s}}} \,, \tag{2.2}$$

where Ω is the Rabi frequency. The saturation intensity is given by

$$I_{\mathrm{s}} = \frac{\pi h c}{3 \lambda^3 \tau} \tag{2.3}$$

and is for Na for circular polarized light 6.3 mW/cm^2 for the $|F = 2, m_F = \pm 2\rangle \rightarrow |F = 3, m_F = \pm 3\rangle$ transition.

The transition frequency of an atom moving with a velocity v is shifted by the Doppler shift $\delta_{\text{Doppler}} = kv = \frac{2\pi v}{\lambda}$. Therefore the scattering rate of an atom depends on the velocity vector, a velocity towards a laser beam shifts the atomic transition up, in the other direction the transition shifts down. For a moving atom in a magnetic field, the total detuning with respect to the atomic transition is the sum of four frequency shifts,

$$\delta = \delta_{\text{Doppler}} + \delta_{\text{laser}} + \delta_{\text{Zeeman}} + \delta_{\text{Stark}} \,, \tag{2.4}$$

where δ_{laser} the detuning of the laser from the atomic transition, δ_{Zeeman} is the shift due to the magnetic field, and δ_{Stark} the shift due to an electric field. For a MOT system δ_{Stark} is negliglible[1].

In figure 2.1 the principle of the MOT is shown. A moving atom from the right start scattering photons from the left laser beam, already when it is on the right side of the trap center. The Doppler shift is compensated both by the laser detuning and the Zeeman shift. The energy level, for which the right laser beam can make the transitions, shifts in the opposite direction. Atoms which enter the laser beams primarily scatter photons from the laser beam opposite to their direction of moving and are slowed down.

Momentum transfer between a laser beam and an atom with mass m is the result of asymmetry in the direction of the absorption of the photons and the direction of the decay of the photons. The absorption takes place from a single direction, while the decay process is (almost) isotropic. Each photon contributes

$$\Delta v = \frac{\hbar k}{m} \,. \tag{2.5}$$

The force from a single laser beam is

$$F = \hbar k \gamma_{\text{p}} = m v_{\text{r}} \gamma_{\text{p}} \,, \tag{2.6}$$

where the recoil velocity is

$$v_{\text{r}} = \frac{h}{m\lambda} \,, \tag{2.7}$$

which is 2.95 cm/s for Na.

The net force from a pair of counter-propagating laser beams is a velocity dependent force. For a red (negative) detuned laser frequency the force decelerates atoms, for a blue (positive) detuned laser beam the atoms are accelerated. An example is shown in figure 2.2a. By using three orthogonal pairs of counter-propagating laser beams an Optical Molasses (OM) is created: from all three directions the atom is slowed until near zero velocity. OM were demonstrated first by Chu *et al.* [133] using sodium atoms in 1985, they achieved a trap time of about 0.1 s. The capture velocity of an OM is (to within a factor of 2) Γ/k [134], which is in the case of sodium 6 m/s.

[1] For an optical dipole trap potential, as we will encounter in section 2.9, it has to be included.

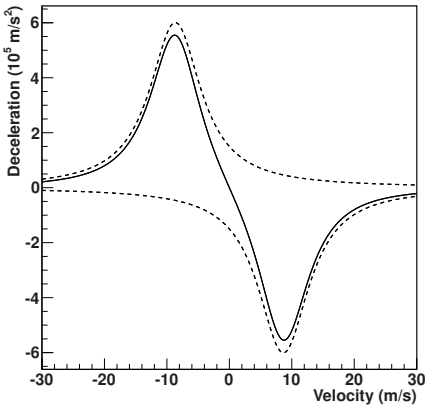

(a) *Optical Molasses (OM), the magnetic field and the magnetic field gradient are zero.*

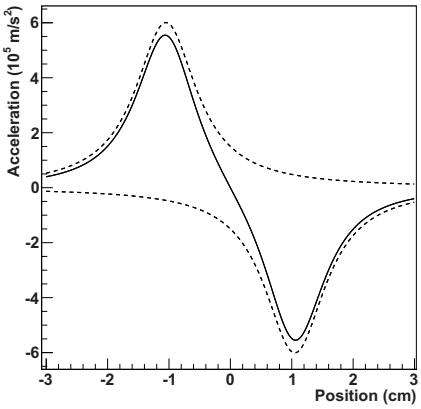

(b) *The spatially restoring force in a MOT due to a linearly increasing magnetic field of 10 Gauss/cm. The velocity is zero. At the center position the magnetic field is zero.*

Figure 2.2: *The velocity (a) and spatially (b) dependent force in a MOT for a sodium atom. The deceleration is due to the optical forces from a pair of counterpropagating laser beams (dashed, equation 2.6) and the sum of both forces (solid). The laser intensity is* $2s_0$ *and the laser detuning is* $\delta = -1.5\Gamma$.

By adding a magnetic quadrupole field to the OM, a restoring force which depends on the position is introduced (see figure 2.1). The acceleration due to the Zeeman shift induced by a quadrupole field gradient of 10 Gauss/cm is shown in figure 2.2b. For a magnetic quadrupole field, generated for example by a pair of coils in anti-Helmholtz configuration, the magnetic field lines in the axial direction go in opposite direction of the field lines in the radial direction. In figure 2.1, the handedness of the light is therefore also opposite. In one axis, the same handedness of the light is needed, although the labeling with $\sigma^{\pm}$ suggests that the properties of the pair of laser beams are different. As shown in figure 2.1, for a magnetic field going inwards right handed circular polarized light is required[2].

It is no coincidence that the deceleration has the same dependence on position as on velocity. For a quadrupole field the magnetic field is linearly dependent on the position. The shape is the same as the Doppler shift and Zeeman shift are both linear in velocity and position, respectively. Such a configuration of a magnetic field combined with laser fields is called a Magneto-Optical Trap (MOT), where slowing and spatial trapping of neutral atoms can be achieved. The first time that this was experimentally demonstrated was for sodium atoms by Raab *et al.* [27] in 1987.

[2]Circular polarized light is mostly used to create a MOT, there are others other possibilities, for example using only linearly polarized light also a MOT can be created [135, 136].

The scatter rate of photons is maximal when the laser beam is on resonance with the atomic transition, about 30 million photons are then scattered per second. As each photon results in a momentum change of about 3 cm/s, the corresponding maximal deceleration is $9 \cdot 10^5$ m/s^2, *i.e.* about 10^5 times the gravitional acceleration. The laser detuning and the Zeeman shift can compensate for the Doppler shift of a moving atom, bringing the atom on resonance with the transition.

The combination of the detuning and the magnetic field gradient has to be such that during the whole slowing process the deceleration can still be provided by the scattering rate. The magnetic field gradient also affects the density of the atom cloud. For high atom density collisions between trapped atoms may lead to trap loss. In section 2.3 we will study the dependence of the capture velocity of the MOT on the MOT parameters.

The capture efficiency of a vapor MOT depends on the capture velocity, its dependence can be found by calculating the fraction which can be captured by a MOT from a vapor at room temperature. The velocity distribution of an atomic gas is described by the Maxwell-Boltzmann distribution,

$$f(v)d^3v = \frac{2}{\pi^{3/2}v_p^3} e^{-\left(\frac{v}{v_p}\right)^2} v^2 \sin\theta \, dv d\theta d\phi \quad , \tag{2.8}$$

with $v_p = \sqrt{\frac{2kT}{m}}$ is the most probable velocity and the average velocity $\langle v \rangle = \frac{2}{\sqrt{\pi}} v_p$. At room temperature $v_p = 460$ m/s. The fraction of the Maxwell-Boltzmann distribution which is captured is found by integrating the velocity distribution from 0 to the capture velocity v_c,

$$P = 4\pi \int_0^{v_c} f(v) v^2 dv \; . \tag{2.9}$$

In leading order this fraction of the Boltzmann distribution is

$$P = \frac{4}{3\sqrt{\pi}} \left(\frac{v_c}{v_p}\right)^3 \quad , \tag{2.10}$$

which is a good approximation as $v_c \approx 30$ m/s.

As the trapping efficiency is proportional with v_c^3, maximizing the capture velocity is of crucial importance to achieve an efficient MOT operation.

2.2 Determination of the capture velocity from the loading and loss rate

In an equilibrium situation, the number of trapped atoms in a MOT loaded from a background vapor depends on the loading rate of atoms into the MOT and the loss rate of trapped atoms. The loading rate depends on the single-pass capture efficiency of the MOT, the MOT volume and the vapor density. The loss rate is primarily due to

collisions of trapped atoms with untrapped atoms from the vapor[3]. As we will see the loading rate and collision rate under these conditions depend both linearly on the vapor density, *i.e.* the number of trapped atoms is independent of the vapor density. If the number of trapped atoms, the trap volume and the loss rate is known, the capture velocity can be calculated. In this section we calculate the loading and loss rate for this purpose.

A Zeeman slower is used to load only cold atoms in a MOT, this circumvents the problem of the vapor MOT, where increasing the vapor density does not increase the number of trapped atoms. In a Zeeman slower, a spatial varying magnetic field[4] keeps the slowing atoms on resonance with a counterpropagating laser beam [138]. However, a Zeeman slower only cools one dimension of an atomic beam and requires for efficient operation a beam which is already cooled in the other two dimensions[5]. In the Zeeman slower the initial velocity in the transverse direction increases due to the recoil-induced heating from the slowing process. This transverse velocity becomes important especially towards the end of the Zeeman slower, where the beam velocity is low and approaches the capture velocity of the MOT.

For vapor cell based experiments overall efficiencies of order 1% have been demonstrated [81]. A Zeeman slower approach typically has a slowing efficiency of about 10-100%. The efficiency of the the source to be used with a Zeeman slower is generally lower than that for a vapor MOT.

The decision was made early for the ^{21}Na experiment to use a vapor cell based system instead of a Zeeman slower based system. In the context of the production of other elements the vapor based setup is more generic. Therefore we focus the discussion here only onto a study on v_c and do not discuss the Zeeman slower approach. However, we will use data obtained with Zeeman slowers, because they provide valuable information on the capture velocity of a MOT.

Loading rate

For a MOT loading from a background vapor the rate equation for the number of trapped atoms N is given by

$$\frac{\mathrm{d}N}{\mathrm{d}t} = R - \frac{N}{\tau} - \beta \int n_{\mathrm{M}}^2(\vec{r},t)\mathrm{d}^3r \approx R - \frac{N}{\tau} - \beta n_{\mathrm{M}} N \ , \tag{2.11}$$

where R is the loading rate and τ is the lifetime of the MOT cloud due to collisions of the trapped atoms with the background gas. The last term represents the losses which depend quadratically on the density profile $n_{\mathrm{M}}(\vec{r})$. For the right-hand side, it is assumed that the density of trapped atoms n_{M} is constant throughout the MOT cloud.

[3] For a high atom density in the MOT also collisions between cold, trapped atoms can result in a loss.

[4] Similarly, laser cooling of a sodium atomic beam using the Stark effect has also been demonstrated [137].

[5] This can be accomplished with a transverse cooling stage, as for example is demonstrated in [139].

In the case that the contribution of density dependent loss can be neglected the solution to the rate equation is

$$N(t) = R\tau(1 - e^{-\frac{t}{\tau}}) . \tag{2.12}$$

Both R and the loading (and decay) time τ can be deduced from a measurement of the fluorescence of the trapped atoms.

At pressures $\geq 10^{-8}$ mbar the collisions with the background gas dominates. For such a pressure the loading time τ is about 1 s [48, 140]. To give an impression, for a loading time of 15 sec the density dependent loss results in a reduction of a factor of 2.5 in the equilibrium number of trapped atoms for Na [141]. For better vacuum conditions the situation is reversed [142]. From a certain number of trapped atoms, the density of trapped atoms remains constant and the volume of the MOT cloud increases. In a MOT density dependent losses are then not always recognized as such [143].

As the lifetime of the MOT is not only due to the sodium vapor, we write

$$\frac{1}{\tau} = \frac{1}{\tau_{\mathrm{Na}}} + \frac{1}{\tau_{\mathrm{res}}} , \tag{2.13}$$

with τ_{Na} the lifetime due the partial pressure of sodium and τ_{res} the lifetime due to the remaining residual background gases. Unless mentioned otherwise, we assume that the lifetime of the MOT cloud is dominated by the vapor from which the atoms have to be trapped. For the equilibrium situation, where the number of trapped atoms is constant,

$$N = R\tau . \tag{2.14}$$

The lifetime is related to the vapor density n by [144]

$$\tau = \frac{1}{n\langle\sigma v\rangle} , \tag{2.15}$$

with v the velocity of the background gas atoms and σ the cross section to knock out an atom from the MOT. This cross section depends on the energy of the colliding particle. The brackets indicate that the average value over the Boltzmann velocity distribution is taken.

Consider a rate of atoms loading into the MOT with a capture range $0 - v_{\mathrm{c}}$ from a vapor with density n and temperature T. Atoms with a speed between 0 and v_{c} are trapped, the average speed of this lower tail of the velocity distribution is

$$\langle v\rangle = \frac{3}{4} v_{\mathrm{c}} . \tag{2.16}$$

The surface area of the intersecting volume of three cylinders with diameter d at right angles is $6(2 - \sqrt{2})d^2$. The unit flux through this surface is given by $\frac{1}{4}n\langle v\rangle$ (equation B.1). Atoms entering the laser volume with a velocity smaller or equal to v_{c}

are assumed to be trapped. The loading rate is then given by the so-called Reif Model [145]

$$R = \frac{nP\langle v_c\rangle}{4} 6(2-\sqrt{2})d^2 \approx 0.50 \frac{nd^2 v_c^4}{v_p^3} , \tag{2.17}$$

with P the fraction of the Boltzmann distribution given by equation 2.10. The maximal number of atoms trapped is

$$N \approx 0.50 \frac{d^2 v_c^4}{v_p^3 \langle \sigma v\rangle} , \tag{2.18}$$

In appendix B we show that the atom density may not be uniform, as we assume here. This may modify the loading rate slightly.

In deriving this loading rate we assumed that every atom with $v \leq v_c$, which enters the MOT trapping volume, will be trapped. Atoms which have a velocity which is close to v_c, but intersect the MOT volume only a fraction of the diameter can not be decelerated sufficiently to be trapped. When the atom density is uniform, the distribution of the length s for the atoms passing through a sphere (the trap volume) with diameter d is linear, see appendix B. Compared to the situation where all atoms entering the trapping volume are stopped for $v < v_c$, the loading rate is lowered by a factor

$$\frac{8}{d^2 v_c^4} \int_0^d \mathrm{d}s \int_0^{v_c\sqrt{\frac{s}{d}}} \mathrm{d}v \; v^3 s = \frac{1}{2} . \tag{2.19}$$

We assume here that the atoms are subject to a constant deceleration. The loading rate, based on this simple 1D estimate, is thus given by

$$R_{\text{geo 1D}} = \frac{1}{2} R . \tag{2.20}$$

In the next section we address this factor again when we discuss the results of a 3D Monte Carlo simulation of the MOT capturing process.

Summarizing, we calculated the loading rate of atoms from a vapor for a MOT with a capture velocity v_c. Our calculation assumes that the intra-trap collision loss rate in the MOT system can be neglected. Because of the constant density regime this is difficult to confirm experimentally. As a rule of thumb the loading time should be at most 1 s. Furthermore we calculated that, because of the distribution in intersection lengths in a MOT, the loading rate is reduced by a factor of 2 compared to the commonly used estimate for the loading rate based on the Reif model.

Loss rate model for a vapor MOT

In appendix A we introduce the model for the loss rate for a vapor MOT. In short, the model entails the following: Two types of collisions can occur between trapped (cold) atoms and hot background atoms: the cold atom is in the ground- (S) or excited (P) state; the hot atoms are in the ground state. Not all collisions lead to trap loss. Only

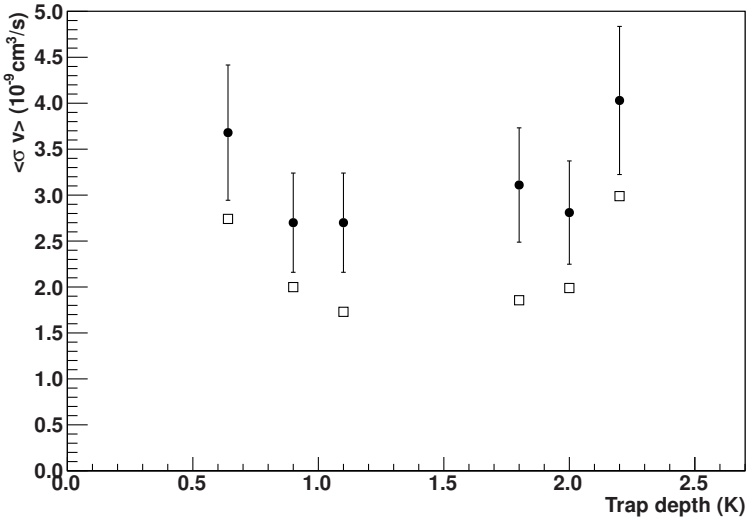

Figure 2.3: *The measured loss rate (solid symbols) from the Madison group and the theoretical values from the loss rate model (open symbols), as function of the trap depth [146].*

Table 2.1: *Measured knock-out cross sections $\langle\sigma_{\mathrm{exp}}\rangle$ and the calculated value $\langle\sigma_{\mathrm{th}}\rangle$.*

Trapped species	Background species	$10^{14}\langle\sigma_{\mathrm{exp}}\rangle$ (cm^2)	$10^{14}\langle\sigma_{\mathrm{th}}\rangle$ (cm^2)	$\frac{\langle\sigma_{\mathrm{exp}}\rangle}{\langle\sigma_{\mathrm{th}}\rangle}$	Ref.
Na	N_2	3.3	2.6	1.3	[147, 148]
Na	Na	∼100	15	6.7	[149]
Rb	N_2	3.5 ± 0.4	2.7	1.3	[148, 150]
Rb	Rb	∼30	9.0	3.3	[150]
Cs	Cs	20	20	1.0	[145]

when the collision results in a transferred momentum, leading to a velocity exceeding the escape velocity, the initially cold atom escapes from the MOT. The loss rate from excited-ground state collisions is typical a factor of 10 larger than ground-ground state collisions, but the atoms only spend typically 10% of the time in the excited state, making the contribution from both types of collisions about equal.

To calculate the loss rate, which is proportional to $\langle\sigma v\rangle$, the values for the Van der Waals coefficient C_6 (for the $S-S$ collisions) and for C_3 (for the $S-P$ collisions) are needed. Both values can be found in literature (see appendix A). We use the

peak intensity of the laser beams and the detuning of the laser from the transition to calculate the fraction of the time the atoms spend in the excited state. The overall loss rate has a slight dependence on v_c itself (equation A.4 and A.9), as the escape velocity is related to the capture velocity.

To see to which extent our calculation of $\langle\sigma\rangle$ and $\langle\sigma v\rangle$ are realistic, we compare our calculations with experimental values. In appendix A, we find in figure A.1 good agreement with the experimental data from a Rb MOT where the dependence of the collision rate due to argon gas was studied. Our calculation is about 10-20% above the experimental data.

A source of systematic error for the loss rate model is the excited-state fraction (see appendix A). The scatter rate per atom is the excited-state fraction times Γ [48]. A determination of the excited-state fraction is thus directly related to the determination of the number of trapped atoms. Throughout this thesis we calculate the number of atoms in the MOT by using the saturation intensity for isotropic, instead of circular, polarized light for the $|F = 2, m_F = \pm 2\rangle \rightarrow |F' = 3, m_{F'} = \pm 3\rangle$ transition, which is 13.41 mW/cm^2 for Na [151]. Using this value gives the most accurate number of atoms in a MOT [152]. We became aware later of the work done by Shah *et al.* [153], who accurately studied the excited state fraction as function of the laser intensity. We use their factor of 2.8 (first we used the factor of 2 mentioned before) for the calculation of the excited state fraction for the loss rate model.

In figure 2.3 measured loss rates for a ^{87}Rb MOT are compared with the predictions of the loss rate model. The measured data are preliminary and are from the Madison group at UBC, Vancouver [146]. More details about their setup and the used methods can be found in [154, 155]. To measure the trap depth of the MOT, they use the Photo Association (PA) technique, pioneered by Walker's group [156]. In short, an extra laser (referred to as the catalysis laser) excites two colliding Rb atoms to an excited molecular state. After dissociation both atoms fly apart with opposite momentum, each carrying half the energy of the absorbed photon from the catalysis laser. By measuring the loss dependence on the catalysis laser frequency the trap depth of the MOT can be determined.

In figure 2.3 the theoretical values fall approximately 30% below the measured values. The source of this disagreement is still subject of investigation. In table 2.1 we compare more experimental values for the loss rate observed in vapor MOTs to our calculations. For the Cs-Cs experiment the agreement is good[6]. For two other measurements the disagreement is a factor of 1.3, but for both the C_6 value is not known, this results in a smaller theoretical value. For Na-N we assume a capture velocity of 15 m/s and a vapor at room temperature. For the two values (Na-Na and Rb-Rb) for which the disagreement is large, unfortunately no estimate for the error is given[7].

[6] A later publication suggests at least a factor two as error for the experimental value, see page 46 of [157].

[7] For the ^{85}Rb experiment from [158], agreement with the experimental value is found in a calculation similar to ours.

The loss rate model gives a satisfactory description within a factor of 1.5. Only for Na-Na a significant discrepancy is observed.

The relationship between the loading and loss rate, enabling extraction of the capture velocity can now be quantified. Combining equations 2.14, 2.15, 2.17 and equation A.11, the capture velocity is approximated as

$$v_c \approx \sqrt[4]{\frac{2Rv_p^3}{nd^2}} \approx v_p \sqrt[4]{\frac{2\alpha\langle\sigma\rangle N_0}{d^2}} \,. \tag{2.21}$$

The parameters to calculate v_c are the number of trapped atoms N_0, the laser beam diameter d and the temperature of the vapor (v_p). $\langle\sigma\rangle$ is the Boltzmann averaged knock-out cross section, α is a factor between 0.97 and 1.05 (equation A.13). This phenomenological determination allows to estimate v_c in an alternative way provided some basic MOT observables are known.

2.3 Capture velocity: level structure and geometrical effects

The dependence of the capture and escape velocity on magnetic field gradient, laser intensity, laser detuning and laser beam diameter can be calculated with a simple 1D numerical simulation as can be found in textbooks [48]. In the 1D simulation the sum of the forces due to two counterpropagating laser beams (equation 2.6) are integrated numerically over a fixed distance $2r$: the laser beam diameter.

With the MOT, besides a capture velocity, also an escape velocity (or trap depth) is associated. The capture velocity is defined as the velocity for which the atom starting from the edge of the laser trap volume will be trapped. The escape velocity is defined as the maximal velocity an atom trapped in the center can have such that it cannot be slowed down again by the MOT and is lost. When the atom is trapped the velocity is practically zero. The escape velocity plays a role in processes with an instantaneous increase of the velocity such as occur in collisions. The larger the escape velocity v_e, the more robust the MOT is against loss processes.

Both the capture and escape velocity might be non-isotropic in nature and are, of course, closely related to each other. As the atom can be slowed down over about twice the distance as compared to the escaping atom, the capture velocity can be considered as an upper bound of the escape velocity. The difference can be expected to be about a factor of $\sqrt{2}$. This has also been observed for Na [159–161]. Also for Rb a similar factor of 1.29 ± 0.12 was recently found [155, 162].

In figure 2.4 we show the dependencies of the capture and escape velocity on four MOT parameters. The capture efficiency depends on the third power of the capture velocity v_c (equation 2.10). For the four MOT parameters we have chosen typical values for a Na MOT. For these values the capture velocity depends strongly on the laser detuning and the magnetic field gradient. The capture velocity drops sharply when the intensity becomes less than 0.2 s_0, this is also the case when the beam diameter falls below 10 mm.

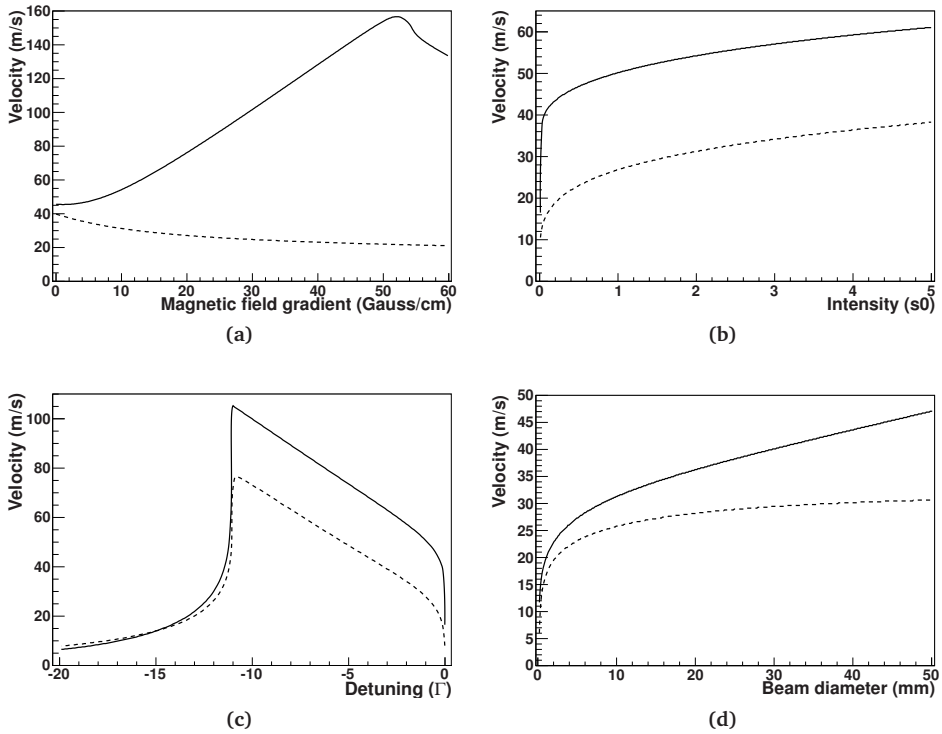

Figure 2.4: *Results obtained with a numerical simulation in 1D of the capture process in a MOT of atoms with a two level system. Shown are the dependence of the capture velocity v_c (solid lines) and escape velocity v_e (dashed lines) on the magnetic field gradient (a), the laser intensity (b), the laser detuning (c) and the laser beam diameter (d). In these figures, unless the parameter is varied, the magnetic field gradient is 10 Gauss/cm, the laser intensity is $2s_0$, the laser detuning $\delta = -1.5\Gamma$ and the total stopping distance (laser beam diameter) is 25 mm.*

From figure 2.1 it can be seen that besides providing the spatial trapping, the magnetic field in a MOT actually acts as a small Zeeman slower [48]. However, compared to a Zeeman slower the shape of the magnetic field in a MOT is suboptimal: the deceleration is maximal near the edge of the laser beam. It can be expected that the magnetic field gradient has to be decreased when the laser beam diameter is expanded, this is indeed observed in experiments [163].

Our model of the capture process assumes that the state of the atom can be represented by two levels. Most alkaline isotopes have more levels, figure 2.5 shows the level scheme for ^{21}Na and ^{23}Na. Both have two ground hyperfine levels and four hyperfine levels in the $^2P_{3/2}$ excited fine level. Usually the MOT is operated on the $F = 2 \rightarrow F' = 3$ transition as a cooling transition and the $F = 1 \rightarrow F' = 2$ transition

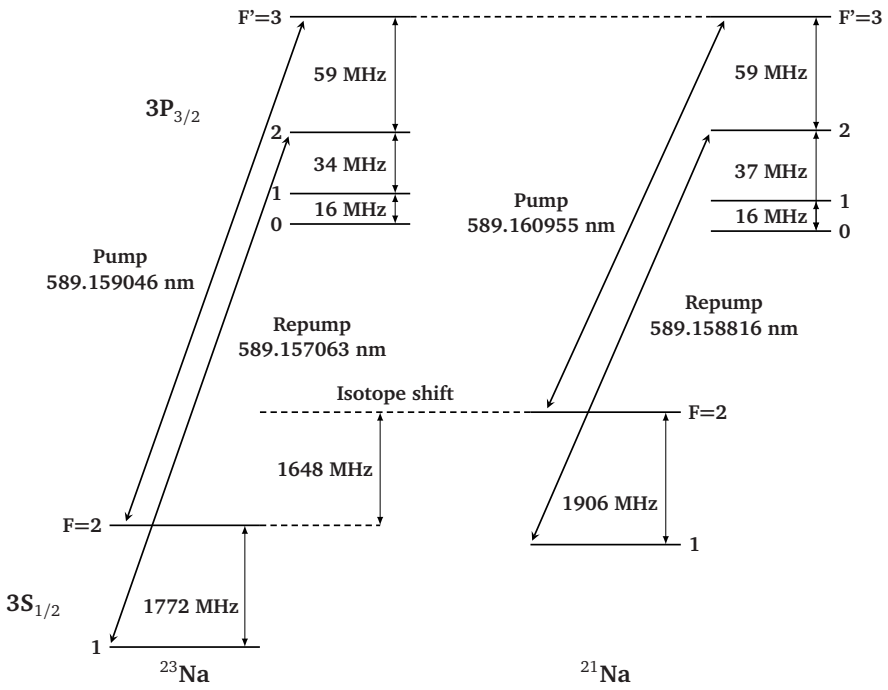

Figure 2.5: *The hyperfine ground (F) and excited states (F') relevant for optical trapping of ^{23}Na and ^{21}Na [123, 151]. The natural linewidth of the transitions is 9.8 MHz. With the S and P states; only the hyperfine splittings are to scale. The Zeeman shift for the $|F = 2, m_F = \pm 2\rangle \rightarrow |F' = 3, m_{F'} = \pm 3\rangle$ transition is 1.4 MHz/Gauss [151].*

is used as a repump transition. A repump laser is necessary as the cooling cycle is not closed perfectly, the atoms end up in the $F = 1$ ground state after some time. Also initially the atoms are distributed over both ground states. The laser saturation intensity is the lowest for the combination of the highest F and highest m_f magnetic sub-state in the ground and excited state, in literature this combination of cooling and repump transition is called a Type I MOT. For a certain amount of laser power therefore the maximal force is exerted on the atoms.

For a typical red detuning of -15 MHz the atoms scatter mostly photons from the cooling laser, only a fraction of the time the atom scatters light from the repump laser. When a considerably larger negative detuning than -15 MHz to the $F = 2 \rightarrow F' = 3$ transition is used, the result is an increase of the anti-trapping force, as the detuning is positive, from $F = 2 \rightarrow F' = 2$ transition. Also the atoms are driven more strongly to the $F = 1$ hyperfine ground state where they have to be pumped back into the cooling cycle, requiring more repump laser intensity.

MOT experiments show that for a Type I Na MOT the optimal detuning is in the range of -20 to -10 MHz and the optimal axial magnetic field gradient is in the range

5-10 Gauss/cm [164–167]. The capture velocity is largest for a laser beam intensity of about 8 mW/cm^2, corresponding to an intensity of 1.3 s_0 [161].

The anti-trapping problem is only entirely avoided for Na when a red detuning with respect to the $F = 1 \rightarrow F' = 0$ transition is chosen. A combination of a type I and a type II (where the $F = 2 \rightarrow F' = 2$ is used as a cooling transition) trap has been demonstrated for Na [168]. Tanaka *et al.* found a detuning of -11 MHz for the former to be optimal, for the latter this was a detuning of -18 MHz. Using this two-color trap the number of trapped atoms increased with a factor of 3, compared to a type I MOT. The disadvantage is that the saturation intensity of the $|F = 1, m_F = \pm 1\rangle \rightarrow |F' = 0, m_{F'} = 0\rangle$ transition is three times the saturation intensity of the $|F = 2, m_F = \pm 2\rangle \rightarrow |F' = 3, m_{F'} = \pm 3\rangle$ transition [48], so more laser light is required.

Two possible methods to increase the flux of slowed atoms from an atomic beam is to chirp the laser frequency or apply broadband light. In case of frequency chirping the laser frequency is swept from large to small detunings [169], broadband light, or "white-light" containing several closely spaced frequency components [170]. Besides using to slow atomic beams, "white-light" has also been successfully demonstrated for an ion beam [171]. However, Lindquist *et al.* [157] found that for MOT, both methods did not improve the number of trapped atoms in the case of Cs. For another Cs experiment and also a Na experiment, adding sidebands and chirping did not improve the collection process of the MOT [163]. Possible reasons why the situation for a MOT is more complicated than for an atomic or ion beam can be found in [157, 172, 173].

In the previous section in the derivation of the loading rate we assumed that all atoms, which enter the MOT trapping volume, were captured. A rough estimate using a 1D model of the slowing process gave that this approximation results in an overestimate of the true loading rate with a factor of 2. We performed Monte Carlo simulations in 3D to determine the error introduced by this approximation more precisely, here we describe the model we used.

The complicated level structure of the sodium atom is approximated with a simple two level system representing the $|F = 2, m_F = \pm 2\rangle$ and $|F' = 3, m_{F'} = \pm 3\rangle$ cooling cycle. In the calculation we include the stimulated emission of excited states from the same laser beam causing the excitation, but neglect the stimulated emission from the other five laser beams. This is a good approximation for the slowing process.

In the simulation the laser beams fill a cubic cell. We use a Gaussian profile for the intensity. The peak intensity, the beam waist and the aperture size can be chosen differently for each axis. For the angular distribution of the particle release three types have been implemented. The atoms are released from all six walls of the cubic cell according to a cosine emission angular distribution, isotropically or are released perpendicular to the cell wall. A Zeeman slowed atomic beam can be simulated by letting the atoms enter the MOT beams under an angle of 45°in the horizontal plane (usually the axial direction is perpendicular to the Zeeman slower axis). The size of the atomic beam can be set arbitrarily (including zero).

We use a quadrupole field generated by an anti-Helmholtz configuration, where

the separation of the coils is 63 mm. The calculated field can be found in figure 3.11. Almost anywhere in the MOT trap volume the polarization components of the light have to be transformed, as they are not in the direction of the magnetic field lines, according to

$$E'_{\sigma'} = \sum_{\sigma} D^{1*}_{\sigma,\sigma'}(0,\theta,\phi)E_{\sigma} \ , \tag{2.22}$$

where $D^{1*}_{\sigma,\sigma'}(0,\theta,\phi)$ is the Wigner D-function and θ and ϕ are the spherical coordinates for the magnetic field vector [174]. The polarization is labeled with $\sigma = 0$ for linearly polarized light, $\sigma = -1, 1$ stands for left and right polarized light, respectively. In Wigner d-matrix elements gives $D^{1*}_{\sigma,\sigma'}(0,\theta,\phi) = d^{1}_{\sigma,\sigma'}(\theta)\mathrm{e}^{i\sigma'\phi}$. We do not calculate the transition strength of the $\sigma^{\pm,0}$ transitions for all five magnetic sub-states of the $F = 2$ ground state to all the seven magnetic sub-states of the $F = 3$ excited state combinations. We assume that the scattering from the $F = 2, m_F = \pm 2$ to the $F = 3, m_F = \pm 3$ magnetic sub-state dominates the slowing force. We take the reduced slowing force for this component into account by reducing the intensity with a factor

$$d^{1}_{1,1} = \frac{1+\cos(\theta)}{2} \ . \tag{2.23}$$

As we neglect optical pumping to the other magnetic sub-state levels, which results in a decrease in the trapping force, or even an anti-trapping force, this Monte Carlo simulation gives an upper bound for the capture and escape velocity.

The Monte Carlo (MC) simulation is implemented in Matlab and vectorized to speed up the calculation. Typically 10^4 particles are simulated at once, the simulation stops when the slowest particle has been tracked for a time of 5 ms. The condition to be trapped is that at the end of the simulation the particles are within a sphere which has a radius of 2 cm and the magnitude of the velocity has to be within 3 m/s. These values are chosen relatively large as for the chosen time scale the fastest atoms, which went through the center and were stopped, are still moving back to the center. In the meantime untrapped particles are not anymore in the trapping volume. To determine the escape velocity, the atoms are released isotropically from the center of the MOT.

2.4 Comparison of 3D simulation with experimental observations

To test the validity of the 3D MC simulation we compare several predictions with experimental data from a ^{87}Rb MOT of which the properties were studied in great detail [146, 154, 155]. We are primarily interested in the comparison of the MC results with the experiment. The main goal is to verify the MC estimate of the reduction in the loading rate due to geometrical reasons.

For the simulation we use the parameters from table 2.2. The repump laser is tuned to the $F = 1 \rightarrow F = 2$ resonance and its intensity is typically around 1.4 mW/cm^2.

The data in table 2.2 are preliminary and are from the Madison group at UBC, Vancouver [146]. More details about their setup and the used methods can be found

Table 2.2: *The parameters used for the Vancouver ^{87}Rb MOT.*

	x, y axis	z axis
Aperture diameter (mm)	9	10
$1/e^2$ intensity diameter (mm)	7.4	8.4
Magnetic field gradient (Gauss/cm)	14	28

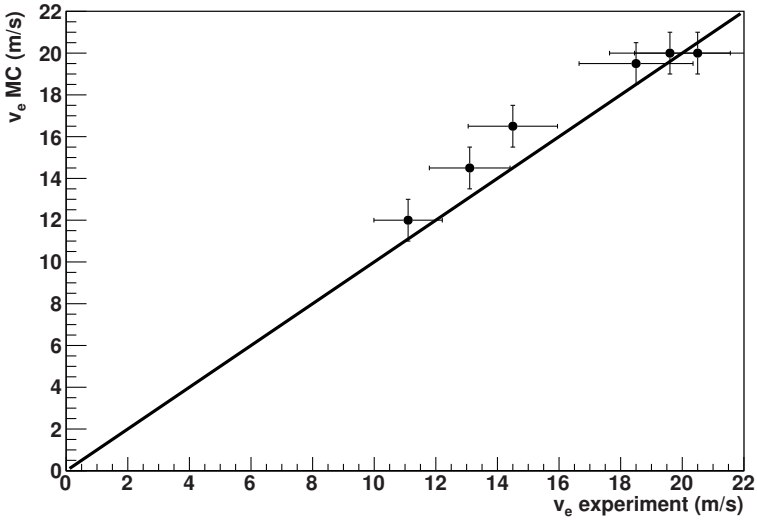

Figure 2.6: *The prediction for experimental measured values for the escape velocity for a ^{87}Rb MOT and the predictions from the 3D Monte Carlo (MC) simulation (see text).*

Table 2.3: *The atom number for a given trap depth and the corresponding MOT parameters for the ^{87}Rb Vancouver setup. The trap depth is measured with the Photo Association technique (see text).*

Trap depth	Detuning	Peak intensity	Atom number
(K)	(MHz)	(mW/cm^2)	(10^7)
2.2	-12	84	7.7
2.0	-12	21	9.5
1.8	-12	16	10
1.1	-10	6	3.0
0.90	-8	6	3.2
0.64	-5	6	1.4

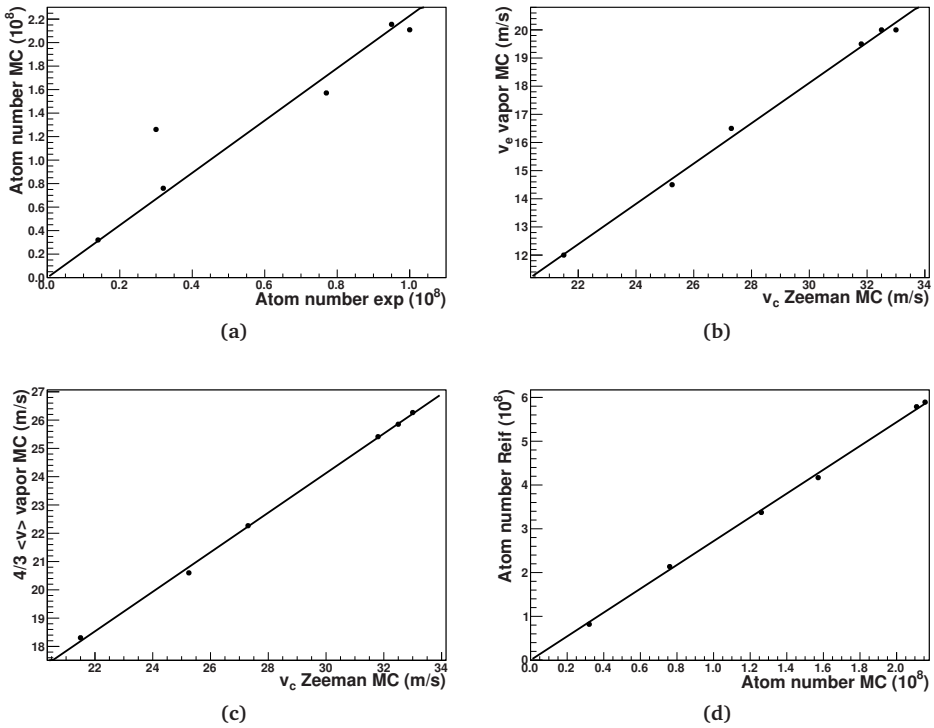

Figure 2.7: *Comparisons between experimental values, results of the 3D Monte Carlo (MC) simulation and the prediction by the Reif model. The points are obtained with different laser detunings and/or laser intensity (see table 2.3). The correlation between the number of trapped atoms observed experimentally and the prediction of the MC model (a). The relation between the escape velocity and the capture velocity in the plane (for a Zeeman slowed beam) (b). The relation between the capture velocity (equation 2.16) and the capture velocity in the plane (c). The number of trapped atoms predicted, using the value of v_c from (b) and the number of trapped atoms predicted by the MC model (d).*

in [154, 155]. To measure the trap depth of the MOT, they used the Photo Association (PA) technique, pioneered by Walker's group [156]. They determined the number of trapped atoms with a method developed by Chen *et al.* [175], which is supposed to be more robust than the standard fluorescence and absorption method to determine the atom number[8]. We calculate the number of atoms by combining the result from the MC simulation with the result of the loss rate model (appendix A),

$$N = \frac{1}{4}\langle v\rangle 6\pi(d/2)^2 \frac{\epsilon\eta}{\langle\sigma v\rangle} \ . \tag{2.24}$$

where $\langle v\rangle$ is the average velocity of the atoms which end up trapped, assuming a thermal gas. In the MC simulation the atoms are uniformly released from a circle with diameter d (the laser beam diameter) and ϵ is the fraction of the Boltzmann distribution, which is captured by the MOT. Finally, we take into account $\eta = 0.28$, the isotopic abundance of ^{87}Rb in the source used.

In figure 2.6 we compare the predictions of the model with experimental values from the Madison group, found using Photo Association (PA). The mean value for the simulation is the velocity for which 50% of the atoms are lost, the error is the velocity range for which 10% and 90% of the atoms escape from the trap. The fit of the scaling factor gives 1.1 ± 0.05. The model is thus in good agreement with the data.

In figure 2.7 the measured atom numbers for different MOT parameters are compared with the results of the 3D MC simulation and the Reif model prediction (equation 2.18). Figure 2.7a shows the number of trapped atoms observed experimentally and the prediction of the MC model. Only the data point for a trap depth of 1.1 K deviates significantly.

We conclude that the MC simulation overestimates the number of trapped atoms with a factor 2.2. This mismatch is either due to an (combination of an) overestimate of the loading rate in the MC simulation, or an underestimate of the collision rate in the loss rate model. From figure 2.3 we already concluded that the collision rate might be underestimated by about a factor of 1.4. This would leave a disagreement in the observed and the calculated atom number of a factor 1.6, which is very reasonable considering the simplicity of the MC simulation and the difficulty in obtaining the experimental observables.

In figure 2.7b we show the relation between the escape velocity and the capture velocity. The capture velocity is determined by simulating a Zeeman slowed beam, with no initial beam size, entering the MOT beams under 45 °. The axial direction of the MOT is perpendicular to the direction of the atomic beam. This is a usual configuration for a MOT loaded from a Zeeman slower. The fitted linear function has an offset of 3 m/s and a slope of 0.72. So from the MC simulation the relationship between the capture and escape velocity is $v_c = 1.4 v_e$. This is in very good agreement with the experimental value of 1.29(0.12) [155].

[8] The atom number found in this way was a factor of about 1.4 higher than estimated by measuring the fluorescence of the atoms.

We compare in figure 2.7c the mean speed (equation 2.16) with the capture velocity, determined via the MC for a Zeeman slowed beam. The data are fitted with a linear function, the offset is 3 m/s and the slope is 0.70. The slope would be 1 if all atoms below the capture velocity would be captured.

Finally, in figure 2.7d the number of trapped atoms predicted, using the value of v_c from figure 2.7b and the number of trapped atoms predicted by the MC model are compared. The data is fitted with a scaling factor. The conclusion is that the Reif model overestimates the number of trapped atoms with a factor 2.7. This factor is independent of the laser intensity and detuning. The loading rate for the Reif model is thus

$$R_{\mathrm{mod}} = \frac{1}{2.7} R \,. \tag{2.25}$$

Note that our 1D estimate of a factor 1/2 (equation 2.20) is close to this value.

2.5 Estimate of the capture velocity for vapor cell loaded MOTs

Using the modified Reif model (equation 2.25) we calculate the capture velocities for alkaline MOT experiments and use the outcome to put the particular properties of Na in perspective.

In table 2.4 we review the key parameters for some alkaline experiments reported in literature. The MOTs are loaded from a vapor background gas. Although it is not always explicitly mentioned in the references, we assume that background gas collisions dominate the loss rate. The list includes to the best of our knowledge the experiments with the highest trapping efficiency. For comparison we added a few experiments with lower efficiencies.

The table is organized as following. The first column specifies the isotope which is trapped in the MOT. The second and third column give the hyperfine frequency splitting of the ground and second excited state, respectively, between the two levels with the highest quantum numbers of these states. The laser beam diameter (aperture) is listed in the fourth column. The fifth column contains the number of trapped atoms, divided by the abundance of the used atom source. The laser beam diameter, the number of trapped atoms, the MOT parameters and the Van der Waals coefficients are used to calculate the sixth and seventh column: the knock-out collision cross section and the capture velocity. The Doppler shift corresponding to the capture velocity is calculated in the eighth column. The laser detuning, with respect to the transition with the highest quantum numbers is given in the ninth column, the Zeeman shift in the axial direction is listed in the tenth column. The captured fraction from a Boltzmann distribution is shown in the eleventh column, the used reference can be found in the last column.

Table 2.4: *The calculation for the capture velocity and cross section for MOT systems loading from an alkaline vapor. Per isotope the highest value is indicated in bold. The experimentally observed number of trapped atoms is divided by the atomic abundance of the source. The hyperfine separation Δ is for the pair of the highest quantum number with the next-highest value. Input for the loading rate are the laser diameter and vapor temperature. The calculated value $\langle\sigma\rangle$ uses two theory values for the atom-atom collision model (C_c and C_6 Van der Waals coefficients) and the laser detuning δ and intensity to estimate the excited state fraction. The Doppler shift corresponding to the capture velocity v_c is δ_{v_c}. The maximal Zeeman shift in the axial direction is δ_{Zee}.*

Isotope	$\Delta S_{1/2}$ (MHz)	$\Delta P_{3/2}$ (MHz)	Laser $\varnothing$(mm)	Trapped atoms	$10^{14}\langle\sigma\rangle$ (cm^2)	v_c (m/s)	δ_{v_c} (MHz)	$-\delta$ (MHz)	δ_{Zee} (MHz)	Boltzmann fraction	Ref.
^{6}Li	228	2.8†	8	$8.3\cdot10^7$	4	**94**	141	34	13	$1.8\cdot10^{-4}$	[176]
^{7}Li	804	9.2†	11	$3.2\cdot10^6$	9	**43**	65	6	5	$1.7\cdot10^{-5}$	[177]
^{23}Na	1772	59	22	$1.5\cdot10^{7*}$	6	17	28	20	23	$1.6\cdot10^{-5}$	[166]
^{23}Na			20	$3.7\cdot10^{7*}$	9	**22**	27	15	28	$4.1\cdot10^{-5}$	[178]
^{39}K	462	21	10	$5.4\cdot10^8$	11	48	63	50	7	$9.4\cdot10^{-4}$	[179]
^{39}K			20	$3.2\cdot10^9$	12	**57**	74	50	21	$1.4\cdot10^{-3}$	[179]
^{40}K	1286†	49†	30	$9.3\cdot10^8$	9	32	42	24	20	$2.6\cdot10^{-4}$	[180]
^{40}K			42	$4.0\cdot10^9$	11	**45**	59	35	30	$5.0\cdot10^{-4}$	[181]
^{41}K	254	13	20	$4.5\cdot10^9$	9	56	73	36	21	$1.4\cdot10^{-3}$	[179]
^{41}K			10	$2.2\cdot10^9$	9	**85**	111	36	7	$2.8\cdot10^{-3}$	[179]
^{87}Rb	6835	267	18	$4.0\cdot10^8$	9	21	28	15	15	$2.4\cdot10^{-4}$	[150]
^{87}Rb			30	$1.1\cdot10^{10}$	7	35	45	21	17	$1.3\cdot10^{-3}$	[182]
^{87}Rb			30	$1.3\cdot10^{10*}$	8	39	50	24	20	$1.6\cdot10^{-3}$	[180]
^{87}Rb			40‡	$9.3\cdot10^{10}$	6	**51**	66	23	22	$3.8\cdot10^{-3}$	[183]
^{133}Cs	9193	251	5	$1.8\cdot10^7$	20	18	22	6	4	$3.3\cdot10^{-4}$	[145]
^{133}Cs			40	$3.6\cdot10^{10}$	14	**37**	43	20	22	$3.4\cdot10^{-3}$	[163]

† The hyperfine structure is inverted.

* Light Induced Atomic Desorption (LIAD) is used to load the MOT, we assume the vapor velocity distribution to be Maxwell-Boltzmann like, this might not be the case [178].

‡ The 2.2 cm diameter mentioned in the article is 1/e, the aperture beam diameter is 4 cm and the MOT cloud size is 8mm×8mm×6mm [184].

Table 2.5: *The measured capture velocity for alkaline MOT systems loaded from Zeeman slowed beams. The Doppler shift corresponding to the capture velocity v_c is δ_{v_c}. The laser detuning is with respect to the largest F quantum number. The peak laser beam intensity is I_0, ∇B is the magnetic quadrupole field gradient in the axial direction.*

Alkaline isotope	Laser $\varnothing$(mm)	v_c (m/s)	v_c 1D (m/s)	δ (MHz)	I_0 (mW/cm^2)	∇B (G/cm)	Ref.
^{6}Li	18	45.5	65^{+10}_{-4}	-35	7.9	19	[185]
^{7}Li	13	70	66^{+9}_{-6}	-40	12	14	[186, 187]
^{7}Li	10	80	89^{+12}_{-6}	-45	94	15	[188, 189]
^{23}Na	12	27	26^{+4}_{-2}	-10	8.8	10	[161]
^{23}Na	25	27	34^{+7}_{-3}	-15	8.8	11	[164]
^{87}Rb	25	43	36^{+11}_{-3}	-18	5.3	16.5	[164, 190]
^{87}Rb	15	50	42^{+7}_{-3}	-18	57	10	[188, 189]

As discussed in section 2.3 the structure of the hyperfine splittings affects in the capture velocity. The size of the frequency splittings of the ground and excited state are relevant, they have to be compared with the typical Doppler shift and the linewidth of the transition. The Doppler shift is typically maximally about 100 MHz, the linewidths of the transitions considered here are on the order of 10 MHz. As the frequency splitting of the ground state is at least 200 MHz, the size of the frequency splitting of the ground state does not play a role.

For the excited state there are three possibilities: the frequency splitting between the highest and next-highest angular momentum number is small (about a 30 MHz or less), it is large (100 MHz or more), or it is medium (between 30-100 MHz). When the splitting is small, the laser can be red detuned with respect to all the transitions. For a large frequency splitting the influence of anti-trapping is small. Only in the medium case a limited capture velocity can be expected, because the frequency detuning can only be chosen relatively small.

However, for some atoms the order of the hyperfine levels is inverted. This means that the energy level increases for a decreasing total quantum number. As the cooling cycle is chosen to be the cycle between the highest quantum numbers, an inverted structure is advantageous because the laser is red detuned to all transitions. Therefore there is no constraint on the laser detuning because of possible anti-trapping from neighboring transitions.

Now turning to the discussion of table 2.4, we indeed observe that the level structure is advantageous for the trapping of K. In the ^{39}K and ^{41}K experiments high-power laser light is frequency detuned with respect to the whole hyperfine structure of the excited state, -6 Γ and -8 Γ respectively ($\Gamma = 6.2$ MHz). ^{40}K and ^{7}Li have an inverted hyperfine structure in the excited state, these two isotopes also show high capture velocities. For ^{87}Rb and Cs we observe that large laser beam diameters result in a larger capture velocity.

Concerning the Boltzmann fraction, there is a trend towards higher trapping efficiencies in the table for a larger mass m, as can be expected from equation 2.10: the capture efficiency is proportional to $m^{3/2}$. Na stands out, together with Li, in the sense that its highest trapping efficiencies are two orders of magnitude lower than reported for all the other alkaline element systems.

Two different loading methods of MOTs also provide information on the capture velocity: Zeeman slowers and push beams. To achieve the highest loading rate in the MOT, the velocity of the atom beam from the Zeeman slower has to be optimized to the maximum value that is still trapped by the MOT. Therefore this velocity is a direct estimate of the capture velocity of the MOT. In table 2.5 the velocities for the highest loading rate are listed for several experiments. We include the simple, one-dimensional estimate for the capture velocity, obtained by a numerical simulation of the slowing process, as we used before.

The uncertainty for the 1D estimate for the capture velocity, described on page 26, is obtained by varying the stopping distance. Typically in a Zeeman slower the atoms cross the MOT beams with an diameter d under an angle of 45°. Therefore we choose three values for the stopping distance to be d, $\sqrt{2}d$ and $\frac{1}{2}\sqrt{2}d$ (the last for atoms off-axis by $\frac{1}{2}\sqrt{2}d$).

The mean value of the 1D calculation reproduces for the capture velocity within 10-20%, only for ^{6}Li the deviation is larger. A direct comparison of the results of table 2.5 with the results for v_c from table 2.4 is not possible, as the experiments are all different. It seems however that the values measured with the Zeeman slower are somewhat larger than the predicted values. Especially for Na the value is considerable lower.

Another possibility to get an impression of the capture velocity of a MOT system is in a transfer efficiency measurement with a near-resonant push beam. The faster the atoms are pushed, the smaller the divergence and the higher the transfer efficiency (see section 5.3). The optimal push velocity in such transfer schemes is therefore close to the capture velocity of the receiving MOT system. From table 2.9 we find for the optimal push velocity of a ^{41}K MOT system 40 m/s. The first entry for ^{41}K in table 2.4 gives a representative value of 56 m/s from the same experiment. The optimal velocity is expected to a bit lower than the capture velocity of the MOT as the measured Gaussian width of the velocity distribution of the push atoms is 5 m/s.

Na exhibits the lowest capture velocity. The reason is due to the frequency separation between the two transitions of the excited state which is unique among the isotopes listed in the table: it is medium sized and not inverted. Therefore the laser detuning must be kept small, which reduces the capture velocity.

Summarizing this section we have calculated the capture velocity for MOTs loaded from a background vapor. As input for this calculation we have used an atom-atom model for the collision cross section. From the comparison of high efficiency MOT systems for alkaline isotopes we found that the nature of Na is unfavorable for trapping. It has a relative low capture velocity, related to the particularities of its hyperfine structure.

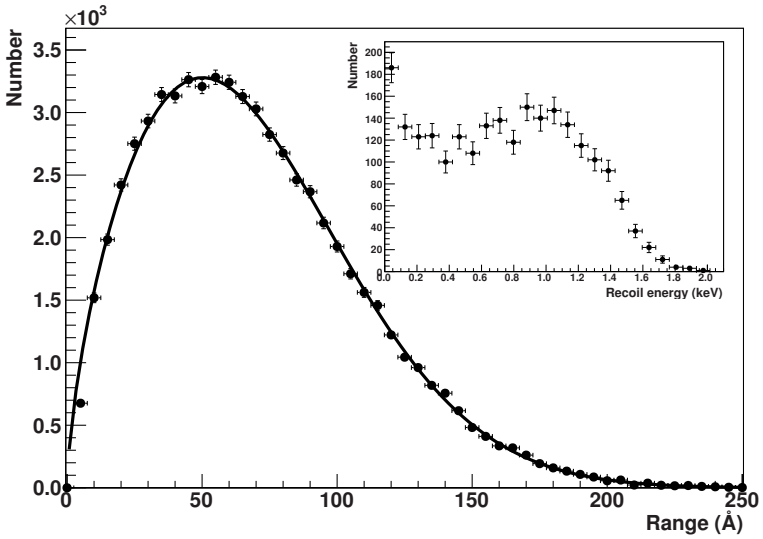

Figure 2.8: *The implementation depth of a 2.8 keV ion beam into a Zr neutralizer, simulated using the SRIM software package [194]. The inset shows a histogram of the energy of the back-scattered ions, the total back scattered fraction is 19%.*

2.6 Ion beam neutralization

There are two options to stop and neutralize an ion beam: using a solid or a gas target. In the first method the ion beam is shot into a metal foil. By heating the foil the particles diffuse towards the surface and are released primarily as atoms. The method with gas uses resonant charge exchange. This can be very efficient but requires a fast (keV) ion beam [191]. A variant of this method has been used by Aubin *et al.*, where about 90% of a 5 keV Fr^+ ion beam is neutralized and stopped in 4 cm of Rb vapor at 115 °C [192, 193]. The vapor pressure of Rb at this temperature is about 10^{-3} mbar, incompatible with the vacuum requirements for a suitable MOT lifetime of 1 s, which requires 5 orders of magnitude better vacuum. Therefore, we consider here only neutralization using a neutralizer foil.

Implantation

The lifetime of 32 s of ^{21}Na requires online production, therefore the setup is coupled to the TRIμP production facility, which is described in section 3.1. For reference we briefly describe the production and thermalization of the particles already here. The ^{21}Na particles are produced by colliding a high-energy (23 MeV/nucleon) ^{20}Ne ion beam with a deuterium target [195, 196]. After separating the reaction products in the dual magnetic separator the ^{21}Na beam is stopped in a stack of heated thin metal

foils inside the Thermal Ionizer (TI) [129]. The ^{21}Na particles diffuse out of the foil. A small fraction of the time they are singly charged. These ions are extracted with a -6.9 kV electric field potential and after deceleration the final beam energy is 2.8 keV.

This low-energy ion beam is transported from the TI about 10 meters downstream, into the Collector Chamber (CC). There the ions are stopped by a thin neutralizer foil, typically 25 μm thick. The neutralizer foil is located in the glass cell, around which the collector MOT is built. At a neutralizer foil temperature of about 1100 K the ^{21}Na atoms diffuse out of the foil in about 1 second. The hot atoms then pass the laser trap volume before colliding with the walls of the glass cell, covered with a non-stick coating. The atoms bounce from the wall and re-enter the trap volume. In this way the atoms have multiple chances to be trapped. The atoms are eventually lost due to permanent sticking on the walls, escaping through one of the cell openings or by nuclear decay.

Diffusion and atomic release

To get an impression of the temperature required to release a significant fraction from the neutralizer foil we discuss the process of stopping and diffusion of the particles inside a solid. Consider the parameters of the present experiment: a Na ion beam at an energy of 2.8 keV shot into a Zr foil. For an idealized foil we performed simulations to determine the distribution of the depths at which the ions are stopped. The result is shown in figure 2.8. The fit is given by $x^{\alpha}\mathrm{e}^{-(x/d)^2}$, here d is 88 Å and $a = 0.65$. To simplify we set $a = 1$, which is still a good approximation [197]. The value for d is then 71 Å, $\sqrt{2}$ times the maximum of the particle distribution (the depth) of 50 Å, which is shown in figure 2.8.

Another outcome of this simulation, shown in figure 2.8 in the inset, is that about 20% of the ions are back scattered at these low energies. The typical recoil energy is of the order of a keV. After being scattered back from the neutralizer foil, these ions might be neutralized on the glass wall of the cell.

Diffusion sets the time scale at which the particles reach the surface from below. The time scale of the diffusion is

$$t = \frac{d^2}{4D}, \tag{2.26}$$

with d the characteristic implantation depth [197]. The explicit time dependence of the release will be discussed in more detail in section 4.4. The diffusion constant D depends on the temperature by the Arrhenius function,

$$D = D_0 e^{-E_a/k_B T} \ . \tag{2.27}$$

The diffusion constant D_0, and the activation energy E_a depend on the isotope and the neutralizer material. For Na and typical neutralizer materials no such data is known. However, studies by Melconian *et al.* [197] indicate that for a temperature of 1200 K about 50% of the implanted ions will be released.

The interaction of the surface with the particle determines whether it leaves the surface as an ion or a neutral atom. The energy difference between the work function

$E_{WF} = 4.05$ eV for Zr and the ionization potential $E_{IP} = 5.139$ eV for Na has to be overcome by the temperature T according to the Langmuir-Saha equation

$$\frac{n+}{n_0} = \frac{w+}{w_0} e^{(E_{\mathrm{WF}} - E_{\mathrm{IP}})/k_{\mathrm{B}}T} \ . \tag{2.28}$$

For the alkali elements the ratio of the statistical weight $\frac{w+}{w_0}$ is 1/2 [198]. For 1200 K the ratio is $1.3 \cdot 10^{-5}$, therefore we do not need to consider ionization. Note, however, that this is the mechanism used to extract ions from the Thermal Ionizer (TI). The TI is made of tungsten, where $E_{\mathrm{WF}} = 4.55$ eV. At a temperature of 2000 K Na is ionized at the percent level [129].

For the release of the implanted particles from a surface two types of interaction are relevant: chemical bonding (chemisorption) and sticking (adsorption) [199]. These processes are of importance both for the number of bounces inside a glass cell and for the release from the neutralizer.

We therefore discuss the adsorption process for three types of surfaces: the neutralizer material, a bare glass surface and a non-stick coated glass surface. Physical adsorption is characterized by an adsorption energy E_{ads}. The atom can be trapped by a Van der Waals potential on the surface, which determines the sticking time

$$\tau_s = \tau_0 e^{E_{\mathrm{ads}}/k_{\mathrm{B}}T}, \tag{2.29}$$

where τ_0 is of the order of h/kT. Typically $10^{-12} - 10^{-13}$ s is used [200].

As the neutralizer is heated to about 1200 K to release the atoms efficiently, we conclude from table 2.6 that the atoms will not stick to the neutralizer surface.

2.7 Adsorption energies and wall coatings

A lot of literature is available on coatings and the several mechanisms associated with it. We here give a critical review of the experimental results and combine several insights obtained using different methods to establish some interrelations.

From studies on efficient atom collection in vapor cell laser traps by Wieman *et al.* adsorption energies were deduced from measurements on the sticking time on several (coated) surfaces [199, 201]. From Light Induced Drift (LID) experiments some adsorption values for alkalines on (coated) surfaces are known. See for example [202] and references therein. We summarize these values in table 2.6.

It can be seen for sodium on uncoated surfaces three experiments report a value of about 0.8 eV, but Buřič *et al.* [203] report a much higher value of 2.5 eV. They speculate that a monolayer of sodium probably covered the sapphire surface in the other experiments, which was absent in their experiment due to the high temperature. The low adsorption values for Na could therefore be the adsorption energy of sodium atoms on a sodium surface.

Table 2.6: *The adsorption energy and sticking timescale for (non)coated surfaces. In the literature for Na $\tau_0 = 10^{-13}$ s is used [203], for Cs and Rb $\tau_0 = 10^{-12}$ s [200].*

Surface material	Atom	Adsorption energy (eV)	Residence time (s)	Ref.
Zr	Na	0.97	1000	[196]
Zr, 700 K	Na	0.97	$1 \cdot 10^{-6}$	[196]
Sapphire	Na	0.75 ± 0.25	$\sim 4 \cdot 10^{-6}$	[204]
Sapphire, 1700 K	Na	2.5 ± 0.1	$\sim 10^{-3}$	[203]
Gehlenite, T=500 K	Na	0.9	$\sim 10^{-3}$	[205]
Pyrex, 400 K	Na	0.71 ± 0.02	$8.3 \cdot 10^{-5}$	[206, 207]
Pyrex, silane, 440-470 K	Na	0.1	-	[208]
Paraffin coated pyrex	Rb	0.1	$4 \cdot 10^{-10}$	[200]
Tetracontane coated glass	Rb	0.06	10^{-11}	[209]
Tetracontane coated pyrex	Rb	0.062	10^{-11}	[210]
Pyrex	Cs	0.53 ± 0.03	$1.6 \cdot 10^{-3}$	[201]
Sapphire, 300 K	Cs	0.43 ± 0.1	$2 \cdot 10^{-5}$	[201]
Pyrex, OTS coating	Cs	0.40 ± 0.03	$9 \cdot 10^{-6}$	[201]

For Na and Rb, on paraffin coated glass very low adsorption values of about 0.1 eV are reported. For Cs, the adsorption energy is about 0.4 eV on the coated surface, close to the 0.5 eV for the uncoated surface. This might have to do with the previously discussed mechanism: the surface might be covered with the alkaline itself.

In order to compare the surfaces we look at various bonding energies of the alkaline atoms [205]. Glass is mainly made of SiO_2, about 80% for pyrex. A bond might be formed between the oxygen and the alkaline atom. The second possibility is that the alkaline atom forms a bond with another alkaline already present on the surface. In the extreme case a mono-layer or thicker has been formed on the surface. In the former case the bonding energy between two alkaline atoms is relevant, in the latter case the heat of evaporation of the element can expected to give an indication of the bond energy [205].

In table 2.7 we list these three energies for the alkaline atoms, except Fr. The bond energy with oxygen is in the range of 2.8-3.5 eV, the bond energy with itself and the evaporation energy are both monotonic decreasing for heavier species.

Comparing the values from table 2.7 with table 2.6 it might indeed be that the low adsorption values are due to covering of the surfaces with the alkaline atoms themselves. For Cs the adsorption energies for coated and uncoated surfaces, reported in table 2.6, are compatible with a surface covered with Cs.

Table 2.7: *The two left columns contain the bond energy for diatomic species, the right column is the enthalpy of formation of gaseous atoms. For the bond energy of the alkali diatomic pair the sticking time scale is calculated, equation 2.29, with $\tau_0 = h/kT$. The data are from the section "Bond dissociation energies" from [211].*

Species	Bond energy with oxygen (eV)	Bond energy with itself (eV)	Timescale (s)	Enthalpy gas (eV)
Li	3.53	1.09	10^6	1.65
Na	2.80	0.78	4	1.11
K	2.81	0.59	$2 \cdot 10^{-3}$	0.92
Rb	2.86	0.51	10^{-5}	0.84
Cs	3.04	0.46	10^{-4}	0.79

Table 2.8: *Energy threshold of the desorption light for the LIAD effect on different surfaces.*

Species	Surface material	Coating	LIAD threshold (eV)	Ref.
Na	SiO_2	-	$2.0 - 3.8$	[212]
Na	Pyrex	-	2.6	[178]
Na	Glass	PDMS	1.2	[213]
Na_2	Glass	PDMS	1.4	[213]
^{40}K	Quartz	-	1.9 ± 0.1	[180]
K	pyrex	PDMS	1.43	[214]
^{87}Rb	Quartz	-	1.85 ± 0.2	[180]
^{87}Rb	Stainless steel	-	1.9 ± 0.1	[180]

Desorption

When the coating is not perfect, inevitably the atoms will be bound to the surface. In the chemisorption process the atom chemically reacts and is permanently bond to the wall [201]. The most important desorption mechanism, in which this bond is broken, is provided by Light Induced Atomic Desorption (LIAD). In this process, an ultraviolet (UV) photon results in the release of the atom off the wall. LIAD was demonstrated in 1993 by Gozzini *et al.* with Na, K and Rb [215] in a polydimethylsiloxane (PDMS) coated cell. LIAD is especially powerful because it can act as a fast (of the order of 100 ms) switchable atom source [216]. In this way a short loading time can be combined with a long lifetime of the trapped atoms.

For Na Yakshinskiiy and Madey explain the desorption by either photo-excitation of an electron from a surface state to neutralize surface Na^+ or an indirect process [212]. In the latter the photons excite electrons to the conduction band from bulk defect

states or directly. At the surface they then neutralize Na^+, which is then desorbed with a non-thermal velocity distribution.

The dynamics of LIAD can be described quantitatively. Pioneering work was done by Atutov *et al.* in 1999 [217]. Rębilas *et al.* presented 10 years later a different approach describing the data better [218, 219]. If the LIAD photon energy $h\nu$ is larger than the energy threshold χ, the desorption yield has a $(A+\delta^2)$ dependence, with $\delta = (h\nu - \chi)/kT$ [213]. In table 2.8 we list various observations of the energy threshold for the LIAD effect. Comparing with the bond energies from table 2.7 we observe that the LIAD energy threshold is in the same range.

For Rb, the wave number dependence of the LIAD effect was studied for a constant light intensity on a stainless steel and quartz cell [180]. The loading rate for quartz was about 40% larger than for steel at the highest LIAD photon energy of 3.13 eV. This might indicate that several monolayers of Rb were formed at the surfaces. Up to 75% of stored Rb atoms could be released in a single flash from a photographic flash lamp using up to 0.3 J/cm^2 [220].

For Na the sticking time for a non-coated pyrex surface at room temperature is of order of $0.2^{+0.4}_{-0.1}$ s using the most precise value for the adsorption energy from [206]. As the typical number of bounces is in the order of 1000, a coating is necessary for Na. With light of 455 nm, a few mW/cm^2 is sufficient to load a MOT efficiently with Na [178]. LIAD is thus a valuable tool to check whether sodium got stuck on the surface and should be used as a diagnostic tool.

Curing/passivating/ripening of the non-stick coating

Stephens *et al.* were the first who systematically studied wall coatings to improve the collection efficiency of a MOT [201]. They conclude that after coating the cell, it must be cured with a vapor to prevent chemical reactions with the dry-film coating. Guckert *et al.* [221] used an OTS coated cell to trap radioactive ^{82}Rb, they report maximally about 30 bounces, where they expected about 600. By using a collimated NaI-γ counter they found that a large portion of the activity sticks to the wall.

It can be hard to establish a good quality of the coating and understand possible factors which influence it during the coating procedure and degradation during the experiments. A systematic study of coating materials with different surface techniques was performed to learn about the bulk and surface properties by Seltzer *et al.* [222]. Alkaline atoms diffuse slowly into the coating towards the glass [200].

So-called ripening, or curing, plays an important role for the desorption properties of the wall coating [223]. Atutov *et al.* for example reported for Rb that curing with a Na vapor for 4 days long at a pressure of 10^{-7} mbar was necessary to achieve the maximal number of about 1400 bounces (see also figure B.1). However, as was realized early by Guckert *et al.* [224], for the radioactive atom an exchange process with a stable atom that cures the coating can result in a loss, whereas this effect will go unnoticed for a stable atom exchange.

On the other hand, there have been many experiments which studied the relaxation rates of polarized atoms on surfaces [200, 225]. An atom which is present on the wall is

quickly depolarized, therefore such an exchange process would manifest itself through a higher relaxation rate. For Na Swenson *et al.* [226, 227] studied the relaxation rate for polarized Na atoms colliding with a silicone surface. They looked for the influence of the duration of exposure to Na vapor, wall temperature, Na density, and magnetic field strength. They found that such surfaces have spin relaxation times corresponding to over 100 wall collisions even after weeks of exposure to Na vapor. This provides strong evidence that such exchange processes are not relevant for Na and therefore achieved collection efficiency with ^{23}Na should be the same for ^{21}Na.

This is also reported on in literature in another type of experiments. Many experiments in quantum optics and magnetometry use alkaline atom vapor cells coated with anti-relaxation coating to improve the spin relaxation time of the spin polarized atomic vapor [200, 228]. To their experience paraffin coated cells need a special process of 'ripening' just after the coating preparation [229].

The explanation behind the ripening process is that chemical active areas get passivated. However, it might also be possible that a (or more) monolayer(s) of the curing element are created on the surface. The corresponding sticking times range from about 1 s for Na to μs for Cs (see table 2.7). Except for Li and Na the adsorption energy for the alkalines is so low that effectively it does not matter.

Swenson *et al.* carried out a detailed study on the relaxation rate of optically pumped polarized Na vapor [226, 227]. They find that even after weeks of exposure to Na vapor at 225 °C, the relaxation rate still corresponds to over 100 bounces. For the adsorption energy of Na on a dryfilm surface they estimate about 0.07 eV, a bit smaller than the 0.1 eV for Rb on paraffin found by Bouchiat *et al.* [200].

Summary of wall coatings

In summary, a variety of methods exists to reduce the sticking time or to release the stuck particles. The temperature of the neutralizer foil is so high that the atoms will not stick to it, the studies are concerned with sticking of the atoms to the glass and metal at room temperature. These studies are almost always done with stable particles. These results can be transferred to radioactive particles, where the abundance is very low. However, even in the case of stable atoms conditions under which the experiments are performed are unclear.

For radioactive atoms the interpretation of the overall efficiency is challenging. The contribution from the neutralizer release efficiency, the single pass trapping efficiency, the sticking time and number of trap passages are hard to disentangle. Some of these problems can also be identified in literature. Discussions with authors of above-mentioned papers [230–232] have confirmed the currently unsatisfactory level of understanding. Nonetheless, clear recommendations can be made for the efficient trapping of Na atoms from the heated neutralizer: for Na a coating is necessary, as the sticking time on bare glass is on the order of a second. Furthermore LIAD should be used as a diagnostic tool.

2.8 Number of bounces and trap passages

The most reasonable procedure to increase the collection efficiency is to have multiple trap passages. Because we use radioactive atoms, the sticking time has to be short. The quality of the coating should be such that the number of bounces is limited by the geometry of the cell. Here we discuss the geometrical limitation for the number of bounces and trap passages.

A non-stick wall coating offers improvements from both categories: hot atoms thermalize on the room temperature wall and the atoms will pass the laser trap volume several times (depending on the geometry of the cell). Thermalization from a temperature of 1100 K to room temperature (293 K) brings a factor of 7 improvement. To achieve the desired collection efficiency of 1% the number of trap passages needs to be about 100.

The number of bounces for our cell geometry and the corresponding number of passages through the laser volume was calculated with a Monte Carlo simulation of the effusion process. To test our calculation we also did the calculation for the experiment of Atutov *et al.* [233]. This is discussed in appendix B. An important conclusion drawn there is that for our purposes the effusion process is best described using an isotropic emission pattern for particles when coming off the surface. That an isotropic emission pattern describes effusion best has also been found elsewhere [234].

We used the Monte Carlo simulation to calculate the expected number of bounces and trapping passages for one of the two glass cells we used in our experiments, the results can be found in section 3.6.

2.9 Double MOT transfer

We need a transfer efficiency from the collector to the science MOT of about 50% for ^{21}Na. The distance between the two MOTs is 69 cm. Additionally a reliable operation is required and compatibility with the constraints imposed by the β-decay science chamber with respect to the detection equipment. Also the hardware requirements (laser power, frequency requirements) have to be taken into account.

To achieve a Bose-Einstein Condensate (BEC), a high number of cold atoms in an ultra-high vacuum (UHV) environment is required as a starting point. One strategy for creating a BEC is to load atoms from a vapor into a Magneto-Optical Trap (MOT) which can be done fast. Next the trapped atoms are transferred to a second MOT setup with better vacuum [235, 236]. Consequently, there exist many experiments in which atoms are transferred between two atom traps. We identified five types of transfer: by gravity (A), by magnetic transport (B), with a dipole push-guide (C), with an optical dipole trap (D) and with a resonant push beam (E). We discuss for each type the principle, its (dis)advantages and its applicability to our setup.

Gravity (A)

The simplest method is to let the atom cloud fall from a first MOT in a second MOT below. Under the gravitational acceleration of about 9.8 m/s^2 the atoms fall and are recaptured in the second MOT system. To improve the transfer efficiency, the temperature of the cloud is reduced just before the transfer (optical molasses) to achieve very low temperatures. A high transfer efficiency is therefore still a challenge. However, for reasons of space requirements, our double MOT system is in the horizontal plane and the gravity method is thus not an option.

Magnetic transfer (B)

In this method a conservative potential created by magnetic fields is used to confine the atoms during the transfer. Either the transfer is done only using magnetic potentials (the atoms are moved with the potential), or a magnetic guide is used and the atoms are accelerated and recaptured with another mechanism. The moving magnetic potential can be implemented in two ways: by varying the magnetic fields or by moving magnets mechanically [237]. The first kind is a magnetic conveyor belt. It is a chain of quadrupole coils where the potential minimum is moved by applying time-varying currents to the coils. In essence it is a moving magnetic trap which is loaded in the MOT region. The initial temperature of the MOT cloud has to be reduced with additional cooling schemes to be efficient with this approach. For a β-decay correlation measurement, the conveyor belt is taking too much solid angle of the particle detectors. Similarly, when the magnetic trap is moved mechanically; solid angle is lost to the moving mechanisms.

Optical methods

For the optical method two strategies can be followed. Either the push beam is far-off or near resonance. The off resonance beam creates a conservative dipole potential. To trap the atoms a strong (of order 20 W) laser beam with a red detuning of several hundred nm is focused to a spot of order 30 μm[9]. By moving the focus the atoms can be transported using this Optical Dipole Trap (ODT) force [239].

The ODT force can also be used to create a confining guide. In this case the detuning is chosen to be relatively small, typically a GHz. The spontaneous scattering rate is then still sufficient to accelerate the atoms to a few m/s. The near-resonance push beam accelerates the atoms much quicker but does not provide a confining potential.

In the case of the near-resonance transfer method the atoms can be cooled in two dimensions by an atom funnel, which is a two dimensional version of a conventional MOT [240–242]. This reduces the transverse velocity spread of the atomic beam and in this way the transfer efficiency can considerable enhanced.

[9] An exception to these typical conditions is an experiment done by the Wieman group [56, 238], where a combination of a red detuning of 4 nm and 0.5 W laser power was used.

Table 2.9: *An overview of experiments using five techniques to transfer atoms between two atom traps: gravity (A), magnetic transfer (B), dipolar push-guide (C), optical dipole trap (D) and a resonant push beam (E). PM stands for permanent magnet, MG for magnetic guide. δv is the standard deviation of the velocity distribution. The diameter of the push laser beam is indicated in mm. Vertically separated MOT systems are indicated with* †.

Type	Parameters	Atom	Dist. (cm)	$\bar{v} \pm \delta v$ (m/s)	Eff. (%)	Ref.
A	Molasses 5 μK	^{133}Cs	70†	1.9	20	[243]
B	Time-varying	^{87}Rb	33	0.8	30	[244]
	Static, mechanically	^{87}Rb	45	0.5	50	[152]
C	+1.5 GHz, 70 mW	^{133}Cs	20	1.5	3	[245]
	+6 GHz, 55 mW	^{87}Rb	24	10.0	3	[246]
	-1.5 GHz, 63 mW, 1.3 mm	^{133}Cs	57†	5.5	70	[247]
	-1.0 GHz, 21 mW, 0.6 mm	^{87}Rb	72†	12.6	50	
	-1.2 GHz, 20 mW, 1.6 mm	^{133}Cs	19†	≤ 20	2-9[1]	[248]
D	Lattice, 0.24 W, -5.5 GHz	^{23}Na	40	16.5	20	[249]
	40 W 1550 nm	^{226}Ra	50	0.06	73 ± 4	[250]
E cont.	0.8 mm hole in retro-optics	^{87}Rb	30	14 ± 1.1	70	[251]
	2 mm hole in retro-optics	^{7}Li	30	13	0.3	[186]
	-22 MHz, 100 μW, 1 mm	^{87}Rb	36	14	7	[252]
	-43 MHz, 70;78 mW/cm^2	^{39,40}K	35	-	6	[253]
	200 μW, 1.1 mm	^{87}Rb	67	14 ± 9	50	[254]
E pulsed	PMG	^{23}Na	25	≤ 20	10	[255]
	Magnetic lauch	^{23}Na	40	7	2	
	6 PM	^{82}Rb	45	20	20 ± 10[2]	[77]
	No MG				5 ± 2	
	6 PM	^{39,41}K	50	33	30	[179]
	No MG				10	
	Three 21 cm long PM	^{85}Rb	50	20	39	[256]
	Three 23 cm long PM[3]	^{85}Rb	50	16	90 ± 15	[257]
	PM only			27	50	
	No MG			16	15	
	0.5 mW, 2 ms	^{87}Rb	70	20	50	[258]
	+47 MHz, 3.2 mW, 20 ms	^{41}K	48	40 ± 4.7	55 ± 9	[259]
			75		40 ± 5	
	1 funnel		48		78 ± 14	
	2 funnels		75		78 ± 10	
	Three 33 cm long PM	^{21}Na	51	11	40 ± 20	[68]
		^{23}Na			80	
	Six 30 cm long PM	^{87}Rb	50	15	80	[260]

[1] Estimated value, the reported transfer efficiency of 85% is incorrect, see page 164.
[2] In earlier measurements with the setup with ^{85}Rb a transfer efficiency of 75 ± 15 was obtained [221].
[3] Additionally a hexapole field, generated by 6 wires carrying a current of up to 300 A, is used.

Dipolar push-guide (C)

For the transfer with off-resonance light two possibilities exist, both provide a conservative guiding potential. The first is to create an attractive potential, created by a red detuned laser beam. The second option is to create a repulsive potential with a hollow, blue detuned laser beam. However, there is a caveat in the transfer efficiency reported for this technique, which we discuss in appendix C. In short, the total transfer efficiency obtained with the dipolar push-guide type is lower than the transfer efficiency, because the time between the atom being captured and being transferred can be long compared to the lifetime of the MOT. Therefore, the atom can be lost before it is transferred, for radioactive isotopes this loss has to be taken into account.

A difference between the achieved results for Rb and Cs on one hand and Na on the other is that the optimal detuning of -1 GHz for Cs and Rb is to be compared with the hyperfine splitting of the ground-state of of 6.8 and 9.2 GHz for Rb and Cs, respectively, while for Na this is 1.7 GHz. Whether this transfer method is suited for the transfer of Na isotopes mainly depends on the required laser power and detuning. Probably only with an extra laser system it is a workable solution, which is less of a problem when diode lasers are available like for Rb and Cs. However, for Na this is an issue. Furthermore, with the other transfer methods transfer efficiencies close to 100% have been demonstrated, with this method maximally only an estimated 25%.

Optical Dipole Trap (D)

With an optical dipole trap (ODT), one can transport atoms by moving the focus of the laser beam. However, the dipole trap is a conservative potential and for typical parameters shallow (about 1 mK). Therefore this method requires very low temperature (and small) atomic clouds to be loaded efficiently and during the transfer heating mechanisms have to minimized. Using an ODT at a wavelength of 1030 nm and 2.5 W power, Feldbaum *et al.* [58] transferred 14% of the trapped radioactive ^{82}Rb MOT atoms into the ODT.

On resonance push (E)

For the on-resonance push beam method, the push beam accelerates the atoms but does not provide a confining potential. Also for the near-resonance push methods two approaches can be used. Either the push has a relatively low intensity and pushes continuously, or the transport uses a short, high intensity laser pulse to accelerate the atoms.

We implemented the resonant transfer scheme to transfer the atoms in our experiment. The model to find the optimal settings for a resonant push beam and optionally a funnel can be found in chapter 5 where also the experimental results are presented. One of the main conclusions there is that to limit the transverse extent of the pushed atomic cloud, it is advantageous to push the atoms with the highest velocity which can still be recaptured by the receiving MOT (see section 5.3).

A resonant push beam can also be combined with a magnetic guide. The first implementation by Myatt *et al.* [257] achieved a transfer efficiency of about 90%. Myatt *et al.* simplified their transfer method which is described in [257]: instead of using a combination of a hexapole field generated by currents and permanent magnets, they achieved a similar transfer efficiency (about 80%) using a 30 cm long permanent magnetic guide to transfer the atoms over a distance of about 50 cm [260]. As they used six magnets, arranged with alternating poles, instead of the previously used configuration with three magnets (with the same pole towards the transfer line), the fringe field decreased more rapidly: as $1/R^5$ rather than $1/R^3$. This allowed to bring the magnetic guide made up of six magnets closer to the MOTs. During the transfer absolutely no laser light should be present in the guide: a few photons will depolarize the atomic sample, leading to loss.

Efficiency comparison

In table 2.9 we list an overview of experiments which use double atom trap transfer methods of one of the five preceding types. The table is not complete, but gives an indication what has been typically achieved for each transfer strategy. Note that in several of the experiments, to enhance the transfer efficiency, the temperature of the MOT cloud is reduced before the transfer. Due to the different techniques used, it is nearly impossible to normalize the obtained transfer efficiencies to a particular distance. A direct comparison is therefore hampered.

For the near-resonant push technique, in leading order the transfer efficiency is inversely proportional to the square of the transfer distance and proportional to both the push velocity and the mass of the atom (see in chapter 5 equation 5.9 and table 5.3). With this method a high push velocity and a high mass are thus favorable in achieving a high transfer efficiency.

We conclude that the highest transfer efficiency using a push beam is obtained with ^{41}K. In that experiment also the highest push velocity of 40 m/s was used. Two funnels doubled the transfer efficiency over a distance of 75 cm.

Looking forward to the results obtained in chapter 5 we can say that for a capture velocity of the receiving MOT system of 25 m/s about 15% can be transferred with a push beam only and with the aid of an optical funnel a transfer efficiency of 60% is feasible.

The dipole trap method is attractive as spin polarization can be easily achieved in such a trap. Transfer and polarization can then be combined. However, achieving a 50% loading efficiency is harder for Na than for heavier elements due to its hyperfine structure, also achieving a fast and efficient transfer is technically more challenging.

During the last stage of writing this thesis, we became aware of the double-MOT transfer experiments performed at Berkeley for their ^{21}Na experiment.The results, showing a transfer efficiency of 80%, are only published in the thesis of M. Rowe [68]. The double MOT setup was used to suppress background from untrapped atoms. As the capture efficiency of the Zeeman slowed atom beam into the MOT was increased from 1% to 25%, the second MOT was not needed anymore [261].

The advantage of the magnetic guide compared to the push beam with funnel method is that the hardware is less complex and this method is very frugal with laser light. The required capture velocity of the receiving MOT is relaxed as the atoms can be transferred at a low speed of about 10-15 m/s. The magnetic guide will also require less maintenance. A disadvantage is that the magnetic guide requires good shielding from laser light, which pumps the atoms to an anti-trapped state, leading to a decrease in transfer efficiency.

2.10 Summary of the efficiency of a double MOT system

The collection efficiency of a MOT system which loads from a vapor originating from a neutralized ion beam, depends on three factors: the neutralization efficiency, the single pass capture efficiency and the number of times the atoms pass through the trap volume before they are lost. The neutralization of the ion beam can be best done with a neutralizer foil. An efficiency of about 50% can be expected for a temperature of 1200 K. The single pass trapping efficiency directly depends on the loading rate of a MOT system. An analytical calculation which oversimplifies the slowing process showed that the commonly used loading rate overestimates the true loading rate with a factor of 2. Using a 3D Monte Carlo simulation for a Na MOT, with a known capture velocity, we could establish that the loading rate is overestimated with about a factor of 3.

To calculate the capture velocity from the loading rate also the loss rate in a MOT system due to collisions with the vapor needs to be known. Using a classical model we found good agreement between the calculated loss rate and experimental data obtained with a Rb MOT.

Having tested both loss and loading rate, we calculated the capture velocity for a vapor cell MOT system trapping alkaline elements. We found that from all alkaline isotopes Na has the lowest capture velocity. An explanation may be found in the details of the hyperfine splittings in the excited state.

A non-stick coating reduces the sticking time of the particles on the wall and therefore allows for multiple trap passages before the particles get definitely lost. An extensive search in literature on efficient trapping shows that the exact conditions required to achieve a large number of bounces are unclear. We find indications that the non-stick coating might actually be covered with a layer of the alkaline of interest. The quality and condition of the coating might be critical in the case of Na. A possible diagnostic to determine the state of the coating can be provided by Light Induced Atomic Desorption (LIAD).

To estimate the number of bounces and the number of passages the atoms make through the laser trap volume we performed Monte Carlo simulations of the effusion process. We find good agreement of our calculations with experimental data for different geometries from which the number of bounces could be extracted.

We conclude that to achieve an overall capture efficiency of 1% two ingredients are crucial:

- A non-stick coating which reduces the sticking time to a negligible timescale.
- A cell geometry in which the atoms pass on average the trap volume about 100 times before exiting.

We decided to implement the near-resonant transfer scheme, which has shown high transfer efficiencies for other alkalines for the transfer from the capture to the science MOT. For the on resonance push beam solution two ingredients are required to achieve a 50% transfer efficiency:

- A resonant push beam, either continuous or pulsed.
- An optical funnel or a permanent magnetic guide to reach the level of 50%.

CHAPTER 3

Experimental setup

In this chapter the experimental setup of the double Magneto-Optical Trap (MOT) system for ^{21}Na, which is coupled to an online production and separation facility, is described. In figure 3.1 an overview of the setup is shown. A high-energy ion beam collides with a gas target and the various particles are separated in the TRIμP dual magnetic separator. The particles are then stopped in a stack of heated foils: the Thermal Ionizer (TI). The ions are extracted from the TI and transported at low energy through the Low Energy Ion Beam (LEBL) towards the collector MOT section. The setup for the ^{21}Na experiment consists of two MOT systems, separated by 69 cm. The first MOT setup consists of a glass cell and collects the neutralized ions. The trapped atoms are then transferred to a second MOT setup where the decay measurement will take place. To enhance the efficiency of the transfer process, optical access is provided by six-way cross half-way the transfer line.

In section 3.1 we introduce the production of ^{21}Na and the stopping of the high-energy radioactive ion beam in the TI. The setup for the LEBL is described in section 3.2. In the collector cell setup the ions are neutralized, and after being evaporated, trapped optically in a MOT. We introduce the four laser systems that have been used for the trapping of radioactive ^{21}Na and stable ^{23}Na in section 3.3. The frequency calibration of spectroscopy signals, used to lock lasers, is discussed in section 3.4. The glass cell that was used for the collector MOT setup is described in section 3.5. Section 3.6 contains the description of its successor, the cubic cell setup. In section 3.7 the push beam and the optical funnel which were used to transfer the atoms are discussed. The MOT system, which is situated in the vacuum chamber in which the correlation coefficients will be measured, is treated in section 3.8. In section 3.9 a brief description of the data-acquisition system is given.

3.1 Production, stopping and extraction of ^{21}Na

The ^{21}Na for our experiment is produced in the inverse d(^{20}Ne,^{21}Na)n reaction at an energy of 22.3 MeV/u. The reaction products have velocities corresponding to the

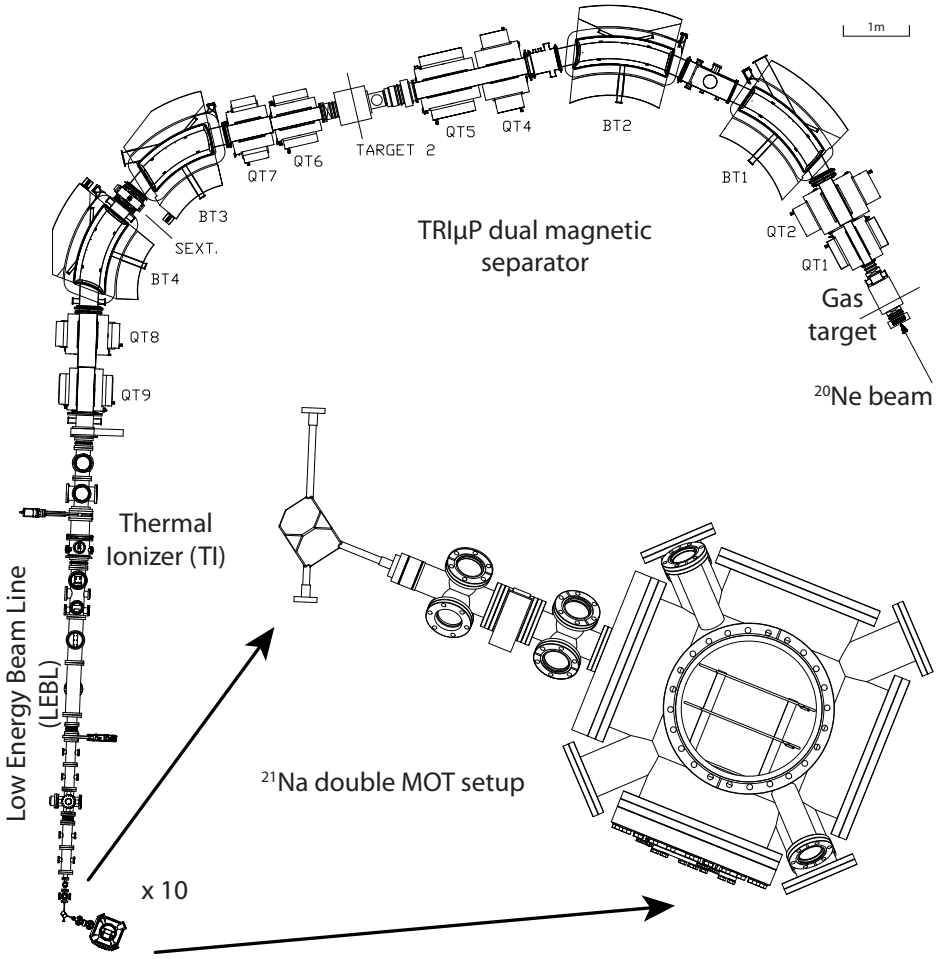

Figure 3.1: *The top view of the experimental setup for the ^{21}Na experiment.*

velocity of the primary beam. The D_2 gas target at a LN_2 temperature of 77 K and at a pressure of 1.7 atm is separated from the beam-line vacuum with two 4 μm thick Havar windows. The gas target is bombarded with about 10^{12} $^{20}Ne^{6+}$ particles/s from the AGOR cyclotron, the total beam power is about 100 W. The reaction products and the remaining primary beam are separated in the TRIμP magnetic separator [126]. Under these circumstances up to $3 \cdot 10^6$ ^{21}Na ions/s are produced that reach the end of the separator section.

The high-energy ^{21}Na ion beam has to be stopped and released as an atomic beam to be able to trap ^{21}Na in an atom trap. This stopping stage is implemented by shooting the beam into a stack of typically ten 1.5 μm thick tungsten (W) foils, which are housed in a W cavity, collectively referred to as the Thermal Ionizer (TI) [129]. Heating of the cavity is done by electron bombardment (4-5 A at 200 V) from surrounding tungsten filaments. At a temperature of about 2500 K the particles diffuse out of the foils on the timescale of milliseconds. Collisions with the surface of the foils and cavity walls can ionize these atoms according to the Langmuir-Saha equation (equation 2.28). For W the work function is 4.55 eV and the ionization potential of Na is 5.139 eV. At $T = 2500$ K about 3% of the particles are ionized. During this effusion process the charge state of the particle can change in each collision with the surface. If the particle is an ion in the extraction volume it will be pulled out, it is lost if it diffuses out as an atom or decays.

The overall TI efficiency is about 50% at a temperature of 2800 K [129]. To increase the lifetime of especially the foil stack of the TI we run typically at a temperature of 2500 K. We have an extraction rate of about $3 \cdot 10^5$ ^{21}Na/s from the TI (see section 4.2). This corresponds to a TI efficiency of 10%, as expected for this temperature [129].

As the foils of the TI contain traces of several alkaline(-earth) elements off-line studies can be done using a stable ^{23}Na ion beam.

3.2 Low energy ion beam-line and neutralizer setup

After being extracted from the TI, the ion beam enters the Low Energy Beam Line (LEBL). Figure 3.2 gives an overview of its various components. The ion beam passes a Wien filter, consisting of a static magnetic field and perpendicular to this a variable electric field. For a fixed ion beam energy this gives a mass resolution of one in the region of Na isotopes. After the Wien filter the ions enter a drift tube. By switching the voltage on the tube between the beam extraction energy of -2.8 keV and the ground potential, the rest of the setup can be kept at ground potential [69]. When the tube is filled with ions, the voltage is switched to extract the ions. Therefore, the maximal transportation efficiency of the drift tube is 50%. As the optimal switch frequency is mass dependent, the drift tube also acts as a mass filter. In section 4.2 more details of both the Wien filter and drift tube are given.

Using a quadrupole and several Einzel lenses and steering plates the ion beam is guided onto a thin metal foil, mounted inside the glass cell of the Collector Cell

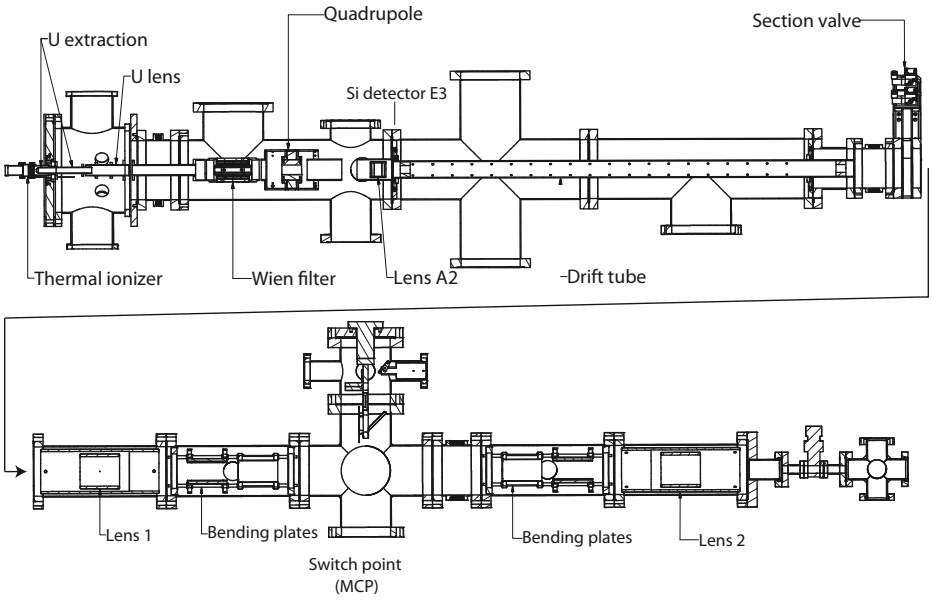

Figure 3.2: *Overview of the Low Energy Beam Line (LEBL) (two sections). The high energy ion beam is stopped in the Thermal Ionizer. The glass cell of the collector MOT setup is connected to the end of the lower. The figure is courtesy of L. Huisman.*

(CC) MOT setup. This neutralizing foil is made of zirconium (Zr). The shape of the foil is a square with sides of about 7 mm and is 25 μm thick. It is heated resistively with a typical current of 6.3 A to a temperature of about 1100 K. The work function of Zr is 4.05 eV and surface ionization is negligible. No values for diffusion of Na in Zr have been reported, but the release fraction of a ^{37}K ion beam implanted with 12 keV energy from different neutralizer materials, including Zr, has been studied by Melconian *et al.* [197]. Based on their results and the diffusion of Na in other metals the expected diffusion time scale is about 1 s at 1200 K [196], more details are in section 4.4.

3.3 Laser-systems

Both ^{21}Na and ^{23}Na require cooling and repump laser light to trap atoms in a MOT. ^{21}Na has the same level scheme structure as ^{23}Na, only the laser frequencies are slightly different (see figure 2.5). The wavelength is around 589 nm, for the same red detunings the frequency difference between the pump and repump transition

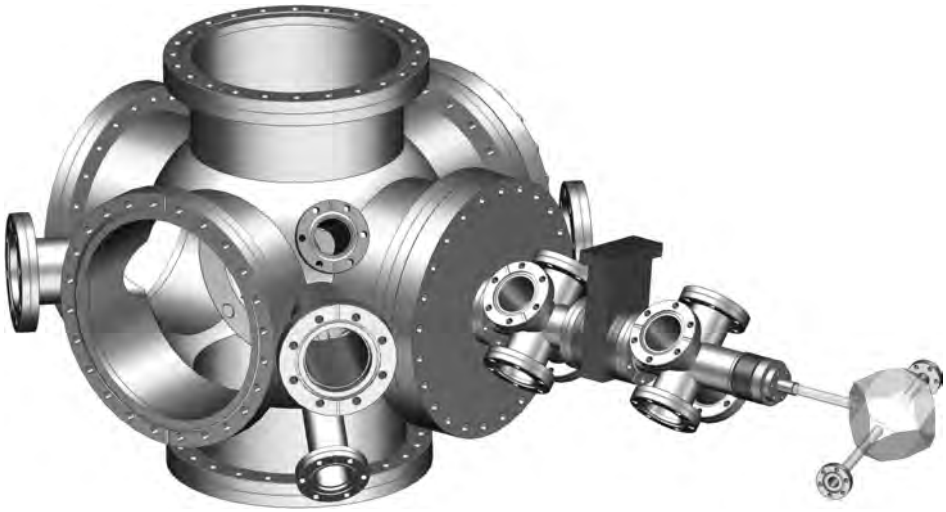

Figure 3.3: *The vacuum chambers of the double MOT setup. The glass collector cell (CC MOT), the funnel and the science chamber (SC).*

is for ^{23}Na 1712 MHz, for ^{21}Na it is 1847 MHz. Here we will give typical operating conditions for the three single mode lasers we used in our experiments. We also briefly describe the frequency comb, which we use to calibrate the laser frequencies and to which we locked lasers.

Spectra Physics Dye laser

The first laser system is a frequency stabilized ring dye laser (Spectra Physics Model 380D), with a stabilization system (Stabilock, Spectra Physics Model 388) ensuring short-term stability of the laser by using feedback signals from two stabilized interferometers. This dye laser system is in a separate room outside the A-cell and is shared with the MOTRIMS experiment of the Atomic Physics group at the KVI [262, 263]. The dye jet is pumped by 3.6 W of laser light at 532 nm. The dye circulator pumps the Rhodamine 6G dye solution around with a pressure of 6 bar. About 350 mW of light at 589 nm is produced with a linewidth of about 1 MHz. For creating two sidebands with a total power of about 20% of the laser power, a 1720 MHz resonant Electro-Optical Modulator (EOM, New Focus model 4421) is used.

Via an optical launcher the laser light is coupled into a 100 m long single mode fiber (460HP, Thorlabs). With a coupling and transport efficiency of 40% about 120 mW of laser light is available for the experiment in the A-cell. Optical feedback from the fiber at high coupling efficiencies caused the laser to frequently mode-hop[1]. This

[1]This might be due to cavity like effects, or to stimulated Brillouin scattering (SBS), also observed by

optical feedback is suppressed by an optical isolator. The isolator is from Altechna and is coated for 589 nm, its TCG crystal has a 3 mm clear aperture, the damage threshold of the crystal is 200 W/cm^2. The isolator provides more than 38 dB isolation and a 95% transmission.

Coherent 699 Dye laser

The second laser system is a CR-699-21 Ring dye laser from Coherent, also operated with Rhodamine 6G dye. It is primarily used by the radium atom experiment of the TRIμP group [34]. A Verdi-V10 Nd:YAG laser pumps the dye jet with 4 W laser power at 532 nm. Typically around 350 mW of 589 nm light is produced, the linewidth is about 1 MHz.

First this laser system was situated in a laser laboratory about 70 m from the A-cell, where the ^{21}Na setup is located. About 100 mW of light was available in the A-cell, using a fiber of about 100 m. Later the laser system was put in the A-cell and light was brought directly to the setup through periscopes over a distance of about 6 m, roughly doubling the available power at the setup.

Toptica Solid State laser

The third laser system is a high-power solid state laser from Toptica Photonics (DL-RFA-SHG PRO), which is completely based on diode laser technology. It was installed in the A-cell at the end of 2010. Its main advantages are a high output power and better long term frequency and power stability. It also requires less maintenance time compared to the dye laser systems. It consists of three subsystems that we discuss here: a seed laser, an amplifier and a frequency doubling stage.

The first system is the master laser, which is a diode laser at 1178 nm (DL pro) with typically 30 mW single mode output power. After coupling 60% into a single mode fiber the light enters a Raman Fiber Amplifier (RFA) stage. This second subsystem amplifies the seed light at 1178 nm light to 3.5 W. The pump light for the RFA is provided by a 25 W fiber laser (MPB Ytterbium YFL-P), which itself is pumped by 1120 nm diode banks. The light from the fiber laser is transported via a fixed fiber connection to the RFA. From the RFA the amplified 1178 nm seed light is transported by a fixed fiber connection to the enclosure which contains the diode laser and also the third subsystem, the frequency doubling stage (DL-SHG 110).

A module (Digilock 110) provides several ways to control and lock the laser frequency of the laser diode via a computer interface. The coarse tuning range of the laser is 588-590 nm. The mode hop free tuning range is at least 10 GHz and more than 2 W of 589 nm light can be produced. With the fiber laser producing 15.3 W of laser power, after the RFA stage 3.5 W is coupled into the Second-Harmonic Generation (SHG) stage, which produces 2.7 W at 589 nm (the linewidth is about 1 MHz). The frequency stability of the laser is excellent, only the coupling of the seed laser light

Walker *et al.* for a K experiment. They observed the SBS effect for a 45 m long fiber with $\sim$ 200 mW [264].

into the fiber needs some maintenance. As the laser can be controlled by computer, we could also remotely control the laser during experiments with ^{21}Na, when the laser setup can not be accessed because of radiation safety reasons.

The laser light was brought, properly shielded, to the double MOT setup via periscopes over a distance of about 6 m. The optical table on which the laser system is situated is actively stabilized. With such a 6 m large arm, pointing effects were clearly visible through moving fringes at the mm scale. The net drift required frequent realignment of the beams at the MOT position. Therefore the stabilization mechanism of the table was turned off. Although some more noise was noticeable in the signals that are used to stabilize the laser, the laser operation and stability was not affected by turning off the stabilization system of the table.

Menlo frequency comb

In the beginning of 2010 a femtosecond frequency comb (model FDC1500/075 from Menlo Systems) was installed in the laser laboratory. It serves as a frequency reference and also lasers can be locked to it. The accuracy of the frequency comb itself is derived from a Rb atomic clock (FS725 Rubidium Frequency Standard clock, Stanford Research Systems), which itself is synchronized to atomic clocks in GPS satellites via timing events produced by a GPS receiver (Navteq). The frequency stabilization of the frequency comb is better than 10^{-11}.

The frequency comb was first used to calibrate the spectroscopy signals that were used to generate a locking signal for the laser. Later we locked lasers to the frequency comb directly. A typical, stable operation was to offset lock the Toptica laser to the frequency comb and offset lock one of the two dye lasers to the Toptica laser. With an optimized frequency comb the whole system kept the frequency locks for several hours. The reading of a wavelength meter (HighFinesse Ångstrom WS6 VIS) provided double checking of the lock.

3.4 Absolute laser frequencies

For laser cooling and trapping of ^{21}Na and ^{23}Na the laser frequencies need to be accurate in the order of 1 MHz on a scale of $5 \cdot 10^8$ MHz, *i.e.* a $2 \cdot 10^{-9}$ stability. We used three locking methods. Two of them are absolute references and the third is a relative frequency lock. All methods require a few mW of laser light.

The first locking scheme uses amplitude modulated (AM) saturation absorption spectroscopy. This setup is situated next to the Spectra Physics Dye laser. A pump beam and counterpropagating probe beam are crossed in a heated Na vapor cell. The pump beam is modulated with a chopper wheel and the probe beam intensity is measured with a photo diode (lock-in technique). This Lamb-dip spectroscopy signal does not provide us with zero-crossings, therefore only locks can be made using a non-zero lock point. As the height of such a spectroscopy signal depends on the laser power, the frequency corresponding to this lock-point changes when the laser power changes.

This leads to a changing laser detuning and the MOT will perform less efficiently or eventually not at all anymore. Therefore we abolished this locking method and replaced it with a more robust method, which we discuss next.

The second frequency stabilization method we use is robust against large power changes. We designed it such that it provides a lock-point both for ^{21}Na and ^{23}Na without realignment of the spectroscopy setup. This is desirable, as during a ^{21}Na beamtime, checks can be made with ^{23}Na without altering the setup too much. The method uses, like the previous one, Lamb-dip spectroscopy and was set up in the A-cell. The difference with the AM setup is that here the pump laser beam is frequency modulated (FM). The spectroscopy signal is the derivative of the signal of the AM method [265]. Therefore the FM locking method is much more robust against changes in the laser power than the AM spectroscopy method, as long as the intensities of the pump and probe beams do not broaden the transitions significantly.

The optical layout for the FM spectroscopy setup is shown in figure 3.4. If trapping light for a ^{23}Na MOT is required, the undiffracted order of the 80 MHz AOM is used. As the difference between the repump frequency for a ^{21}Na MOT and the pump frequency for ^{23}Na is 199 MHz (see figure 2.5), the necessary frequency shift for ^{21}Na is achieved by using a 100 MHz RF frequency for this AOM and double passing the -1 order. In this way we can switch between laser trapping of ^{21}Na and ^{23}Na by opening one aperture and closing another. The second 40 MHz AOM in double pass configuration modulates the pump beam for the saturation spectroscopy setup. The light of the probe beam is detected with a split photo diode and the resulting signal is put into a lock-in amplifier.

We give here the values which are used for taking calibration data with this setup. The 80 MHz AOM generated a 100.3 MHz sideband, the 40 MHz double pass AOM was set at 42.0 MHz. The frequency modulation of the 40 MHz double pass AOM setup was done at 21 kHz with a peak to peak modulation depth of 0.8 MHz. For the lock-in amplifier the integration time constant was 10 ms. The laser power in the pump beam was 200 μW, for a 2.5 mm beam diameter. The two probe beams of each 20 μW had a 0.5 mm beam diameter. The intensities for the pump and probe beam were thus about 1 and 0.5 times the saturation intensity of the transition, respectively, some power broadening can thus be expected.

The third locking method is a frequency offset-lock by which the laser is locked to another laser, which itself might be stabilized to an absolute frequency reference. Two offset locks have been used. Either an offset lock was made between two single mode lasers, or a laser was offset locked to the frequency comb. For the lock between two single mode lasers a good steering signal is obtained when the beat note between the lasers is between a few MHz and 2 GHz [266]. When the laser was locked to the frequency comb typically a fixed offset lock of 30 MHz was used, because of a fixed bandpass filter. Typically both offset locks were used simultaneously: an unlocked offset lock is easily detected when a spectrum analyzer is used to keep an eye on the beat note signal.

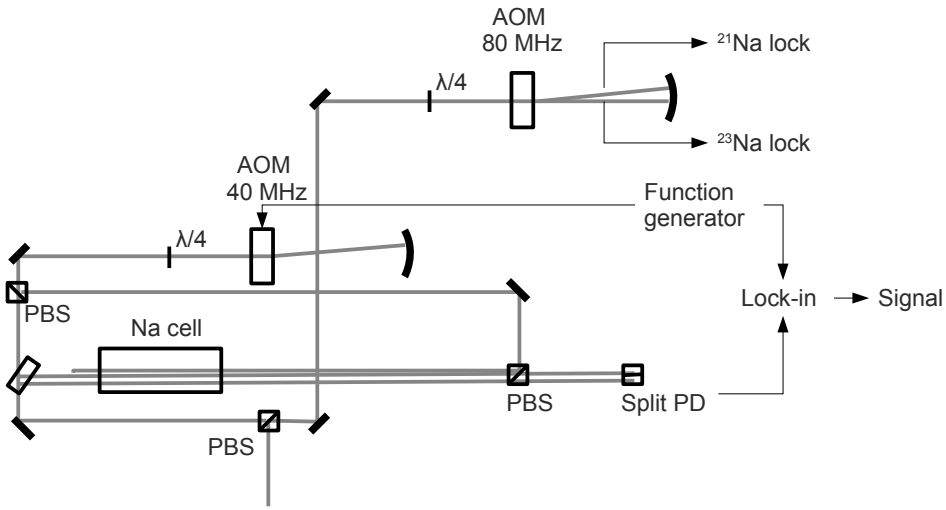

Figure 3.4: *The optical layout for the FM spectroscopy (lenses are not shown). PBS stands for polarizing beam splitter, PD for photo diode.*

FM spectroscopy calibration

First we discuss the frequency calibration of the FM spectroscopy signal, using the frequency comb, the Toptica laser and the Spectra laser. We locked the Toptica laser with a frequency ν_{Topt} to the frequency comb in such a way that ν_{Topt} was a few MHz away from the 3s $^2S_{1/2}$(F = 2) - 3p $^2P_{3/2}$(F = 3) transition, enabling the calculation of the absolute frequency. Secondly the light of the Spectra laser entered the FM spectroscopy setup and the optical beat note with the Toptica was recorded. The absolute frequency of the Toptica laser was

$$\nu_{\text{Topt}} = m \cdot f_{\text{rep}} + f_{\text{CEO}} + f_{\text{beat}} \,. \tag{3.1}$$

The repetition rate used was $f_{\text{rep}} = 250,041,573.000$ Hz, the carrier-envelope-offset frequency was $f_{\text{CEO}} = 40,000,000$ Hz and the beat of the comb with the locked laser was $f_{\text{beat}} = 25.4$ MHz. For these settings the mode number of the comb line which is closest the frequency of laser 1 is $m = 2035054$. Using these value in equation 3.1 yields that ν_{Topt} is detuned -5.5 MHz from the 3s $^2S_{1/2}$(F = 2) - 3p $^2P_{3/2}$(F = 3) transition.

The absolute frequency of the second laser is

$$\nu_2 = \nu_{\text{laser1}} + f_{\text{LL}} \,. \tag{3.2}$$

By scanning the frequency of the second laser with the laser light, FM saturated absorption spectroscopy on a heated ^{23}Na cell is performed. The spectroscopy section

shifts the frequency ν_{Spect} effectively by $2\nu_{\text{dp1}} + \nu_{\text{dp2}}$ after passing two double pass AOM setups (see figure 3.4). For the 80 MHz AOM ν_{dp1} is the used frequency, ν_{dp2} the frequency used for the 40 MHz AOM. The beat note between the two lasers ν_{LL} is counted and with the constant $\delta = -5.5$ MHz detuning we rewrite the frequency of the scanning laser frequency relative to the 3s $^2S_{1/2}$(F = 2) - 3p $^2P_{3/2}$(F = 3) transition (denoted as δ_{23}) to

$$\delta_{23} = \nu_{LL} - 2\nu_{\text{dp1}} - \nu_{\text{dp2}} - N\nu_{\text{rep}} + \delta \ . \tag{3.3}$$

To improve the signal to noise ratio of the beat note we moved the first laser frequency $N = 5$ comb teeth away from the transition to bring the beat note between the two lasers out of the low frequency range to the GHz range where the signal to noise ratio was better.

In figure 3.5 the result of a single frequency scan of the Spectra laser is shown. The frequency on the horizontal axis is calculated using equation 3.3. The zero crossing in figure 3.5 appears at 5 MHz, close to 0 MHz where it can be expected. The spectrum in figure 3.5 contains several cross-overs (features appearing in Lamb-dip spectroscopy [267]) of the transitions. The first cross-over next to the 3s $^2S_{1/2}$(F = 2) - 3p $^2P_{3/2}$(F = 3) transition is strong and might effectively move the zero crossing in which we are interested in, to the higher frequencies. It might also be that some systematic effects shifts the zero crossing to higher frequency.

AM spectra calibration

For some of the data we only used the AM method to lock the lasers. Here we calibrate the spectroscopy signal with the frequency comb. This allows us to determine afterwards the laser detunings by looking up at which fraction of the height of the spectroscopy signal the laser was locked to. In figure 3.6 the spectrum is shown, the middle dip is a crossover resonance, a feature arising from the Lamb-dip spectroscopy method. The frequency is derived by locking one laser to the frequency comb and recording the beat note between the second laser and the locked laser. We fit the sum of the transitions and crossover with Lorentzian lineshapes on a constant background to have an estimate of the effective center and width, this is accurate enough for our purposes.

In figure 3.6, in the left inset, the spectrum which includes the transition which is used to cool the atom is shown. The derivative is maximally about 5 MHz per 10% of the peak fraction. At the right side of the peak the pump transition is at 30% of the maximal value, locking at 60% of the maximum results in a detuning of -18(1) MHz.

In figure 3.6 in the right inset the spectrum including the transition which is used to bring the atom back into the cooling cycle is shown. At the right side of the peak at 80% of the maximal value is the repump transition. At 75% of the maximum of the left side corresponds to a detuning of -34 MHz, the F=1 to F'=1 transition.

To have an estimate of the precision of the detunings of both lasers we set the frequency offset lock between the lasers at 1712 MHz. For this value the detuning

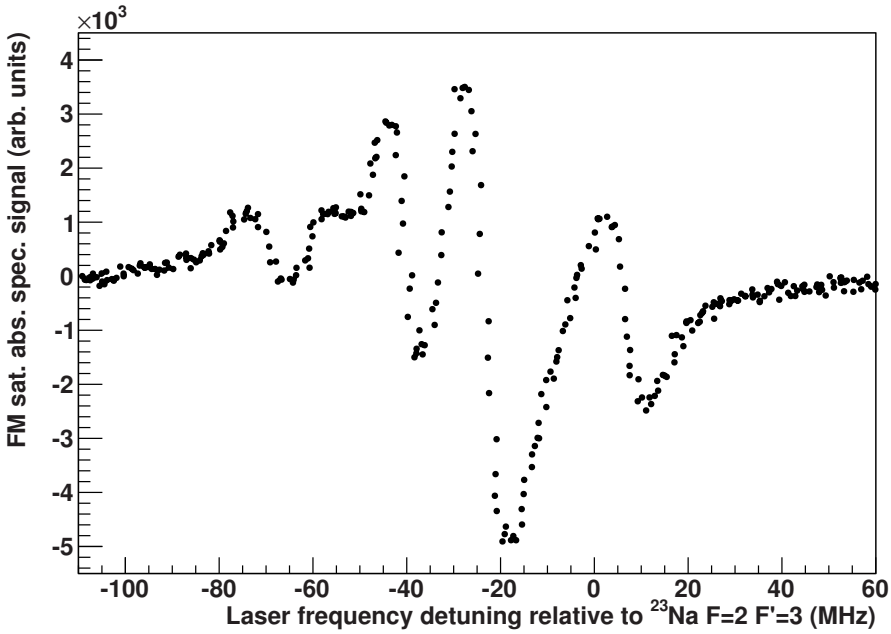

Figure 3.5: *The FM saturation absorption spectroscopy signal. The frequency axis is derived from the frequency comb. Each data point represents 10 ms of data.*

of both the pump and repump laser are identical and by changing the lock point of the repump laser the 3s $^2S_{1/2}$(F = 1) - 3p $^2P_{3/2}$(F = 2) transition is exactly where the MOT cloud appears, starting from a blue detuning. See section 3.4 for the relation between the lock position (fraction of maximum) and the detunings of lasers. So we start to lock to the repump spectroscopy resonance (in figure 3.6 the right peak) far on the right side. At a fraction of 73% the MOT cloud appears. This corresponds to a detuning of both lasers of 2 MHz. We conclude therefore that the error for the AM frequency calibration is of about 2 MHz.

3.5 Six way cross cell Magneto-Optical Trap

The glass cell in a six-way cross design was made by Precision Glassblowing of Colorado, Technical Glass Division, Centennial USA. A photo of the cell can be seen in figure 3.7. The design is similar to the glass cell used in a predecessor cell [196], the difference is that the viewports are made by AR coated glass, to reduce stray light. Furthermore the tube connecting to the LEBL is made longer compared to its predecessor. This reduces the loss rate through this exit port.

The magnetic field gradient for the MOT is provided by a standard anti-Helmholtz

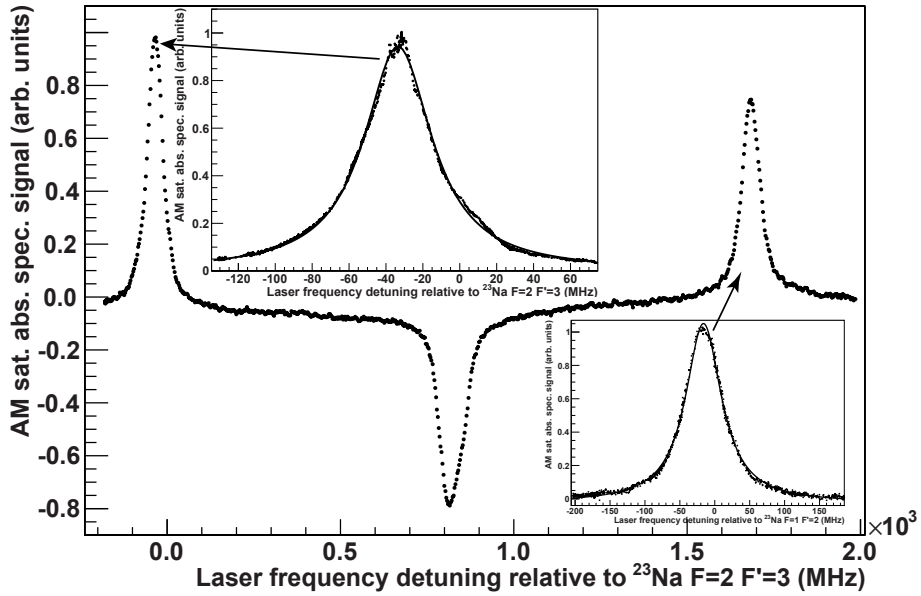

Figure 3.6: *The frequency range which includes the $F = 2 \rightarrow F' = 3$ cooling (left inset) and repump (right inset) transition of ^{23}Na. Both peaks consists of several transitions and their cross-overs, the fit with a single Lorentzian is used to provide a coarse frequency calibration. The center fit result is -34 (-16) MHz and has a FWHM of 45 (62) MHz for the left and right inset, respectively.*

configuration of two coils. The magnetic field gradient is 26 Gauss/cm for a current of 4.0 A.

The fluorescence light from the MOT cloud is collected by a 1 inch lens 6 cm away on top of the glass cell (see figure 3.7). The solid angle of this detection system is determined by an adjustable aperture just in front of the lens. Typically the aperture is set to a diameter of 6 mm and 2.5‰ of the solid angle of 4π is used. Similarly to figure 3.12, by focusing the MOT image onto a pinhole, spatial filtering is performed. After spatial filtering and a narrow band filter for yellow light (50% transmission) and a 50/50 beam splitter, the light is sent collimated onto a photo multiplier tube (PMT) (Hamamatsu R7449). The other 50% of the light is used for a camera.

The PMT has an active area of 25 mm diameter and the 11 stages are operated at 1 kV. When the number of photons entering the PMT becomes too large, the acceleration voltage might drop because of the currents flowing through the resistor chain of the PMT base, this sets a maximum for the detectable photon flux of about $30 \cdot 10^6$ /s. The dead time of our data acquisition system for these rates is still negligible.

Figure 3.7: *The cross glass cell seen from the top. The LEBL is connected to the right flange, on the left is the neutralizer foil mounted. The lower flange is connected to the second MOT chamber, the viewport through which the push beam is aligned on the MOT cloud can be seen opposite to it.*

The efficiency of this filter-splitter-PMT combination was measured with laser light. The PMT count rate is limited to about 30 MHz, this corresponds to a power of about 10^{-11} W for photons with a wavelength of 589 nm. Therefore, the intensity had to be strongly reduced. Three attenuation stages were individually calibrated with a power meter and then used combined. The resulting 26 pW ($7.8 \cdot 10^7$ photons/s) entering the filter-splitter-PMT system gave a count rate of $6.4 \cdot 10^5$ counts/s. The quantum efficiency of the PMT is thus about 3.3%. This value for the quantum efficiency is consistent with the specifications of the PMT [268].

The gain, measured by integrating the current due to a single photon, was measured to be about $2 \cdot 10^6$, which is also the specified value for the PMT. The threshold of -5.8 mV, as we use, is also clearly below the single photon peak height of about -10 mV. Summarizing, the measured threshold, gain, and quantum efficiency are consistent with the specifications of the PMT.

Throughout this thesis, the detection efficiency of the PMT varies as the tube voltage for the PMT tube has not always been the full value. The measured quantum efficiency was obtained with the maximal voltage, at a voltage of 94% of the maximal value of the acceleration voltage the yellow light related count rate was a factor of 2.6 lower. At a value of 91%, the difference was a factor of 5.7.

In all, a typical detection efficiency of the MOT fluorescence of 10^{-5} was used.

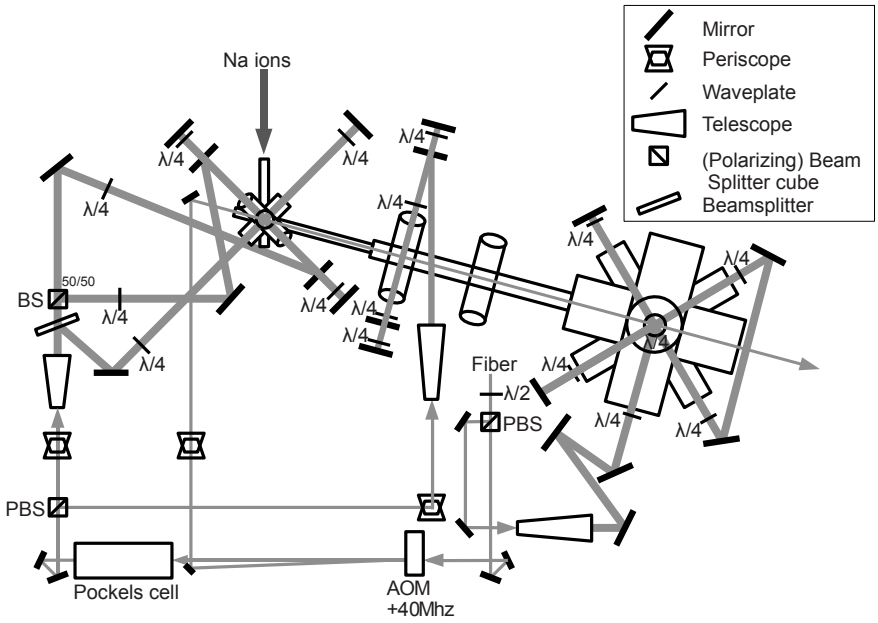

Figure 3.8: *The optical layout of the double MOT system with the push beam for the cross cell setup. The cubic cell setup has instead of a single beam expander, one expander per axis.*

3.6 Cubic cell Magneto-Optical Trap

The cubic cell design is shown in figure 3.9, it was installed in October 2010. This high-quality cubic cell has an inner diameter of 56 mm and an outer diameter of 63 mm. It was made by Precision Glassblowing of Colorado, Technical Glass Division, Centennial USA. The triangular shaped corner windows have a flat surface of about 10-20 mm and can be used for detecting the fluorescence of the cloud of atoms trapped in the MOT and to apply a push beam on the MOT cloud. The glass tube which connects the cell to the LEBL has a length of 110 mm from the corner to the metal of the CF 16 flange on the end of the tube. The length of the tube which connects to the science chamber is 55 mm. The length of the glass tube on which the neutralizer is mounted is 30 mm. We only are interested in the length over which it is glass, as the non-stick coating only works on glass and not on metal. The circumference of the tubes is midway about 43 mm, the estimated thickness is 1.5 mm, giving an estimated inner diameter of 10.6 mm.

We performed Monte Carlo simulations, as described in section 2.8, for the cube with two tubes connected to it. We did not include the third tube as the neutralizer

Figure 3.9: *The cubic cell in which the neutralized ions are trapped by the Collector Cell MOT. The ions enter through the long, left tube, the neutralizer is mounted on the opposite tube and the atoms are transported to the Science Chamber setup through the third tube.*

foil largely covers the exit area. For estimating the number of trap passages four parameters are relevant. The first parameter is the number of bounces in the cube before the atom exits through one of the two tubes. The second parameter is the average number of times the atom returns into the cube after having entered one of these exits. The third parameter is the fraction of time the atom spends inside a sphere with a certain, fixed radius representing the laser trap volume[2]. The fourth parameter is the fraction of the bounces inside the cube that results in a passage through this volume. The third and fourth are related and indicate whether the particles which enter the trap volume spend most time near the surface of the trap volume (short paths) or passes more often the center of the sphere (long paths).

The angular distribution for the particle emission pattern when the particles are emitted from a surface has to be chosen in the Monte Carlo simulation. We use in the simulation the isotropic distribution, but for completeness we also mention the results based on the usual cosine distribution. See appendix B for more details on the Monte Carlo simulation and the argument to use an isotropic distribution. In the cubic cell with an inner side of 56 mm a particle bounces 67 times on average before it enters one of the tubes. For the tube length of 110 mm (LEBL connection) the probability to

[2]The volume of the three intersecting laser beams can be well approximated by a sphere.

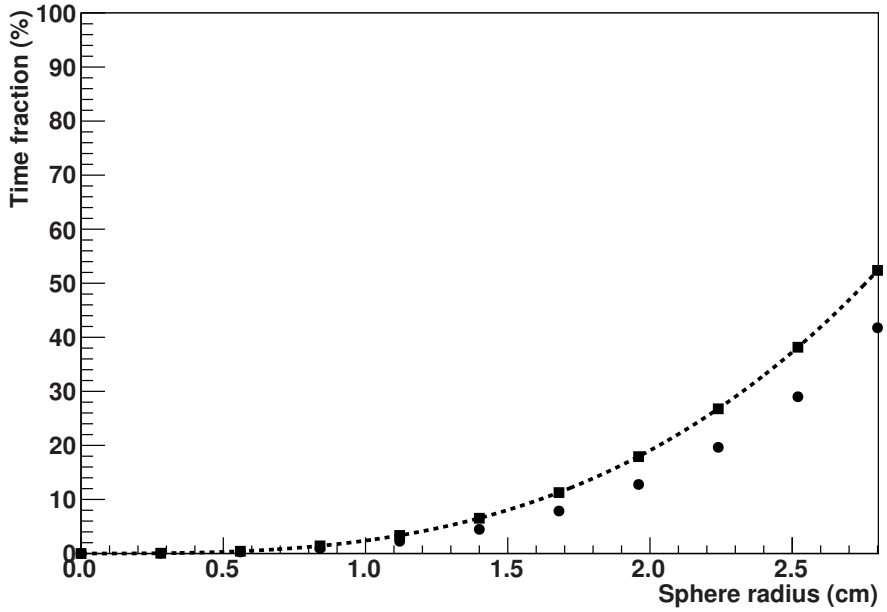

Figure 3.10: *Monte-Carlo results for cosine distribution (squares) and isotropic emission (dots) for the fraction of the time that is spent inside a sphere in a cubic cell. The curve is the fraction of the volumes.*

exit, when entering the tube, is about 10%. For the tube leading to the SC setup this probability is 17%. Therefore on average the particle bounces 500 times in the cube before it is permanently lost. With a cosine distribution the numbers are 9%, 16% and 830 bounces. The loss through the exit area around the neutralizer foil we assume to be negligible. We can estimate the allowable exit area by calculating the ratio of the exit surface to the total surface. The cube has an inner surface area of in total 216000 mm^2. For 500 bounces therefore an exit area of about 40 mm^2 would result in a loss rate twice as high: 250 bounces. This latter area is the area of a ring with a diameter of 7 mm by 2 mm. The size of this area is subject to a trade-off, as the non-sticking coating will be damaged sooner the closer the heating foil comes to the glass wall.

For a sphere diameter of 45 mm about 20% of the time the atoms are inside the sphere for the isotropic case (see figure 3.10). The fraction of all bounces that the atoms enters the sphere is about 20% for the isotropic distribution. For the cosine distribution this value is slightly higher.

Table 3.1: *The estimated collection efficiency for the cubic cell setup.*

Capture velocity of 27 m/s, 293 K vapor	$1.5 \cdot 10^{-4}$
Trap passage	20%
Collection efficiency for 500 bounces	1.5%

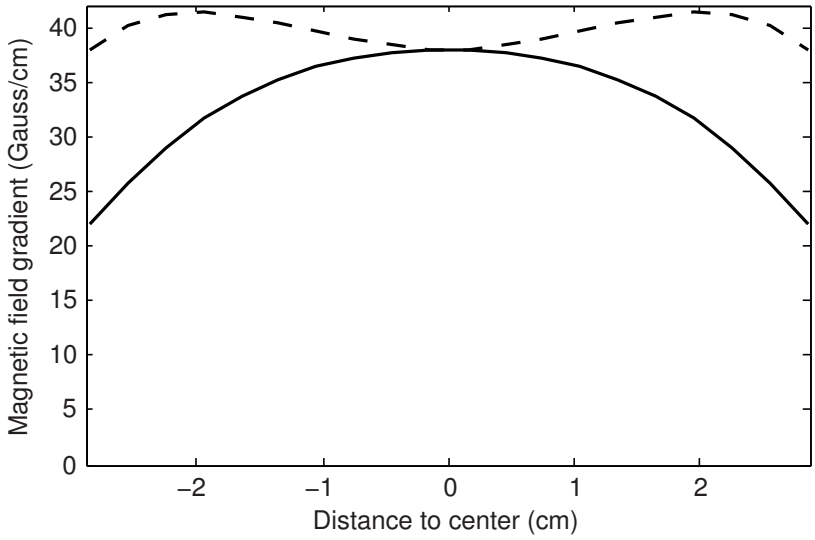

Figure 3.11: *The calculated magnetic field gradient in the axial direction ($\frac{dB}{dz}$, dashed line) and in the plane normal to this ($\frac{dB}{dx} = \frac{dB}{dy}$, solid line) for a current of 6 A. For comparison the latter values are multiplied by -2. The center of the trap is at 0 cm.*

Quadrupole magnetic field

The magnetic quadrupole field for the cubic glass cell of the CC MOT setup is generated by a standard anti-Helmholtz configuration of two coils. The calculated magnetic quadrupole field gradient is shown in figure 3.11. The coil holders were made of aluminum, cooling was provided by water flowing through a copper wire with a hollow cubic profile which was fixed to the coil holder. For a current of 6 A the dissipation power per coil is 43 W. We measured a magnetic field gradient of 39 Gauss/cm at the center for a current of 6.0 A. This is in good agreement with the design value of 38 Gauss/cm at this position, see figure 3.11. Typically we used a current of 4.0 A, this gives a magnetic field gradient of 25 Gauss/cm in the strong axis. We also include a pair of correction coils, each with 92 windings. These give a measured magnetic field of 6.4 Gauss/A, in agreement with the design value of 6.3 Gauss/A.

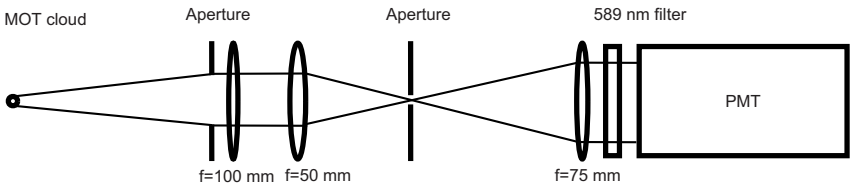

Figure 3.12: *The MOT fluorescence detection scheme for the cubic cell setup.*

Optical layout

The optical layout is similar to the layout used with the cross cell setup, see figure 3.8. All three beams have the same distance from the first beam splitter (122 cm), to have equally large expanded beams. The beam expanders (20x, BE20M-A, maximal input $1/e^2$ beam diameter is 2.25 mm, 350-650 nm AR coating range, Thorlabs) with a maximal output diameter of 45 mm are mounted on aluminum holders. On these holders also the quarter wave plates (zero-order waveplates, 45 mm clear aperture, VM-TIM, Jena) are mounted.

For LIAD applications a 350 mW 385 ± 5 nm light emitting diode is available (Nichia, [269]). A TTL signal controls the optical output, the rise and fall time of the diode are less than 1.5 μs for a current of 0.4 A.

Fluorescence detection system

The layout of the detection system is shown in figure 3.12. The MOT cloud has a size of about a mm. To improve the signal to noise ratio spatially filtering is performed before the light can enter a photon detector. The first aperture determines the solid angle, then two lenses focus the light onto a second aperture which does the spatial filtering. A third lens collimates the beam again. To suppress the detection of photons due to stray light and black body radiation from the hot neutralizer foil we use a 25 mm diameter optical filter of 5 mm thick with a center wavelength of 589 nm (bandwidth 15 nm) with 93% transmission (FF01-589/15-25, Semrock Inc.). The photon detection is done with a Hamamatsu R7449 Photo Multiplier Tube (PMT), for which we measured a quantum efficiency of about 3%, consistent with its specifications, *cf.* section 3.5.

To improve the collection efficiency the glass walls should be coated with a non-stick, transparent film. This layer of coating prevents chemical bonding (chemisorption) to the surface and reduces the sticking time due to adsorption from a ms time scale to a μs time scale (see table 2.6). The coating only works on a glass surface, not on metal. We tried two types of coating chemicals, SC-77 (Fluorochem Ltd) and PDMS (Xiameter, viscosity of 100 000 centistokes). To create a thin layer, the glass surface has to be very clean [264, 270, 271]. The layer should be at least so thin that a clear interference pattern should be observable. For the SC-77 coating we followed the procedure as it was developed at Stony Brook [272]. For PDMS only a prepared

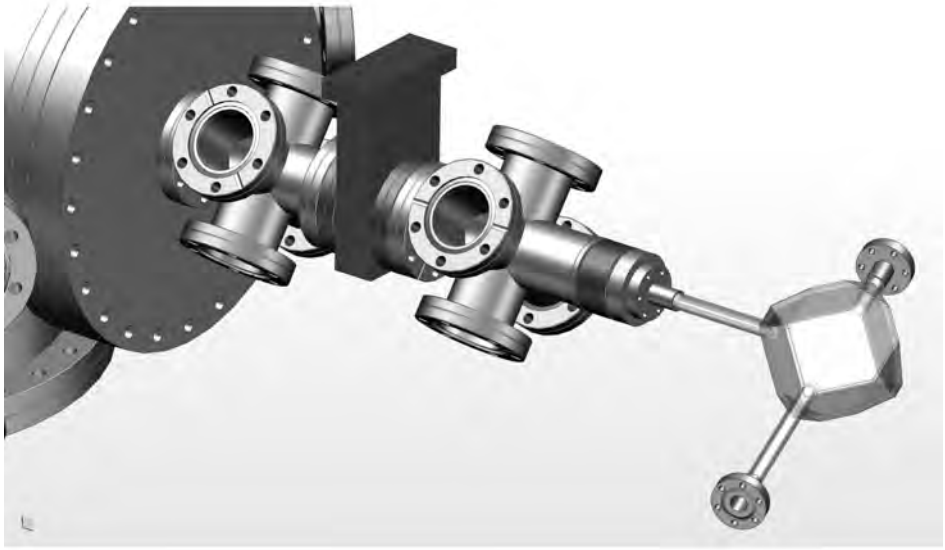

Figure 3.13: *The funnel (first six-way cross from the cubic cell). The quadrupole magnetic field gradient for the 2D MOT system is created by a single wire in hair pin configuration (not shown). Also not shown are two pairs of compensation coils in Helmholtz configuration.*

surface is necessary [233]. In contrast to the SC-77 coating chemicals, for PDMS no chemical reactions are involved.

Behind the neutralizer foil a Rb dispenser (SAES, Italy) is mounted. According to Atutov *et al.* [233] and others the Rb vapor can be used to cure/passivate/ripen the non-stick coating and therefore increase the number of bounces. Atutov used Na to cure their PDMS coating to trap Rb more efficiently and observed an increase with three orders of magnitude in the number of bounces. Whether such curing is necessary to get a high number of bounces and whether Rb can also be used to enhance the number of bounces for the trapping of Na is not clear yet. Also the nature of this repairing mechanism has not been identified yet.

3.7 Optical transfer

We describe here the hardware used for the push beam and optical funnel. For further details see section 5.1.

The push beam is created from the first order diffracted beam of a 40 MHz AOM

and has typically a diameter of 2 mm. The push beam enters the cell through the window opposite to the transfer tube shown in figure 3.13.

The funnel is created using the first six-way cross after the collector cell (figure 3.13). The setup for the laser beams is shown in figure 3.4. The beams are made with a beam expander (Thorlabs BE20M-A), the 2D MOT beams are created with a single beam configuration: after passing the center twice the beam is reflected back onto itself. To create circular polarized light four quarter-wave plates (zero order 589, 40 mm clear aperture, Altechna) are mounted on aluminum mounts. The magnetic field gradient for the funnel is created by four wires in a single wire hair pin configuration. The maximal current is 500 A. The magnetic field gradient is in leading order

$$\nabla_B = \frac{4\mu_0 I}{\pi a^2}(1 - 20\left(\frac{r}{a}\right)^4)\,, \tag{3.4}$$

with a the separation between the wires with current I and $\mu_0 = 4\pi \cdot 10^{-3}$ Gauss m/A. For $a = 5.5$ cm and $I = 500$ A the magnetic field gradient is 26 Gauss/cm at the center ($r = 0$).

When the funnel section is optimized, the quadrupole field can be generated using two sets of permanent magnets, simplifying the setup. Tiecke *et al.* [185] generates such a field for a 2D MOT with two sets of magnets, each set consisting of two stacks of three 25×10×3 mm neodymium magnet bars separated by 12 mm to make an effective dipole bar of 62 mm total length. Each set has had measured magnetization of $8.8(1) \cdot 10^5$ A/m, equivalent to a magnetic field of 1.1 T. For a separation of 84 mm such a configuration generates a magnetic field gradient of 50 Gauss/cm [273].

3.8 Science Chamber MOT system

The chamber which contains the second MOT system is called the Science Chamber (SC) and its detailed description can be found in [69], here we summarize its key features. Three of the six 200 CF flanges were originally to be used for mounting β detector systems. In this phase of the experiment we use it to transfer the atoms through. For alignment purposes on the opposite side a viewport is mounted.

To create the MOT trapping beams four 63 CF viewports are used in the horizontal plane. The vertical beam for the MOT is created by a mirror with a 1 inch diameter which is mounted in the vacuum under 45°, which reflects the laser beam in the vertical direction. The magnetic field gradient is provided by an anti-Helmholtz pair of 16 hollow copper wires cooled with water, generating at the center a field gradient of 20 Gauss/cm in the axial direction for a current of 300 A. To compensate residual magnetic fields and the effect due to the presence of the optical table three pairs of compensation coils in Helmholtz configuration are used.

MOT cloud fluorescence light is collected by a 2 inch lens behind a 40 CF viewport with 34 mm visible diameter, 270 mm away from the MOT center. By focusing on an aperture the image is spatially filtered and then after collimation sent on a photo multiplier tube (PMT, Hamamatsu R7449). The solid angle of the light collection is

$1.2 \cdot 10^{-2}$ sr and the PMT efficiency is 3% at 589 nm (*cf.* section 3.5). The loss in the lenses is negligible. The overall photon collection efficiency is therefore $3 \cdot 10^{-5}$. For a typical scattering rate of $6 \cdot 10^{6}$ photons/s/atom results the count rate would be 180 counts/s/atom.

3.9 Data-acquisition

The core of the DAQ system is formed by VME based computer boards which are connected to the local area network. A versatile software framework by the name of CADDIE (Control and Distributed Data-acquisition Integrated Environment) runs on the VME computer. It takes care of the initialization and the configuration of the various VME cards and reads out the data of these VME modules [274]. The CADDIE software is developed to allow for maximal flexibility. It has been made by F. Zwarts of the IT department of KVI.

On standard PC's, another software framework called Bogey can connect over the network to the CADDIE software. Bogey can unpack the data from the module and interpret it in real time. Bogey is mainly developed by G. Onderwater from the TRIμP group. The voltages of the LEBL can be controlled via MEN M-Modules. The multidimensional optimization of the LEBL has been performed using this interface.

Bogey is written in C++ and is embedded in the open source ROOT framework, which is developed at CERN. Therefore Bogey is able to use the very rich plotting, fitting and data manipulating features offered by ROOT [275]. The Bogey software is also used to do the off-line data analysis, the input data stream is then coming from a file buffer instead of a network buffer.

CHAPTER 4

Towards an efficient Magneto-Optical Trap for ^{21}Na

4.1 Introduction

The efficient collection of radioactive atoms after online production is the crucial step in a competitive measurement of the correlations between the ^{21}Na nuclear decay products [126, 276]. Since 2008 the TRIμP production, separation and slowing facility at the KVI offers a wide range of low-energy, radioactive ion beams including ^{21}Na for experiments which test physics beyond the Standard Model [128, 129, 277, 278]. The goal of this chapter is to determine the efficiencies and limiting factors of the conversion of the low-energy ion beam into a neutral atomic vapor using a heated catcher foil and the subsequent trapping of the Na atoms in a Magneto-Optical Trap (MOT) [27].

The relevant processes for the measurements discussed in this chapter are shown in figure 4.1. After extracting the ions from the Thermal Ionizer (TI), which is the last device of the TRIμP facility, the ions are transported through the Low Energy Beam Line (LEBL) towards the collector chamber (CC) setup. The ions are collected on a neutralizer foil which is in essence an atomic oven. By heating the foil to about 1000 K the atoms are released.

If the velocity of a released atom is below the capture velocity of the MOT it will be trapped. Under typical conditions capture can happen for only 1 atom out of 10^5. Most of the atoms collide with the glass cell wall. A non-sticking coating can be used to prevent permanent sticking. When released from the wall the atoms have another chance to be captured. Due to thermalization with the wall at room temperature the trapping probability increases with about an order of magnitude. In our setup, up to 1000 bounces are possible until the atoms are lost through one of the exit ports of the cell. Taking into account the number of trap passages (which is a fraction of the number of bounces) and assuming a neutralizer release efficiency of 50%, the maximum collection efficiency that can be reached is about 1%.

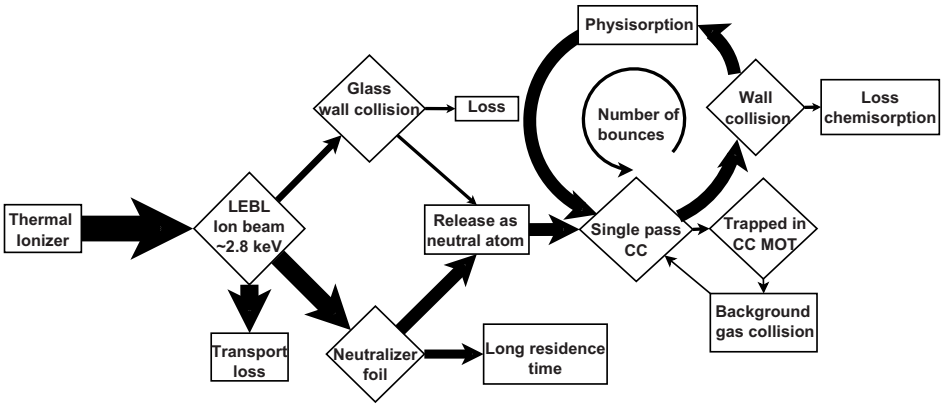

Figure 4.1: *The schematic overview of the neutralization and laser trapping setup. The goal is to efficiently trap neutralized ions from the Thermal Ionizer in the CC MOT.*

Current rare-isotope facilities using an accelerator have low-energy particle production rates in the range of 10^6 [78] to 10^8 particles/s [120, 125]. Including the extraction and transport losses for our experiment and the present beam current limit due to the target window, 10^5 ^{21}Na ions/s enter the CC (the maximal yield is projected to be $5 \cdot 10^7$/s). Under the current conditions the expected number of continuously trapped atoms is thus of order 10^3 for a MOT lifetime of 1 second. The number of continuously trapped atoms depends also on the number of bounces of the atom in the trapping cell, only part would be trapped when no bounces occur.

For characterization and optimization purposes we use a stable ^{23}Na ion beam from the TI which provides an ion flux of up to 10^9 ions/s. However, we have to take into account the history of the beam and have to discriminate between the last deposited ^{23}Na ions and ^{23}Na already present in the foil or originating from previous deposits. As the ^{21}Na trapping signal is small the residual presence of ^{23}Na has to be considered.

Two different CC setups have been used for the collector stage. We call the setup which was used up to the end of 2010 the cross cell setup. Its successor, which allows for larger laser beams, is called the cubic cell setup. The most important and reliable measurements have been done with the latter setup. We discuss the ion transport efficiency in section 4.2 for both setups. The results of the characterization and calibration of these MOT systems is in section 4.3. We establish in section 4.4 the neutralizer efficiency using the cubic setup. In section 4.5 we study time dependent background signals we observed for ^{23}Na. In section 4.6 we summarize all measurements obtained and establish the overall efficiency of the setup. In section 4.7 we compare the obtained overall efficiency with other experiments where radioactive atoms are trapped with a MOT. We draw conclusions, identify limiting factors and give an outlook.

4.2 Ion transport efficiency

The LEBL has two isotope dependent parts: the Wien filter and the drift tube. See figure 3.2 for an overview of the various elements in the LEBL. The Wien filter consists of a crossed variable electric and fixed magnetic field. The force on an ion with kinetic energy K is $F = q(E + vB)$, which results in a deflection of the ion beam with an angle $\theta = \arctan(qd(\frac{E}{2K} + \frac{B}{\sqrt{2K}\sqrt{m}}))$ for a Wien filter of length d. The electric field is tuned such that $\theta = 0$ for the particles of interest. The relative change in the electric field from ^{21}Na to ^{23}Na is thus 4%. The mass dispersion of the Wien filter is 4.2%/mm at 2 keV at the MCP focus [69] (the MCP is situated on position E3, see figure 3.2). This is insufficient for our use. Indeed, the filter was designed to be used with the Radio Frequency Quadrupole (RFQ) cooling and buncher [195] which has a much smaller entrance aperture than the drift tube. Therefore contaminations can be expected to be present, both for ^{21}Na and ^{23}Na.

The transmission of the $l = 1$ m long drift tube is mass dependent as well. The maximal transmission is 50%, which is achieved for a switching frequency of $\frac{1}{2l}\sqrt{\frac{K}{2m}}$. The transmission decreases linearly with a higher or lower frequency. For a beam energy of 2.8 keV the expected optimal frequency for ^{23}Na is 76.6 kHz. Experimentally however, 68 kHz is found to be optimal, which implies a duty cycle of 44% at this energy.

The ion transport efficiency is the ratio of the ion implantation rate into the neutralizer foil and the ion extraction rate from the Thermal Ionizer,

$$\epsilon_{\text{ion}} \equiv \frac{R_{\text{ion}}}{R_{\text{source}}} \ . \tag{4.1}$$

A measurement of this ratio is non-trivial as explained below. Our strategy is to determine the ion transport efficiency in two different ways, providing a consistency check. For the stable isotopes we measure the electrical current at two positions in the Low Energy Beam Line (LEBL). For ^{21}Na we measure the transport efficiency by detecting the 511 keV photons originating from the annihilation of the β^+ particle.

Transport of ^{23}Na

The hot materials of the Thermal Ionizer (TI) contain trace elements, among which is ^{23}Na. We assume that the ion beam produced from these trace elements has identical properties to that produced from the radioactive particles stopped in the TI foils. We measure the current after the drift tube, using the microchannel plate as a Faraday cup. The second position that we have used is the neutralizer foil.

We have measured the transport efficiency for four mass groups as listed in table 4.1 by observing the image of the focused ion beam on a phosphorescent plate after the drift tube (position E3 in figure 3.2). It was checked that the transport efficiency of the drift tube scales linearly with the drift tube frequency. The H_2O^+ setting is close to the ^{23}Na setting, which might affect the efficiency measurement for ^{23}Na, leading to

Table 4.1: *The transport efficiency of the LEBL for stable isotopes. At the ^{21}Na setting also stable ions are coming onto the neutralizer (about 20 pA).*

Cell	Isotope setting of the Wien filter	LEBL efficiency (%)
Cross	H_2O^+	32(4)
	[Contamination at ^{21}Na]	[20(2)]
	^{23}Na	26(3)
	^{39}K/^{40}Ca	22(2)
	^{133}Cs/^{137}Ba	15(2)
Cubic	^{23}Na	32(4)

an apparent lower efficiency. The observed dependence of the transport efficiency on mass may indicate a residual velocity dependence. We estimate the overall systematic error due to the secondary electron yield and possible beam contamination to be 10%.

After installation of the cubic cell the ^{23}Na beam parameters were checked by maximizing the optical signal of the MOT. This eliminates contributions other than ^{23}Na. All relevant voltages of the LEBL are controlled by computer, allowing for this multidimensional scan to be performed in a few hours. The optimal LEBL settings found for ^{23}Na using this procedure are the same as found by optimizing on the current. From these values the LEBL setting for ^{21}Na is calculated and used as a starting point for further optimization. Measuring the transmission at the ^{21}Na settings shows that a clean beam of ^{21}Na is not possible with the current setup (see table 4.1). The transport efficiency into the cross setup was measured to be 26(3)% and into the cubic setup 32(4)% (see table). The most probable reason for the difference between these two cells is that for the cubic cell we aligned the neutralizer foil optically in line with the LEBL, for the cross setup we found that only 2/3 of the neutralizer foil was visible by eye from the TI extraction point.

Transport of ^{21}Na

The determination of the transport efficiency using ^{21}Na requires knowledge of the efficiency of the detectors used to measure the 511 keV photons from the β^+ annihilation. In table 4.2 their calibration with a ^{22}Na source and typical numbers from a ^{21}Na beam time are reported. It is important to note the difference between the calibration source ^{22}Na and ^{21}Na. The annihilation detection efficiency is different because the range of the β^+ particles from ^{21}Na is much larger than the range of the β^+ particles from the decay of ^{22}Na (where the β^+ annihilates inside the source). For this reason we apply a reduction of 50% to the detection efficiency when ^{21}Na hits a thick stopper, *i.e.* only the β^+ particles moving into the stopper contribute. The neutralizer foil is not thick enough to stop the β^+ particles, therefore we measure here in singles mode, avoiding a strong dependence on position. For the efficiency of the pair detection at

Table 4.2: *Decay detection efficiency for a calibrated ^{22}Na source and typical ^{21}Na beam time conditions.*

	Isotope	
Decay properties	^{22}Na	^{21}Na
Mean β^+ energy (MeV)	0.2	1.1
Range in pyrex (mm)	0.35	6.5
Thermal Ionizer extraction		
β^+ coincidence detection efficiency	$3 \cdot 10^{-3}$	$1.5 \cdot 10^{-3}$
^{21}Na current I_{TI} (/s)	-	$3 \cdot 10^5$
Collector chamber		
β^+ detection efficiency in singles mode	$1.3 \cdot 10^{-2}$	
^{21}Na current I_{CC} (/s)	-	$5 \cdot 10^4$
Transport efficiency $\epsilon = \frac{I_{\mathrm{CC}}}{I_{\mathrm{TI}}}$	-	20(10)%

the position after the TI, the source was put at the cup position where also the ^{23}Na current was measured.

Putting the source inside the CC is not practical, so we average the efficiency from two positions. The source is first put close to the neutralizer and then on the other side at the entrance to the cell about 10 cm further away. The difference by a factor of 3 is taken as the uncertainty on the final value.

In figure 4.2 the 511 keV photon count rate in the cubic glass cell is shown, as function of the Wien filter setting. This establishes the dispersion at the glass cell. The line in the figure is a fit of a Gaussian function, it gives a mean of 565 V, with a width $\sigma = 18$ V. The value for the mean is the voltage predicted from the scaling of the optimal transmission of other isotopes and the optimized settings for the LEBL obtained by maximizing ^{23}Na fluorescence signal from the MOT related to the ion beam. The Wien filter setting of ^{23}Na, expected and found at 540 V predicts then a ^{23}Na contamination of about 36% for the ^{21}Na setting.

Summarizing this section, we have used various methods to estimate the efficiency of the transport from the Thermal Ionizer to the glass cell. We find a value of 30(3)% for the cross setup and 35(4)% for the cubic setup using ^{23}Na. In standard conditions the yield of ^{21}Na is $5 \cdot 10^4$ ions/s in the glass cell for the cubic setup. With ^{21}Na we find a transport efficiency of 20(10)% for the cubic setup.

During the writing of this thesis, it was found from off-line measurements that the transmission efficiency for Ba could be substantially increased (close to 100%) by increasing the trapping frequency of the RFQ, the reason being the details of the end trap of the RFQ [279]. It might be worthwhile to check for ^{21}Na if this variable has

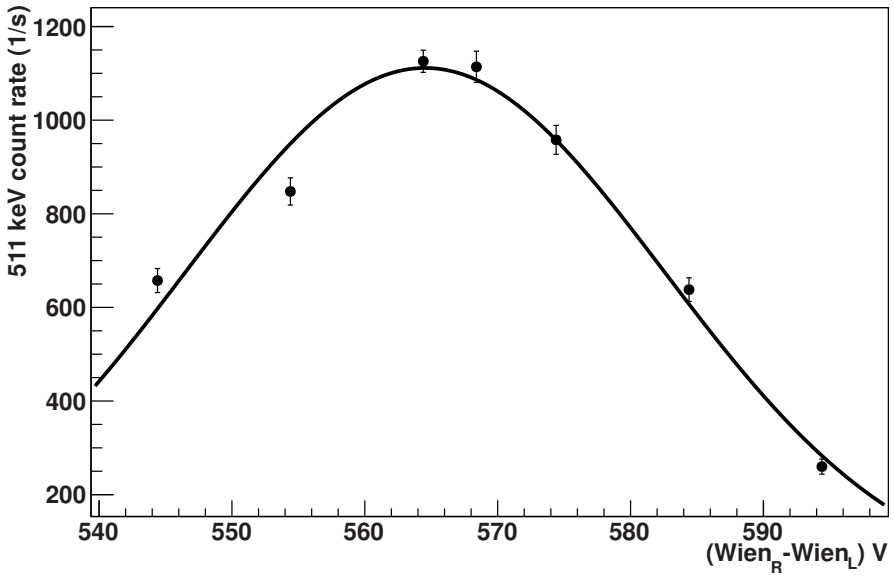

Figure 4.2: *The 511 keV count rate from ^{21}Na decays in the glass cell walls (3.5 mm thickness) measured by a NaI detector as function of the Wien filter voltage. The line is a fit of a Gaussian function.*

been correctly optimized in the first test with ^{21}Na. The transport efficiency of 35% for Na might then be brought close to 100% and would also result in less contamination in the ion beam. Using the RFQ instead of the drift tube thus might result in a factor 3 higher ion transport efficiency. Note that, although the RFQ has previously been used with Na, it was omitted as making the system unnecessarily complex. If the RFQ could only achieve a total transmission of 40% [69], similar to the drift tube, the latter should be preferred.

4.3 Magneto-Optical Trap parameters

We have studied a number of Magneto-Optical Trap (MOT) parameters by loading the MOT using a beam of stable sodium ions. The timing scheme for these experiments is shown in figure 4.3a. Shown is a macro cycle, which is built up from a number of cycles of each 10 - 40 s long. Only during the first cycle the ^{23}Na ion beam is present. At the beginning of each cycle the neutralizer foil is heated for 2.5 - 3 s. In figure 4.3b the ^{23}Na MOT fluorescence is shown as function of time for a ^{23}Na ion beam. We observe a small MOT fluorescence signal when no ion beam is injected. Although we

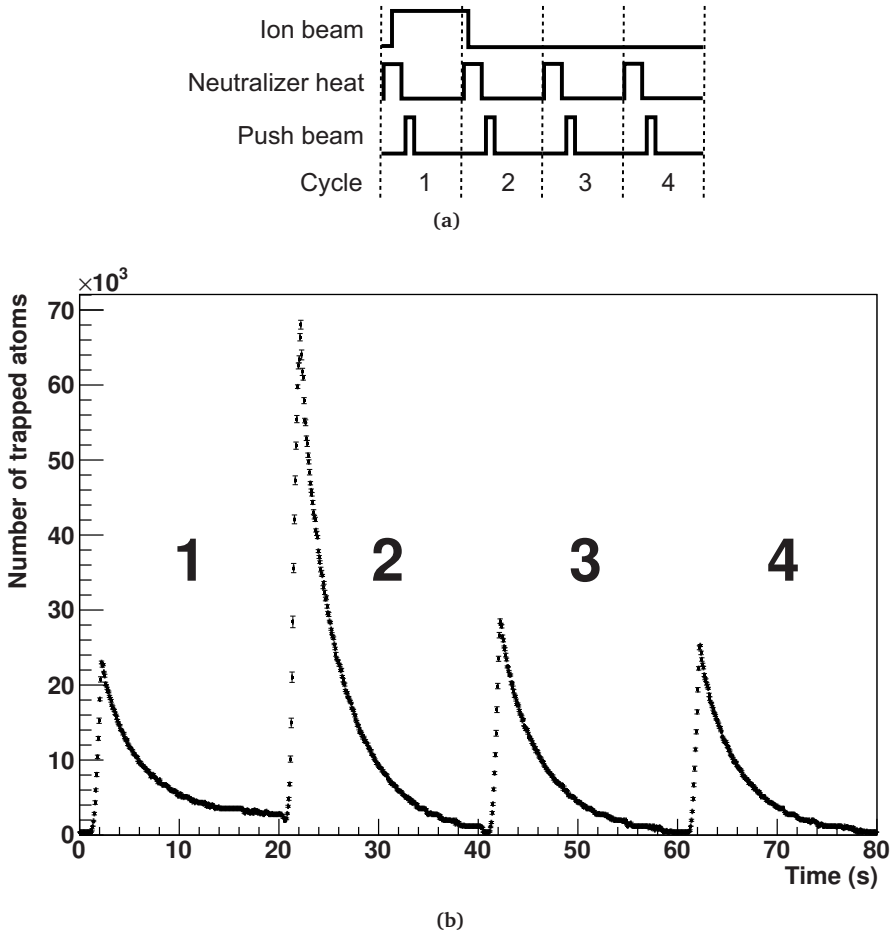

Figure 4.3: *The timing scheme for the collector chamber setup (a). A typical observation of an ion beam related MOT signal for a single macro cycle, consisting of four cycles (b). The fluorescence rate has been converted to the number of trapped atoms (see text). An increase in the number of trapped ^{23}Na atoms after the deposition of the ions in cycle 1 is clearly visible in cycle 2. By taking the difference between cycle 2 and cycle 4 the increase in the number of trapped atoms due to the release of neutralized ions can be obtained.*

can study the overall efficiency using the stable ^{23}Na ion beam, we therefore must take into account the ^{23}Na already present in such studies.

Note also the 'cold' neutralizer effect: At $t = 20$ s of the ion beam period (cycle 1) the MOT signal ends up higher than at the same time within the cycle when the ion beam extraction is off (cycle 2 ($t = 40$ s), 3 and 4). We will study this effect in section 4.5. The difference of the signal between the cycle 2 and cycle 4 is shown in figure

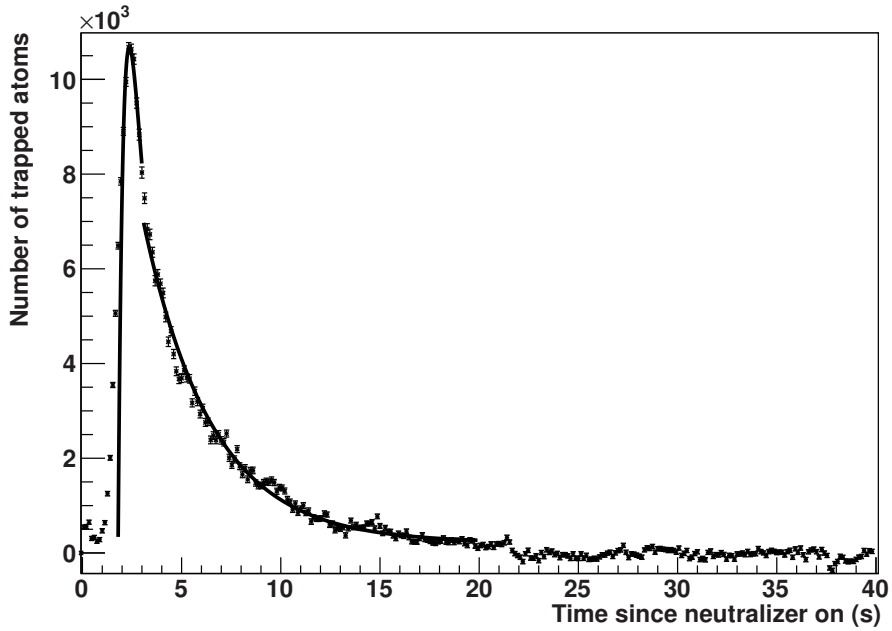

Figure 4.4: *The difference in the ^{23}Na MOT population for the cycle 2 - cycle 4 combination (see for the timing scheme figure 4.3a). This is a different dataset than used in figure 4.3b. This dataset is part of a measurement series on the temperature dependence of the released fraction. The left curve is a fit of the diffusion model (which is explained in section 4.4). The right curve is a fit of the exponential lifetime of the MOT cloud, on top of an offset. The fit results are given in table 4.4.*

4.4. Here the neutralizer foil is heated by a current of 6.3 A, from $t = 0$ to $t = 3$ s. The ion beam is present from $t = 2$ to 22 s and its current measured on the neutralizer is 13.5 pA.

Laser light intensity

The MOT fluorescence rate is our main observable for studying the overall efficiency of the CC setup. We analyze its dependence on the primary laser light intensity to determine the laser light intensity (in units of the saturation intensity) experienced at the MOT cloud and compare it to the directly measured light intensity (in mW/cm^2). From that we can calculate the scatter rate per atom and study the number of trapped atoms as function of the MOT parameters. First we calculate the pump and repump laser light intensity from the beam diameters and powers. As a consistency check we then fit the scatter-rate equation, with the maximal intensity as fit parameter, directly to the fluorescence signal. The MOT fluorescence rate is directly related to the number

Table 4.3: *The parameters to determine the pump and repump laser intensity for the cubic setup. The saturation intensity for the $F = 2 \rightarrow F' = 3$ transition is 13.41 mW/cm^2 for isotropic light polarization.*

Laser beam	Pump	Repump
Transmission of expander (%)	68	30
$\varnothing$ after expander (cm)	6.0	11
Peak intensity (mW/cm^2)	14	0.7
Peak intensity (I/I_s)	1.0	0.11

of trapped atoms through equation (see also chapter 2)

$$\Gamma_{\text{scat}} = \frac{\gamma}{2} \frac{s_0}{1 + s_0 + 4(\delta/\gamma)^2} , \tag{4.2}$$

with γ the linewidth of the transition (10 MHz), δ the total frequency shift and $s_0 = I/I_s$ the total intensity due to the six laser beams in units of the saturation intensity. The pump and repump laser frequency detunings for the sodium isotope considered are relative to the 3s ^{2}S$_{1/2}$(F = 2) - 3p ^{2}P$_{3/2}$(F = 3) transition and 3s ^{2}S$_{1/2}$(F = 1) - 3p ^{2}P$_{3/2}$(F = 2) transition respectively. This fluorescence to atom conversion is valid for a relatively low number of atoms (up to 10^5 for Na), for a larger atom number the optical density starts to significantly influence the scattering rate observed outside the MOT cloud [280].

For the cubic cell setup a magnetic field gradient of 25 Gauss/cm in the axial direction (strong axis) was always used, see also section 3.6.

Pump laser intensity

Here we first estimate the laser intensities at the MOT cloud position and then study the fluorescence dependence on the intensities. For the direct determination of the pump and repump laser power intensity at the MOT position for the cubic cell setup, we measure the transmission through the beam expander and calculate the beam diameter after the expander, giving a peak intensity. The total pump power entering the setup is 100 mW and the total repump power is 16 mW. In front of each beam expander of the three retro-reflected MOT arms the power is on average 32 mW and 5 mW for pump and repump power respectively. For a Gaussian beam profile with the $1/e^2$ intensity diameter $2w$ the peak intensity is $I_0 = \frac{2P_0}{\pi w^2}$ and the fraction transmitted through a circle of radius r is $1 - \mathrm{e}^{-2r^2/w^2}$. The 20x beam expanders have a maximal expansion diameter of 45 mm. The beams are clipped to 40 mm by the usable area of the quarter wave plates. For a 10% loss in the retro-reflected beam this results in the peak intensities given in table 4.3. The error on the peak intensities we estimate to be 20%. Note that due to the different beam diameters for the pump and repump light, the repump intensity is about 5% of the pump intensity at the MOT cloud position.

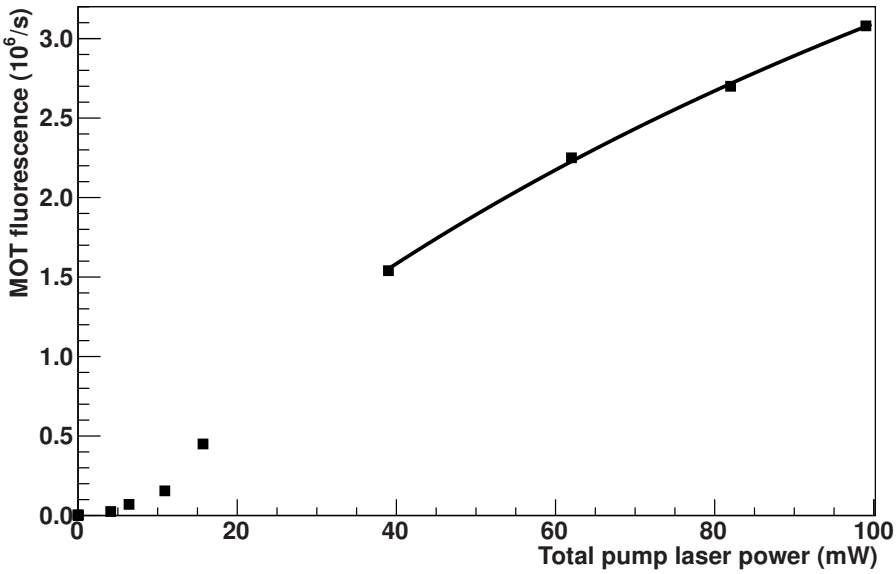

(a) *^{23}Na MOT fluorescence as function of pump intensity for the cubic cell setup. The repump power is maximal. The curve through the data is a fit of the scattering rate with the intensity as free parameter.*

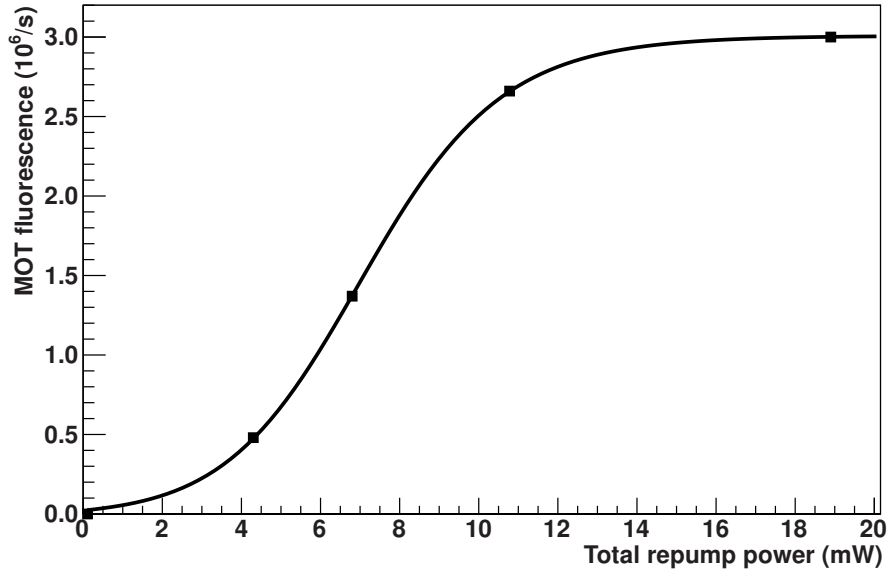

(b) *MOT fluorescence dependence on the repump laser intensity for the cubic cell setup. The pump power is maximal. The curve is to guide the eye.*

Figure 4.5: *^{23}Na MOT fluorescence dependence on the pump (a) and repump laser intensity (b).*

We will now use equation 4.2 to determine the laser intensity at the MOT cloud position by studying the pump laser intensity dependence of the fluorescence rate, under the assumption that the number of trapped atoms stays constant and the loading rate is not changing significantly. In figure 4.5a this dependence is shown. The repump and pump laser frequency detuning are -3 MHz and -6 MHz respectively. The axial magnetic field gradient is 25 G/cm and the repump intensity is maximal. The data is fitted with equation 4.2 from 40 to 100 mW with a scaling factor and the saturation parameter, s_0, at maximal power in units of the saturation intensity. The scaling factor is the product of the number of atoms, the scattering rate and the photon detection efficiency.

For the lower intensities the loading rate is not constant but decreases, trapping fewer atoms and these data can, therefore, not be used to fit equation 4.2. With a reduced $\chi^2 = 1.0$ at 2 degrees of freedom, we conclude that the total laser intensity experienced by the MOT cloud is 1.25(14) s_0 (or 0.2 s_0 per beam). This is in agreement with the value of 1.0(2) s_0 found before and is summarized in table 4.3.

Repump laser intensity

The dependence on the repump intensity is shown in figure 4.5b. The pump intensity is 100 mW, other conditions are the same as for the pump intensity measurement. We observe that the fluorescence rate saturates at the maximal repump intensity. At this intensity the repump laser intensity is about 5% of the pump laser intensity. For 2.5% it is still about 80% of the maximal value, in agreement with the repump to pump laser intensity ratio of 5% reported for sodium MOT systems [281].

Number of trapped atoms

We determined that the total pump laser intensity at the position of the MOT cloud is 1.25(14) s_0 and we also found that we have sufficient repump power. Using equation 4.2 and the detection system parameters as described in section 3.6 the detected fluorescence can be converted to the number of trapped atoms in the MOT. In figure 4.6a the fluorescence rate (and the equivalent number of trapped MOT atoms) is shown as a function of pump laser detuning. The frequency detuning of the repump laser is -5 MHz. The background PMT count rate of $53 \cdot 10^3$ counts/s is subtracted. The fluorescence rate is maximal for a pump laser detuning of -7 MHz. The number of atoms is a factor of 1.6 higher for a detuning of -15 MHz, compared to the detuning which gives the maximal fluorescence rate. Both distributions are about 15 MHz wide in frequency. Because we want to be able to detect a small MOT population optically, we set the detunings for maximal fluorescence instead of the maximal number of trapped atoms. The corresponding trapping efficiency is thus a factor of 1.6 lower for this detuning.

The dependence of the fluorescence rate on the repump detuning is shown in figure 4.6b. The pump laser detuning is -7 MHz. The background count rate is $60 \cdot 10^3$ counts/s. While slowly scanning the repump laser frequency the neutralizer is

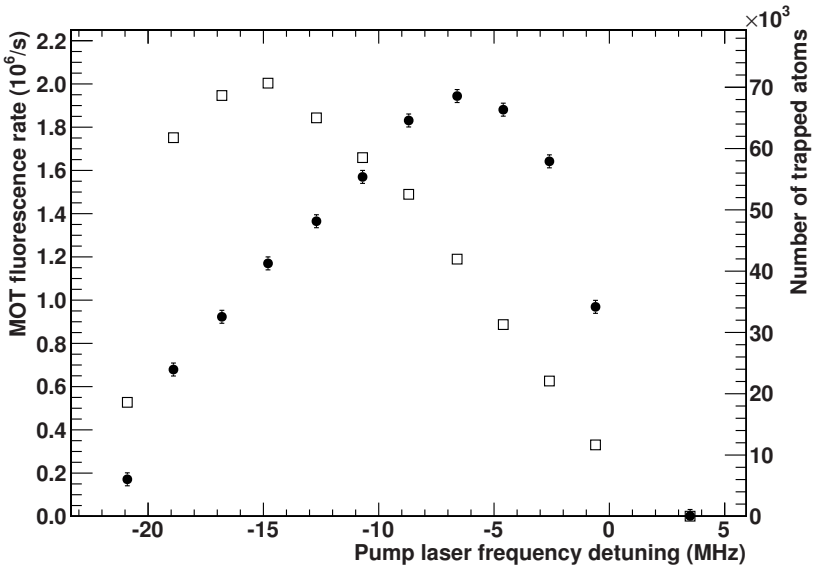

(a) *The fluorescence rate from (circles) and the number of trapped ^{23}Na atoms (squares) as function of the pump laser detuning.*

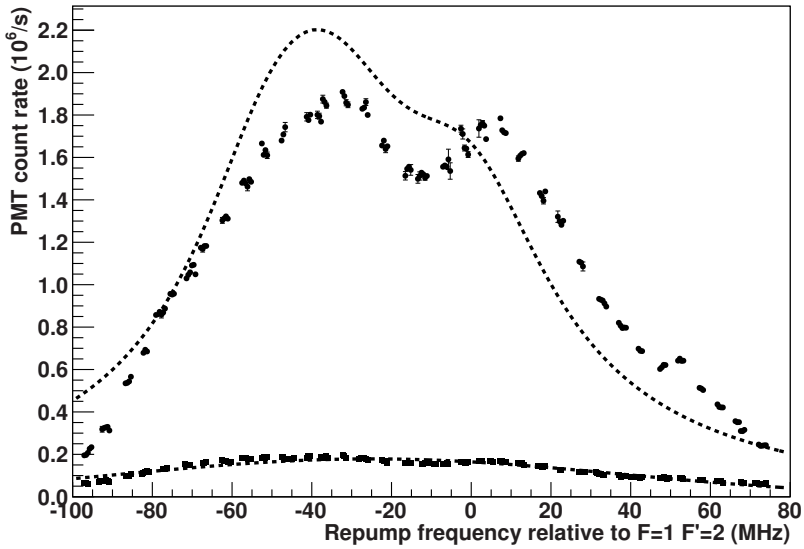

(b) *The dependence of the fluorescence from the MOT cloud containing ^{23}Na atoms on the frequency detuning of the repump laser using the cubic glass cell (pump detuning is -7 MHz). The upper data points are from a time interval when the neutralizer pulses, the lower points when it is off (see text). The upper fitted curve is only used to establish qualitative agreement and uses two fit parameters, the lower fit is used to subtract the continuously present MOT signal (see text).*

Figure 4.6: *The MOT fluorescence dependence on the cooling laser frequency (a) and on the repump laser frequency (b).*

periodically heated. The upper data points are for the condition that the time within the cycle t is in the interval $2.95 - 3.05$ s. When the neutralizer is not heated also a MOT cloud is present as the MOT lifetime is comparable to the cycle length. The lower data points are for the time interval $0.95 - 1.05$ s. The actual signal is therefore the difference between the upper data points and the lower points. Using the hyperfine frequency splittings from figure 2.5 we can identify, in addition to the F=1→F'=2 transition at 0 MHz detuning, the F=1→F'=1 transition around -34 MHz. The origin of the increase around 50 MHz is unknown. The FWHM frequency range for the repump detuning is from -70 MHz to +30 MHz.

We performed a simple calculation to see whether the observed dependence of the fluorescence rate in figure 4.6b on the detuning of the repump laser frequency can be expected. For a branching ratio ϵ from the pump cycle (with scatter rate γ_{pump}) to the repump state (with scatter rate γ_{repump}) the average total scattering rate of the MOT cloud is

$$\gamma = \frac{1/\epsilon + 1}{(1/(\epsilon\gamma_{\text{pump}}) + 1/\gamma_{\text{repump}}} \,. \tag{4.3}$$

This is under the assumption that both the capture rate of the MOT and the lifetime of the MOT are not affected by the changing repump frequency, which is not true for large detunings. Therefore this model can only be expected to give a upper bound estimate for ϵ at larger detunings.

Two calculated curves are shown in figure 4.6b, both are fits to the data. The fit to the lower data points is only used as background subtraction when fitting the upper data points. Two parameters were used to fit equation 4.3 to the former: ϵ and a scaling parameter (absorbing the scattering rate, detection efficiency and number of atoms). The contribution of the F=1→F'=0, the F=1→F'=1 and the F=1→F'=2 transition were taken to be equal. For the repump intensity we use the value from table 4.3, for the pump intensity we used the value we found previously, 1.3 s_0. The fit value for the parameter ϵ, the branching ratio from the cooling cycle to the repump state, gave 1.6%. Around a percent is what can be expected (see the subsection about the repump laser intensity). The fit clearly overestimates the fluorescence rate for larger detunings, as expected.

In summary, the detuning for the maximal number of trapped atoms has to be 10 MHz larger than the detuning for the maximal fluorescence. The former gives about a factor of 1.6 more trapped atoms. A change of $^{+7}_{-4}$ MHz for the pump laser detuning halves the number of trapped atoms. For the repump detuning the allowed detuning is less strict, $^{+30}_{-70}$ MHz keeps half of the atoms.

4.4 Neutralizer efficiency

First we discuss the determination of the temperature of the neutralizer, as this is a prerequisite to compare our values to literature. With the calibration established we analyze the time dependence of the release of ^{23}Na. From measurements where we changed the heating current for the neutralizer foil, we extract the diffusion time

scale and calculate the Arrhenius parameters. The release of ^{21}Na, observed by the time dependence of the β^+ annihilation signals from the decay of ^{21}Na, concludes this section.

Temperature determination

For the data that we took to determine the diffusion time scale and the release efficiency of implanted ions, the temperature of the Zr neutralizer foil was too low to be measured directly with our pyrometer. We worked with relative low temperatures as we did not want to damage the foil or non-stick coating. Later, we used larger heating currents to obtain a calibration curve. We find an excellent agreement of the temperature dependence on the dissipated power. We extrapolate these data downwards to estimate the temperatures for our release efficiency measurements. The electrical resistivity of the neutralizer material is well known, therefore we also have an indication of the overall accuracy of our temperature measurements with the pyrometer at these higher temperatures.

We measured the temperature of the neutralizer foil with an optical pyrometer (Optix PB05AF3, N° 20123, Keller, effective wavelength $\lambda = 650$ [282]). The lowest reading for the pyrometer is 750 °C, the highest reading goes above 2000 °C. The temperature, as read off on the pyrometer, needs to be corrected as metals are not perfect blackbody radiators. The spectral radiance temperature T_r is related to the true temperature T through

$$\frac{1}{T} - \frac{1}{T_r} = \frac{\lambda}{c_2} \log \epsilon(\lambda, T), \tag{4.4}$$

where $\epsilon(\lambda, T)$ is the spectral emissivity, λ the effective wavelength and $c_2 = hc/k_b = 0.014$ m·K [283]. Because $\epsilon \leq 1$, the real temperature is $\geq T_r$. For Zr the value for ϵ can be found in [284]. At a mean temperature of 825 °C, using an optical pyrometer with a mean wavelength of 652 nm, reference [283] gives $\epsilon = 0.436 \pm 0.013$.

We measured the temperature with the pyrometer[1], as function of the dissipated electrical power. The dissipated power in the neutralizer foil and the feedthrough connectors is the product of the voltage drop over this part with the current. We started at a low temperature and waited until the voltage did not change anymore before going higher in the heating current. At the highest temperature, we went down again. In this way possible degrading of the foil or a hysteresis effect can be noticed.

The temperature dependence on the dissipated power can be found by assuming that the heat is primarily radiated away, *i.e.* that convection and heat conduction are negligible. The net energy flux F emitted by a blackbody with temperature T and total surface area A to its surrounding at room temperature is given by

$$F(T) = \frac{I^2 R}{A} = \epsilon_{\text{eff}} \sigma (T^4 - 293^4)\,, \tag{4.5}$$

[1]The emitted light from the neutralizer foil passes the glass of the cell before it reaches the pyrometer. We did not correct for the fact that part of the emitted light at the effective wavelength of the pyrometer is reflected or absorbed in the glass of the cell. This results in an underestimation of the true temperature.

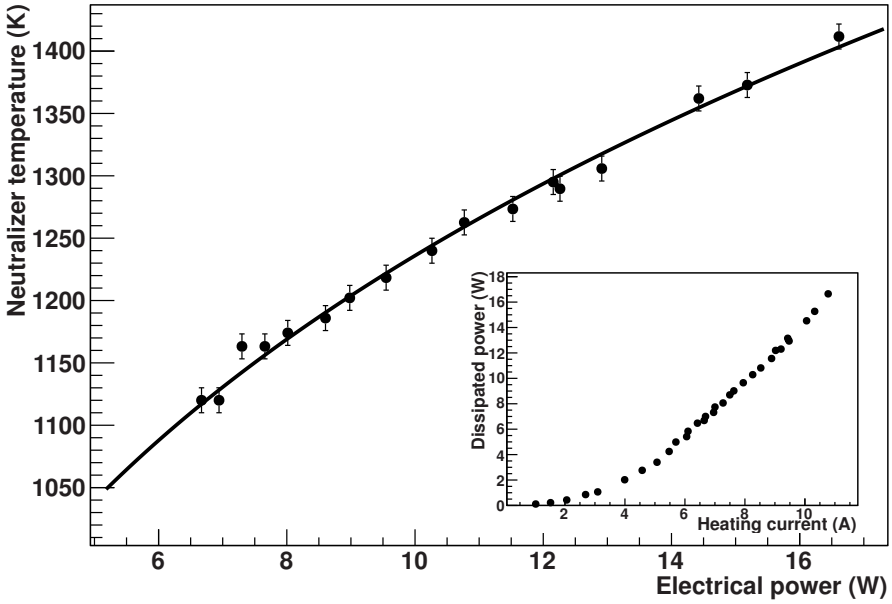

Figure 4.7: *The neutralizer temperature dependence on the electrical power dissipated in the neutralizer foil and vacuum feedthrough connectors. Equation 4.5 is fitted to the data, with the effective emissivity ϵ_{eff} as the only fit parameter. The temperature values are corrected pyrometer readings (equation 4.4). The inset shows the dissipated electrical power as function of the heating current.*

where $\sigma = 5.7 \cdot 10^{-8}$ W/m^2/K^4 and with an emissivity ϵ_{eff}. The emissivity of a material depends on the wavelength, temperature, surface shape and texture and even the thickness of the foil [285]. Therefore we use an effective value for the emissivity in equation 4.5. In principle it can be calculated, by weighting $\epsilon(\lambda)$ with the Planck blackbody curve, but we choose to fit this value to the data.

In figure 4.7 the dependence of the neutralizer temperature on the dissipated power is shown. We measure the temperature always in the middle of the foil, where it has the highest value. A temperature gradient over the foil could clearly be seen. As expected the temperature near the connectors of the foil was lower than in the middle.

Fitting equation 4.5 to the data gives an emissivity of $\epsilon_{\text{eff}} = 0.77 \pm 0.01$ (*cf.* figure 4.7). The main uncertainty is the resistance of the foil, the resistance of the foil might account only for half of the total resistance, this we will see later on. This gives a value of $\epsilon_{\text{eff}} = 0.39 \pm 0.01$. A second uncertainty is the surface area of the foil. Because the foil is wrapped around the corners of the connectors, the actual surface area

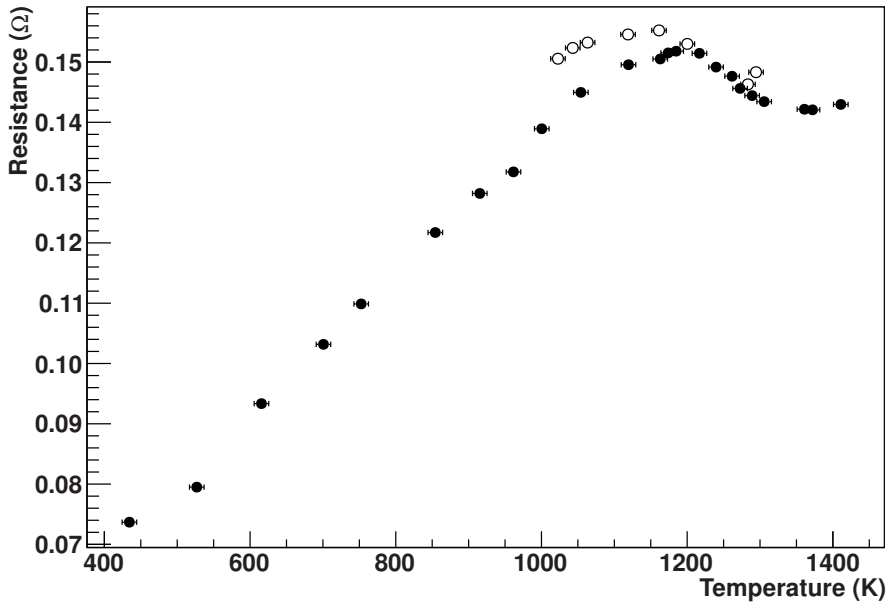

Figure 4.8: *The resistance of the neutralizer and vacuum feedthroughs as function of temperature. Only temperatures $\geq$ 1000 K are measured with the pyrometer directly, the lower values are calculated using the relation with the dissipated power using equation 4.5. The measurements were done first for increasing temperatures (solid symbols) and then by decreasing the temperature (open symbols).*

might also be slightly larger. For a 1.2 cm^2 area instead of 1.0 cm^2 the emissivity is $\epsilon_{\text{eff}} = 0.52 \pm 0.004$. These values seem high, according to Wien's displacement law the radiation peaks around 2.6 μm for a temperature of 1100 K. For Zr, at these wavelength the emissivity is in the range 0.25-0.35 [285] and it steadily decreases for longer wavelengths. However, as the agreement in figure 4.7 is excellent we assume that for our purposes this discrepancy is not an issue. Furthermore, the correction to the temperature reading (equation 4.4) is small and only becomes smaller when we use a value in the range 0.52-0.77 instead of 0.43. The uncertainty which fraction of the resistance is due to the neutralizer might result in a larger shift in ϵ_{eff} and thus for the value of the temperature. However, this issue is solved as we discuss in the next paragraphs an absolute estimator of the temperature scale exists, associated with a phase transition in Zr.

In reference [286] the electric conductivity of Zr as function of temperature can be found. At 1137 K, a phase transition from a hexagonal closed packed (HCP) to a body-centered cubic (BCC) structure occurs [197]. At this temperature, the resistance

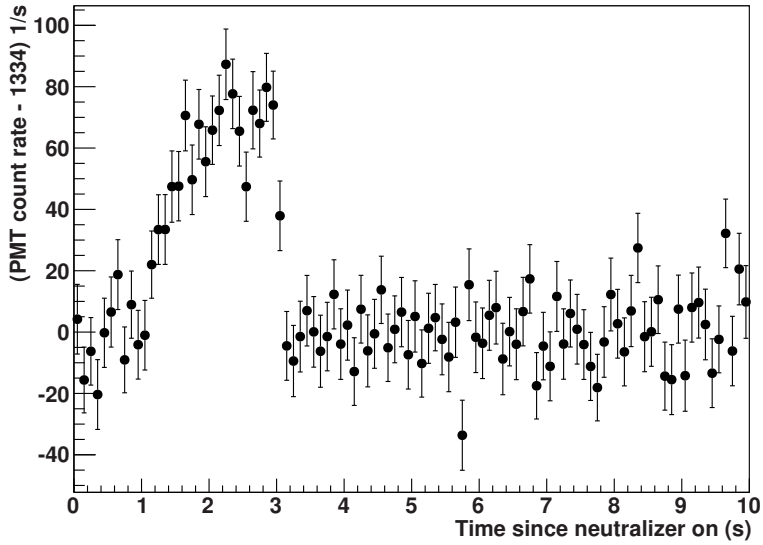

Figure 4.9: *Blackbody radiation from the heated neutralizer foil, observed with the detection system measuring the fluorescence from the MOT cloud.*

drops sharply with about 15% [286]. Also the diffusion process is expected to take place significantly faster in the BCC than in the HCP structure [197].

In figure 4.8 the resistance of the neutralizer and its connectors as function of temperature is shown. At a temperature of 1200 K the resistance starts to decrease, at a temperature of about 1350 K it starts to rise again. The decline is not as sharp and in magnitude only half of the decline found in [286]. A smooth drop in resistance can be expected as the temperature of the foil is not uniform over the foil and therefore the phase transition appears to be broadened in figure 4.8 over a range of about 150 °C. The fact that the decline is smaller might be due to the resistance of the current feedthroughs, which may result in a considerable offset. The foil has also been made by rolling a thick foil of Zr, the crystal structure might also have changed due to this [282]. If we take the onset at 1200 K as an estimate for the phase transition which should occur at 1137 K [286], the systematic shift on the temperature calibration is about 60 K. As this value is about the size of the expected precision, we do not correct the temperatures for this and use this value as an estimate of the uncertainty.

Figure 4.9 shows that the detection system, which is used to detect the fluorescence light from the MOT cloud, is sensitive enough to the detect the blackbody radiation coming from the neutralizer, even after spatially filtering the MOT cloud image and with an optical filter being present. The neutralizer foil is heated from $t = 0$ to $t = 3$ s with a current of 6.3 A, no laser light is further present and the main room lights are turned off. By eye one sees a red-orange glow, it takes about a second for the glowing

to reach its maximum. The neutralizer is not in the direct sight of the detection system. The various optical elements (reflection from the glass, filter, PMT) have an unknown (strong) wavelength dependence in the relevant wavelength regime and therefore the signal in figure 4.9 does not allow for a determination of the temperature. (The offset of about $1 \cdot 10^3$ counts/s is due to light sources which remain after turning off the room lights.) The signal rises in about 1 second, saturates after an additional second and within 1/10 of a second it drops when the heating of the neutralizer foil stops. Thus at 6.3 A the peak temperature is reached after about 2 sec. While these data characterize the time dependence of the heating, we can safely neglect their contribution of about 100 counts/s to the PMT rate observed in the measurements reported in this thesis.

Released fraction as function of the temperature

We define the neutralization efficiency as the ratio of the incoming ion rate R_{ion} to the atom release rate,

$$\epsilon_{\text{neu}} \equiv \frac{R_{\text{atom}}}{R_{\text{ion}}} \,, \tag{4.6}$$

where R_{atom} is the rate of atoms coming off the neutralizer [81, 197]. The ions shot into the neutralizer foil diffuse through the neutralizer material. They accidentally come to the surface at the timescale of (*cf.* equation 2.26),

$$t = \frac{d^2}{4D} \,, \tag{4.7}$$

with d the mean implantation depth. Using the TRIM software package [194] we have calculated that $d = 66$ Å for an ion beam energy of 2.8 keV. The diffusion constant D depends on the temperature T according to the Arrhenius function (*cf.* equation 2.27),

$$D = D_0 e^{-E_a/k_{\text{B}}T} \,, \tag{4.8}$$

with E_a the activation energy. For Na in Zr no diffusion data are known. For ^{37}K diffusing in Zr $D_0 = 1.8^{+7.8}_{-1.5} \cdot 10^{-10}$ m^2/s and $E_a = 1.41(0.15)$ eV [197]. At room temperature this gives a timescale of order 1000 years, at 1000 K this corresponds to a timescale of $0.2^{+0.35}_{-0.12}$ s. On one hand a hotter neutralizer results in a faster diffusion and a larger released fraction, on the other hand a higher temperature degrades the neutralizer foil as well as the nearby wall coating and results in more outgassing and therefore in a shorter MOT lifetime. Also the mean velocity of the released atoms is higher, although this can be neglected. If the atoms bounce at least once with the wall they are thermalized to room temperature [200]. The released and surviving fraction as function of time is [197]

$$\eta = \left(1 - \frac{1}{\sqrt{1 + \frac{4Dt}{d^2}}}\right) \mathrm{e}^{-\frac{t}{\tau}} \,, \tag{4.9}$$

with τ the lifetime of the implanted isotope.

To study the dependence of the released fraction on the peak temperature of the neutralizer we varied the heater current. In figure 4.10 the number of trapped atoms is shown for three currents which have been converted to a temperature using equation 4.5. As we did not want to damage the neutralizer foil or non-stick coating, we did not go to higher temperatures. The temperature dependence of the conductivity is taken into account following [286]. When using a higher heating current the heating period has to be increased to reach the peak temperature. It was checked that the atom yield in consecutive heatings is consistent with the time evolution given in equation 4.9 using the values of the diffusion coefficients we derive in the following.

In these measurements the laser frequency detunings for pump and repump laser are -4 MHz and 0 MHz, with respect to the cooling and repumping transition. The cycle length is 20 s and the current on the neutralizer foil is 14.4 pA (which we assume to contain ^{23}Na only).

The time evolution of the trapping signal depends on the release rate of the neutralizer and the lifetime of the MOT during the heating. When the atoms are released from the neutralizer, they enter the cell volume. The atoms either stick or bounce off the glass walls. Eventually some are trapped in the MOT or exit through one of the connecting tubes. Because the average time a particle spends in the glass cell before it is removed via these processes is much shorter than the typical diffusion time in the neutralizer, we can describe the flux of trapped atoms as

$$\frac{\mathrm{d}N}{\mathrm{d}t} = S(t) - \frac{N}{\tau_{\mathrm{M}}} \,, \tag{4.10}$$

where τ_{M} is the mean time of an atom in the MOT and $S(t)$ is the source term. Following [197] and equation 4.9 with $\mathrm{e}^{-t/\tau}$ removed as $\tau \gg \tau_{\mathrm{M}}$ we have that

$$S(t) = I t_{\mathrm{cyc}} (1-F) N_B \frac{\epsilon_{\mathrm{col}} \alpha}{2(1+\alpha t)^{3/2}} \,. \tag{4.11}$$

Here $I t_{\mathrm{cyc}}(1-F)$ is the number of particles implanted in the neutralizer, where I is the ion current and t_{cyc} the duration of the beam. The fraction of back-scattered ions is F. The collection efficiency is ϵ_{col}, it depends on the average number of passes through the laser trap volume N_B and the single pass trapping efficiency P_1. The above terms combined we refer to as $N_{\mathrm{effective}}$, only the last term describes the time dependent release with $\alpha = 4D/d^2$.

The solution of this differential equation is fitted to the data in the restricted range 1.8 to 3.0 s of figure 4.11. The reason to only fit to part of the data will be explained below. The four fit parameters are the diffusion time-scale $1/\alpha$, the lifetime of the MOT during the heating τ_{on}, a time offset which is the start time of the heating (3-t_{heat}) and the maximal number of trapped atoms for an infinite MOT lifetime $N^{t\to\infty}_{\tau_{\mathrm{on}}\to\infty}$.

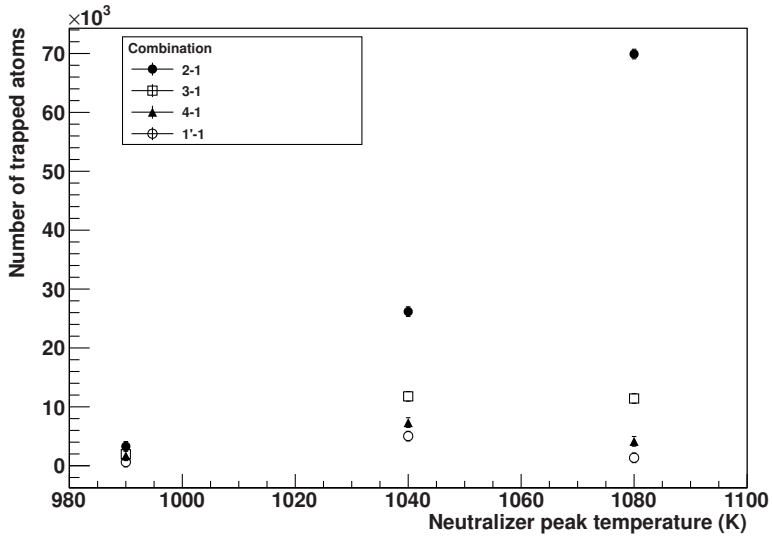

Figure 4.10: *The number of trapped atoms for three neutralizer temperatures. Which cycles are subtracted from each other is indicated by the combination,* cf. *figure 4.3b for the definition of the cycles.*

Table 4.4: *The values of the fitted parameters from four measurements. From left to right the data is from figure 4.11, figure 4.4, figure 4.12a and figure 4.12b. For d we take 71 Å (see text). The systematic uncertainty on the temperature is 60 °C (see text).*

Fit parameters	6.3 A	6.3 A	5.8 A	5.3 A
Diffusion time $1/\alpha = d^2/4D$ (s)	0.9(15)	0.60(20)	9.3(6)	56(1)
MOT lifetime τ_{on} (s)	0.63(6)	0.51(11)	1.83(4)	1.4(1)
MOT lifetime τ_{off} (s)	3.80(1)	3.44(3)	3.60(1)	3.58(2)
Effective heating time t_{heat} (s)	1.48(5)	1.20(1)	1.48†	1.48†
Atom number $N^{t\to\infty}_{\tau_{\text{on}}\to\infty}$ (10^5)	4.9(6)	0.7(2)	4.9†	4.9†
Peak temperature (K)	1080(10)	1080(10)	1040(10)	990(10)
D (10^{-13} cm^2/s)	1.5(3)	2.4(9)	0.14	0.02
Released fraction (%)	40(5)	42(5)	7	1
Number of implanted ions	$1.8\cdot10^9$	-	$1.8\cdot10^9$	$1.8\cdot10^9$
Collection efficiency	$2.7\cdot10^{-4}$	-	-	-
Peak released fraction (%)	15 ± 4	15 ± 4	5 ± 1	0.9 ± 0.2

† Fixed parameter.

From figure 4.9 it can be seen that the temperature becomes constant between 1.8

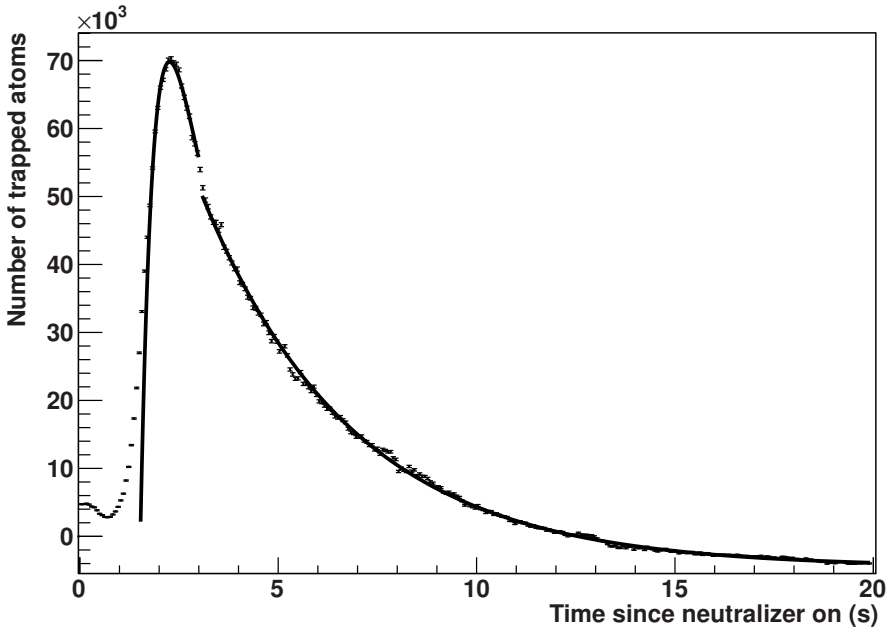

(a)

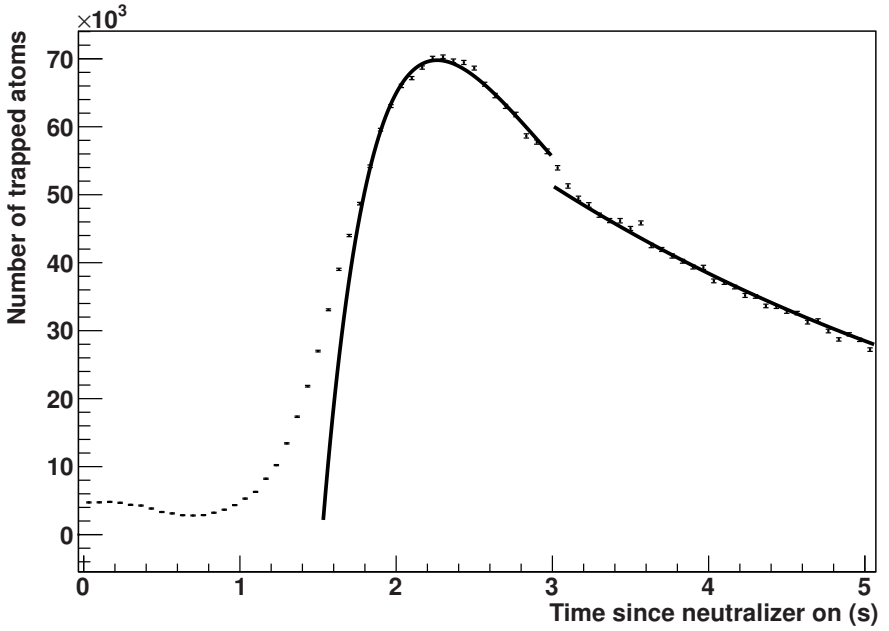

(b)

Figure 4.11: *Atoms trapped in the MOT, which are related to the ion beam ((b) shows a zoom of (a)). The neutralizer is heated with a current of 6.3 A from t=0 to t=3 s. The left curve is a fit using the diffusion model, done from t=1.8 to 3.0 s. The right curve is a fit of the lifetime of the MOT cloud, on top of a negative offset. The discontinuity at t=3 s is explained in the text.*

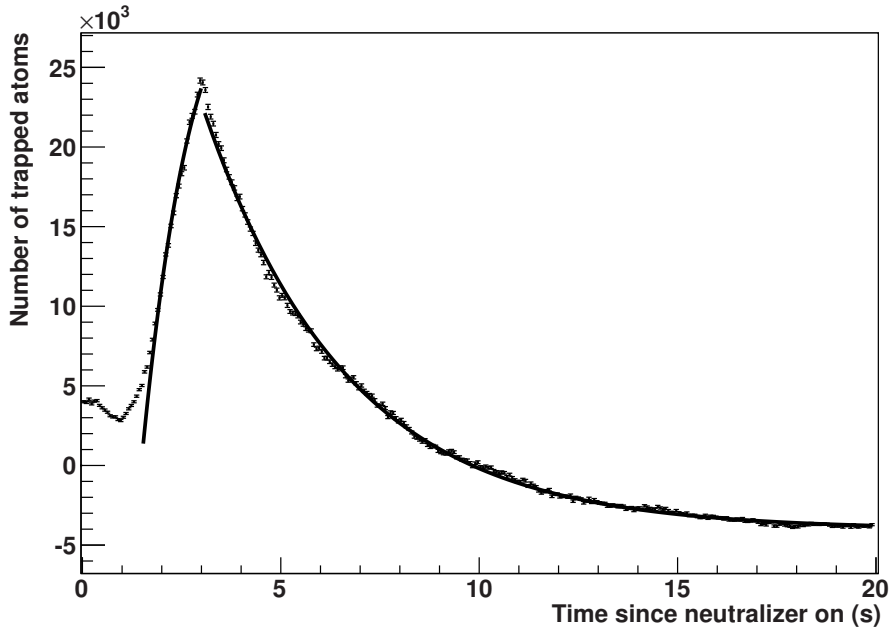

(a)

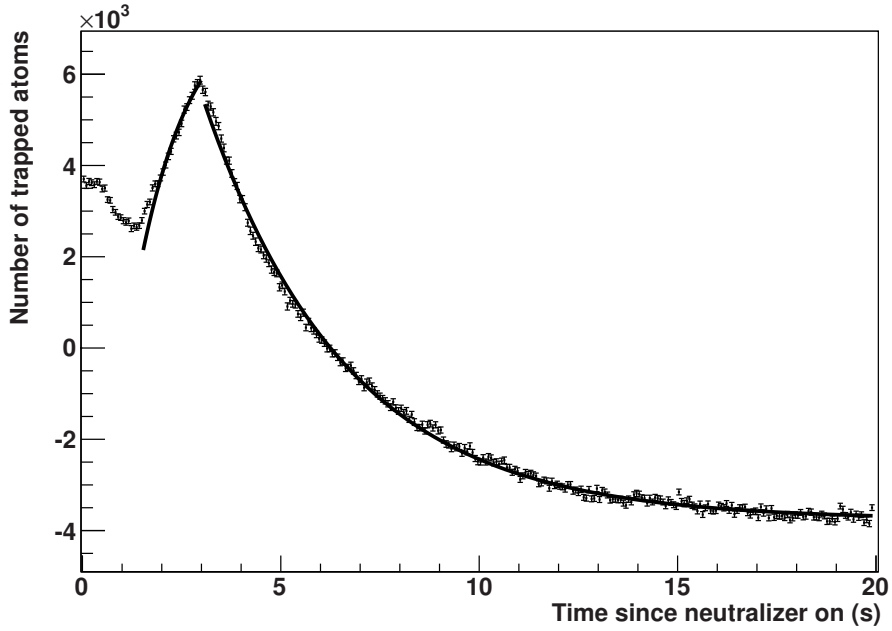

(b)

Figure 4.12: *As in figure 4.10 but with a heating current of 5.8 A (a) and 5.3 A (b). Some of the parameters are fixed using the data from figure 4.11 (see text).*

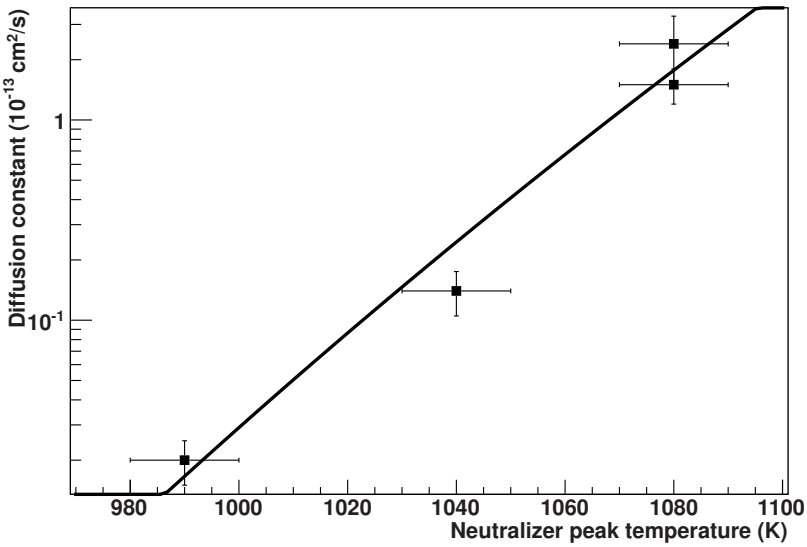

Figure 4.13: *The temperature dependence of the diffusion constants from table 4.4, fitted to the Arrhenius function (equation 4.8). The highest temperature has been directly measured and has an uncertainty of 60 K, the two lower values indirectly determined using equation 4.5 using the dissipated power in the neutralizer foil.*

and 3.0 s and the diffusion thus also. The fitted curve falls below the data points at earlier times as the actual temperature is still low. Here the diffusion is slower and the MOT fluorescence signal rises less steep than the fitted curve. At $t > 3$ an exponential decaying signal is assumed with a lifetime τ_{off} of the MOT. Because the heating of the neutralizer foil has stopped the pressure improves and $\tau_{\text{off}} > \tau_{\text{on}}$, this leads to a discontinuity of the fitted curves.

In figures 4.4, 4.11, 4.12a and 4.12b we show the results of these fits to the fluorescence yield of the MOT. The results for the fit parameters are summarized in table 4.4. The MOT lifetime with the heater off is also extracted. Note that during the first second no signal is observed. This is consistent with the dependence we found earlier, displayed in figure 4.9. This is the reason that t_{heat} is a parameter in the fit. It assumes that the temperature dependence in figure 4.9 can be approximated by a step function. This rough approximation hampers a good description of the leading part of the MOT signal. The trend for τ_{on} is that it is shorter for higher heating currents as can be expected.

Listed in table 4.4 are the five fit parameters, four stem from the diffusion model and one is a MOT lifetime τ_{off} after the neutralizer is switched off. The first three diffusion model parameters are the diffusion timescale $1/\alpha$, the MOT lifetime during the heating of the neutralizer τ_{on} and the effective heating time t_{heat}. The fourth

Table 4.5: *Measured diffusion parameters and timescales for some alkaline elements in Y and Zr. The diffusion time at temperature T is τ_T. For αZr points above its phase transition are included, this is not the case for βZr.*

Isotope	Foil	E_a (eV)	D_0 (cm^2/s)	T (K)	τ_T (s)	Ref.
^{23}Na	βZr	4.8 ± 0.7	$2.9 \pm 1.3 \cdot 10^{-2}$	1100	0.7 ± 0.1	this work
^{37}K	αZr	1.18 ± 0.09	$1.5^{+2.2}_{-1.3} \cdot 10^{-7}$	1200	0.15 ± 0.01	[197]
^{37}K	βZr	1.41 ± 0.15	$1.8^{+7.8}_{-1.5} \cdot 10^{-6}$	1200	0.11 ± 0.02	[197]
^{85,87}Rb	Y	1.8 ± 0.4	-	1000	6.1 ± 2.3	[287]
^{210}Fr	Y	1.8 ± 1.1	-	1000	4.1 ± 2.5	[287]

parameter is the asymptotic cumulative number of trapped atoms, *i.e.* this is the number of trapped atoms for an infinite heating time and an infinite MOT lifetime during the heating. From the table one can conclude that because of the short lifetime of the MOT during the heating of the neutralizer, the maximal number of trapped atoms is significantly reduced.

For the third column of table 4.4 the cycle length was twice the cycle length of the measurement in the second column, the LEBL was set for ^{21}Na and the ion current was not determined. The ion current for the ^{23}Na condition was 11.1 pA, whereas for the other measurements it was 14.4 pA. From this we find that for the LEBL ^{21}Na settings about 10% of the ion related ^{23}Na MOT signal that was measured before with ^{23}Na LEBL settings. This information we will later use to estimate the contribution of background process involving ^{23}Na atoms when looking for an optical signal from trapped ^{21}Na atoms. Here we assume that the collection efficiency and release efficiency did not change in the week between these measurements.

Diffusion constant of ^{23}Na in Zr

With the results listed in table 4.4 we can now calculate the Arrhenius parameters (equation 4.8). Note that the time to come off the surface (desorption time scale) can be neglected, as discussed in section 2.6. In figure 4.13 we show the diffusion constant as function of the neutralizer temperature. The Arrhenius constants D_0 and E_a are determined by a fit. We find indeed an exponential dependence.

The fit results are in table 4.5, together with some results from other experiments. It is not uncommon for this type of measurement that the extracted value for D_0 is not very meaningful because of the larger error, caused by the extrapolation to infinite temperatures [197, 287]. For ^{37}K Melconian *et al.* [197] observe that for many different neutralizer materials, about 50% is released for a temperature of about 0.55 of the melting temperature. For Zr, the melting temperature of Zr is 2127 K [286], therefore the temperature for a 50% release efficiency can expected to be around 1200 K. This is indeed what we observe for ^{23}Na.

In earlier work done within this ^{21}Na experiment, Rochachevskiy *et al.* [196] measured also for Zr and Y the MOT population as function of the neutralizer temperature. However, they convert the temperature, as read off on the pyrometer, by multiplying it with $1/\sqrt[4]{\epsilon}$ [288]. This leads to an overestimation of the real temperature with about 200 K for the highest temperatures they report. The optimal release temperature of 1400 K they find is actually 1190 K. This last value is in good agreement with the temperature of about 1100 K which we found here. At this temperature about 40% is released. Rochachevskiy *et al.* might have had a higher release efficiency because of the higher temperature.

We have seen earlier that the temperature of the neutralizer foil is not uniform over the foil. The broadening of the phase transition with 150 K at 1200 K is an indication of this. If this were the case, it would complicate the determination of the diffusion constant and activation energy. To extract more reliable values the neutralizer has to be heated to higher temperatures. From figure 4.7 we see that we can increase the temperature with about 400 K, although the hysteresis like curve in figure 4.8 might be an indication that the neutralizer degrades fast at higher temperatures. To have confidence that our model describes reality the temperature range from low release efficiency to the saturation value has to be covered.

In summary:

- To extract low-uncertainty diffusion parameters, the release process has to be measured at higher temperatures.
- The diffusion value at the highest temperature is in excellent agreement with other alkaline elements using Zr as a neutralizer material.
- An apparent discrepancy with earlier measurements by Rochachevskiy *et al.* can be explained.
- At an operating temperature of about 1100 K 40% of the implanted ions are released.
- The number of simultaneously trapped atoms depends strongly on the lifetime of the MOT and on the temperature of the neutralizer.

Observation of release of ^{21}Na

The release of ^{21}Na can be studied by measuring a neutralizer related change in the count rate of the annihilation radiation of the β^+ particles. For the cross cell setup this rate is shown as function of time in figure 4.14a and figure 4.14b, averaged over many cycles. Two small volume CsI detectors are used in singles mode, one close to the neutralizer and one near the entrance of the cell. The neutralizer is heated for up to 3 s. The build-up time constant in figure 4.14a is 30(8) sec, in agreement with the ^{21}Na decay lifetime of 32.4 s. The decay time in figure 4.14b is also consistent with this value. The decrease in the near-neutralizer detector and increase in the entrance

detector indicates that ^{21}Na is released from the neutralizer foil. The fractional change for the dip is about 8% and it is 1% for the rise.

The conclusion is that at least 8% of the ^{21}Na particles are released from the neutralizer for the cross cell setup, however the count rate change is a poor indicator and gives a lower bound for the release as the annihilations are not localized at one particular position. The β particles stop distributed over the chamber walls. Therefore we cannot discriminate between ^{21}Na which decays inside the neutralizer foil or has been released and decays outside the neutralizer foil.

For the cubic cell a measurement is done with a single large volume NaI detector, the result is shown in figure 4.15. The data belongs to the same run as the data in figure 4.21, where the MOT from ^{21}Na was observed. The neutralizer is heated starting at t=0 for 3 s long. Here a change in the count rate of only 0.7% is seen. It may be interpreted that in the cross setup ^{21}Na leaves the cell, while in the new setup more ^{21}Na remains in the cell.

4.5 Trapping of ^{21}Na and ^{23}Na from a neutralized ion beam

We first discuss time dependent backgrounds which we observed when studying the collection efficiency of the setup with ^{23}Na. This can be relevant information in understanding the diffusion process and possible chemistry on the neutralizer surface. Then we discuss the impact of the Doppler background fluorescence from ^{23}Na for an optical signal from a ^{21}Na MOT cloud. Finally we discuss in this section the observation of a MOT signal with a neutralizer at room temperature.

^{23}Na; time dependent background

We observed that ^{23}Na is present in the neutralizer foil upon installation and this amount increases when not all ions from an ion beam are released. Therefore, we have to distinguish between the atoms that originate from the freshly deposited ions and those that originate from previous depositions or were already present in the foil when it is built into the setup.

Without any ion beam present, just starting pulsing the neutralizer already shows a time dependent signal, see figure 4.16. Here the cycle is 20 s long and the neutralizer is heated 3 s long with a current of 6.3 A. Fitting individual peaks in the spectrum shows that the first MOT signals have a short lifetime, after ten pulses it becomes longer and reaches a constant value. We additionally observed that if the neutralizer is not heated for a few cycles the situation of the cold start is reproduced, though it is faster it still takes hours to reach the peak value again (in figure 4.16 the heating is not interrupted). Apparently in absence of heating the surface rapidly returns to its original state.

In figure 4.17a we show a measurement where we change the cycle time from 10 s to 20 s and to 40 s, the neutralizer is heated during 3 s. An additional time constant of $\sim$ 500 s is involved each time the cycle length is changed. In figure 4.17b the number

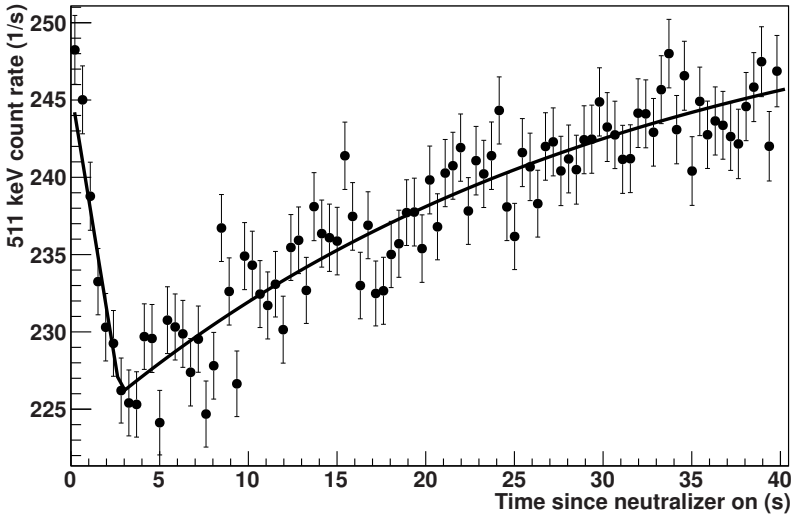

(a)

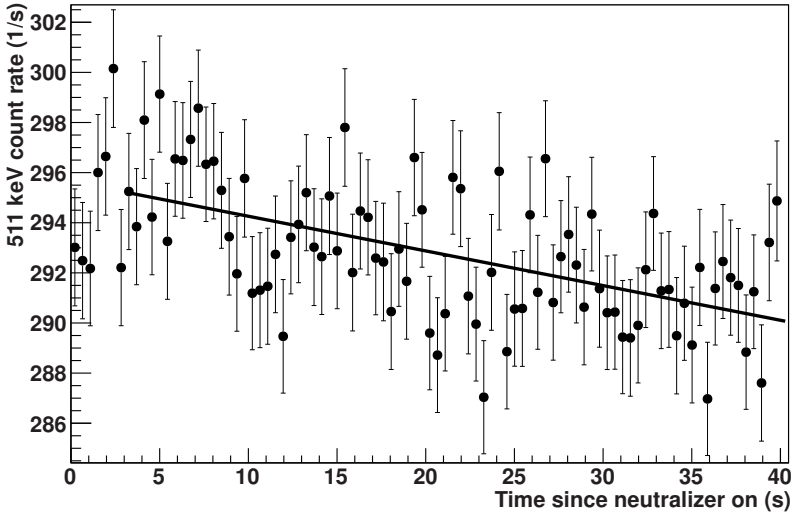

(b)

Figure 4.14: *The 511 keV count rate for two CsI detectors, near (a) and further away (b) from the periodically heated neutralizer foil.*

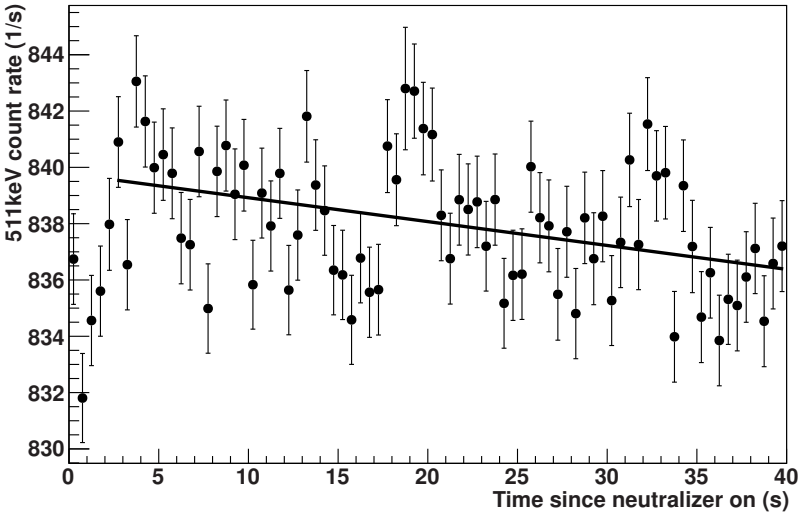

Figure 4.15: *The 511 keV rate as detected in the cubic cell setup.*

of trapped atoms and the lifetime of the MOT cloud is shown as function of the length of the cycle. We see from figure 4.17b that the MOT lifetime gets longer when going to longer cycle times. This is expected as less outgassing takes place. However, the MOT signal is higher for shorter cycle length.

A possible explanation for this behavior is the surface condition of the neutralizer. During a longer cycle more deposits from gas molecules are building up at the surface. For a Zr surface the incident rate of oxygen molecules at a pressure of 10^{-6} mbar is 1/s per adsorption site [289]. For the typical $3 \cdot 10^{-9}$ mbar, derived from the MOT lifetime, this means an adsorption timescale of order 300 s for a single monolayer. This timescale is comparable with $\sim$ 500 s timescale we observe. At low temperatures of the neutralizer this monolayer might form a significant barrier to diffuse through.

Doppler background fluorescence from ^{23}Na

In a MOT a strong isotope selectivity is naturally provided by the narrow bandwidth of the laser frequencies and narrow linewidth of the atomic transitions. This is also the case for the combination of ^{21}Na and ^{23}Na. Nevertheless Doppler fluorescence from the atomic vapor is much less dependent on the actual laser frequency and therefore ^{23}Na can contribute to the signal of the ^{21}Na MOT.

Such background signals are shown in figure 4.18 for four different detunings with only pump laser light present. The signal does not dependent on the presence of the MOT magnetic quadrupole field, as expected as no repump light is present.

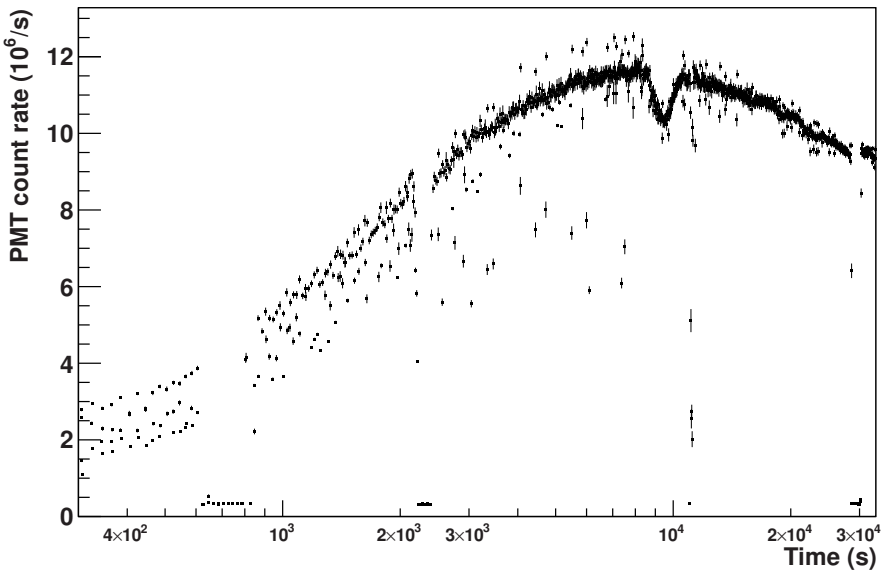

Figure 4.16: *The MOT fluorescence rate for a periodically heated neutralizer. The dropouts are due to lasers which lost their frequency lock. The data points are the average of the PMT rate on the time interval* $2.5 - 3.5$ *s within a cycle, note the logarithmic horizontal scale.*

The large blue and red detuning prove that the fluorescence signal is due to Doppler background fluorescence.

For a blue detuning of the pump laser and a red detuning of the repump laser a signal of about $1.5 \cdot 10^3$ counts/s can be seen (figure 4.19). This figure corresponds to the right most point from figure 4.6a where the MOT atom number appears to be zero, but in fact the signal is just small. Therefore we can compare the MOT fluorescence rate and the rate observed here. The ratio between the maximal fluorescence rate in figure 4.6a to the rate for this detuning is $1.3 \cdot 10^3$.

We now do an order of magnitude estimate of the expected signal for Doppler background fluorescence: An atom with velocity v spends a time of order $\frac{d}{v}$ in the detection region approximated by a sphere of diameter d. Its fluorescence is recorded with a detection efficiency ϵ. The scattering rate from a laser beam is given by equation 4.2. With the polar angle θ to the laser beam, the laser frequency detuning due to the Doppler shift is given by $\delta = 2\pi/\lambda = kv\cos\theta$ (for example 6 m/s gives a 10 MHz Doppler shift for $\theta = \pi$). The velocity is distributed according to the Maxwell-Boltzmann distribution, equation 2.8. The total number of photons N_c for a single

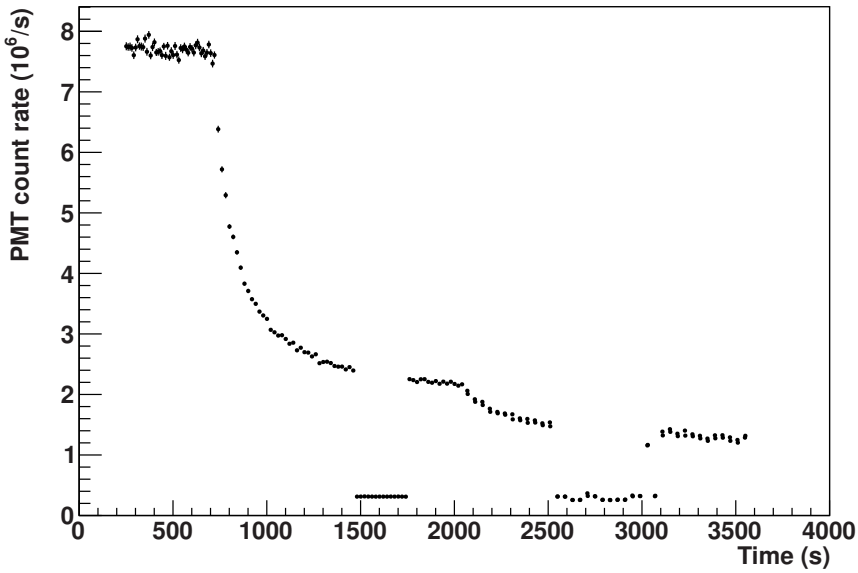

(a) *Transition of 10 s to 20 s cycle at ∼700 s and at ∼2000 from 20 s to 40 s (the neutralizer started pulsing at t=-28000 s). The dropouts are due to unlocked lasers. The data points are the average of the PMT rate on the time interval* $2.5 - 3.5$ *s within a cycle.*

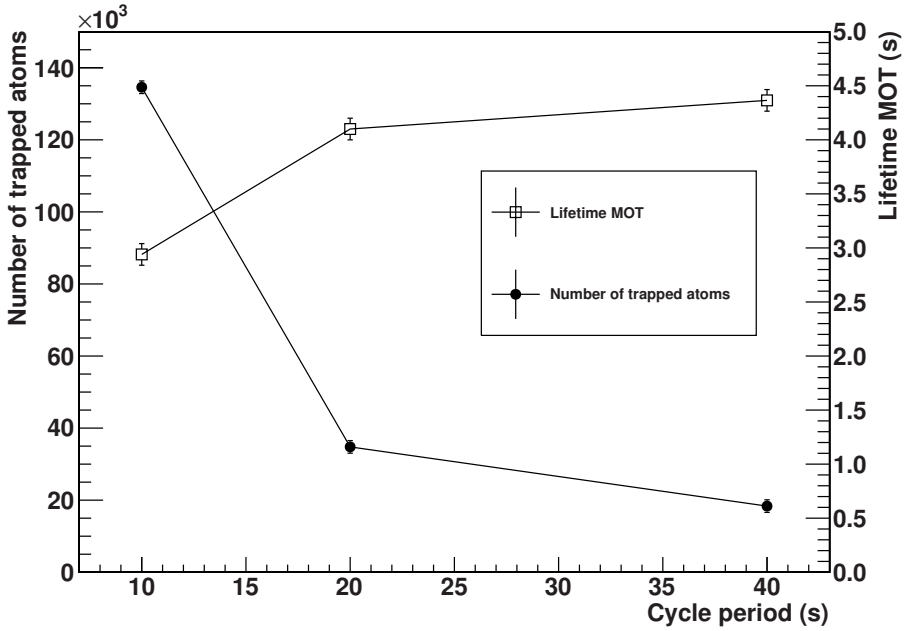

(b) *The* ^{23}Na *MOT signal and MOT lifetime as function of the cycle length. The lines are to guide the eye.*

Figure 4.17

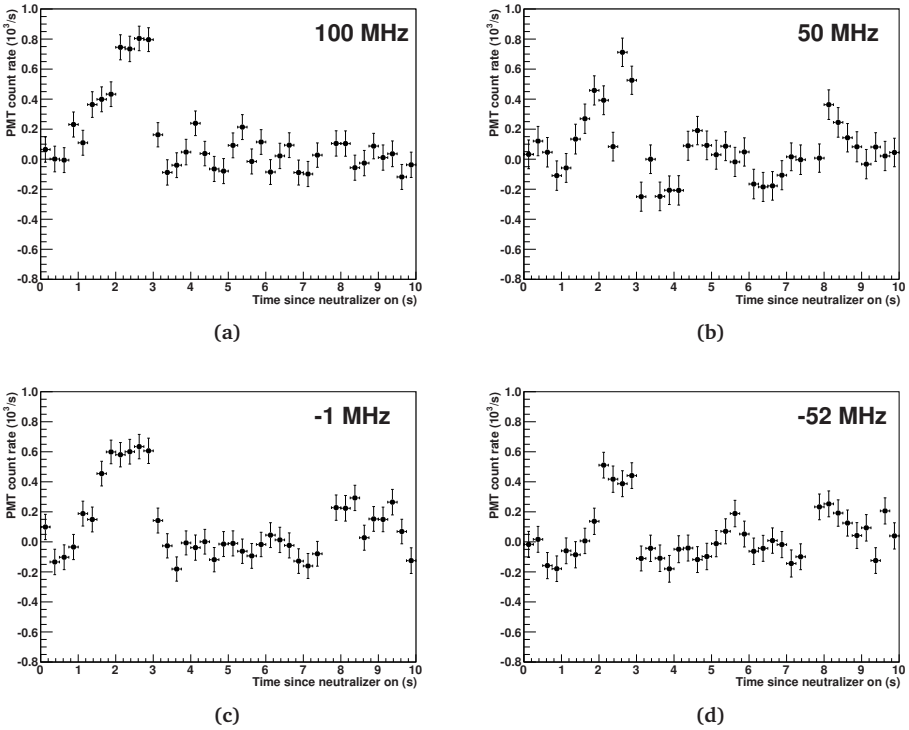

Figure 4.18: *The Doppler background fluorescence signal from ^{23}Na, only pump laser light is present. The detuning from the ^{21}Na pump transition is indicated in the figures, a constant background rate is subtracted from the data.*

laser beam is thus

$$N_c = \int_0^\infty d\nu \int_0^{2\pi} d\phi \int_0^\pi d\theta \frac{d}{\nu} \frac{\gamma}{2} \frac{s_0 \sin\theta \frac{4}{\sqrt{\pi} v_p^3} \nu^2 e^{-(\frac{\nu}{v_p})^2}}{1 + s_0 + 4((k\nu\cos\theta + \delta)/\gamma)^2}, \tag{4.12}$$

with δ the laser detuning and $v_p = \sqrt{\frac{2kT}{m}}$ the most probable velocity. Integrating numerically we have for six laser beams, $d = 1$ cm, $s_0 = 1$ and $T = 900$ K on average 60 photons scattered by an atom. Not all the atoms fly through the detection volume, for the cubic cell setup the detection volume is about 40 mm away from the neutralizer foil. The solid angle is therefore about $8 \cdot 10^{-3}$, including an extra factor of two as the atoms are released into a solid angle of 2π.

Table 4.6 collects the data relevant for the discussion on the Doppler background fluorescence. From table 4.4 we take the number of implanted ions, the released fraction and the trapping efficiency. For ^{21}Na two laser frequencies are present which

Table 4.6: *Estimated ^{23}Na Doppler background and MOT fluorescence rates for the cubic cell setup.*

Number of implanted ions	$1 \cdot 10^9$	
Released fraction	40%	
Fluorescence mechanism	Doppler	MOT
Photons/atom/s	60	10^7
Collection efficiency	-	10^{-5}
Solid angle atom release	$8 \cdot 10^{-3}$	-
Fluorescence detection efficiency	10^{-5}	
Count rate (/s)	$2 \cdot 10^3$	$2 \cdot 10^6$

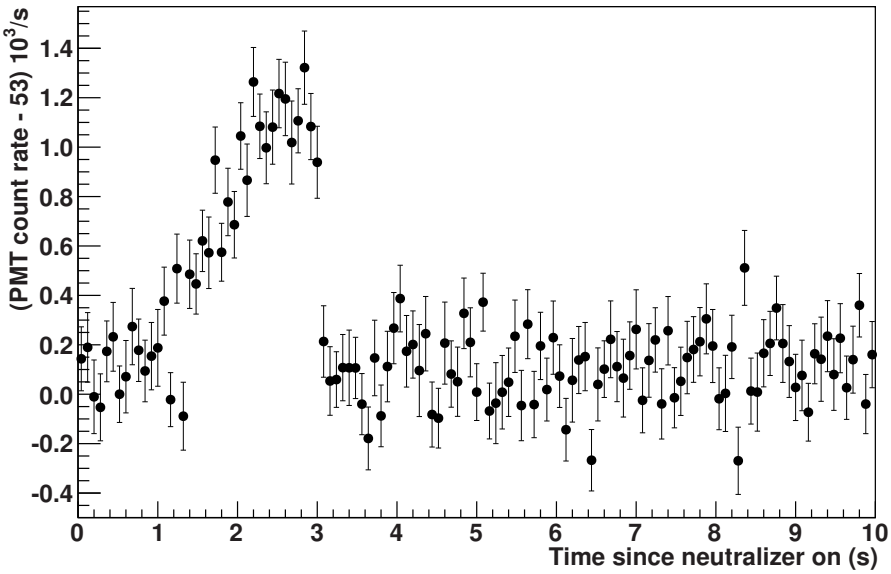

Figure 4.19: *The PMT count rate for a 4 MHz pump and -5 MHz repump laser frequency detuning for ^{23}Na.*

both contribute to the Doppler background fluorescence. The largest contribution comes from the repump laser frequencies of ^{21}Na, which is 199 MHz above the pump frequency of ^{23}Na. This results in about 50 photons/atom/s (equation 4.12). The pump frequency of ^{21}Na is 1648 MHz below the pump frequency of ^{23}Na, this gives 20 photons/atom/s. In total about 70 photons/atom/s can thus be expected from ^{23}Na background gas for ^{21}Na laser settings. As this is close to the value of 60 photons/atom/s we found for ^{23}Na in table 4.6. The same ratio can thus be used. The count rate due to Doppler background fluorescing ^{23}Na when using ^{21}Na laser settings is about a factor of 1000 smaller than the count rate from the ^{23}Na MOT count rate, keeping the LEBL settings for ^{21}Na.

We conclude that the Doppler background fluorescence rate of ^{23}Na contributes to the ^{21}Na MOT signal. For the laser frequency setting of ^{21}Na a background rate due to Doppler fluorescence from ^{23}Na of the order of 100 counts/s can be expected for a current of 1 pA of ^{23}Na, see discussion in section 4.2. This is about 10% of the expected MOT fluorescence rate on basis of the input currents of ^{23}Na and ^{21}Na respectively. For a fluorescence rate of 1000 counts/s for a ^{21}Na, as can be expected from measurements with ^{23}Na, the rate from Doppler broadened scattering from ^{23}Na atoms would then be about 100 counts/s.

Ion beam induced MOT cloud with a room temperature neutralizer

The diffusion at room temperature is negligible (section 4.4). Surprisingly we observe with a cold (room temperature) neutralizer clearly a MOT cloud (*cf.* figure 4.20). The extraction of the 14 pA ion beam is switched on for 20 s, the lifetime of the MOT cloud is 3.9 s. We use different ion beams to see whether the ^{23}Na MOT is due to the ^{23}Na ion beam or if any ion beam shows this effect. The results are listed in table 4.7. Although the K, Ca ion beam gives also an ion related MOT cloud, the effect is a factor of 30 lower than for a ^{23}Na ion beam.

We optimized the 'cold' neutralizer MOT signal by changing the LEBL parameters. These settings do not coincide with the optimal settings for a heated neutralizer. This setting reduces the beam current measured on the neutralizer with about 70%. Especially this last observation indicates that the neutralization might take place on the glass surface; in that case the neutralizer is not playing any role here.

For the francium setup at Legnaro, also a 'cold' neutralizer effect was observed for Fr by De Mauro *et al.*, see page 63 of [78]. With the ion beam continuously on and the neutralizer continuously heated, they observe about 350 trapped Fr atoms in a steady state. With a cold neutralizer they observe about 80 trapped atoms in a steady state. The MOT lifetimes can be quite different in both situations and therefore the steady state atom number most probably changed for that reason as well. De Mauro *et al.* suspect that the 'cold' neutralization effect might be due to sputtering and that this effect depends on the intensity of the ion beam (local melting of the bulk material). They observed the 'cold' effect only for high ionic beam intensities and never observed it with the Rb ionic beam (where the ions have, in contrast to Fr, a mass comparable to the neutralizer material Y, which has a mass of about 90 amu, Zr has a mass of

Table 4.7: *The number of trapped ^{23}Na atoms with a room temperature neutralizer for different isotope settings of the Wien filter.*

Wien filter	Current (pA)	Trapped atoms	Trapped atoms (/pA)
^{23}Na	11.5(0.3)	512(30)	45
K,Ca	35(0.5)	44(3)	1.3
Cs,Ba	2(0.5)	0(3)	0

about 91 amu). Finally, they state that the back-scatter fraction for Fr at Y at their beam energy is very low[2].

To consider this further we calculate the combined neutralization and collection efficiency from the cold neutralizer by converting the ion current assuming no secondary electron emission:

$$\epsilon = \frac{N_{\mathrm{MOT}}}{\tau I} , \tag{4.13}$$

where I is the number of ions/s, τ the MOT lifetime and N_{MOT} is the number of continuously trapped atoms. From the measurement shown in figure 4.20 we find a combined neutralization and collection efficiency of $2.2 \cdot 10^{-6}$ on a cold neutralizer surface. As 27% of this ion beam is not hitting the neutralizer foil (section 4.2), it may be that the atoms are neutralized at the glass surface. Then this process would have an efficiency which is at least 3 times larger than neutralization on the cold neutralizer.

Further, a possible explanation might be that these trapped atoms are originating from the neutralization of back scattered ions. According to simulations about 20% of the 2.8 keV beam will be back scattered with a recoil energy of about 1 keV (see section 2.6). The back scattered fraction of Rb and Fr is negliglible, but still the 'cold' neutralizer effect is observed. It remains unclear what the underlying mechanism is.

For practical purposes the origin of the neutralization of ions for a room temperature neutralizer is not very important. The fraction of the beam lost during transport is comparable to the expected back scattered fraction, therefore the calculated efficiency does not depend on which of these two processes we assume. The atoms which are neutralized continuous are not available for trapping in pulsed mode, where the atoms are released at once. Therefore it has a minor impact on the pulsed trapping efficiency, as can already be concluded from the measurements shown in figure 4.3b (cycle 1).

[2]We did a simulation to determine the stopping distribution and to determine the back scattered fraction of a 2.8 keV Na ion beam on a Zr target (see figure 2.8 for the results). We also did the simulation for a 3 keV Rb and Fr ion beam on a Y target. The ion range for Rb is about 51 Å and the back scattered ion fraction is about 2%, for Fr the values are an ion range of about 54 Å and no back scattered ions.

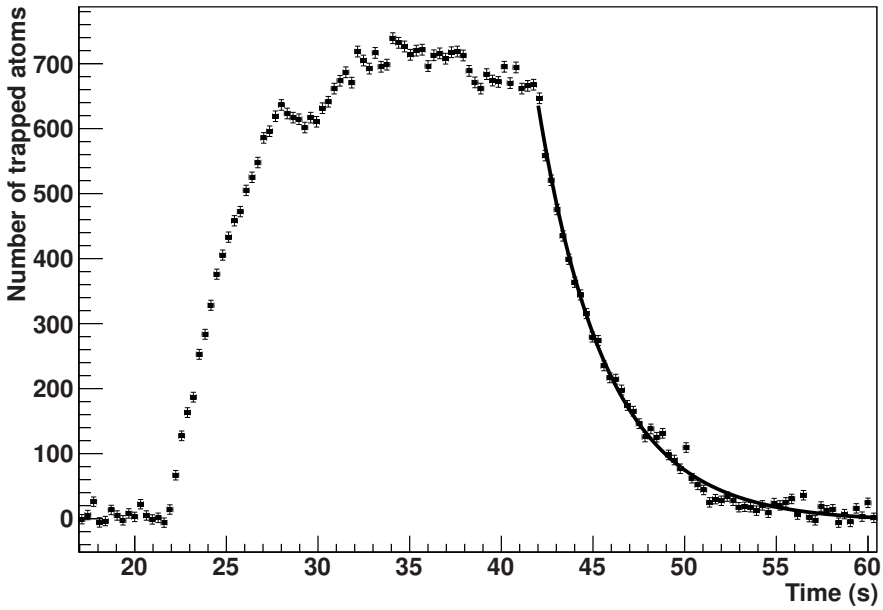

Figure 4.20: *An example of a ^{23}Na MOT cloud for a 'cold' (room temperature) neutralizer foil. The ion beam (13.5 pA) is extracted from the Thermal Ionizer from t=22.2 s to t=42.2 s. The fit of the MOT lifetime gives $\tau = 3.8$ s.*

4.6 The overall efficiency of the setup

In continuous mode we define the collection efficiency as [290]

$$\epsilon_{\mathrm{col}} \equiv \frac{R_{\mathrm{MOT}}}{R_{\mathrm{atom}}} = \epsilon_{\mathrm{MOT}}(T_{\mathrm{neu}}) + \epsilon_{\mathrm{MOT}}(T_{\mathrm{glass}}) N_{\mathrm{M}} \,, \tag{4.14}$$

where R_{MOT} is the loading rate of the MOT and R_{atom} is the rate at which atoms are brought into the cell volume. The average number of trap passages before the atom is adsorbed on the wall or escapes permanently through one of the exits of the cell is N_{M}. At maximum N_{M} is the number of bounces. It can be attributed to two parts: the capture of atoms coming directly from the neutralizer and indirectly from the glass walls of the cell. In the first case the atoms have the temperature of the neutralizer and in the second case they have the temperature of the glass [291]. In the case the cell volume is comparable to the laser trap volume the number of bounces is a good estimator (and upper bound) for the number of trap passages. For a MOT with a velocity capture velocity v_c it captures a fraction per passage of

$$P_1(T) = \frac{4 v_c^3}{3\sqrt{\pi}} \left(\frac{m}{2kT} \right)^{3/2} \,, \tag{4.15}$$

from the Maxwell-Boltzmann distribution with temperature T. For $T_{neu} = 1100$ K and $T_{glass} = 293$ K the ratio is $P_1(T_{glass})/P_1(T_{neu}) = 6.3$, thus capturing from the vapor which has been collided once with the glass wall is much more efficient.

In table 4.9 we have collected all data that allow the extraction of the various efficiencies we have introduced in section 4.1. The table shows the results for both ^{21}Na and ^{23}Na and for the two cell types, the cross-cell and cubic-cell configuration.

Section I of the table summarizes the measurements on the number of particles which are accumulated in the neutralizer (see section 4.2). The accumulated number of particles is It where t is the cycle time and I the incoming particle current. In equilibrium the observed average decay rate is equal to the average incoming current. To calculate the efficiencies we calculate the number of ^{21}Na which are available at the moment of the heating pulse, as a fraction of the accumulated atoms that has already decayed. It is not possible to know if all ^{21}Na ions were deposited on the neutralizer. Therefore, the number of ^{21}Na atoms that can be trapped may still be lower.

Section II of the table describes the MOT cloud fluorescence detection efficiency. For the cubic cell the first aperture of the detection system (thus the solid angle) is chosen for the best signal-to-background ratio for the ^{21}Na measurement. The background count rate was not limiting for the ^{23}Na measurements.

In section III the laser parameters are listed which are used to convert the fluorescence rate from the MOT cloud to a number of trapped atoms. The scattering rate per atom times the fluorescence detection gives the count rate per atom in the detection system. The ion related fluorescence peak rate then results in a maximum (peak) number of trapped atoms.

Section IV summarizes the LEBL transport efficiency from section 4.2 and the release efficiency from section 4.4. Combined with the peak number of trapped atoms and the number of ions accumulated in a cycle this gives the collection efficiency. For the cubic setup we use the peak trapped fraction from table 4.4 as the neutralizer efficiency. As the release efficiency was not measured for the cross setup we use the change in decay rate as observed for ^{21}Na. By setting the laser detuning to the maximal atom number instead of to the detuning corresponding to maximal fluorescence, the number of trapped atoms is increased (section 4.3). For completeness we also include the 'cold' neutralizer, continuous efficiency discussed in section 4.5.

The errors on the experimental data are taken as uniform distributions, the error propagation is Monte Carlo simulated. For the non-Gaussian distributions, the median is taken as the central value and 68% of the points are taken within the upper and lower limit.

We show in figure 4.21 the ^{21}Na trapping signal for the cubic setup. To make sure that we observe fluorescence from a ^{21}Na MOT cloud, we deliberately set the laser frequency such that the cooling light was blue detuned. For the trapping signal, the peak atom number corresponds to a PMT count rate of $1.2 \cdot 10^3$ counts/s. The cycle length was 40 s and the data for the trapping conditions represents about 1 hour of data. The error bars are the width of a Gaussian fit to the bin distribution and is thus not the statistical error.

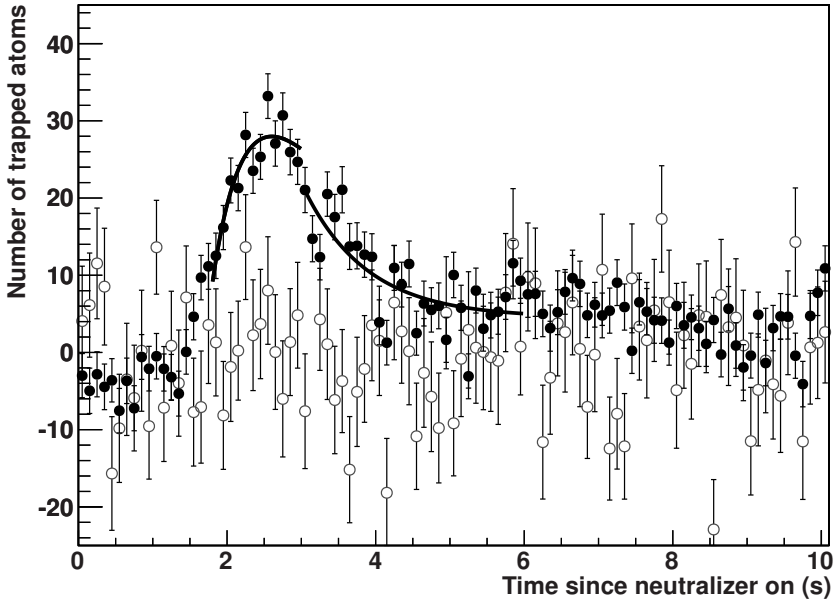

Figure 4.21: *Trapped ^{21}Na atoms in the CC, for trapping (closed symbols) and anti-trapping detunings (open symbols). The fit to the data is based on the diffusion model (see the text). The fit parameters can be found in table 4.8. The pump and repump laser detuning are -8 MHz and -2 MHz respectively (closed symbols), and are 2 MHz and 8 MHz (open symbols).*

Table 4.8: *The diffusion and MOT parameters from the fits to the data in figure 4.21 from trapped ^{21}Na atoms. To compare we show data from the second column from 4.4, obtained from measurements with ^{23}Na. For both measurements the neutralizer was heating with a current of 6.3 A.*

Fit parameters	^{21}Na	^{23}Na
Diffusion time $1/\alpha = d^2/4D$ (s)	1.3	0.9(15)
MOT lifetime τ_{on} (s)	0.7	0.63(6)
MOT lifetime τ_{off} (s)	0.9	3.80(1)
Effective heating time t_{heat} (s)	1.3	1.48(5)
Atom number $N^{t\to\infty}_{\tau_{\text{on}}\to\infty}$	240	$4.9(6)\cdot 10^5$
Peak temperature (K)	1080(10)	1080(10)
D (10^{-13} cm^2/s)	1.0	1.5(3)
Released fraction (%)	30	40(5)
Number of implanted ions	$1\cdot 10^6$	$1.8\cdot 10^9$
Collection efficiency	$2.4\cdot 10^{-4}$	$2.7\cdot 10^{-4}$
Peak released fraction (%)	13	15 ± 4

The errors in figure 4.21 are about a factor of 10 above the shot noise limit. Correcting the PMT rate using the signals from photodiodes recording the laser powers near the MOT setup does not remove the non-statistical scatter of the data. Most probably pointing effects of the laser beams are the dominating source of long term systematic drifts of the background count rate.

In section 4.5 we estimated that the Doppler background fluorescence rate is about 10% of the fluorescence signal from trapped ^{21}Na atoms. The distinct feature is that the trapped atoms have a lifetime, whereas the Doppler fluorescence is only present when the neutralizer is heated. The Doppler background fluorescence from ^{23}Na atoms in figure 4.21 is estimated to be the size of 3 trapped atoms, which is within the scatter of the data.

The trap signal (red detuning) data in figure 4.21 are fit to the diffusion model, which is described in section 4.4. For the fit an additional offset value of -2 was used, also for the fit of the MOT lifetime after $t = 3$ s an offset was included. The results of the fits are shown in table 4.8. For comparison we also included in this table a measurement with ^{23}Na, which was done with the same heating current for the neutralizer. For ^{21}Na the systematic errors dominate. We observe that all values are in reasonable agreement with the values obtained with ^{23}Na, except for the value for τ_{off}, which is about a factor of 4 smaller for ^{21}Na than for ^{23}Na.

For the cubic glass cell the overall efficiency for ^{21}Na is in agreement with the value found using ^{23}Na. The main uncertainty arises from the number of ^{21}Na which are incident on the neutralizer. As at the same temperature ^{21}Na has a slightly higher thermal speed than ^{23}Na, the collection efficiency of the MOT is expected to be 4% lower for ^{21}Na than for ^{23}Na.

For the cross glass cell no clear MOT related ^{21}Na signal could be extracted. The detection sensitivity was limited by the fluctuation in the background count rate due to scattered laser light. Also we were less certain about the absolute laser frequency, compared with the trapping signal obtained with the cubic setup where the lasers were locked to the frequency comb.

For the measurements with the cubic cell setup in table 4.9, we coated the cell with a PDMS solution. Simple tests of the quality of the coating indicated that something went wrong during the coating procedure[3]. As the beamtime was close, there was not enough time to coat the cell again and we decided to continue with the sub-optimal coating. However, we cannot exclude that part of the coated surface might actually work and give a bit of enhancement of the collection efficiency. In table 4.10 we therefore calculate the capture velocity for the cubic cell setup as function of the number of trap passages. The large difference between 1 and 2 trap passages is due to thermalization of the hot atoms having the temperature of the neutralizer foil of 1100 K, to the temperature of the glass cell wall of about room temperature. The typical

[3] A simple test we did and failed, was the 'droplet' test. A droplet of water shows a reduced contact angle at a coated surface and does not wet it (slide frictionless over the surface).

Table 4.9: *The overview of the efficiencies characterizing the two MOT systems (cross and cubic) used in the collector chamber MOT setup.*

Glass cell type, sodium isotope	^{23}Na	Cross	^{21}Na	^{23}Na	Cubic	^{21}Na
I Incoming particles						
β detection efficiency	-		$1.6^{+0.7}_{-0.1} \cdot 10^{-3}$	-		$1.3^{+0.5}_{-0.1} \cdot 10^{-2}$
511 keV rate (/s)	-		194(10)	-		$1.1(0.1) \cdot 10^{3}$
Electrical current (pA)	18(2)		-	11(1)		-
Secondary electron yield	0.5(5)		-	0.5(5)		-
Particle current (/s)	$7.5^{+2}_{-1} \cdot 10^{7}$		$1.0^{+1.3}_{-0.4} \cdot 10^{5}$	$5(1) \cdot 10^{7}$		$6^{+4}_{-2} \cdot 10^{4}$
Cycle time (s)	20		40	20		40
Decay during accumulation	-		0.57	-		0.57
Particles per cycle (N_{in})	$1.5^{+0.4}_{-0.3} \cdot 10^{9}$		$4.0^{+5}_{-2} \cdot 10^{6}$	$9.0^{+3}_{-2} \cdot 10^{8}$		$2.6^{+1.7}_{-0.7} \cdot 10^{6}$
II MOT cloud detection						
Solid angle	$1.6^{+0.8}_{-0.6} \cdot 10^{-4}$		$1.6^{+0.8}_{-0.6} \cdot 10^{-4}$	$9.0(1) \cdot 10^{-4}$		$4.0(7) \cdot 10^{-4}$
Photon detection efficiency	$4.9(3) \cdot 10^{-3}$		$4.9(3) \cdot 10^{-3}$	$1.0(2) \cdot 10^{-2}$		$1.0(2) \cdot 10^{-2}$
Fluorescence detection efficiency	$6.9^{+7}_{-4} \cdot 10^{-7}$		$6.9^{+7}_{-4} \cdot 10^{-7}$	$9(2) \cdot 10^{-6}$		$3.9^{+1}_{-0.9} \cdot 10^{-6}$
III Trapped atoms in MOT						
Laser detuning (MHz)	$-13(5)$		$-13(5)$	$-5(1)$		$-8(1)$
Six beam laser intensity (s_0)	20(4)		20(4)	1.3(2)		1.3(2)
Fluorescence rate (/atom/s)	$2.3(3) \cdot 10^{7}$		$2.3(3) \cdot 10^{7}$	$1.3(1) \cdot 10^{7}$		$8.7^{+9}_{-8} \cdot 10^{6}$
Detected rate (/atom/s)	16^{+15}_{-9}		16^{+15}_{-9}	110^{+30}_{-20}		34^{+10}_{-8}
Observed detector peak rate (/s)	$310(50) \cdot 10^{3}$		≤ 200	$2.5(1) \cdot 10^{6}$		$1.4(1) \cdot 10^{3}$
Observed number of trapped atoms	$2.0^{+3}_{-1} \cdot 10^{4}$		$\leq 23^{+40}_{-16}$	$2.4^{+0.7}_{-0.5} \cdot 10^{4}$		36^{+11}_{-8}
IV Overall efficiency						
Released fraction neutralizer	$\geq 8^{+8}_{-0}$% @ 900 K			40(10)% @ 1080(50) K		
Peak trapped fraction ϵ_{neu}	$\geq 8^{+8}_{-0}$% @ 900 K			15(4)%		
Detuning optimization	-		-	2.2		1.6
MOT collection efficiency ϵ_{col}	$1.1^{+1.6}_{-0.6} \cdot 10^{-4}$		$\leq 4^{+9}_{-3} \cdot 10^{-5}$	$4.0^{+1.7}_{-1.2} \cdot 10^{-4}$		$2.6^{+1.5}_{-1.1} \cdot 10^{-4}$
Release and collection efficiency $\epsilon_{\text{col}}\epsilon_{\text{neu}}$	$1.3^{+1.8}_{-0.7} \cdot 10^{-5}$		$\leq 5^{+11}_{-4} \cdot 10^{-6}$	$1.6^{+0.7}_{-0.5} \cdot 10^{-4}$		$1.0^{+0.6}_{-0.4} \cdot 10^{-5}$
'Cold' release and collection efficiency	-		-	$(0.5 - 1.8) \cdot 10^{-5}$		-
Ion transport efficiency ϵ_{ion}	30(3)%			32(4)%		
Overall efficiency $\epsilon_{\text{overall}} = \epsilon_{\text{col}}\epsilon_{\text{neu}}\epsilon_{\text{ion}}$	$3.9^{+5}_{-2} \cdot 10^{-6}$		$\leq 1.5^{+3}_{-1} \cdot 10^{-6}$	$5.0^{+2.4}_{-1.6} \cdot 10^{-5}$		$3.2^{+2.1}_{-1.4} \cdot 10^{-5}$

Table 4.10: *The required capture velocity as function of the number of trap passages (not known) for the ^{23}Na collection efficiency ϵ_{col} from table 4.9. Thermalization from the neutralizer temperature to room temperature is assumed to take place within 1 bounce.*

	Cubic cell			
Number of trap passages	1	2	10	100
Capture velocity (m/s)	71^{+9}_{-8}	37^{+5}_{-4}	17 ± 2	8 ± 1

capture velocity of a sodium MOT is around 20 - 35 m/s [166]. These values are for MOTs which use smaller beam diameters than we have. Therefore it can be expected that we can achieve a larger capture velocity.

Our conclusion is that most probably the number of trap passages is of order 1 and the number of bounces of the order 5 (see section 3.6 for the relation between the number of trap passages and the number of bounces). An improvement of a factor of 100 is possible (section 3.6), ultimately limited by the total effective exit area of the cell design. Improvement of the quality of the coating is thus of foremost importance. The capture velocity, and therefore the collection efficiency, can be expected to be increased further. The laser beam intensity is still low, the peak intensity is about 1/6 of the saturation intensity. Note that the capture velocity can be determined with a push beam measurement (see section 5.2).

4.7 Conclusions

The conclusions for the current setup are that

1. ^{23}Na can be used to establish all relevant efficiencies of the collection setup on the quantitative level in preparation for the efficient trapping of ^{21}Na.

2. The fraction of ions extracted from the Thermal Ionizer which ends up trapped in the collector cell MOT is currently $5.0^{+2.4}_{-1.6} \cdot 10^{-5}$. The collection efficiency of $4.0^{+1.7}_{-1.2} \cdot 10^{-4}$ is the main limiting factor.

3. The collection efficiency is now limited by the quality of the non-stick coating. Improving this will result in an estimated factor of 100 higher collection efficiency.

Comparison and outlook

Because the final efficiency depends strongly on the number of bounces we made an extensive search in the literature to see what one may expect and how a 1% collection efficiency can be achieved with a neutralizer based vapor MOT setup. In table 4.11 a compilation of the most relevant experimental parameters is listed for high efficiency trapping experiments.

Some of the entries of the table need some clarification, we discuss briefly each experiment. For the Cs experiment the expected collection efficiency, based on the capture velocity and number of bounces, is a factor of 18 higher than measured experimentally. This is also not understood by the authors [230]. We use here the direct measured value. It is possible that either their reported collection efficiency is higher than in reality, or their number of bounces is higher than measured.

For the ^{210}Fr experiment the number of bounces was only measured in a test setup. The authors estimate a single pass trapping efficiency of about 10^{-5}, assuming a thermalization factor of 6 we calculated the number of bounces.

For the ^{221}Fr experiment the number of bounces is not derived. However, the average time the atoms spend in the cell is known to the authors. At room temperature the mean velocity is 168 m/s, combined with the average distance of 2/3 times 4.4 cm inner diameter of the trapping cell (equation B.5), gives an estimated average amount of $3.6 \cdot 10^3$ bounces for the average residence time of 630(40) ms.

For the ^{37,38m}K TRINAT experiment at TRIUMF, the number of bounces is not mentioned. However, they describe the cell geometry in detail [72]. It is a cube with an edge of 5 cm and three holes of 6 mm diameter. The cell has no tubes attached to it and is placed inside a vacuum chamber. An atom exiting is thus practically lost for the trapping process. Based on relative exit area, the number of bounces is expected to be in the order of 180. In the second MOT chamber, a population of about 5000 trapped ^{38m}K ($t_{1/2} = 0.92$ s) atoms is maintained [292]. With a transfer efficiency of 75% and a ^{38m}K production yield of $8.7 \cdot 10^6$ for a 1.1 μA beam current [72], this gives an estimated efficiency for the target to the collector MOT of order $6 \cdot 10^{-4}$. With the same dual MOT setup also ^{80}Rb has been trapped and transferred [74, 293, 294]. In these references only two numbers are mentioned which give an indication of the overall efficiency: $2 \cdot 10^9$ ions/s are extracted from the target and about $2 \cdot 10^6$ atoms are continuously trapped in the collector MOT. Assuming a trap lifetime of about 1 s, this gives an overall efficiency of 10^{-3}.

The high number of bounces reported for the ^{209,210}Fr experiment was based on measurements with Rb, without a neutralizer device being present. It is possible that during the beam time the coating quality degraded due to the hot neutralizer [231].

The best collection efficiency is achieved with the ^{210}Fr setup, but it did not have a neutralizer and the exits were also closed to prevent loosing the atoms from the trapping volume. The top three best performing experiments all have a proper working non-stick coating. It can also be concluded that a setup with a Zeeman slower does not necessarily give a better overall efficiency.

Using the cubic cell setup a state-of-the art high efficiency MOT can be established by improving on two points:

- A non-stick wall coating, bringing the number of bounces from 1 to 500 and increasing ϵ_{col} with a factor 100 (see section 3.6).

- Improving the capture velocity by going from the current peak intensity per beam of 0.2 s_0 to an intensity of 1 s_0 over the whole laser beam area.

Further, the RFQ might be operated in a more efficient way for ^{21}Na, resulting in an increase of the transport efficiency with maximally a factor 3. Additionally, the usage of the RFQ instead of the drift tube will remove ^{23}Na from the ion beam.

If we only include the expected improvement from the number of bounces, this measure would result in a projected collection efficiency of $\epsilon_{\text{col}} = 1\%$ and an overall efficiency of $\epsilon_{\text{overall}} = 0.3\%$.

Table 4.11: *The overall efficiency for unstable isotope experiments, defined as the ratio of the MOT loading rate to the source rate. The laser beam diameter is the $1/e^2$ intensity diameter. The glass types are Pyrex (P) and Quartz (Q).*

Atomic species	Overall efficiency	Collection efficiency	Bounces	Neutralizer efficiency	E_{ion} (keV)	Neutralizer T (K)	LEBL eff.	Glass type	Coating	Laser ⌀ (cm)	Ref.
^{210}Fr	$6 \cdot 10^{-3}$	$1 \cdot 10^{-2}$	300†	0.52	5	Y, >1000	0.90	P	SC-77	4.2	[80]
^{135,137}Cs	$5 \cdot 10^{-3}$	$3 \cdot 10^{-2}$	350	0.45	20	Zr, 1100	0.35	Q	SC-77	5	[291]
^{221}Fr	$4 \cdot 10^{-3}$	$6 \cdot 10^{-1}$	2400†	Oven based, $\epsilon = 7 \cdot 10^{-3}$				Q	SC-77	4	[290]
^{82}Rb	$1 \cdot 10^{-3}$	$4 \cdot 10^{-3}$	30	0.30	20	Y, 1000	0.35	Q	OTS	5	[221]
^{38m}K	$7 \cdot 10^{-4}$	-	-	0.2	30	Zr, 1100	-	P	SC-77	4.5	[72]
^{21}Na	$2 \cdot 10^{-4}$	Zeeman slower based, $\epsilon = \frac{R_{\text{MOT}}}{R_{\text{source}}}$								3.2	[65]
^{209,210}Fr	$2 \cdot 10^{-4}$	$3 \cdot 10^{-4}$	$1.4 \cdot 10^3$	0.7	3	Y, 1100	0.50	P	OTS	4	[78]
^{37,38m}K	-	$2 \cdot 10^{-4}$	-	-	-	Hf, 1100	-	P	Dry-film	4.5	[295]
^{21}Na	$5 \cdot 10^{-5}$	$4 \cdot 10^{-4}$	~ 5	0.4	2.8	Zr, 1100	0.32	P	PDMS	4	this work

† Estimated value (see text).

Chapter 5

Double MOT transfer of ^{23}Na atoms

As demonstrated in chapter 2 and 3 the requirements for a high collection efficiency Magneto Optical Trap (MOT) setup are incompatible with the conditions for a measurement of the β-decay correlations of ^{21}Na. A high collection efficiency critically depends on the degree of enclosure of the atom vapor with a coated glass surface, which prevents sticking of the atoms, and allows only for small exit areas. The presence of particle detectors which reconstruct the decay kinematics as well as the need for a high pumping speed to ensure long trap lifetimes for the correlations measurements requires a second, spatially separated atom trap for the decay measurement to which the atoms are transferred.

In our case the atoms are collected in the collector chamber (CC) MOT, which is described in chapter 4. The science chamber (SC) MOT system, situated 69 cm away, is surrounded by particle detectors which have been setup to reconstruct the full decay kinematics [69]. The main goal of this chapter is to characterize and optimize the transfer from the collector chamber to the science chamber using stable ^{23}Na atoms and to identify possible improvements to achieve the projected transfer efficiency of 50% for ^{21}Na.

We discussed in section 2.9 the advantages and disadvantages of possible transfer strategies. We chose in our experiment to set up the resonant pulsed transfer, combined with an intermediate cooling stage. In this approach the trapped atoms in the CC MOT are accelerated by a short resonant laser pulse and recaptured by the SC MOT. Additionally, the atoms are cooled by an optical funnel (a two dimensional MOT). The funnel compresses and cools the pushed, heated atom cloud and therefore enhances the transfer efficiency. This transfer method is the preferable method for Na and has been used to demonstrate for ^{41}K a transfer efficiency of 78% and 40% over a distance of 78 cm with and without two funnel stages, respectively [259].

The transfer process can be described in three steps: push, funnel and recapture, which is sketched in figure 5.1. A typical sequence is as follows. First the intensity of the CC MOT beams is decreased by a factor of almost 200 within 1 ms, to prevent that the CC MOT counteracts the pushing process. The push beam is switched on

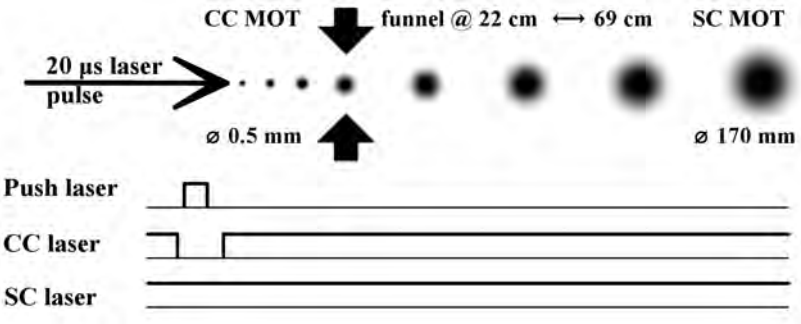

Figure 5.1: *The scheme of the atom transfer. The initially mm size trapped atom cloud expands to several cm during the transfer. During the pushing phase the CC MOT intensity is decreased. The figure is not to scale.*

and the trapped atoms are accelerated with $4 \cdot 10^5$ m/s^2 to a velocity of 10 m/s. The acceleration takes 25 μs and the atoms are then 125 μm away from the initial position. The second step is the compression and cooling by the funnel section. The time the atoms spend in the funnel section depends on the push velocity. The third step is the recapture of the atoms in the SC MOT.

The main parameters that determine the transfer efficiency can be understood from a numerical simulation of the transfer process. The results are summarized in figure 5.2. In this figure the atom cloud diameter and transfer efficiency are shown as function of the push velocity. The calculations assume the expansion of a heated atomic cloud as will be explained in detail later. The capture velocity and the beam diameter of the SC MOT determines the fraction of the pushed atoms that can be recaptured. As a first conclusion we see that for a high transfer efficiency a push alone is insufficient to achieve the desired 50% transfer efficiency. We will come back to this figure in section 5.3.

This chapter begins with an overview of the setup used to transfer the atoms in section 5.1. Then the transfer method is described in more detail and in this way we transferred for the first time atoms between the two chambers, which is described in section 5.2. Section 5.3 discusses the optimization and characterization of our transfer method, the alignment of the push beam, its intensity and duration were varied. The chapter ends in section 5.4 with the obtained transfer efficiency and possible strategies to enhance it to achieve the projected transfer efficiency of 50%. As a first step towards this goal an improvement of transfer efficiency using a push beam only was achieved by using a funnel.

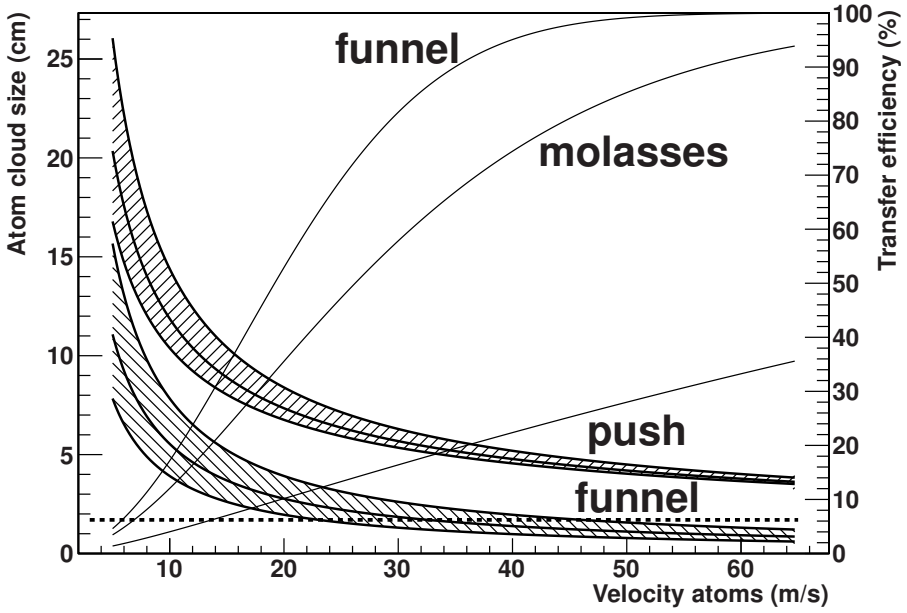

Figure 5.2: *The size of the atom cloud at the SC MOT position for a push beam and a funnel at 22 cm (left axis), the shaded area indicates the initial temperature of* 240^{+240}_{-120} *μK. The transfer efficiency (right axis) of a push beam without or with either a molasses or a funnel. The laser beam diameter in the receiving SC MOT is taken to be 17 mm is (dotted line).*

5.1 The double MOT system characteristics

We start with discussing the main experimental parameters of the double MOT system. The optical layout can be found in figure 5.3. The Spectra Physics Dye laser laser generates the laser light for the double MOT system and the push beam. The laser is frequency locked to an amplitude modulated spectroscopy setup. An EOM generates sidebands at 1712 MHz and provides the repump power. The CC MOT setup is operated in the cross glass cell with three retro-reflected beams. The SC MOT is operated in a collimated single beam configuration.

The light for the push beam is switched on and off using an AOM and is frequency shifted by +40.0 MHz. The push beam is linearly polarized and has a maximal push power of 14.3 ± 5 mW. The push beam is aligned on the atom cloud by maximizing the pushing effect in continuous mode. By steadily going down in push power a minimal push power is found. This alignment is used as a starting point for further optimizations.

The non-diffracted beam of the AOM passes a Pockels cell. During the pushing

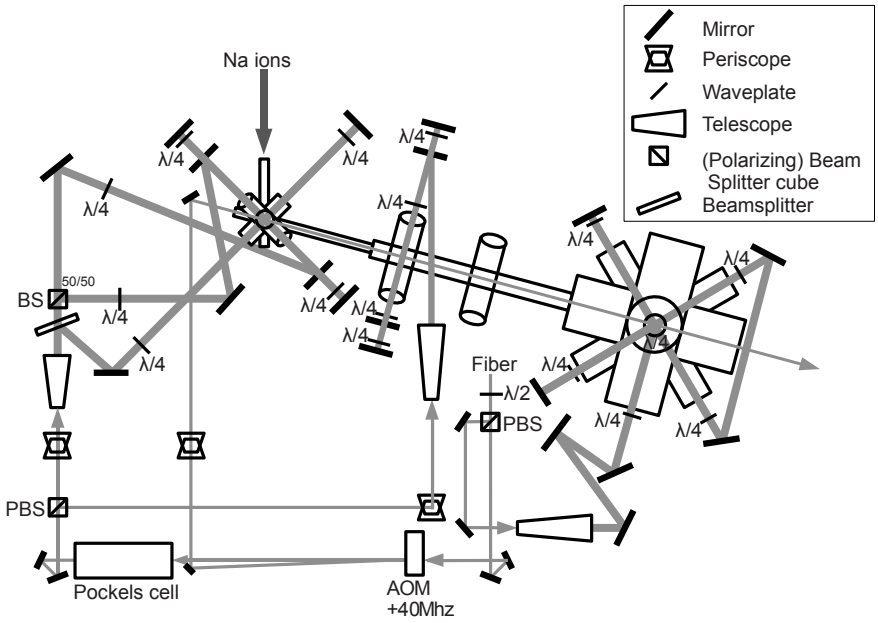

Figure 5.3: *The optical layout of the double MOT system with the push beam for the cross cell setup.*

phase, the CC MOT beam intensity is decreased within 1 ms by a factor of 190 by switching the voltage on the Pockels cell, which rotates the linear polarized light by 90°. The diverted light is used for the funnel section, which is used in a single beam 2D MOT configuration. A quadrupole field gradient is formed by four wires in a hair pin configuration. Two pairs of coils in Helmholtz configuration give an offset field. Attenuators in front of the beam expander of the funnel section can decrease the laser intensity. The main settings of the double MOT system are summarized in table 5.1.

The laser intensity and detuning are used to calculate the scattering rate of a single atom from the push beam. As can be seen from table 5.1 the minimum intensity of the push beam to push the atoms away continuously is comparable to the intensity of the MOT beams. This can be expected as the detuning of the counterpropagating MOT beam differs by a minus sign from the detuning of the push beam. If both beams have the same intensity the push beam is accelerating the atoms until they have a Doppler shift of 2Γ (corresponding to 12 m/s). The cloud temperatures of both MOT systems have not been measured but are assumed to be around the Doppler limit of 235 μK [151], which corresponds to a one-dimensional Gaussian spread of 0.3 m/s and to an average velocity of 0.5 m/s.

Table 5.1: *Summary of the double MOT and the push beam parameters. The minimal push intensity is the required intensity in continuous mode to push the MOT cloud away from the MOT system which is operated with the normal intensity. The saturation intensity for isotropic polarized light of the MOT is $s_0 = 13\ mW/cm^2$ for the $F = 2 \rightarrow F' = 3$ transition, for the linearly polarized push light $s_0 = 11\ mW/cm^2$ [151].*

Property	CC MOT	Push beam	Funnel	SC MOT
Laser beam $1/e^2$ ⌀ (mm)	15	2.0 ± 0.2	95	17
Maximal intensity (s_0)	0.3	70 ± 10	1/300	0.7
Intensity during pushing (s_0)	0.002	-	0	-
Push intensity threshold (s_0)	0.35	-	-	0.81
Field gradient (Gauss/cm)	25	-	8	21
Laser detuning $S_{1/2}(F = 2)$-$P_{3/2}(F = 3)$	-2Γ	2Γ	-2Γ	-2Γ

As we are interested in the absolute transfer efficiency we briefly discuss the possible systematic errors involved in the determination of the number of trapped atoms. The dominant systematic uncertainty for the transfer efficiency measurement is the absolute peak laser intensity at the MOT position. The second dominant effect is the absolute laser frequency. The CC MOT cloud temperature and the capture velocity of the SC MOT depends on the laser detuning. The alignment of the SC MOT was not as stable as the CC MOT, due to the single beam design of the SC MOT. A slight change in optical alignment made the MOT disappear. Vibrating, sharp fringes close to the MOT position were clearly visible. The SC MOT cloud position also shifted several mm as function of the laser detuning, indicating a significant intensity inbalance. The CC MOT operated much more reliable and did not show these problems. An improvement of the SC MOT would therefore improve the transfer measurement stability and systematic studies.

We swapped the Photo Multiplier Tubes (PMTs) of the SC and CC MOT detection systems. The thresholds of the discriminators of the PMTs were the same. The MOT related count rates did not change significantly. The laser intensity was stable at the few % level, which is also sufficiently stable for our purposes.

5.2 Double MOT transfer using a resonant push beam

We transfer the atoms between the two MOT systems by accelerating the trapped atoms with a pulsed, near resonant laser beam and recapturing them in the second MOT setup. The atoms are captured if they are within the MOT volume and if their velocity is below the capture velocity of the MOT. Due to the temperature of the atom cloud the initial velocity is non-zero. In the push direction the velocity is the product of the number of photons scattered during the pushing phase and the recoil velocity. In all three directions the initial velocity spread is enlarged due to the heating from

pushing process. Most relevant is the heating in the transverse direction, as it directly affects the transfer efficiency.

Experimental observation of pushed atoms

We will now describe two measurements of the pushing process in the CC MOT. To determine the fraction of atoms that is pushed away from the CC MOT, we look at the fluorescence rate just after the push pulse has been applied for two different push times of 10 μs and 40 μs. The result of these measurements are shown in figure 5.4 and figure 5.5, respectively. When the push beam is switched on we lower the CC MOT beam intensity to avoid that the CC MOT recaptures the pushed atoms. For the trapping beam in the CC MOT of 15 mm diameter and a pushing speed of 7.5 m/s the minimal time in which the MOT beam intensity has to be lowered is 2 ms. When the MOT beam intensity is reduced the fluorescence rate drops to nearly zero. When the MOT beams return back to normal laser intensity two different sequences evolve. For the short push pulse the fluorescence increases in a few ms, then the MOT reaches its saturation fluorescence level with the time constant of the MOT lifetime (drawn curve shows the exponential loading curve). For the long push of 40 μs only the standard loading curve can be seen. Thus in the latter case all atoms were removed, while in the former case about 38% was recaptured.

This type of measurement in fact provides a way of measuring the escape velocity. The escape velocity is directly related to the capture velocity via equation A.5. However, we did not perform such a measurement ourselves, as we realized this during the data analysis process, after the experiments were done. The idea to measure the escape velocity by using a push beam, has been first been implemented by Aubin *et al.* [81]. They determined for a ^{85}Rb MOT an escape velocity of about 20 m/s (or a capture velocity of about 28 m/s).

Experimental observation of the recapture process

After the acceleration by the push beam, the atoms fly towards the SC MOT region. When the atoms enter the SC MOT laser volume, they start to fluoresce. Either the atoms are slowed and trapped, or they leave (slowed) the trapping volume. We make the approximation that only the velocity distribution of the pushed atoms determines the time dependence of the fluorescence rate in the receiving MOT. We assume that the influence of the slowing process, which happens on the timescale of the order of ms, is either negligible or effectively broadens our observable. With this simple model we extract the mean and width of the velocity distribution of the pushed atoms.

The initial velocity distribution in the MOT cloud is described by a Maxwell-Boltzmann distribution, each of the three components is Gaussian distributed. The scattering of N photons from the push beam results in a final velocity along the push beam direction of

$$v = N v_r \,, \tag{5.1}$$

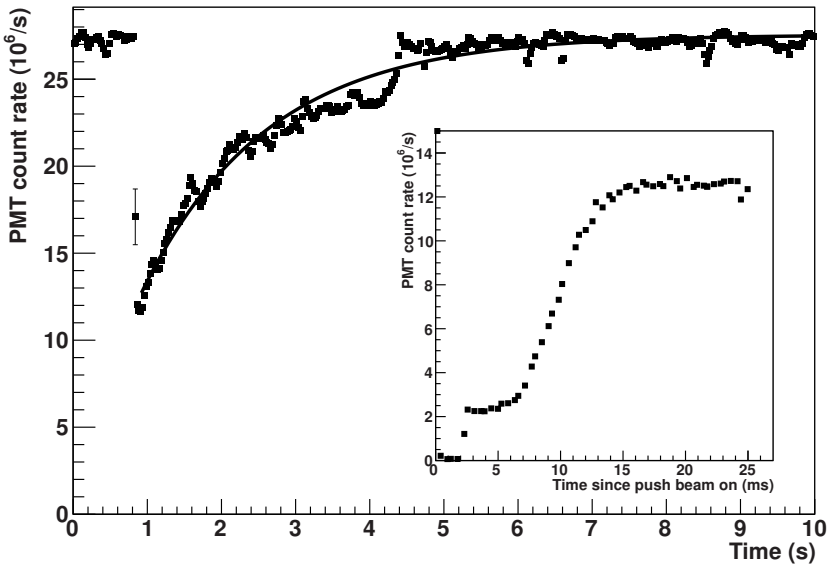

Figure 5.4: *A single trace of the PMT count rate signal from the CC MOT for a push pulse duration of 10 μs. The inset shows the signal during the first 25 ms. About 40% of the atoms are re-trapped by the MOT after being accelerated by the push beam. The fluorescence rate to the number of trapped atoms conversion factor is 45 counts/s/atom.*

Table 5.2: *Summary of the data in figure 5.6.*

Observable	Value
Background count rate	$736 \pm 3 \cdot 10^3$ 1/s
Mean velocity v	8.9 ± 0.1 m/s
Velocity spread σ	1.1 ± 0.1 m/s
Number of trapped atoms SC MOT N_{SC}	$1.1 \pm 0.4 \cdot 10^4$
Number of pushed atoms CC MOT N_{CC}	$6.0 \pm 2 \cdot 10^5$
Transfer efficiency $\epsilon = N_{SC}/N_{CC}$	$1.8 \pm 0.5\%$

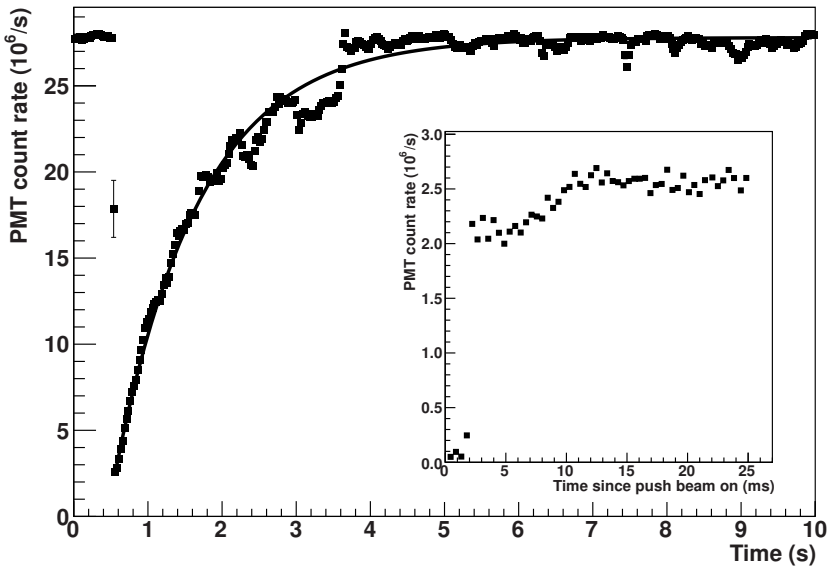

Figure 5.5: *See the description of figure 5.4, the push time is 40 μs.*

with $v_r = \frac{h}{m\lambda}$ the recoil velocity, which for Na is 2.95 cm/s. The pushing process increases the initial velocity spread. A random walk of N steps in three dimensions results in a spatial Gaussian distribution with a standard deviation $\sigma = v_r\sqrt{\frac{N}{3}}$ in each of the three dimensions. When the initial velocity spread is v_0, after pushing it is

$$\sigma_v = \sqrt{v_0^2 + \frac{\sigma^2}{3}} = \sqrt{v_0^2 + \frac{N v_r^2}{3}} = v_0\sqrt{1 + \frac{v v_r}{3v_0^2}}\,. \tag{5.2}$$

Assuming that the atoms start fluorescing, after being slowed, in the MOT center first, the time dependent fluorescence rate can be obtained by integrating the normalized velocity distribution,

$$N_{SC}\int_{d/t}^{\infty} dv' \frac{1}{\sigma\sqrt{2\pi}} e^{-\frac{1}{2}(\frac{v'-v}{\sigma})^2} = \frac{N_{SC}}{2}\mathrm{Erfc}\left(\frac{d - vt}{\sqrt{2}t\sigma}\right)\,, \tag{5.3}$$

with v the push speed and N_{SC} the number of atoms captured by the SC MOT.

In figure 5.6 the fluorescence signal as recorded by the SC MOT detection system is shown for a push time of 17.5 μs and a push beam power of 14 mW. Four parameters are fitted to the data: the constant background due to stray light and equation 5.3 with three parameters. The fit results of the latter are summarized in table 5.2.

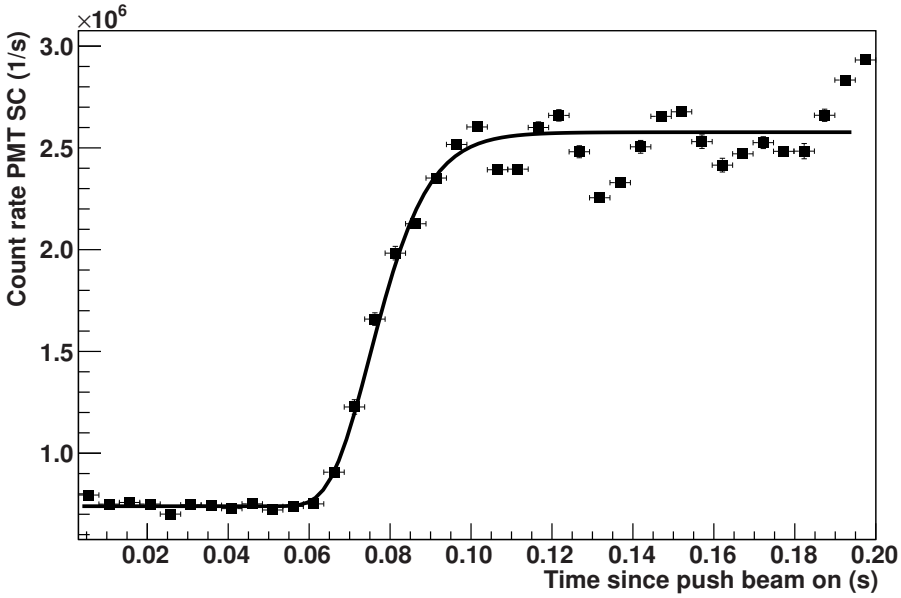

Figure 5.6: *The recorded PMT fluorescence in the SC MOT setup, due to the arrival of a single shot of transferred atoms. The data is fitted by equation 5.3, on top of background due to stray light. The fluorescence rate to the number of trapped atoms conversion factor is 167 counts/s/atom. The fit parameters are tabulated in table 5.2.*

5.3 Transfer studies

Dependence of the push velocity on the push beam duration

To predict the mean velocity for a total laser detuning δ and power s_0 (in units of the saturation intensity), we integrate the acceleration $a(t,v)$ due to scattering photons from the push beam,

$$v = \int_{\text{push time}} a(v)\mathrm{d}t \ . \tag{5.4}$$

The velocity dependent acceleration constant is given by the recoil velocity times the scattering rate, equation 2.1,

$$a(v) = v_\mathrm{r}\gamma_\mathrm{scat} = v_\mathrm{r}\frac{\Gamma}{2}\frac{s_0}{1+s_0+4(\delta/\Gamma)^2} \ . \tag{5.5}$$

By integrating this acceleration we take into account the changing Doppler shift during the acceleration.

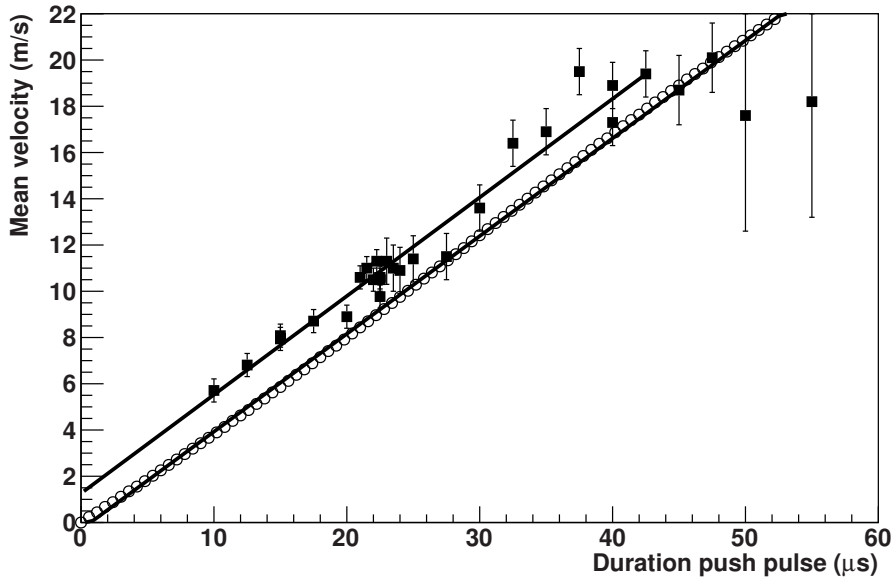

Figure 5.7: *The mean speed of the pushed atoms as function of the push beam duration (squares) and the numerical calculation (circles). The linear fits determine the acceleration and the offset in velocity.*

We compare this to the measurements shown in figure 5.7 for a push power of 14 mW. A linear fit to the data results in an offset velocity of 1.3 ± 0.4 m/s and an acceleration of $4.3 \pm 0.2 \cdot 10^5$ m/s^2. For the calculated data we find an acceleration of $4.2 \cdot 10^5$ m/s^2 and an offset velocity of -0.3 m/s. The acceleration found experimentally agrees well with the calculated value. The origin of the offset is not known. It might be related to movement of the MOT cloud during the extinction of the MOT laser intensity, or due to an overall time delay of 3 μs in the electronics.

Dependence of the push velocity on the push beam intensity

The acceleration depends on the push power (equation 5.5). In figure 5.8 the experimentally found dependence of the mean velocity on the push beam intensity is shown. The push time was kept constant at 22.5 μs. In section 5.3 we observed an offset in the velocity of the atoms of 1.3 ± 0.4 m/s. The error band of the calculation is due to the uncertainty in the offset velocity. The calculation is in reasonable agreement with the data, although it is on one side of the data. At the highest push power of 14 mW the mean velocity is robust against power fluctuations, the mean velocity changes by 20% while the push power varies between 3 and 14 mW.

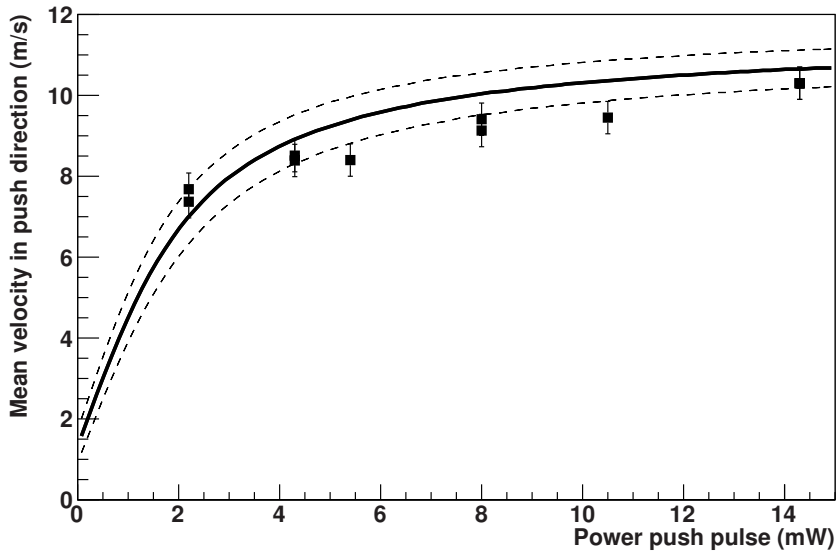

Figure 5.8: *The measurement of the mean velocity of the transferred atoms as function of the push beam intensity with the calculation (curve).*

Velocity spread of the pushed atoms

In figure 5.9 we plot the spread in the longitudinal velocity. The large errors for velocities larger than 12 m/s are due to asymmetry in the arrival signal. Most probably this is due to the asymmetry in the recapture efficiency around these velocities. The lower part of the velocity distribution of the pushed atoms is still recaptured, the higher part less efficient as it exceeds the capture velocity. The origin of the overall large discrepancy is unknown at the moment, the velocity spread is significantly larger than expected. A possible explanation could be that the recapture process effectively broadens the arrival of the atom distribution, *i.e.* that our assumption that the recapture process can be neglected might not be valid (see section 5.2). A more precise determination of the velocity spread will be obtained when the atoms are not recaptured, but are detected for example using a weak adsorption beam [165].

Dependence of the transfer efficiency on the push velocity

The divergence of the atomic cloud after scattering N photons from the push beam is

$$\tan\theta = \frac{\sigma_v}{v} = \frac{1}{\sqrt{3N}}\sqrt{1+\frac{3}{N}\left(\frac{v_0}{v_r}\right)^2} = \frac{\sqrt{v_r}}{\sqrt{3v}}\sqrt{1+\frac{3v_0^2}{vv_r}}. \tag{5.6}$$

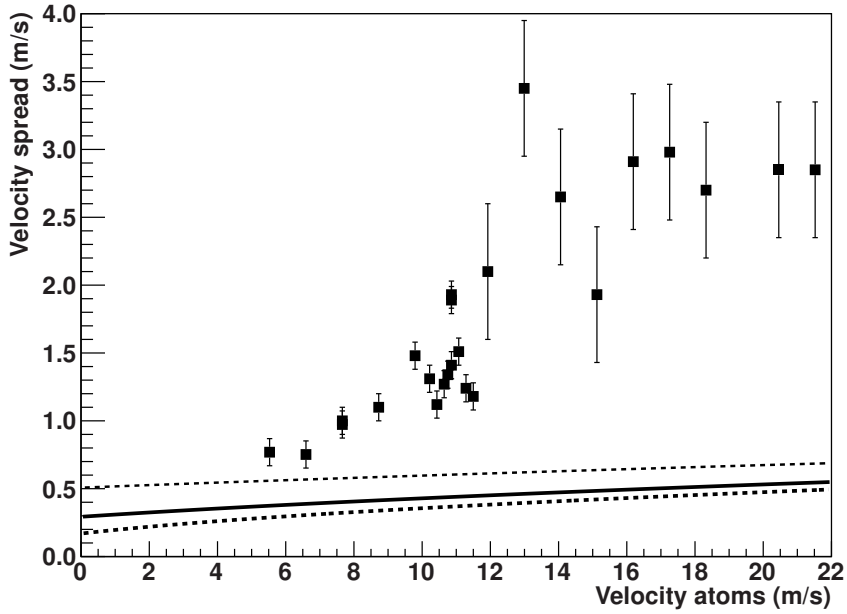

Figure 5.9: *The velocity spread in the push direction. The solid line is the calculation, based on an initial MOT cloud temperature of* 240^{+480}_{-160} *μK and recoil-induced heating from the push beam.*

No extra heating is caused by stimulated emission as only one laser beam is present during the push process [48], therefore we do not pay attention to this mechanism. The atom cloud size after traveling a distance d between the MOTs can be described with the width

$$\sigma_{\mathrm{x}} = \sigma_{\mathrm{y}} = \sigma_{v}\frac{d}{v} = d\tan\theta. \tag{5.7}$$

The fraction of a two dimensional Gaussian beam with a $1/e^2$ diameter a (or $\sigma_x = 1/2a$) through a circle of diameter l is

$$\epsilon_{\mathrm{r}} = (1-\mathrm{e}^{-2(l/a)^2}) \approx 2(l/a)^2 + \mathcal{O}((l/a)^4) = \frac{1}{8}(l/\sigma_{\mathrm{x}})^2 + \mathcal{O}((l/\sigma_{\mathrm{x}})^4)\,. \tag{5.8}$$

So in leading order in l/σ_{x} the transfer efficiency is

$$\epsilon_{\mathrm{r}} = \frac{1}{8}\left(\frac{l}{d}\right)^2\left(\frac{3v}{v_{\mathrm{r}}}\right)\frac{1}{\left(1+\frac{3v_0^2}{vv_{\mathrm{r}}}\right)}\,, \tag{5.9}$$

The difference which can be expected based on their mass and wavelength between ^{23}Na and the other alkaline atoms is given in table 5.3, the recoil velocity is equal to $h/(m\lambda)$. As the influence of the MOT temperature (assuming the Doppler limit) is

Table 5.3: *The scaling of the transfer efficiency, equation 5.9, with the mass of the push atom, for a fixed push velocity $v = 25$ m/s and a MOT cloud cooled to the Doppler temperature limit. The values for $m\lambda$ are normalized to the value of ^{23}Na.*

Isotope	^{7}Li	^{21}Na	^{23}Na	^{41}K	^{87}Rb	^{133}Cs	^{210}Fr
$m\lambda$	0.40	0.91	1.0	2.3	5.0	8.4	11
$\frac{3v_0^2}{vv_r}$	0.24	0.35	0.35	0.27	0.28	0.27	0.33

more-or-less the same for the alkaline metals and the wavelength is also not much different, the transfer efficiency is indeed larger for larger mass.

In figure 5.10 the transfer efficiency is plotted as function of the velocity of the push atoms. The transfer efficiency is the ratio of the number of trapped atoms in the SC MOT and the number of atoms in the CC MOT which were pushed away. Now we consider what dependence we expect theoretically. The spatial dependence is the fraction of the atomic cloud which falls within the laser trap volume,

$$\epsilon_r = \int \mathrm{d}x \int \mathrm{d}y \frac{1}{2\pi\sigma^2} \mathrm{e}^{-\frac{x^2+y^2}{2\sigma^2}} , \tag{5.10}$$

where σ is the spatial width of the cloud after traveling a distance d. Inserting equation 5.2 we have

$$\epsilon_r = \int_{-R}^{R} \mathrm{d}x \int_{-R}^{R} \mathrm{d}y \frac{v^2}{2d^2\pi\left(v_0^2 + vv_r/3\right)} \mathrm{e}^{-\frac{\left(x^2+\left(y-\frac{1}{2}g\left(\frac{d}{v}\right)^2\right)\right)^2}{2\left(\frac{d}{v}\right)^2\left(v_0^2+vv_r/3\right)}} . \tag{5.11}$$

Here v is the mean push speed and $v_0 = \sqrt{\frac{kT_0}{m}}$ is the velocity corresponding to the initial temperature T_0. The acceleration due to gravity is g, the laser capture area is taken to be a square of R by R. Integrating yields

$$\begin{aligned}\epsilon_r(v, v_0) = &\frac{1}{2}\mathrm{Erf}\left(\frac{Rv}{d\sqrt{2v_0^2 + 2vv_r/3}}\right) \\ &\left(\mathrm{Erf}\left(\frac{(R - \frac{d^2g}{2v^2})v}{d\sqrt{2v_0^2 + 2vv_r/3}}\right) + \mathrm{Erf}\left(\frac{(R + \frac{d^2g}{2v^2})v}{d\sqrt{2v_0^2 + 2vv_r/3}}\right)\right) .\end{aligned} \tag{5.12}$$

This expression describes the spatial dependence of the transfer efficiency function. To include the velocity dependence in the model, we introduce a cut-off velocity with a Lorentzian lineshape with FWHM Γ,

$$\epsilon(v, v_0, v_b, \Gamma) = \epsilon_r(v, v_0)\left(H(v_b - v) + \frac{H(v - v_b)}{1 + \frac{2(\delta-\delta_0)}{\Gamma}}\right) , \tag{5.13}$$

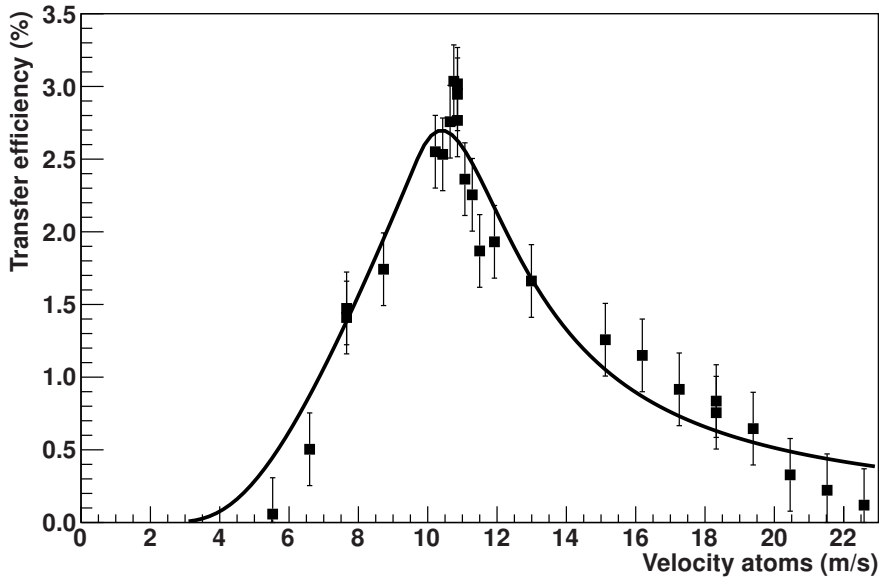

Figure 5.10: *The transfer efficiency measurement, the data is fitted with equation 5.13 with* $R = 15$ *mm.*

with $H(v)$ the Heaviside step function. The cutoff velocity v_b is a lower bound for the capture velocity, as the maximum transfer efficiency is higher. The fit parameter δ_0 is the Doppler shift of the atom.

In figure 5.10 we also show the experimental data. The fit to the data is equation 5.13 with three free parameters. The fit value for the CC MOT cloud temperature is 310 ± 60 μK. The fitted value for the cutoff velocity is 9.6 ± 0.3 m/s, the Lorentzian width is 9 ± 1 MHz.

For the ^{41}K double MOT experiment by Swanson *et al.* [259] we can compare their experimental values and our calculations using equation 5.9. For a distance of 48 cm they report a transfer efficiency of 55 ± 9%. Our model, assuming a MOT cloud temperature of the Doppler limit predicts for this setting 63%. For a distance of 75 cm they find 40 ± 5%, our calculation is 33%. For the same distance the push beam is aligned 8 mm below the MOT and due to the worse overlap the efficiency drops to 21 ± 3%, where we expect 23%.

We conclude that the calculations of the model agree well with the experimental data for the push speed and the transfer efficiency. The observed velocity spread in the push direction is significantly higher than expected, but this most probably due to the detection method. Maximally 2.7 ± 0.5% is transferred at a push velocity of 10.5 m/s. Both the capture velocity of the receiving SC MOT as well as the transverse

temperature of the pushed atom cloud currently limit the transfer efficiency.

In section 2.5 we presented a model which allows us to calculate the capture velocity of a MOT system. We apply the method here to the SC MOT system. We use an effusive oven as a source of atoms and determine the loading rate of the MOT as well as the vapor pressure of sodium. For the SC MOT the time constant to trap $8 \cdot 10^4$ atoms is 3.7 s. The MOT lifetime is 5.3 s when the atom source is off and the MOT is loaded from the push beam. The number of trapped atoms is thus a factor of 3 lower due to the background collisions other than Na (equation 2.13). The temperature of the source is estimated to be about 50 °C. Equation 2.21 gives then a calculated capture velocity of 7 m/s and a collision cross section of $\sigma = 15 \cdot 10^{-14}$ cm^2. The value for the capture velocity is considerable lower than the 10.5 m/s we found as the optimal value for the transfer.

For Na it might be that the value for σ is actually larger than calculated (see table 2.1). Setting σ to $100 \cdot 10^{-14}$ cm^2 gives $v_c = 10$ m/s, in good agreement with the optimal push velocity of 10.5 m/s we observe here.

Transverse cooling of the pushed atoms

In figure 5.2 we already gave an outlook on the discussion about transverse cooling. The upper band in that figure indicates the $1/e^2$ diameter of the atom cloud at the SC MOT position as function of the push speed of the atoms for a transfer distance of 69 cm. The bands represent the three initial MOT cloud temperatures, higher temperatures correspond to larger atom cloud sizes.

The lower band indicates what would happen with a transverse cooling stage after 22 cm, bringing the transverse temperature back to the initial value and compressing spatially to a zero cloud size. The dashed line indicates the 17 mm laser beam diameter of the SC MOT, for this diameter the transfer efficiency is plotted on the right axis. A smaller cloud size corresponds to a higher transfer efficiency.

Higher transfer efficiencies can clearly be obtained by applying transverse cooling. To achieve a 60% transfer efficiency a capture velocity of 25 m/s and a laser beam diameter of 10 mm are sufficient. To achieve a 50% transfer efficiency for ^{21}Na, the transfer efficiency for ^{23}Na has to be about 55%, see table 5.3. As other factors are more uncertain we ignore this 10% effect here. By comparing figure 5.11b to figure 5.11a it is clear that transverse cooling and spatial compression would improve the transfer efficiency drastically.

We tried to improve the transfer efficiency by using the funnel, see figure 5.12 for the result. We observe an improved transfer efficiency of about a factor of 2 over the highest efficiency of about 2.7% obtained in section 5.3. Note that about 20% can be expected here, see figure 5.2. The magnetic field gradient of the funnel quadrupole coil was 8.0 Gauss/cm (both axes). For the funnel magnetic the correction coils were necessary and were producing an offset field of 1.5 and 1.4 Gauss, respectively. The peak laser beam intensity ($1/e^2$ diameter of about 95 mm) was 40 μW/cm^2 (a factor of 300 below saturation intensity), the beam was limited by the viewports of 38 mm. The laser light was on for 35 ms in the funnel section and the push time was 22.5 μs.

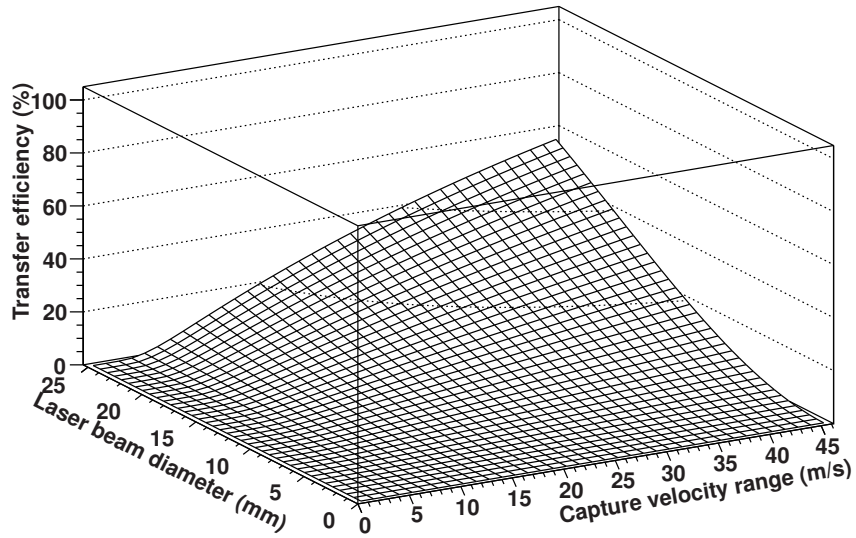

(a) *Transfer efficiency for a push beam.*

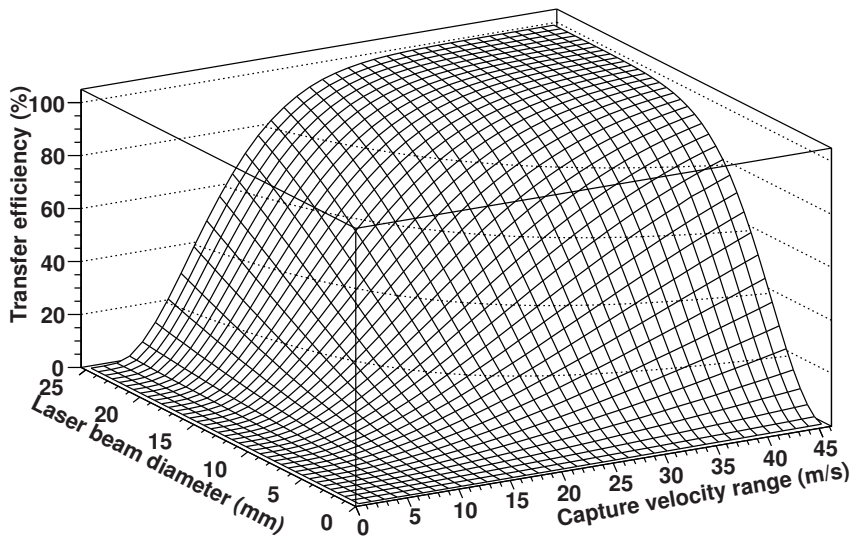

(b) *Push beam and after 22 cm transverse cooling to 240 μK and spatial compression.*

Figure 5.11

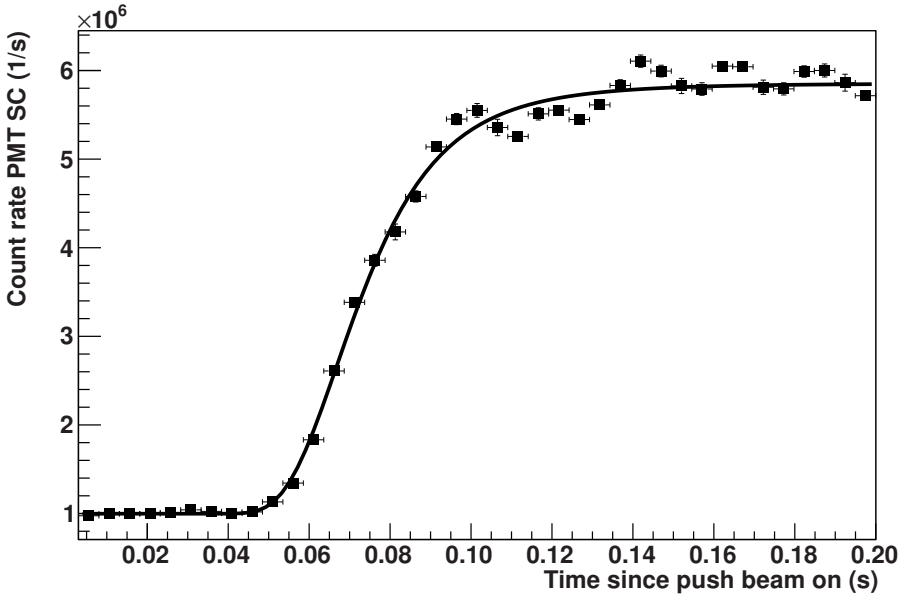

Figure 5.12: *A first attempt to improve the transfer efficiency using the funnel. The data is fitted with equation 5.3. The fit parameters are tabulated in table 5.4.*

Table 5.4: *Summary of the data in figure 5.12.*

Observable	Value
Background count rate	$998 \pm 4 \cdot 10^3$ 1/s
Mean velocity v	9.5 ± 0.1 m/s
Velocity spread σ	2.1 ± 0.1 m/s
Number of trapped atoms SC MOT N_{SC}	$2.9 \pm 1 \cdot 10^4$
Number of pushed atoms CC MOT N_{CC}	$6.2 \pm 2 \cdot 10^5$
Transfer efficiency $\epsilon = N_{SC}/N_{CC}$	$4.8 \pm 1.3\%$

The efficiency critically depended on the laser power, going higher decreased the efficiency. We could not check whether we could improve on this point using a different combination of magnetic quadrupole field, offset fields and laser power, as with the funnel the transfer was not stable enough.

For this push speed, the atom cloud diameter at the position of the funnel (at 22 cm) is about 35 mm, see figure 5.2. The magnetic field at this radius was thus about 13

Gauss (equation 3.4), the corresponding Zeeman shift is about 19 MHz. The photons scattered per atom per beam were, using equation 2.1, at this radius maximally about 300 photons and in the center about 20 photons. A 10% inbalance in the scattering rate per beam results then at the SC MOT position in a net displacement of 3 mm to 6 cm, which is considerable compared to the atom cloud size of about 11 cm. The size of the magnetic field correction also gives in indication. In both directions about 1.5 Gauss had to be applied, which corresponds to a 3 MHz Zeeman shift. At the SC MOT position this results in a displacement of about 4 cm, which is also considerable.

We conclude that the improvement in the transfer efficiency might indeed be attributed to (a combination of) cooling and spatial compression in the funnel stage. There are also clear indicators that the funnel is operating far from optimal and might be unbalanced. This might be due to power imbalances, the degree of circular polarization, misalignment or offsets in the magnetic field.

5.4 Conclusions

For a resonant push beam, the push beam parameters (detuning, intensity, duration) essentially only influence the push velocity of the atoms. The present double MOT transfer efficiency over a distance of 69 cm is $2.7 \pm 0.5\%$, for a push speed of 10.5 m/s. Our calculations for the expected transfer efficiency are in good agreement with this value as well as transfer efficiency measurements from another experiment. In a first attempt with a funnel we improved the transfer efficiency to $4.8 \pm 1.3\%$, with more effort about 20% can be reached.

Two essential steps have to be made to achieve a 50% transfer efficiency: increasing the capture velocity of the receiving MOT and transverse cooling of the pushed atom cloud using the existing funnel setup. It is feasible to increase the capture velocity of the SC MOT to 25 m/s, as Marcassa *et al.* showed for our conditions a capture velocity of 27 m/s [159, 161]. The present funnel setup has to be carefully balanced and aligned to achieve proper cooling and spatial compression. When the funnel has been characterized, the quadrupole field gradient can be generated by permanent magnets instead of the present hairpin configuration to simplify the setup, see section 3.7.

Another possibility, that we learned about during the final phase of this research, is to duplicate the successful approach used by Rowe *et al.* [68] at Berkeley for their ^{21}Na experiment (see also section 2.9). Instead of using a funnel to enhance the transfer efficiency, they used a magnetic guide created by three permanent magnets. In this way 80% transfer efficiency over 51 cm was achieved, for a push velocity of 11 m/s. To implement this scheme, permanent magnets have to be installed along our transfer line. The quadrupole field of the collector MOT has to be quickly switched off and a small bias magnetic field has to be switched on. A circular polarized push laser beam optically pumps the atoms to a low field seeking magnetic substate. When the adiabatic conditions are fulfilled, the magnetic moments follow the changing magnetic field when entering the magnetic guide. For for example a hexapole configuration the

magnetic field is zero in the center and increases radially. The atoms are therefore confined during the transfer process.

With a very simple measurement scheme the escape velocity of the CC MOT, which is proportional to the capture velocity (equation A.5), can be determined using our push beam method. The capture velocity dependence of the MOT on detuning, intensity and laser diameter can be deduced in this way. Knowledge of the capture velocity is beneficial for achieving a high transfer efficiency as well as for achieving a high collection efficiency, as discussed in chapter 2 and chapter 4.

CHAPTER 6

Conclusions and outlook

6.1 Steps towards β-decay correlation measurements in ^{21}Na

A high-precision measurement in β-decay is one of the possibilities to search for physics beyond the Standard Model (SM) of particle physics. A measurement of various correlations parameters of the ^{21}Na decay with a precision of 10^{-4} will result in competitive constraints on some possible extensions of the SM. In addition, the study of β-decay of mirror nuclei adds to a more precise determination of the V_{ud} quark mixing matrix element [17].

We reviewed the status of different β-decay experiments in chapter 1. Our conclusion is that for studying β-decay, trap experiments have most potential as they offer a point-like source and are substrate free. Contrary to experiments which do not use particle traps, systematic effects do not yet limit the precision. However, the difficulty of trap experiments is on acquiring statistics.

To obtain sufficient trapped ^{21}Na atoms, we use a dual Magneto Optical Trap (MOT) system which is coupled to the TRIμP production and separation facility. In the first MOT system the ions are neutralized and are trapped after being evaporated. The atoms are then transferred to the second MOT, which provides a background free environment for the β-decay correlation measurements.

The aimed precision of 10^{-4} for the measurement of the correlations results in an efficiency budget for the production, collection, transfer and the β-decay detection stage. In this thesis we focus on how to achieve for ^{21}Na a collection efficiency of 1% for the first trap and for the trapped atoms a transfer efficiency of 50% into the second trap. Besides experiments with ^{21}Na, commissioning experiments have been done using the stable ^{23}Na isotope.

6.2 Collection efficiency of ^{21}Na and ^{23}Na

In chapter 2 we discussed the relevant processes for the collection efficiency of a MOT system in detail. The collection efficiency is the product of three independent

parameters: the single pass capture efficiency of the MOT, the average number of times the atoms pass the trap volume and the ion-to-atom conversion efficiency. In chapter 4 we discussed the experiments determining the collection efficiency and identified possible improvements.

The crucial factor for the capture efficiency is the capture velocity v_c, the velocity with which an atom is still captured by the MOT. The collection efficiency of the first MOT system scales with v_c^3. In the transfer scheme we implemented, the transfer efficiency depends linearly on the capture velocity of the second MOT system. For the current implementation the efficiency for the final experiment thus depends on v_c^4, when v_c is equal for both MOT systems. Therefore maximizing v_c is of the utmost importance to achieve the envisioned collection efficiency of 1% and the transfer efficiency of 50%.

We find that the capture velocity for various MOT systems is rarely reported (chapter 2). Using only some basic experimental observables and a simple theoretical model, an estimate of the capture velocity can be obtained. The necessary model for the capture and loss rate, respectively, were separately tested against experimental data from literature. We found good agreement for both and compiled a table of capture velocities for alkaline MOTs loaded from a vapor. From this overview we concluded that Na has from all alkaline elements the least potential to be captured efficiently. The explanation for this can be found in the details of the level structure, which is unique among the alkaline elements.

When the atoms are not slowed and trapped by the MOT, they collide with the cell wall and, with a high probability, stick to it. A non-stick coating prevents this. We found that for heavier alkaline elements the requirements for the coating quality might be less stringent than for the lighter elements. The geometry of the collector cell should allow for a large number of trap passages. We performed a Monte Carlo simulation to determine the number of bounces and trap passages for a cell with a cubic shape. We compared with predictions for another experiment studying the bouncing process and found good agreement.

We upgraded the collector MOT setup at two points: by replacing the laser system and the glass cell. A stable solid-state based laser system, which produces up to 2.5 W of light, provides now the cooling light for the experiment. The glass cell shape is a cube with sides of 6 cm, Monte Carlo simulations show that its shape allows "geometrically" about 500 bounces.

To characterize our MOT system we performed offline measurements with ^{23}Na. A thin neutralizer foil made of zirconium was used to catch the ion beam. By heating the neutralizer foil periodically the atoms were released. To distinguish between ^{23}Na just deposited and already present the ion beam is not present in all cycles. Using an analytical model to describe the time dependence of the MOT signal, we find that 40% of the implanted ions were released within two seconds at a temperature of about 1100 K, in good agreement with the results found by other research groups.

We observed that Doppler background fluorescence from ^{23}Na atoms can mimick a trap signal in the case of ^{21}Na. For our ^{21}Na trap signal the contribution of fluorescence

rate from untrapped ^{23}Na atoms is about a factor of 10 smaller than the optical signal itself and could be neglected.

With the combination of the cubic cell and the new laser system we observed for the first time in our experiment an optical signal from about 30 simultaneously trapped ^{21}Na atoms. At the end of chapter 4 we summarize all findings in table 4.9. The MOT collection efficiency of $(4 \pm 2) \cdot 10^{-4}$, determined using a ^{23}Na ion beam, is consistent with the value we deduced from measurements with the radio-active ^{21}Na. For ^{23}Na the overall efficiency of the setup, defined as the fraction of ions which is trapped once in the MOT, is currently $(5 \pm 2) \cdot 10^{-5}$. The three main conclusions, based on the experiments for the collection stage, described in chapter 4, are that :

- Preparation for the efficient trapping of ^{21}Na can be done with a stable ^{23}Na ion beam from the Thermal Ionizer.
- The collection efficiency of the collector cell MOT is currently the bottleneck towards reaching our goal of a 1% total collection efficiency.
- To achieve a factor of 100 higher collection efficiency the quality of the anti-stick coating can and must be improved. This will result in 1% MOT collection efficiency and an overall efficiency of about 0.5%.

Table 4.11 compares our experiment to other high efficiency MOT experiments utilizing radioactive isotopes. The overall conclusion is that by improving the number of trap passages (and thus the number of bounces) a state-of-the-art overall efficiency can be achieved.

The ion transport efficiency might be increased by replacing the drift tube with the RFQ. Some increase in the single-pass capture efficiency can be expected by increasing the laser intensity with a factor of 5, which is possible with the new powerful laser system.

6.3 Double MOT transfer of ^{23}Na atoms

To reduce background the trapped ^{21}Na atoms need to be transferred over a distance of 69 cm from the collector MOT chamber to the science MOT chamber. A literature study shows that for the efficient transfer atoms between two MOTs five types of approaches have been used (chapter 2). We chose to push the atoms with a pulsed near-resonance laser beam towards the second MOT system. To enhance the transfer efficiency we installed a two dimensional MOT (funnel), which cools and compresses the pushed atomic cloud halfway the transfer line.

We achieved a transfer efficiency of $2.7 \pm 0.5\%$ over a distance of 69 cm, using a push velocity of about 10 m/s (chapter 5). The transfer efficiency scales - in leading order - linearly with the push velocity (and hence the capture velocity v_c) of the receiving MOT system. In a first attempt to improve the transfer efficiency using the funnel, we improved the transfer efficiency with a factor of 1.8 to $4.8 \pm 1.3\%$.

In essence, two steps have to be made to achieve a 50% transfer efficiency between the two MOT systems:

- Increase the capture velocity v_c from the receiving MOT from 10 m/s to 25 m/s.
- Carefully balance the intensity of the funnel laser beams.

The low capture velocity of the current receiving MOT system is probable due to its single beam design. Using a standard configuration of three retro-reflected beam pairs, which has been setup but has not been used yet, will result in a larger capture velocity. Under similar conditions a capture velocity of 27 m/s has been demonstrated for Na in another experiment, thus an increase of the capture velocity to 25 m/s is feasible.

The present funnel setup, which is probably inbalanced and therefore underperforms, has to be carefully balanced and aligned. Even with the present push velocity of about 10 m/s, a transfer efficiency of about 20% is then possible. When commissioned, the funnel section can be simplified by using permanent magnets to generate the quadrupole field, instead of using electromagnets.

Currently the push velocity has to be high to prevent that the pushed atom cloud expands to a cloud larger than the laser beams of the second MOT system. A permanent magnetic guide would prevent this and close to 100% of the atoms can expected to be transferred. The main advantage is the simplicity and stability of the guide system and that this scheme is very frugal with laser power. To implement this scheme the following has to be done:

- Install a permanent hexapole magnetic guide along the transfer path.
- Push the atoms and spin polarize the sample.

6.4 Conclusion

This thesis describes two crucial steps towards the realization of a high-precision test of the Standard Model of particle physics at low energy. The time-reversal symmetry of the Standard Model can be tested by measuring correlations between the particles emerging from decaying radioactive atoms. At the Kernfysisch Versneller Instituut such a test will be performed with radioactive ^{21}Na (sodium) atoms. To achieve a high accuracy, the atoms are brought to nearly standstill by trapping them with laser light.

First, to reach the required precision in the final measurement, the online produced ^{21}Na ions have to neutralized and trapped with 1% efficiency. Second, the trapped ^{21}Na atoms need to be transferred with near unit efficiency to a second atom trap, which provides a shielded environment for the correlation measurements. As this thesis shows, both envisioned efficiencies are within reach of the present setup.

Nederlandse samenvatting

In 1874 informeerde de 16-jarige Max Planck, die in dat jaar aan een studie natuurkunde aan de universiteit van München begon, bij professor Philipp von Jolly naar de vooruitzichten voor het veld van de natuurkunde. Het antwoord dat hij kreeg gaf goed de tijdgeest weer:

> "(...) schilderte mir die Physik als eine hochentwickelte, nahezu voll ausgereifte Wissenschaft (...) Wohl gäbe es vielleicht in einem oder dem anderen Winkel noch ein Stäubchen oder ein Bläschen zu prüfen und einzuordnen, aber das System als Ganzes stehe ziemlich gesichert da, und die theoretische Physik nähere sich merklich demjenigen Grade der Vollendung, wie ihn etwa die Geometrie schon seit Jahrhunderten besitze."*

De jonge Planck liet zich gelukkig niet ontmoedigen door dit toekomstperspectief en antwoordde dat hij geen nieuwe dingen hoefde te ontdekken, hij wilde de bestaande fundamenten van de natuurkunde beter bestuderen. Planck zou in 1918 de Nobelprijs krijgen voor zijn bijdragen aan de kwantummechanica, een baanbrekende theorie die het gedrag van deeltjes op kleine schaal (gekarakteriseerd door de Planck constante) beschrijft.

Nu, 138 jaar later, ligt de situatie volkomen anders. De natuurkunde bevindt zich al dertig jaar in een ernstige crisis. Astronomische waarnemingen uit 1970 toonden namelijk aan dat slechts 4% van de massa en energie in het universum bestaat uit voor ons bekende deeltjes. De overige 96% bestaat uit mysterieuze donkere materie en energie.

Het fundament van de huidige natuurkunde wordt gevormd door vier krachten. Het "Standaardmodel" verenigt drie van deze krachten in één enkele beschrijving.

*Uit [296]. Vrij vertaald: "(...) schilderde mij de natuurkunde als een hoogontwikkelde, bijna volledig gerijpte wetenschap (...) Waarschijnlijk zou er hier en daar nog wat uit te zoeken zijn, maar het systeem als geheel is solide en de theoretische natuurkunde benadert merkbaar de graad van compleetheid, zoals bijvoorbeeld de geometrie deze al sinds eeuwen bezit."

De eerste kracht betreft de wisselwerking tussen elektrisch geladen deeltjes (elektromagnetisme). De tweede kracht zorgt voor het radioactieve verval van deeltjes, zoals dat bij een radium deeltje plaatsvindt. De derde kracht vormt bindingen tussen geladen quarks, elementaire deeljes waaruit protonen en neutronen zijn opgebouwd. De neutronen en positief geladen protonen vormen de kern van een atoom. Om de kern heen bewegen negatief geladen elektronen. Voor een neutraal atoom is het aantal electronen gelijk aan het aantal protonen. Het Standaardmodel heeft uiterst nauwkeurige experimentele testen van elk van deze drie krachten doorstaan.

De algemene relativiteitstheorie van Albert Einstein beschrijft de bekendste, vierde kracht: de zwaartekracht. Het blijkt vanwege diepgaande redenen onmogelijk het Standaardmodel uit te breiden met de zwaartekracht. Een nieuwe, overkoepelende theorie, die alle vier de krachten beschrijft, zal nieuwe deeltjes en krachten introduceren. Deze zouden ook de bron zijn van de donkere materie en energie kunnen zijn. Er zijn een groot aantal verschillende benaderingen en kandidaattheorieën die claimen de huidige problemen te kunnen oplossen.

Eén van de mogelijke manieren om onderzoek te doen naar de vraag, welke van de nieuwe theorieën de juiste is, is door precisiemetingen te doen aan het radioactieve verval van natrium 21 (^{21}Na) atomen[†]. Deze metingen aan het tweede type kracht kunnen licht werpen op schending van fundamentele symmetrieën. De mate van schending van deze symmetrieën is verschillend voor de kandidaat opvolgers van het Standaardmodel en de relativiteitstheorie. Op deze manier kan er onderscheid worden gemaakt tussen theorieën of ze worden minder ingeperkt in hun keuze van bepaalde constantes.

In het ^{21}Na experiment is het doel om nauwkeurig correlaties tussen de vervalsprodukten te meten, die vrijkomen bij het radioactieve verval van het ^{21}Na atoom. Deze vervalsprodukten zijn een neutrino (een neutraal deeltje met een zeer kleine of zelfs geen massa) en een positief geladen electron: een positron. Het positron kan makkelijk worden gedetecteerd. Detectie van het neutrino is zeer lastig, daarom zal de richting en snelheid (de impuls) van dit deeltje indirect worden gemeten. De snelheden van de vervalsprodukten zijn groot vergeleken bij de initiële snelheid van het ^{21}Na atoom in een atoomval. Omdat bij het ^{21}Na bijna stil staat als hij vervalt is de impuls nagenoeg nul. Vanwege het behoud van impuls is de impuls van het neutrino deeltje dan te bepalen door én de impuls van het positron én van de dochterkern te meten.

Dit proefschrift beschrijft de voorbereidende stappen van een dergelijk experiment. Om een hoge precisie te bereiken in metingen worden radioactieve atomen ingevangen in een atoomval. Deze atoomval bevindt zich in vacuüm en bestaat uit een combinatie van zes laserbundels en een magneetveld. Voor een dergelijk precisie-experiment is het noodzakelijk dat er genoeg ^{21}Na atomen beschikbaar zijn om het experiment mee te doen. Het belangrijkste concept in dit proefschrift is dan de efficiëntie van de

[†]Elementen verschillen in het aantal protonen. Isotopen van een element verschillen in het aantal neutronen van elkaar. Het getal bij een isotoop geeft de som van het aantal protonen en neutronen aan.

processen waarbij de radioactieve deeltjes bij betrokken zijn: de fractie van de deeltjes die een proces ingaan en overblijven in de juiste toestand.

De hoogste productiesnelheid van de radioactieve ^{21}Na deeltjes, zoals we die op het KVI kunnen bereiken, is relatief laag voor onze doeleinden. De invangstefficiëntie in de eerste atoomval, de transportefficëntie naar een tweede atoomval en de detectie effiëntie van het verval bepalen samen of het mogelijk is om een experiment te doen binnen een realistisch tijdplan. Het doel van dit proefschrift is het vaststellen van en het zo hoog mogelijk maken van twee efficiënties: de invangstefficiëntie in de eerste atoomval en de transportefficiëntie van de eerste naar de tweede atoomval[‡]. De gewenste invangstefficiëntie van de atomen is 1%, voor het transport is dit 50%. Dit moet met deze efficiënties gebeuren om het experiment binnen een paar dagen met de gewenste precisie te kunnen doen, met de productie methode zoals die we op het KVI gebruiken.

De ^{21}Na deeltjes worden geproduceerd door een bundel snelle neon 20 (^{20}Ne) deeltjes uit de AGOR versneller van het Kernfysisch Versneller Instituut (KVI) te laten botsen met cel gevuld met deuterium gas (waterstof met één extra neutron). Omdat we alleen geïnteresseerd zijn in de ^{21}Na deeltjes, is de eerste stap na de productie het uit elkaar halen van de verschillende soorten deeltjes die ontstaan bij de botsingen. Dit gebeurt in de magnetische scheider van de TRIμP onderzoeksfaciliteit[§].

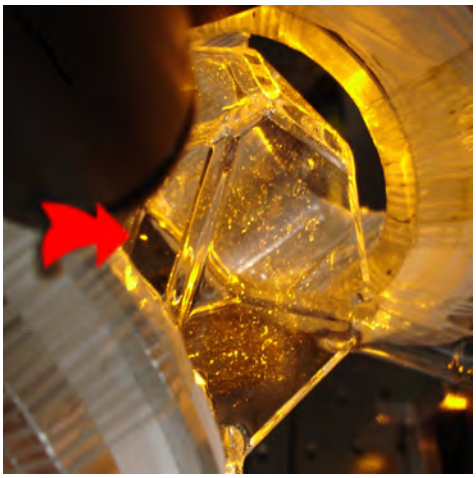

Figuur 6.1: *Een koud wolkje gevangen Na atomen (het gele stipje, aangegeven door de rode pijl) in de glazen kubus. Linksboven een gedeelte van het detectiesysteem dat het licht, uitgezonden door de atomen verzamelt. Linksonder en rechtsboven zijn de twee spoelen te zien die het magneetveld maken.*

De ^{21}Na deeltjes hebben een dusdanig hoge snelheid, dat ze sterk afgeremd moeten worden voordat we ze kunnen invangen met het laserlicht in de atoomval. Ook zijn ze nog geladen (ionen), terwijl de atoomval alleen neutrale deeltjes kan invangen. Door de ^{21}Na deeltjes, die nog een zeer hoge snelheid hebben, door een stapel van dunne wolfraam folies te schieten worden ze tot stilstand gebracht in één van de folies. De folies van wolfraam zijn erg dun, een duizendste van een millimeter. Door de hoge temperatuur van 2500 °C bewegen de deeltjes relatief snel in de folies. Op een gegeven moment komen ze aan het oppervlak tevoorschijn.

[‡]De behandeling van de derde efficiëntie kan worden gevonden in het binnenkort te verschijnen proefschrift van Duurt Johan van der Hoek [18].

[§]TRIμP staat voor Trapped Radioactive Isotopes: μlaboratories for Fundamental Physics.

De deeltjes moeten nu nog naar de opstelling getransporteerd worden. Dit kan vrijwel zonder verliezen gebeuren als ze als ionen worden getransporteerd met electrische velden. Bij kamertemperatuur zijn de deeltjes allemaal neutraal geladen. De hoge temperatuur zorgt ervoor dat een paar procent als een enkelvoudig geladen ion het oppervlak verlaat, de rest is neutraal geladen. Latere botsingen met het hete oppervlak geven de deeltjes opnieuw een kans om geïoniseerd te raken. Daarom heet dit onderdeel ook de Thermische Ionisator (TI).

Een elektrisch veld transporteert de ionen bundel met een lage energie 10 meter verderop naar het opstelling met de atoomval voor ^{21}Na. Hier worden de geladen deeltjes in een dun folie, gemaakt van zirconium, geschoten. Verhitting van dit neutralisatie folie tot 800 °C zorgt ervoor dat ongeveer de helft van de geïmplanteerde ^{21}Na deeltjes als neutraal geladen atoom wordt verdampt.

De verdampte atomen zijn nu beschikbaar gemaakt in de vorm van een neutraal gas, deze kunnen ingevangen worden in de eerste atoomval. De atoomval bestaat uit een glazen cel in de vorm van een kubus. In elk van de drie assen van de kubus schijnen er twee laserbundels in tegengestelde richting door de vlakken van de kubus naar binnen. Door botsingen van de lichtdeeltjes (fotonen) in de laserbundels worden de atomen afgeremd. Een plaatsafhankelijk magnetisch veld zorgt ervoor dat de atomen zich verzamelen in één puntje in het midden. Het wolkje gevangen atomen is duidelijk met het oog te zien als een lichtgevend puntje omdat ze laserlicht verstrooien, zie figuur 6.1.

De temperatuur van de gevangen deeltjes is ongeveer een milli Kelvin. Dit is een duizendste van een graad Celsius boven het absolute nulpunt van de temperatuurschaal, -273.15 °C. De snelheid van de atomen is ongeveer 1 m/s. Ter vergelijking, bij kamertemperatuur is de snelheid zo rond de 500 m/s. Er is dus een hele goede isolator nodig om de gevangen atomen zo koud te houden. Dit wordt bereikt door de hele glazen kubus op vacuüm te houden. De druk is ongeveer 10^{12} keer minder dan de normale luchtdruk van 1 bar. Vanwege het vacuüm kunnen de moleculen in de lucht geen warmtetransport meer verzorgen tussen de warme glaswand en de koude atomen.

In dit hele proces van het invangen van atomen is het belangrijk dat zo veel mogelijk atomen die van het neutralisatie folie afkomen, uiteindelijk in de atoomval worden ingevangen. De meting van de totale efficiëntie waarmee dit plaatsvindt is de eerste van de twee zwaartepunten van dit proefschrift.

De atoomval met laserlicht is 25 jaar geleden voor het eerst gedemonstreerd, maar er is relatief weinig bekend over het efficiënt invangen van atomen. De reden hiervoor is dat verreweg de meeste experimenten stabiele deeltjes invangen. De deeltjesstroom van de bron is in deze gevallen praktisch onbegrensd en de efficiëntie is dus niet zo belangrijk. In ons geval is dit vanwege de beperkte productiesnelheid van radioactieve atomen fundamenteel anders.

De effiëntie van een atoomval is de fractie van de atomen die ingevangen wordt vanuit een stroom inkomende atomen. Deze effiëntie is gerelateerd aan de maximale snelheid van het atoom die de atoomval kan afremmen en dan gevangen kan houden. Bij kamertemperatuur hebben verreweg de meeste atomen een snelheid die veel hoger

ligt dan deze snelheid. Onder typische omstandigheden worden daarom maar 1 op de 100 000 atomen ingevangen in een atoomval.

Om de eigenschappen van de atoomval beter te kunnen bestuderen hebben we twee theoretische modellen met elkaar gecombineerd: een model voor de invangst en een model voor het verlies van atomen. Voor de invangst hebben we met behulp van de computer Monte Carlo berekeningen uitgevoerd die het invangstproces simuleren. In het model van het invangstproces komt een aantal statistische waarschijnlijkheidsverdelingen voor. In een Monte Carlo berekening wordt het effect hiervan op de uitkomst bestudeerd door een groot aantal scenario's door te rekenen. De variabelen worden volgens deze waarschijnlijkheidsverdelingen gekozen. We vinden een goede overeenkomst tussen de uitkomsten van de simulaties en metingen van een onderzoeksgroep uit Vancouver, Canada.

Het andere gedeelte betreft het verlies van de atomen, nadat ze zijn ingevangen in de atoomval: ze blijven niet voor altijd gevangen. De koude atomen botsen met ongevangen atomen die kamertemperatuur hebben, dit kan ertoe leiden dat het atoom uit de atoomval verloren gaat. Een eenvoudig model dat botsingen tussen het achtergrond gas en de gevangen atoom beschrijft, laat een goede overeenkomst zien met experimentele data afkomstig van een onderzoeksgroep uit Ferrara, Italië.

Natrium is één van de vijf stabiele alkalimetalen, dit is groep elementen die chemisch op elkaar lijken: ze hebben een gesloten elektronenschil met één vrij elektron[¶]. Met behulp van de twee modellen voor invangst en verlies hebben we een vergelijkend overzicht kunnen maken van atoomvallen die verschillende alkalimetalen gebruiken. We hebben aanwijzingen gevonden dat het natrium atoom lastiger in te vangen is dan de andere alkalimetaal isotopen. De oorzaak hiervoor ligt waarschijnlijk in de details van het natrium atoom, die uniek zijn vergeleken met de isotopen van de andere alkalimetalen.

Om de invangstefficiëntie te verbeteren is de glazen cel aan de binnenkant bedekt met een dun laagje, op was lijkende, stof. Hierdoor blijven de atomen bij een botsing met de wand niet plakken maar stuiteren ze terug van het oppervlak. De vorm van de cel bepaalt dan hoe vaak de atomen in totaal een kans hebben om ingevangen te worden in de atoomval. Aan de hand van Monte Carlo simulaties hebben we een nieuwe glazen cel, in de vorm van een kubus ontworpen. Dit ontwerp staat toe dat de atomen ongeveer 500 keer stuiteren voordat ze definitief verloren gaan door één van de twee toegangsbuizen (in- en uitgang van de deeltjes) aan de cel.

Met behulp van deze nieuwe cel en een nieuw, stabieler en krachtiger lasersysteem hebben we voor de eerste keer in dit experiment radioactieve ^{21}Na atomen weten vangen in de atoomval. De invangsteffiëntie laat echter zien dat de anti-plak laag nog niet goed werkt. Door de kwaliteit van de anti-plak laag te verbeteren kan deze efficiëntie met een factor 100 verbeterd worden.

Naast het efficiënt invangen van atomen, beschrijft dit proefschrift ook het transport van atomen tussen twee atoomvallen: dit is het tweede zwaartepunt. Voor het ^{21}Na

[¶]In het periodieke systeem kunnen de alkalimetalen gevonden worden in het meest linker kolom (uitgezonderd waterstof, dit is geen alkalimetaal).

experiment is een dergelijk transport noodzakelijk om de juiste omstandigheden te creëren voor de precisiemeting. We hebben de stabiele variant van natrium atoom weten te transporteren over een afstand van 69 cm[‖]. De gevangen atomen in de eerste atoomval werden versneld door middel van een korte puls van laserlicht. Door de lengte van de laserpuls juist te kiezen gaan de atomen zo snel dat ze nog net ingevangen kunnen worden door de tweede atoomval.

Tijdens het transport dijt de initieel kleine atoomwolk uit tot ze groter is geworden dan de diameter van de laserbundels van de tweede atoomval. Door snelheid van de atomen te verhogen wordt dit effect verminderd, maar dan gaan de weer te snel om weer ingevangen te worden. Om dit probleem te omzeilen hebben we een twee dimensionale versie van een atoomval halverwege de transport sectie geïnstalleerd. Deze optische trechter zorgt ervoor dat de atomen weer bij elkaar worden geduwd en worden afgekoeld in de twee richtingen loodrecht op de transportlijn. Dit leverde een verbetering met een factor twee op, vergeleken met de transportefficiëntie zonder optische trechter.

De huidige transportefficiëntie ligt nog een factor 10 onder de gewenste waarde. De redenen hiervoor kon gevonden worden in de implementatie van de tweede atoomval, deze is verbeterd. Dat dit daadwerkelijk de beperkende factor is geweest zullen nieuwe metingen nog aan moeten tonen.

Dit proefschrift bestudeert het efficiënt invangen en transporteren van Na atomen om een precisie-experiment van het β-decay van ^{21}Na mogelijk te maken. Er zijn een aantal veranderingen aan de opstelling doorgevoerd om de beoogde 1% invangstefficiëntie en 50% transportefficiëntie te halen. Metingen laten zien dat de beoogde doelen nog niet zijn gehaald. Om de invangstefficiëntie te verhogen met een factor 100 moet de kwaliteit van de anti-plak laag worden verbeterd, dit is ook haalbaar. Er is beter inzicht verkregen in de onderliggende processen en mechanismen die voorkomen bij het efficiënt invangen en het efficiënt transporteren van atomen met laserlicht. Daarmee komt een precisiemeting aan het verval van ^{21}Na, dat licht kan werpen op het ontstaan van het heelal, weer twee stappen dichterbij.

[‖]De eigenschappen van het stabiele natrium 23 (^{23}Na) atoom zijn identiek aan die van het radioactieve ^{21}Na atoom, alleen de benodigde laserfrequentie voor de atoomval is verschillend.

Dankwoord

Het motto van de Rijksuniversiteit Groningen is ‘Werken aan de grenzen van het weten’. Als promovendus loop je op weg naar deze grenzen zowel op het professionele vlak als op het persoonlijke vlak snel tegen andere grenzen aan, die ook overwonnen dienen te worden. Daarom maak ik in dit gedeelte graag van de gelegenheid gebruik om de mensen te bedanken die mij hebben geholpen en gesteund tijdens dit proces.

Veel dank ben ik mijn promotor Hans Wilschut verschuldigd. Na een vijftal jaren kwam het einde van mijn promotietraject in zicht. Dat hebben we meteen gevierd met een memorabel etentje. Op zijn Gronings gezegd: ‘t kon minder. Bedankt voor je prettige begeleiding van mijn onderzoek, je toewijding en je oog voor detail.

Ik dank ook mijn copromotor, Steven Hoekstra. Eind 2009 keerde je terug uit Berlijn om op het KVI je eigen experiment met moleculen op te zetten. Tevens nam je de dagelijkse begeleiding van mij op je. Je vermogen om snel te kunnen schakelen tussen details en het grotere geheel werkte als katalysator om twee concrete verbeteringen in het ^{21}Na experiment door te voeren: de ingebruikname van een nieuw, krachtiger en stabieler lasersysteem en een glazen cel in de vorm van een kubus. Deze twee verbeteringen zorgden ervoor dat we nu efficiënter dan voorheen atomen kunnen vangen. Ook kon de opstelling beter gekarakteriseerd worden, dankzij de toegenomen stabiliteit van de gehele opstelling. Dank voor je goede en aangename begeleiding.

I thank the members of my reading comittee, Ronnie Hoekstra, Luigi Moi and Christian Weinheimer, for the careful reading of my thesis and your valuable feedback.

Ik bedank ook de TRIμP groepsleider Klaus Jungmann voor alle ondersteuning en de vele natuurkunde die ik van je heb mogen leren. Lorenz, ook jij hebt mij op vele gebieden geholpen en dingen geleerd, hartelijk bedankt hiervoor. Midden in een nacht heb ik als één van de eerste personen ooit een wolkje gevangen barium atomen kunnen aanschouwen: een onvergetelijke ervaring. Ronnie Hoekstra, je hebt mij begeleid bij het opzetten van de optische transportsectie. Verder stond je deur altijd open en daar heb ik dankbaar gebruik van gemaakt. Dank voor alles.

De fundamenten voor het ^{21}Na experiment zijn gelegd door mijn voorgangers Andrey Rochachevskiy, Moslem Sohani en Emil Traykov, jullie ook bedankt voor jullie

werk. Gerco Onderwater: dankzij jou vind ik mijn weg binnen het grote, wonderlijke bos dat ROOT heet. Ook bedankt voor het opzetten en onderhouden van het soepel werkende DAQ systeem (Bogey) waar we binnen TRIμP allemaal dankbaar gebruik van maken. Verder werkt je onuitputtelijke enthousiasme voor alle mogelijk fenomenen erg aanstekelijk. Ik hoop te zijner tijd nog eens in een NWT editie te lezen waarom de natuurkunde 's nachts anders is dan overdag.

Leo Huisman, bedankt voor alle goede (technische) ondersteuning. Zonder jouw vakkundige handen zou de Thermal Ionizer (en TRIμP faciliteit) nooit zo betrouwbaar werken als hij nu doet. Otto Dermois, bedankt voor voor al je hulp, bijvoorbeeld bij de optimalisatie van het ionentransport in de lage energie bundellijn en de funnel sectie. Ronald van Wooning, bedankt voor al je bijdragen, in het bijzonder voor je werk aan de offset lock: deze heeft uitstekend werk verricht. Oliver Böll, bedankt voor je ondersteuning op lasergebied, maar ook voor je inzet tijdens de bundeltijden. De lijst van TRIμP (ex-)collega's is erg lang en bestaat onder andere uit: Hendrik Bekker, Joost van den Berg, Umakanth Dammalapati, Subhadeep De, Gouri Shankar Giri, Samuel Hoekman, Corine Meinema, Stefan Müller, Mayerlín Nuñez Portela, Eric Prinsen, Bodhaditya Santra, Praveen Shidling, en Marlène da Silva e Silva. Allemaal bedankt voor jullie bijdragen aan het ^{21}Na experiment. In het bijzonder wil ik Sander Rikhof noemen. Tijdens je stage en je bachelor afstudeeronderzoek heb je bijgedragen aan bijna alle onderdelen van mijn experiment. Bedankt hiervoor.

Bij mijn experiment gebruikten we het lasersysteem van het natrium experiment bij Atoomfysica. Gabriel Hasan en Ina Blank, bedankt voor het kunnen gebruiken van de laser. Ina: zonder je hulp, tijd, tips en trucs die je erin hebt gestopt was het een stuk minder snel gegaan. Verder wil ik mijn verdere ATF vrienden niet onbenoemd laten: Jos Postma, Erwin Bodewits en Albert Mollema (je hebt zelfs ooit een shift gedaan bij mijn experiment, herinner ik me).

Het is natuurlijk een publiek geheim dat de 'T' in TRIμP eigenlijk voor theorie staat. Mijn dank aan de de leden van de theorie groep die betrokken zijn geweest bij het ^{21}Na gebeuren is dan ook groot. Dit betreffen Jordy de Vries en Wouter Dekens. Bedankt jullie. In het bijzonder: Rob Timmermans, bedankt voor je hulp en steun op uiteenlopend gebied.

Om een typisch experiment zoals we bij TRIμP hebben aan de praat te krijgen en te houden is iedereen binnen het KVI er wel bij betrokken, direct of indirect. Allereerst is er de tekenkamer: bedankt Michel Lindemulder, Henk Smit, Imko Smid en Rick Veenstra. De tekeningen worden in de werkplaats omgezet in concrete onderdelen door onder andere Roelof Dussel, Sandra Eggens, André de Vries en Nanko de Vries. In het bijzonder wil ik Dirk Tilman noemen: bedankt voor de altijd excellente puntlas van de neutralizer folies en je flexibiliteit als het qua tijd weer eens krap werd. Dank aan het team van electronica, bij de vacüumdienst bedank ik Henk Gorter en Jelke Wiersma. Frits Rengers, nog bedankt voor de hulp met de wikkelmachine. Hans Fraiquin: dank voor de neutralizer folies.

Ik dank de cyclotrongroep van het KVI hartelijk voor hun werk en inzet om altijd een goede neonbundel te leveren. Dit betreft de staf, bestaande uit Sytze Brandenburg en Mariet Hofstee en de vele operators van het cyclotron, maar ook de mensen die

de ionenbron in de lucht houden, te weten Hans Beijers, Rob Kremers en Vladimir Mironov. Een paar namen van operators die ik vaak tegenkwam op mijn shifts: Dennis Hofstra, Roel Schellekens en Niek van Wiefferen. Bedankt jullie allemaal voor jullie inzet.

Ook niet te vergeten zijn de meer ondersteunende diensten van het KVI, die ik ben tegengekomen in mijn promotietraject. De ICT afdeling bestaande o.a. uit Peter Kroon, Jacco van der Weele, Fred Zwarts (het brein achter het voortreffelijke data-acquisitie systeem Caddie). De financiële kant van de zaak werd altijd vakkundig afgehandeld door Carla Hemmes, Simone de Meijer, Miranda Ruiter en Robert Springer (ook bedankt voor de organisatie van het KVI 4 mijl team, altijd een mooie happening). Bij personeelszaken dank ik Hilde van der Meer en Annet van der Woude. Dank ook aan facilitaire zaken, Harry Elenius, Henk Merk, Martine ter Wal en Eveline van de Werf.

Bei Toptica möchte ich mich für das wunderbare, stabile Lasersystem bedanken, welches zuverlässig 2.5 Watt gelbes Licht produziert. Meine Kondition ging mit dem neuen System leider auch mit Sprüngen zurück, da ich nicht mehr den ganzen Tag zum alten Farbstofflaser wegen seiner Instabilität (100 m entfernt) hin und her rennen musste. Danke auch an Armin Falkenburger für den schnellen Aufbau vom Laser vor Ort.

Op het sportieve gebied zijn er genoeg mensen binnen het KVI te vinden. Amarins Petitiaux, ik heb veel plezier beleefd aan de vrijdagmiddag volleybaluurtjes. Alfred Felzel, ontelbare uren hebben we doorgebracht op het ACLO sportcentrum. Even de stress eraf sporten bij het spinnen, circuiten of fitnessen, heerlijk. Dat ga ik zeker missen. Emiel van der Graaf, dank voor de leuke uurtjes die ons onder andere door Garnwerd en omstreken voerden. Ik zie je vraag vanuit de oppositie over stelling nummer acht met vertrouwen tegemoet.

Binnen de Dienstraad van het KVI heb ik prettig samengewerkt met Rob Kremers en Lorenz Willmann. Niet alleen heb ik je, Imko Smid, in de werkplaats leren kennen als een door-en-door nuchtere Groninger, maar ook binnen de Dienstraad heb ik prettig met je samengewerkt, net als met jou, Myroslav Kavatsyuk. Eveline van de Werf, zonder de goede ondersteuning van de Dienstraad was mijn werk als secretaris veel zwaarder geweest: dank voor de prettige samenwerking. Ook dank aan alle DR'ers voor de leuke trips die onder de vlag van scholing plaatsvonden. Het was erg leuk en gezellig, vooral de trip op de zeiltjalk is memorabel. Dank ook aan de Personeelsvereniging de Kern, ik keek altijd uit naar de PV dagen, net als naar de haringparties, sinterklaas en wat al niet meer.

Marjan Koopmans, bedankt voor de uitstekend georganiseerde FANTOM scholen. Mijn werkgever FOM wil ik bedanken voor het goede werkgeverschap, wat zich uitte in onder andere in de goede cursussen die je als OiO aangeboden krijgt. Naast een inspirerende cursus in het leren schrijven van een wetenschappelijk tekst en de cursus 'Promotie in eigen regie' heb ik ook erg veel opgestoken tijdens de 38e Nyenrode Business Oriententation Week in Breukelen. Ook bedank ik Harry Linders, bij wie ik via FOM een individuele loopbaanadvies-traject kon volgen.

Fabrice Gerbier, thanks a lot for inviting me to join your sodium BEC experiment at LKB in Paris for three months to learn about trapping sodium atoms with optical

dipole traps. Thanks also to the rest of the sodium LKB team: Luigi Sarlo, David Jacob and Emmanuel Mimoun. I enjoyed my stay in your lab very much and learned a lot.

Fortunately it is allowed to use 'private communication' as a reference in scientific work. Numereous people were willing to share their experiences with me. Especially I mention Sergey Atutov, Seth Aubin, Paul Vetter, Kirk Madison and Peter van der Straten. Thanks for the discussions and your help. You all helped me a lot further.

Oscar Versolato, we hebben op vele gebieden prettig samengewerkt. Je manier van werken heeft mij altijd geïnspireerd. Tijdens de natrium bundeltijden was het productiegedeelte altijd in goede handen bij jou: mijn hartelijke dank voor al je inzet en bijdragen.

Lotje Wansbeek, zonder jou zou mijn verblijf een stuk minder aangenaam zijn geweest. Naast een heleboel vermaak (bijvoorbeeld met je fameuze Hyundai die een keer uit elkaar viel toen Oscar aan het stuur zat en die we toen probeerden te repareren bij je thuis met wat plakband) heb je ook qua natuurkunde altijd een goede neus gehad. Omdat je zo slim, veelzijdig en breed geïnteresseerd bent, hou je je met van alles en nog wat bezig. Daar heb ik altijd handig gebruik van gemaakt. Zet hem op topper, hop!

Duurt Johan van der Hoek, mijn partner in crime bij het ^{21}Na experiment, dank voor alles. Naast vele hilarische momenten (Bonn herinner ik me nog levendig) heb je mij met je optimistische houding door de meer lastige perioden van de promotieperiode heen weten te loodsen. Al dan niet met behulp van een potje badminton ergens in het KVI, 's nachts (plaats delict, in de gang naast de A-cel). Je hebt mij altijd weten te verbazen met je diepgaande intuïtie voor natuur- en wiskunde: je bent een steengoede en veelzijdige natuurkundige. Veel succes met je aanstaande promotie!

Aan mijn paranimfen Lotje en Duurt: dank voor jullie vriendschap. Ik zal jullie missen, net als de therapeutische wandelingetjes rond het KVI gebouw die steeds frequenter werden naarmate de promotiedatum van één van ons drieën dichterbij kwam!

Ik dank hierbij ook mijn familie. De open dag van het KVI was altijd een uitgelezen mogelijkheid het promotietraject enige handen en voeten te geven. In het bijzonder wil ik daarbij Tamme Meijer, Joos en Janny Luteyn noemen voor het prettige contact, jullie interesse in de ontwikkelingen bij mijn promotieonderzoek en jullie steun. Moim teściom Zdzisi i Andrzejowi: Dziękuję za Wasze wsparcie (z odległości) jak również za Waszą gościnę i za pokazanie mi pięknych zakątków Polski.

Naast jullie algehele steun, lieve Annelieke, Femke en Sarike, ook bedankt voor jullie hulp bij mijn Nederlandse samenvatting. Jan en Klaaske, bedankt voor jullie nimmer afnemende vertrouwen in mij en de onvoorwaardelijke steun die jullie mij geven. Betere ouders kan ik mij niet wensen.

Uiteindelijk zijn de laatste zinnen van dit dankwoord gereserveerd voor diegene die het dichtst bij mij staat. Magdusiu: moja kochana żoneczko. Dziękuję Ci za to, że zawsze mnie wspierasz i że bylas przy mnie w trudnym okresie mojego doktoratu. Kocham Cię bardzo!

Appendix A

Calculation of the MOT lifetime

We consider the regime in which the lifetime of a MOT depends only on the cross section of trapped atoms with the background gas with density n,

$$\tau = \frac{1}{n\langle\sigma v\rangle} \,. \tag{A.1}$$

If the vapor of interest dominates the cross section, the number of atoms in equilibrium is given by equation 2.14

$$N_0 = \tau R \,. \tag{A.2}$$

Because the loading rate R is proportional to n, N_0 is independent of n. Here we calculate $\langle\sigma v\rangle$ following [144] and test the calculation against experimental data.

The cold alkaline atom is in one of the two $S_{1/2}$ ground-states, or in an excited $P_{3/2}$ state. The vapor atoms are in the ground state. The interaction energy for the long-range interaction and two colliding particles separated by a distance R can be approximated by

$$U(r) = \pm\frac{C_n}{R^n} \,, \tag{A.3}$$

where n is the order of the interaction and C_n is the corresponding dispersion coefficient [48, 297]. If two atoms collide in the S-state, the interaction is an attractive van der Waals interaction and $n = 6$ [48]. For one atom in the S-state and the other in the P-state, the interaction is of the dipole-dipole type and $n = 3$, see chapter 14 on ultra-cold collisions of [48]. The total cross section for a MOT atom, with a probability P of being in the excited state is therefore

$$\sigma = (1-P)\sigma_6 + P\sigma_3 \,. \tag{A.4}$$

When the velocity change of the cold atom due to a collision is smaller than the escape velocity of the MOT it will not contribute to the trap loss. We use (equation 2.21):

$$v_{\text{esc}} = \frac{v_c}{\sqrt{2}} \,. \tag{A.5}$$

In simulations of a sodium MOT a relation $v_{esc} \sim 0.7 v_c$ was found [159–161]. For Rb a measurement using Photo Association to measure the trap depth revealed a relation between the capture velocity and escape velocity of $v_c = 1.29(0.12) v_e$ [155, 162], which is within 1 σ of our assumption of $\sqrt{2}$.

For a collision with an impulse transfer of $\Delta p = m v_c$ with impact parameter b the cross section is $\sigma = \pi b^2$. Following the expected cross section for knock-out, we have

$$\Delta \vec{p} = \int_{-\infty}^{\infty} \vec{F} dt \tag{A.6}$$

with

$$F = \frac{n C_n}{R^{n+1}}, \quad R = \frac{b}{\cos\theta}, \quad \tan\theta = \frac{vt}{b} \ . \tag{A.7}$$

The momentum change along the direction of the incoming particle cancels for a fast vapor atom, moving past a MOT atom at rest. The transverse momentum is

$$\Delta p = f_n \frac{C_n}{v b^n}, \left(\quad f_3 = 4, \quad f_6 = \frac{15\pi}{8} \right) \ . \tag{A.8}$$

Substituting b gives the cross section to knock out an atom from the trap,

$$\sigma_n = \pi \left(\frac{\sqrt{2} f_n C_n}{m v_c v} \right)^{2/n}, \tag{A.9}$$

with v_c the capture velocity of the MOT and v the velocity of the background atom. As we are interested in deriving a value for equation A.1 we weight σv with the Maxwell-Boltzmann distribution (equation 2.8), this gives

$$\langle \sigma_n v \rangle = \int_0^{\infty} \sigma_n v f(v) d^3 v = \pi \left(\frac{\sqrt{2} f_n C_n}{m v_c} \right)^{2/n} \times \begin{cases} 1.06 v_p^{2/3} & \text{if } n = 6 \\ 1.02 v_p^{1/3} & \text{if } n = 3 \end{cases} , \tag{A.10}$$

with $v_p = \sqrt{\frac{2kT}{m}}$ the most probable speed. Separating the terms, which is useful to compare to measurements of $\langle \sigma \rangle$, gives

$$\langle \sigma_n v \rangle = \langle \sigma_n \rangle v_p \times \begin{cases} 1.05 & \text{if } n = 6 \\ 0.973 & \text{if } n = 3 \end{cases} . \tag{A.11}$$

We are left with determining P, which appears in equation A.4, the fraction of the time the atoms spends in the excited state. We estimate this by using equation 2.1,

$$P = \frac{1}{2} \frac{s_0}{1 + s_0 + 4(\delta/\gamma)^2} , \tag{A.12}$$

with δ the detuning and s_0 the light intensity at the MOT position due to all six laser beams in units of the saturation intensity.

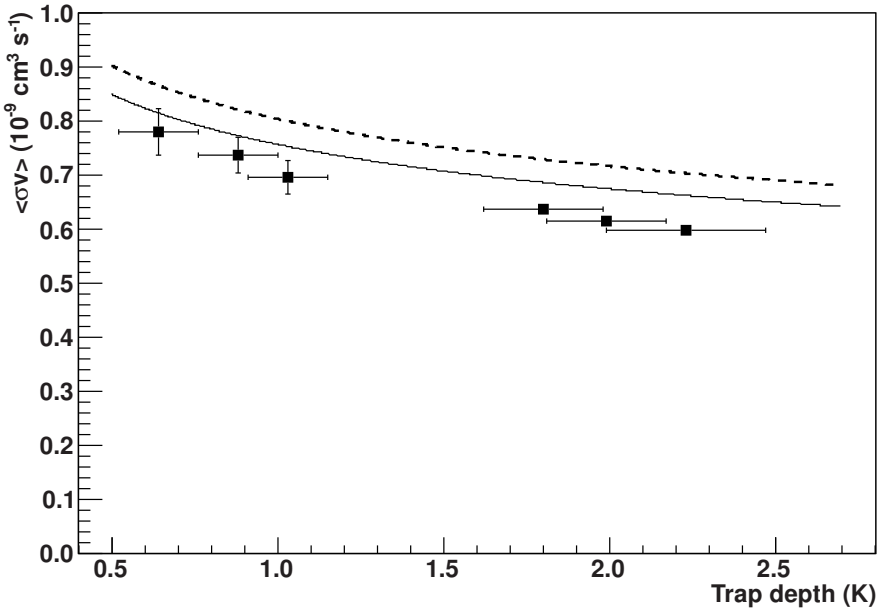

Figure A.1: *The measured loss rate constant $\langle \sigma v \rangle_{\mathrm{Rb,Ar}}$ versus trap depth for trapped ^{87}Rb atoms with ^{40}Ar at room temperature [154]. The solid curve is our calculation using the C_6 value from [154], the dashed line uses the more accurate number from [298].*

The total collision cross-section leading to trap loss is

$$\langle \sigma v \rangle = v_p (1.05 \langle \sigma_6 \rangle (1 - P) + 0.973 \langle \sigma_3 \rangle P) \; . \tag{A.13}$$

Following arguments of [153], we use a saturation intensity of $2.8 s_0$ to calculate the excited state fraction. In figure A.1 we compare our calculation for $\langle \sigma v \rangle$ with the experimental cross section of a Rb MOT cloud with Ar background gas measured by Van Dongen *et al.* [154]. We show two curves as a more accurate C_6 value can be found in [298], which is 20% larger than used by Van Dongen *et al.*. The authors also compare their experimental data (including data for mK trap depths) to a full quantum-mechanical calculation. They find excellent agreement with their calculations. That the classical scattering approach is valid at the energy scales of a MOT follows from the energy scale for diffractive collisions [299]

$$\epsilon_d = \frac{4\pi\hbar^2}{m\sigma} \; . \tag{A.14}$$

For Ar-Rb collisions $\epsilon_d \approx 10$ mK (or an escape velocity of 1.4 m/s), which is indeed well below typical MOT depths. Note that for a magnetic trap, the quantum mechanical calculation is necessary.

In conclusion, the MOT lifetime depends both on the gas density as well on the trap depth of the MOT. The C_6 values for the ground-state ground-state [300] and C_3 [301] values for the first excited ground S state and first excited Pπ are well known for all alkaline atoms. With the calculation of the MOT lifetime established, we deduce in section 2.5 from the loading rate and the MOT parameters the capture velocity of a MOT.

Appendix B

Simulation of effusion

To determine the particle density and number of bounces in the cell geometry we performed Monte-Carlo simulations and compared these to experimental values. In the Monte-Carlo simulation the particles follow straight trajectories and have no interaction with each other. When a particle hits a cell wall it is re-emitted until it escapes the cell geometry. This would be the case if the cell has a non-stick coating applied to the walls.

If the particle density uniform throughout a volume, the flux hitting its surface is distributed with a cosine dependence relative to the surface normal (see *e.g.* [302]). The flux is

$$\phi = \frac{1}{4} n \langle v \rangle \ , \tag{B.1}$$

with $\langle v \rangle$ the average velocity of the particles and n the particle density. By time inversion, when releasing the particles with a cosine angular distribution from the surface, the particle density is uniform throughout an arbitrary geometry. Another possibility we consider here is isotropic emission. Here the particle density cannot be expected to be uniform.

We performed the simulations for two particle emission distribution functions, the isotropic and cosine distribution. We fix the velocity to 1. For the isotropic case in half-space we use two random numbers uniform distributed, $\{r_\phi, r_\theta\} \in (0, 1]$ and generate the velocity components according to

$$\begin{aligned} \phi &= 2\pi r_\phi \\ \theta &= \arccos r_\theta \\ v_x &= \sqrt{1 - r_\theta^2} \cos\phi \\ v_y &= \sqrt{1 - r_\theta^2} \sin\phi \\ v_z &= r_\theta \ . \end{aligned} \tag{B.2}$$

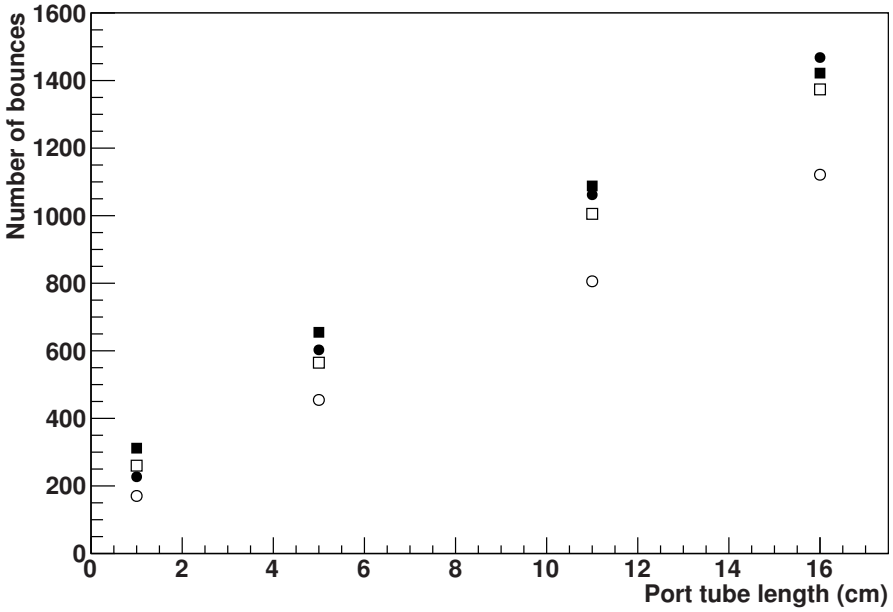

Figure B.1: *Measured values (circles) from [233]: the filled symbols assume an isotropic distribution and the open symbols a cosine distribution. Also shown is our calculation using a Monte-Carlo model (squares), also for both particle distribution.*

For the cosine distribution we have in half-space

$$\begin{aligned} \phi &= 2\pi r_\phi \\ \theta &= \arccos\sqrt{r_\theta} \\ v_x &= \sqrt{1-r_\theta}\cos\phi \\ v_y &= \sqrt{1-r_\theta}\sin\phi \\ v_z &= \sqrt{r_\theta}\ . \end{aligned} \tag{B.3}$$

In the experiment by Atutov *et al.* [233], the escape time was measured as function of the length of a cylindrical port tube connected to a spherical glass cell. The cell had a radius of 7 cm, the tube an inner diameter of 21 mm. Using this geometry we calculated the number of bounces, for both emission distributions. The results are shown in figure B.1. The experimental data depends on the assumed emission distribution, as in the experiment a time scale is measured which needs an average distance to come to a number of bounces.

In the same experiment the trap population (arbitrary units) as function of of the port tube length was measured. For the port length of 16 cm the escape time was

measured to be 0.37 s. To convert this time scale to the number of bounces the mean distance between two bounces is needed.

For the average distance in a sphere with radius r we find analytically that

$$\langle d \rangle_{\text{sphere,cosine}} = \frac{4}{3} r \ , \tag{B.4}$$

where for the isotropic case

$$\langle d \rangle_{\text{sphere,isotropic}} = r \ . \tag{B.5}$$

For a sphere the particle is on average closer to the surface and hence the density there is higher than in the center of the sphere. For a cube with side r we find that numerically, for the cosine distribution the mean distance is

$$\langle d \rangle_{\text{cube,cosine}} = 0.66 r \ , \tag{B.6}$$

where for the isotropic case

$$\langle d \rangle_{\text{cube,isotropic}} = 0.56 r \ . \tag{B.7}$$

The number of bounces depends thus on the underlying particle emission distributions. Our Monte Carlo simulations shows this as well: for the cosine distribution the distribution in length is linear from 0 to $2r$. See figure B.4 and figure B.5 for the case of cosine and isotropic emission, respectively. A linear dependence in the path length distribution like in figure B.4 is also obtained when particles are released uniformly distributed from a circle and intersect a sphere with the same radius (the angle of the particles is perpendicular to circle, the the center of the sphere is at the normal of the circle).

From figure B.1 we conclude that the agreement between the data and calculation is best when in the Monte Carlo simulation the isotropic angular distribution is chosen for the particle emission. The disagreement between the data and the values from the simulation can be contributed to the simplified geometry in the Monte-Carlo simulation and experimental errors. In the experiment for example the sticking time might be larger than assumed, resulting in a steeper dependence. The cosine distribution underestimates the number of bounces by about 30%. Zhang *et al.* [234] also found for their setup that using an isotropic emission pattern in their Monte Carlo simulations gives the best agreement with their experimental results.

For the trapping of atoms it is relevant to know how often particles pass through the volume where the six laser beams are intersecting. We calculated for a spherical glass cell with a radius of 7 cm and a laser volume radius of ≤ 7 cm the fraction of path the atoms spend in the laser trap volume. The result is shown in figure B.2 for the two cases we consider: a cosine and an isotropic emission distribution. The cosine distribution follows the ratio of the two volumes (the dotted line), consistent with an uniform density distribution of particles. The isotropic emission results in a lower fraction meaning a reduced trapping efficiency. Besides that for the cosine distribution,

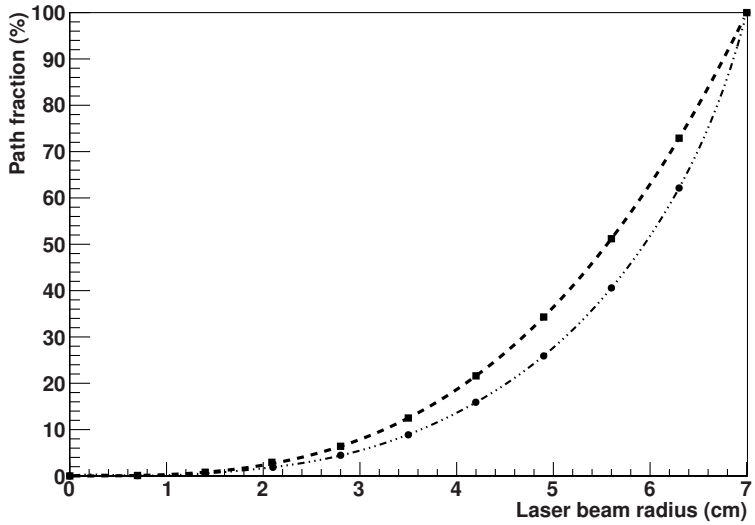

Figure B.2: *The calculated fraction of the path the particles spend inside a sphere with radius r located inside a sphere with radius R = 7 cm for an isotropic (dots) and a cosine emission distribution (squares). The dashed line is the fraction of the volumes, the dot-dash line is to guide the eye.*

relatively more time (path) is spent inside the trap volume, also the absolute value is larger than for the isotropic particle distribution. This can be seen in figure B.3, which shows the ratio of the absolute distances for both particle distributions.

Concerning the number of bounces reported by Atutov *et al.* in [233] we note that in their definition of ϕ_{chem} the authors omit the factor 1/4 from equation B.1. The average number of bounces the atoms make before they adsorb on the wall or permanently exit through one of the tubes is then $5 \cdot 10^3$ instead of the $2 \cdot 10^4$ mentioned in the article.

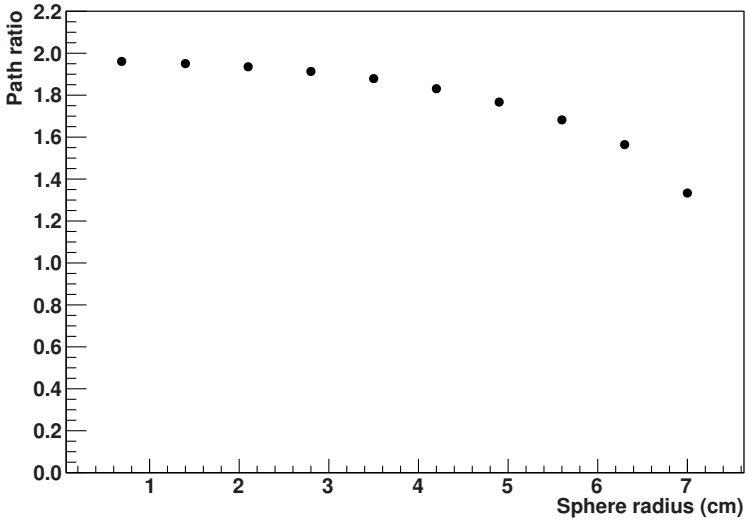

Figure B.3: *The fraction of the path spent in the sphere inside a sphere using a cosine distribution over the isotropic distribution.*

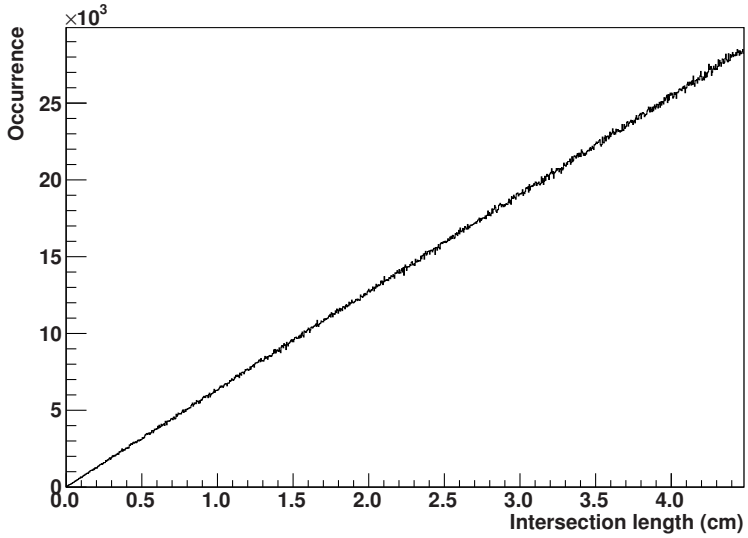

Figure B.4: *The distribution of intersection lengths of the path inside the cube with edge 5.6 cm, with a sphere of 45 mm diameter. The results are obtained with a Monte-Carlo simulation, a cosine distribution is used for the particle angular emission pattern.*

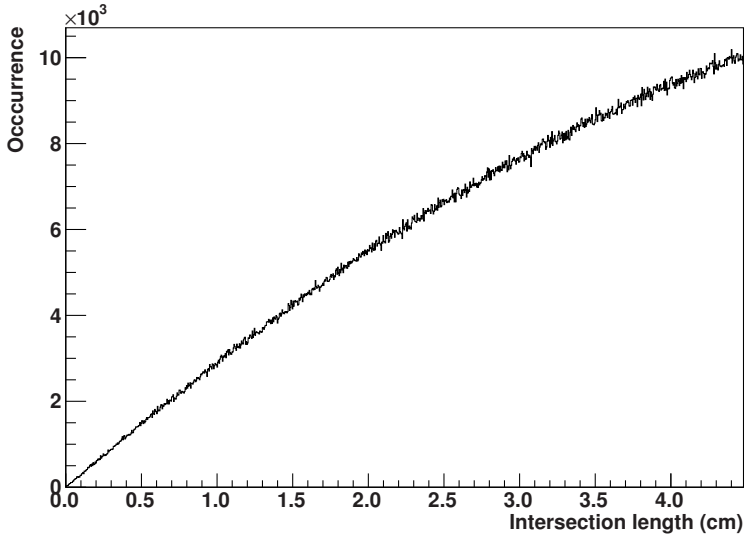

Figure B.5: *As in figure B.4, but with an isotropic distribution for the particle angular emission pattern.*

Appendix C

Efficiencies for a dipolar push-guide

To transfer atoms between two MOTs, a large detuned (typically a GHz) push beam can be used, typically it is used continuously. The detuning and power are chosen such that the laser beams accelerates the atoms but also offers a radially confining, conservative potential through the dipole interaction. During the transfer the radial confinement prevents the expansion of the atomic beam.

Two experiments reported a high transfer efficiency using this method. Wang *et al.* [248] measured for Cs a transfer efficiency of 85% over a distance of 19.3 cm. Dimova *et al.* [247] report for Cs a transfer efficiency of 70% over a distance of 57 cm and for Rb a 50% efficiency over 72 cm. In this appendix we look into more detail how in these experiments the transfer efficiency are calculated[1].

Consider a MOT system where a push beam is continuously present and pushes the atoms from MOT 1 to MOT 2. The number of trapped atoms N_1^{on} in the first MOT system is given by

$$N_1^{\text{on}} = (R - \gamma_p)\tau_1 \,, \tag{C.1}$$

where R is the loading rate, τ_1 the lifetime and γ_p is the loss rate due to the push beam. Two-body collisions between the trapped atoms and a dependence of R on γ_p are neglected. The number of trapped atoms in absence of the push beam is

$$N_1^{\text{off}} = R\tau_1 \,. \tag{C.2}$$

The experimental determination of γ_p is straightforward,

$$\gamma_p = \frac{1}{\tau_1}(N_1^{\text{off}} - N_1^{\text{on}}) \,. \tag{C.3}$$

Consider a second MOT system to which the atoms are transferred with a transfer efficiency ϵ_t. The number of trapped atoms in the second MOT system N_2 in the presence of a push beam is given by

$$N_2^{\text{on}} = \epsilon_t \gamma_p \tau_2 \,. \tag{C.4}$$

[1] A modified version of this chapter can be found in [303].

Two-body collisions and the loss rate due to the push beam are neglected. Let η be the ratio of the maximum steady-state number of cold atoms recaptured in the second MOT to the steady-state number of atoms trapped in the first MOT in the absence of the push beam, *i.e.*

$$\eta = \frac{N_2^{\text{on}}}{N_1^{\text{off}}} \,. \tag{C.5}$$

When the push beam is continuously present the transfer efficiency is

$$\epsilon_{\text{t}} = \frac{N_2^{\text{on}} \tau_1}{(N_1^{\text{off}} - N_1^{\text{on}})\tau_2} \,. \tag{C.6}$$

The overall efficiency, *i.e.* the fraction of the atoms which are loaded into the first MOT and which are captured by the second MOT, is given by

$$\epsilon = \epsilon_{\text{t}} \frac{\gamma_p}{R} = \frac{N_2^{\text{on}} \tau_1}{N_1^{\text{off}} \tau_2} = \eta \frac{\tau_1}{\tau_2} \,. \tag{C.7}$$

Wang *et al.* [248] have performed measurements to optimize the transfer efficiency in a double Magneto-Optical Trap (MOT) setup. Wang *et al.* use $\epsilon_{\text{t}} = \eta$, which is not correct,

$$\epsilon_{\text{t}} = \frac{\eta N_1^{\text{off}}}{\gamma_p \tau_2} \,. \tag{C.8}$$

We estimate τ, to calculate ϵ which is relevant for low yield experiments (as for radioactive atoms). To determine ϵ_{t} also γ_p is needed. Wang *et al.* only give the lifetime of the UHV MOT, $\tau_2 = 20$ s, and therefore we estimate a range for τ_2/τ_1, which is the ratio of the lifetimes of the two MOT setups. The typical pressures for a vapor-cell MOT chamber are 1×10^{-8} mbar and 2×10^{-10} mbar for the UHV MOT chamber [248]. The parameters of both MOT systems are comparable. Therefore the ratio τ_2/τ_1 is the pressure ratio, which is a factor 50.

This is however an upper bound for τ_2/τ_1. The composition of the background gas in the two chambers probably differs. The pressure reading might also be different for Cs compared to other gases, also the collision cross section can be different, leading to different lifetimes for equal pressures [144]. Based on the pressure in the vapor-cell chamber, a conservatively estimate for τ_1 is 2 s [145], giving a lower bound on $\tau_2/\tau_1 \sim 10$.

The range for τ_2/τ_1 is thus $10 - 50$. The reported overall transfer efficiencies reported by Wang *et al.* are then lower by a factor of this order. This leads to an overall transfer efficiency in the range of $2-9\%$, significantly lower than the reported transfer efficiency of 85%. This is due to the long time the push beam needs to push the atoms away, in that time most of the atoms have collided with a background atom and are lost from the MOT.

A second experiment with Cs and Rb by Dimova *et al.* [247] calculates the transfer efficiency correctly. Using information extracted from the published figures the overall transfer efficiency can be estimated to be about 25% instead of 50%.

Refereed publications

(2012) W.L. Kruithof, "Comment on "Transferring cold atoms in double magneto-optical trap by a continuous-wave transfer laser beam with large red detuning" [Rev. Sci. Instr. 79, 123116 (2008)]", submitted to Rev. Sci. Instr.

(2012) T. Roger *et al.*, Precise determination of the unperturbed ^{8}B neutrino spectrum, Phys. Rev. Let. **108**, 162502

(2012) E. J. Stephenson *et al.*, "Correcting systematic errors in high sensitivity deuteron polarization measurements", Nucl. Instr. and Meth. A **664**

(2011) O.O. Versolato *et al.*, "Atomic parity violation in a single trapped radium ion", Can. J. Phys. **89**

(2011) G.S. Giri *et al.*, "Precision spectroscopy of trapped radioactive radium ions", Can. J. Phys. **89**

(2011) O.O. Versolato *et al.*, "Atomic parity violation in a single trapped radium ion", Hyp. Int. **199**

(2011) O.O. Versolato *et al.*, "Hyperfine structure of the $6d^2\mathrm{D}_{3/2}$ level in trapped short-lived $^{211,209}\mathrm{Ra}^{+}$ ions", Phys. Lett. A **375**

(2011) G.S. Giri *et al.*, "Isotope shifts of the $6d^2D_{3/2}$-$7p^2P_{1/2}$ transition in trapped short-lived $^{209-214}\mathrm{Ra}^{+}$", Phys. Rev. A **84**

(2010) O.O. Versolato *et al.*, "Laser spectroscopy of trapped short-lived Ra^{+} ions", Phys. Rev. A **82**

(2010) P.D. Shidling *et al.*, "Thermalization of different alkali and alkali-earth elements at the TRIμP facility", Nucl. Instrum. Meth. A **622**

(2010) H.W. Wilschut *et al.*, "β-Decay and the electric dipole moment: Searches for time-reversal violation in radioactive nuclei and atoms", Pramana J. Phys. **75**

(2010) H.W. Wilschut *et al.*, "β-Decay and the electric dipole moment: Searches for time-reversal violation in radioactive nuclei and atoms", Nucl. Phys. A **844**

(2009) P.D. Shidling *et al.*, "Production of short lived radioactive beams of radium", Nucl. Instrum. Meth. A **606**

(2008) E. Traykov *et al.*, "Development of a thermal ionizer as ion catcher", Nucl. Instrum. Meth. B **266**

(2008) E. Traykov *et al.*, "Production and trapping of radioactive atoms at the TRIμP facility", Nucl. Instrum. Meth. B **266**

References

[1] C. Amsler et al. 'Review of Particle Physics'. In: *Physics Letters B* 667.1-5 (2008). Review of Particle Physics, pp. 1–6. ISSN: 0370-2693. DOI: 10.1016/j.physletb.2008.07.018.

[2] A. Einstein. 'Die Grundlage der allgemeinen Relativitätstheorie'. In: *Annalen der Physik* 49 (1916), p. 769.

[3] K Nakamura and Particle Data Group. 'Review of Particle Physics'. In: *Journal of Physics G: Nuclear and Particle Physics* 37.7A (2010), p. 075021.

[4] Richard P. Feynman et al. *Feynman Lectures On Gravitation (Frontiers in Physics)*. Westview Press, 1995. ISBN: 0201627345.

[5] V. C. Rubin, W. K. J. Ford and N. . Thonnard. 'Rotational properties of 21 SC galaxies with a large range of luminosities and radii, from NGC 4605 /R = 4kpc/ to UGC 2885 /R = 122 kpc/'. In: *Astrophysical Journal* 238 (June 1980), pp. 471–487. DOI: 10.1086/158003.

[6] Adam G. Riess et al. 'Observational Evidence from Supernovae for an Accelerating Universe and a Cosmological Constant'. In: *The Astronomical Journal* 116.3 (1998), p. 1009.

[7] N. Jarosik et al. 'Seven-year Wilkinson Microwave Anisotropy Probe (WMAP) Observations: Sky Maps, Systematic Errors, and Basic Results'. In: *The Astrophysical Journal Supplement Series* 192.2 (2011), p. 14.

[8] Andrei D Sakharov. 'Violation of CP in variance, C asymmetry, and baryon asymmetry of the universe'. In: *Soviet Physics Uspekhi* 34.5 (1991), p. 392.

[9] Antonio Riotto. 'Theories of Baryogenesis'. In: (2007). eprint: hep-ph/9807454.

[10] Tomá š Brauner et al. 'Temperature Dependence of Standard Model CP Violation'. In: *Phys. Rev. Lett.* 108 (4 2012), p. 041601. DOI: 10.1103/PhysRevLett.108.041601.

[11] Y. Fukuda et al. 'Evidence for Oscillation of Atmospheric Neutrinos'. In: *Phys. Rev. Lett.* 81 (8 1998), pp. 1562–1567. DOI: 10.1103/PhysRevLett.81.1562.

[12] Hitoshi Murayama. 'Supersymmetry Phenomenology'. In: (2007). eprint: hep-ph/0002232.

[13] Hermann Nicolai, Kasper Peeters and Marija Zamaklar. 'Loop quantum gravity: an outside view'. In: *Classical and Quantum Gravity* 22.19 (2005), R193.

[14] Michael B. Green, John H. Schwarz and Edward Witten. *Superstring Theory: Volume 1, Introduction (Cambridge Monographs on Mathematical Physics)*. Cambridge University Press, 1988. ISBN: 0521357527.

[15] Michael B. Green, John H. Schwarz and Edward Witten. *Superstring Theory: Volume 2, Loop Amplitudes, Anomalies and Phenomenology (Cambridge Monographs on Mathematical Physics)*. Cambridge University Press, 1988. ISBN: 0521357535.

[16] G. *et al.* (ATLAS collaboration) Aad. 'Search for the Standard Model Higgs Boson in the Diphoton Decay Channel with 4.9 fb^{-1} of pp Collision Data at $\sqrt{s} = 7$ TeV with ATLAS'. In: *Phys. Rev. Lett.* 108 (11 2012), p. 111803. DOI: 10.1103/PhysRevLett.108.111803.

[17] Nathal Severijns and Oscar Naviliat-Cuncic. 'Symmetry Tests in Nuclear Beta Decay'. In: *Annual Review of Nuclear and Particle Science* 61.1 (2011), pp. 23–46. DOI: 10.1146/annurev-nucl-102010-130410.

[18] Duurt Johan van der Hoek. 'Studies for β-decay correlation measurements in ^{21}Na'. PhD thesis. University of Groningen, 2012, in progress.

[19] J. D. Jackson, S. B. Treiman and H. W. Wyld. 'Possible Tests of Time Reversal Invariance in Beta Decay'. In: *Phys. Rev.* 106.3 (1957), pp. 517–521. DOI: 10.1103/PhysRev.106.517.

[20] Nathal Severijns, Marcus Beck and Oscar Naviliat-Cuncic. 'Tests of the standard electroweak model in nuclear beta decay'. In: *Rev. Mod. Phys.* 78.3 (2006), p. 991. DOI: 10.1103/RevModPhys.78.991.

[21] C. S. Wu et al. 'Experimental Test of Parity Conservation in Beta Decay'. In: *Phys. Rev.* 105.4 (1957), pp. 1413–1415. DOI: 10.1103/PhysRev.105.1413.

[22] Julian Schwinger. 'The Theory of Quantized Fields. VI'. In: *Phys. Rev.* 94 (5 1954), pp. 1362–1384. DOI: 10.1103/PhysRev.94.1362.

[23] O. W. Greenberg. 'CPT Violation Implies Violation of Lorentz Invariance'. In: *Phys. Rev. Lett.* 89 (23 2002), p. 231602. DOI: 10.1103/PhysRevLett.89.231602.

[24] P. Herczeg. 'Beta decay beyond the standard model'. In: *Progress in Particle and Nuclear Physics* 46.2 (2001), pp. 413 –457. ISSN: 0146-6410. DOI: DOI:10.1016/S0146-6410(01)00149-1.

[25] P. Herczeg and I. B. Khriplovich. 'Time-reversal violation in β decay in the standard model'. In: *Phys. Rev. D* 56.1 (1997), pp. 80–89. DOI: 10.1103/PhysRevD.56.80.

[26] Zhong Lin et al. 'Laser Cooling and Trapping of Li'. In: *Japanese Journal of Applied Physics* 30.Part 2, No. 7B (1991), pp. L1324–L1326. DOI: 10.1143/JJAP.30.L1324.

[27] E. L. Raab et al. 'Trapping of Neutral Sodium Atoms with Radiation Pressure'. In: *Phys. Rev. Lett.* 59.23 (1987), pp. 2631–2634. DOI: 10.1103/PhysRevLett.59.2631.

[28] R. S. Williamson and T. Walker. 'Magneto-optical trapping and ultracold collisions of potassium atoms'. In: *J. Opt. Soc. Am. B* 12.8 (1995), pp. 1393–1397. DOI: 10.1364/JOSAB.12.001393.

[29] T. Walker et al. 'A vortex-force atom trap'. In: *Physics Letters A* 163.4 (Mar. 1992), pp. 309–312. ISSN: 03759601. DOI: 10.1016/0375-9601(92)91017-L.

[30] D. Sesko, C. G. Fan and C. E. Wieman. 'Production of a cold atomic vapor using diode-laser cooling'. In: *J. Opt. Soc. Am. B* 5.6 (1988), pp. 1225–1227. DOI: 10.1364/JOSAB.5.001225.

[31] J. E. Simsarian et al. 'Magneto-Optic Trapping of ^{210}Fr'. In: *Phys. Rev. Lett.* 76.19 (1996), pp. 3522–3525. DOI: 10.1103/PhysRevLett.76.3522.

[32] K. Sengstock et al. 'Optical Ramsey spectroscopy on laser-trapped and thermal Mg atoms'. In: *Applied Physics B: Lasers and Optics* 59 (2 1994), pp. 99–115. ISSN: 0946-2171. DOI: 10.1007/BF01081160.

[33] Takayuki Kurosu and Fujio Shimizu. 'Laser Cooling and Trapping of Calcium and Strontium'. In: *Japanese Journal of Applied Physics* 29.Part 2, No. 11 (1990), pp. L2127–L2129. DOI: 10.1143/JJAP.29.L2127.

[34] S. De et al. 'Magneto-optical trapping of barium'. In: *Phys. Rev. A* 79.4 (2009), p. 041402. DOI: 10.1103/PhysRevA.79.041402.

[35] J. R. Guest et al. 'Laser Trapping of ^{225}Ra and ^{226}Ra with Repumping by Room-Temperature Blackbody Radiation'. In: *Phys. Rev. Lett.* 98 (9 2007), p. 093001. DOI: 10.1103/PhysRevLett.98.093001.

[36] A. S. Bell et al. 'A magneto-optical trap for chromium with population repumping via intercombination lines'. In: *EPL (Europhysics Letters)* 45.2 (1999), p. 156.

[37] G. Uhlenberg, J. Dirscherl and H. Walther. 'Magneto-optical trapping of silver atoms'. In: *Phys. Rev. A* 62 (6 2000), p. 063404. DOI: 10.1103/PhysRevA.62.063404.

[38] K.-A. Brickman et al. 'Magneto-optical trapping of cadmium'. In: *Phys. Rev. A* 76 (4 2007), p. 043411. DOI: 10.1103/PhysRevA.76.043411.

[39] H. Hachisu et al. 'Trapping of Neutral Mercury Atoms and Prospects for Optical Lattice Clocks'. In: *Phys. Rev. Lett.* 100 (5 2008), p. 053001. DOI: 10.1103/PhysRevLett.100.053001.

[40] Fujio Shimizu, Kazuko Shimizu and Hiroshi Takuma. 'Laser cooling and trapping of Ne metastable atoms'. In: *Phys. Rev. A* 39 (5 1989), pp. 2758–2760. DOI: 10.1103/PhysRevA.39.2758.

[41] Mitsutaka Kumakura and Norio Morita. 'Visible observation of metastable helium atoms confined in an infrared/visible double resonance trap'. In: *Jpn. J. Appl. Phys.* 31 (1992), p. 276.

[42] Hidetoshi Katori and Fujio Shimizu. 'Laser Cooling and Trapping of Argon and Krypton Using Diode Lasers'. In: *Japanese Journal of Applied Physics* 29.Part 2, No. 11 (1990), pp. L2124–L2126. DOI: 10.1143/JJAP.29.L2124.

[43] M. Walhout et al. 'Magneto-optical trapping of metastable xenon: Isotope-shift measurements'. In: *Phys. Rev. A* 48 (2 1993), R879–R882. DOI: 10.1103/PhysRevA.48.R879.

[44] Mingwu Lu, Seo Ho Youn and Benjamin L. Lev. 'Trapping Ultracold Dysprosium: A Highly Magnetic Gas for Dipolar Physics'. In: *Phys. Rev. Lett.* 104 (6 2010), p. 063001. DOI: 10.1103/PhysRevLett.104.063001.

[45] J. J. McClelland and J. L. Hanssen. 'Laser Cooling without Repumping: A Magneto-Optical Trap for Erbium Atoms'. In: *Phys. Rev. Lett.* 96 (14 2006), p. 143005. DOI: 10.1103/PhysRevLett.96.143005.

[46] D. Sukachev et al. 'Magneto-optical trap for thulium atoms'. In: *Phys. Rev. A* 82 (1 2010), p. 011405. DOI: 10.1103/PhysRevA.82.011405.

[47] K. Honda et al. 'Magneto-optical trapping of Yb atoms and a limit on the branching ratio of the $^1P_1$ state'. In: *Phys. Rev. A* 59 (2 1999), R934–R937. DOI: 10.1103/PhysRevA.59.R934.

[48] Harold J. Metcalf and Peter van der Straten. *Laser cooling and trapping*. Springer, 1999.

[49] Rudolf Grimm, Matthias Weidemüller and Yurii B. Ovchinnikov. 'Optical Dipole Traps for Neutral Atoms'. In: *Advances In Atomic, Molecular, and Optical Physics*. Advances In Atomic, Molecular, and Optical Physics 42 (2000). Ed. by Benjamin Bederson and Herbert Walther, pp. 95 –170. ISSN: 1049-250X. DOI: 10.1016/S1049-250X(08)60186-X.

[50] N. D. Scielzo et al. 'Measurement of the $\beta - \nu$ Correlation using Magneto-optically Trapped ^{21}Na'. In: *Phys. Rev. Lett.* 93.10 (2004), p. 102501. DOI: 10.1103/PhysRevLett.93.102501.

[51] Matthew Harvey and Andrew James Murray. 'Cold Atom Trap with Zero Residual Magnetic Field: The ac Magneto-Optical Trap'. In: *Phys. Rev. Lett.* 101.17 (2008), p. 173201. DOI: 10.1103/PhysRevLett.101.173201.

[52] Jai Mai Choi et al. 'Production of spin-polarized cold atoms by optical pumping in a Magneto-Optical Trap'. In: *Journal of Korean Physical Society* 46.2 (2005), pp. 425–430.

[53] T. Walker et al. 'Spin-polarized spontaneous-force atom trap'. In: *Phys. Rev. Lett.* 69.15 (1992), pp. 2168–2171. DOI: 10.1103/PhysRevLett.69.2168.

[54] Subhadeep De. 'Laser cooling and trapping of barium'. PhD thesis. University of Groningen, 2008.

[55] Alan L. Migdall et al. 'First Observation of Magnetically Trapped Neutral Atoms'. In: *Phys. Rev. Lett.* 54 (24 1985), pp. 2596–2599. DOI: 10.1103/PhysRevLett.54.2596.

[56] Kristan Lee Corwin. 'A Circularly-Polarized Optical Dipole Trap and Other Developments in Laser Trapping of Atoms'. PhD thesis. University of Colorado, 1999.

[57] F. Fang et al. 'Polarized atoms in a far-off-resonance yttrium-aluminum-garnet-laser optical dipole trap'. In: *Phys. Rev. A* 79.4 (2009), p. 043406. DOI: 10.1103/PhysRevA.79.043406.

[58] D. Feldbaum et al. 'Trapping radioactive ^{82}Rb in an optical dipole trap and evidence of spontaneous spin polarization'. In: *Physical Review A* 76.5 (Nov. 2007), pp. 3–6. ISSN: 1050-2947. DOI: 10.1103/PhysRevA.76.051402.

[59] F. Fang, D. J. Vieira and X. Zhao. 'Precision polarization measurements of atoms in a far-off-resonance optical dipole trap'. In: *Phys. Rev. A* 83.1 (2011), p. 013416. DOI: 10.1103/PhysRevA.83.013416.

[60] Fouad G. Major, Viorica N. Gheorghe and Günther Werth. *Charged Particle Traps: Physics and Techniques of Charged Particle Field Confinement (Springer Series on Atomic, Optical, and Plasma Physics)*. Springer, 2004. ISBN: 3540220437.

[61] J.J. Bollinger W. M. Itano J. C. Bergquist and D. J. Wineland. 'Laser cooling of trapped ions'. In: *Laser Manipulation of Atoms and Ions, Proc. Enrico Fermi Summer School, Course CXVIII* Edited by E. Arimondo, W.D. Phillips, and F. Strumia (North-Holland, Amsterdam) (1992), pp. 553–567.

[62] Jürgen Eschner et al. 'Laser cooling of trapped ions'. In: *J. Opt. Soc. Am. B* 20.5 (2003), pp. 1003–1015. DOI: 10.1364/JOSAB.20.001003.

[63] N Scielzo et al. 'Detecting shake-off electron-ion coincidences to measure -decay correlations in laser trapped Na'. In: *Nuclear Physics A* 746 (Dec. 2004), pp. 677–680. ISSN: 03759474. DOI: 10.1016/j.nuclphysa.2004.09.048.

[64] P. A. Vetter et al. 'Measurement of the $\beta-\nu$ correlation of ^{21}Na using shakeoff electrons'. In: *Phys. Rev. C* 77.3 (2008), p. 035502. DOI: 10.1103/PhysRevC.77.035502.

[65] N. Scielzo. 'Measurement of the $\beta-\nu$ correlation in laser trapped ^{21}Na'. PhD thesis. University of California, Berkeley, 2003.

[66] X Fléchard et al. 'Measurement of the $\beta-\nu$ correlation coefficient $a_{\beta\nu}$ in the β decay of trapped $^{6}He^{+}$ ions'. In: *Journal of Physics G: Nuclear and Particle Physics* 38.5 (2011), p. 055101.

[67] *Xavier Fléchard, Private communication*. 2012.

[68] Mary A. Rowe. 'Investigations of the ground-state hyperfine atomic structure and beta decay measurement prospects of ^{21}Na with improved laser trapping techniques'. PhD thesis. University of California at Berkeley, 1999.

[69] Moslem Sohani. 'Setup for precise measurements of β-decay in optically trapped radioactive Na'. PhD thesis. Rijksuniversiteit Groningen, 2008.

[70] D Melconian. 'Measurement of the neutrino asymmetry in the beta decay of laser-cooled, polarized ^{37}K'. PhD thesis. Simon Fraser University, 2005.

[71] D Melconian et al. 'Measurement of the neutrino asymmetry in the β decay of laser-cooled, polarized 37K'. In: *Physics Letters B* 649.5-6 (June 2007), pp. 370–375. ISSN: 03702693. DOI: 10.1016/j.physletb.2007.04.047.

[72] Alexandre I. Gorelov. 'Positron-neutrino correlation measurements in the beta decay of magneto-optically trapped ^{38m}K atoms'. PhD thesis. Simon Fraser University, 2008.

[73] A. Gorelov et al. 'Scalar Interaction Limits from the β-ν Correlation of Trapped Radioactive Atoms'. In: *Physical Review Letters* 94.14 (Apr. 2005), pp. 3–6. ISSN: 0031-9007. DOI: 10.1103/PhysRevLett.94.142501.

[74] J. R. A. Pitcairn et al. 'Tensor interaction constraints from β-decay recoil spin asymmetry of trapped atoms'. In: *Phys. Rev. C* 79.1 (2009), p. 015501. DOI: 10.1103/PhysRevC.79.015501.

[75] R. Guckert et al. 'Magneto-optical trapping of radioactive ^{82}Rb atoms'. In: *Phys. Rev. A* 58.3 (1998), R1637–R1640. DOI: 10.1103/PhysRevA.58.R1637.

[76] S. Crane et al. 'Parity Violation Observed in the Beta Decay of Magnetically Trapped ^{82}Rb Atoms'. In: *Physical Review Letters* 86.14 (Apr. 2001), pp. 2967–2970. ISSN: 0031-9007. DOI: 10.1103/PhysRevLett.86.2967.

[77] S G Crane. 'Observation of the parity-violating positron-spin correlation from a magnetically trapped ^{82}Rb source'. PhD thesis. Utah State University, 2001.

[78] Claudio de Mauro. 'The Legnaro Francium MOT: efficient detection, characterization and perspectives'. PhD thesis. Universitá degli Studi di Siena, 2007.

[79] G. D. Sprouse and L. A. Orozco. 'LASER TRAPPING OF RADIOACTIVE ATOMS'. In: *Annual Review of Nuclear and Particle Science* 47.1 (1997), pp. 429–461. DOI: 10.1146/annurev.nucl.47.1.429. eprint: http://www.annualreviews.org/doi/pdf/10.1146/annurev.nucl.47.1.429.

[80] Seth Aubin. 'High efficiency francium trap for precision spectroscopy'. PhD thesis. State University of New York at Stony Brook, 2003.

[81] S. Aubin et al. 'High efficiency magneto-optical trap for unstable isotopes'. In: *Review of Scientific Instruments* 74.10 (2003), pp. 4342–4351. DOI: 10.1063/1.1606093.

[82] X. Fléchard et al. 'Paul Trapping of Radioactive $^{6}He^{+}$ Ions and Direct Observation of Their β Decay'. In: *Phys. Rev. Lett.* 101 (21 2008), p. 212504. DOI: 10.1103/PhysRevLett.101.212504.

[83] Ph. Velten et al. 'The LPCTrap experiment: measurement of the $\beta - \nu$ angular correlation in He^{6+} decay using a transparent Paul trap'. In: *Hyperfine Interactions* 199 (1 2011). 10.1007/s10751-011-0298-4, pp. 29–38. ISSN: 0304-3843.

[84] G. Ban et al. 'Measurements of the $\beta\nu$ angular correlation in nuclear β-decay'. In: *Nuclear Physics A* 752.0 (2005). Proceedings of the 22nd International Nuclear Physics Conference (Part 2), pp. 67 –76. ISSN: 0375-9474. DOI: 10.1016/j.nuclphysa.2005.02.097.

[85] *Search For New Physics in Beta-Neutrino Correlations Using Trapped Ions and a Retardation Spectrometer*. Proposal to the ISOLDE scientific committee, CERN/ISC 99-13, ISC/P111. 1999.

[86] M. Beck et al. 'First detection and energy measurement of recoil ions following beta decay in a Penning trap with the WITCH experiment'. In: *The European Physical Journal A - Hadrons and Nuclei* 47 (3 2011). 10.1140/epja/i2011-11045-0, pp. 1–9. ISSN: 1434-6001.

[87] D. Melconian et al. 'The β^{+} decay of ^{37}K as a multi-faceted probe of fundamental physics'. In: *AIP Conference Proceedings* 1342.1 (2011). Ed. by Dugersuren Dashdorj and Gary E. Mitchell, pp. 53–58. DOI: 10.1063/1.3583167.

[88] H. P. Mumm et al. 'New Limit on Time-Reversal Violation in Beta Decay'. In: *Phys. Rev. Lett.* 107 (10 2011), p. 102301. DOI: 10.1103/PhysRevLett.107.102301.

[89] H. P. Mumm et al. 'emiT: An apparatus to test time reversal invariance in polarized neutron decay'. In: *Review of Scientific Instruments* 75.12 (2004), pp. 5343–5355. DOI: 10.1063/1.1821628.

[90] C. H. Johnson, Frances Pleasonton and T. A. Carlson. 'Precision Measurement of the Recoil Energy Spectrum from the Decay of He^{6}'. In: *Phys. Rev.* 132 (3 1963), pp. 1149–1165. DOI: 10.1103/PhysRev.132.1149.

[91] Frances Pleasonton and C. H. Johnson. 'System for Continuous Generation and Fast Transfer of Radioactive Gases'. In: *Review of Scientific Instruments* 35.1 (1964), pp. 97–102. DOI: 10.1063/1.1718717.

[92] J. Sromicki et al. 'Study of time reversal violation in β decay of polarized ^{8}Li'. In: *Phys. Rev. C* 53.2 (1996), pp. 932–955. DOI: 10.1103/PhysRevC.53.932.

[93] R. Huber et al. 'Search for Time-Reversal Violation in the β Decay of Polarized ^{8}Li Nuclei'. In: *Phys. Rev. Lett.* 90 (20 2003), p. 202301. DOI: 10.1103/PhysRevLett.90.202301.

[94] F. P. Calaprice, E. D. Commins and D. C. Girvin. 'New test of time-reversal invariance in ^{19}Ne beta decay'. In: *Phys. Rev. D* 9.3 (1974), pp. 519–529. DOI: 10.1103/PhysRevD.9.519.

[95] E. G. Adelberger et al. 'Positron-Neutrino Correlation in the $0^+ \rightarrow 0^+$ Decay of ^{32}Ar'. In: *Phys. Rev. Lett.* 83 (7 1999), pp. 1299–1302. DOI: 10.1103/PhysRevLett.83.1299.

[96] A. García et al. 'Positron–neutrino correlations in ^{32}Ar and ^{33}Ar decays: Probes of scalar weak currents and nuclear isospin mixing'. In: *Hyperfine Interactions* 129 (1 2000). 10.1023/A:1012605731737, pp. 237–248. ISSN: 0304-3843.

[97] F. Wauters et al. 'Precision measurements of the ^{60}Co β-asymmetry parameter in search for tensor currents in weak interactions'. In: *Phys. Rev. C* 82.5 (2010), p. 055502. DOI: 10.1103/PhysRevC.82.055502.

[98] Frederik Wauters. 'Search for tensor type weak currents by measuring the β-asymmetry parameter in nuclear decays'. PhD thesis. Universiteit Leuven, 2009.

[99] F. Wauters et al. 'β asymmetry parameter in the decay of ^{114}In'. In: *Phys. Rev. C* 80 (6 2009), p. 062501. DOI: 10.1103/PhysRevC.80.062501.

[100] J S Nico. 'Neutron beta decay'. In: *Journal of Physics G: Nuclear and Particle Physics* 36.10 (2009), p. 104001.

[101] G Konrad et al. 'Neutron Decay with PERC: a Progress Report'. In: *Journal of Physics: Conference Series* 340.1 (2012), p. 012048.

[102] Stephan Paul. 'The Puzzle of Neutron Lifetime'. In: (Feb. 2009). eprint: 0902.0169.

[103] J Murata et al. 'Test of Time Reversal Symmetry using polarized 8 Li at TRIUMF-ISAC'. In: *Journal of Physics: Conference Series* 312.10 (2011), p. 102011.

[104] Frank P. Calaprice. 'The use of atomic beam and optical methods in the study of fundamental symmetries'. In: *Hyperfine Interactions* 22 (1 1985). 10.1007/BF02063981, pp. 83–93. ISSN: 0304-3843.

[105] M. B. Schneider et al. 'Limit on Im($C_S C_A^*$) from a Test of T Invariance in ^{19}Ne Beta Decay'. In: *Phys. Rev. Lett.* 51 (14 1983), pp. 1239–1242. DOI: 10.1103/PhysRevLett.51.1239.

[106] X. Fléchard et al. 'Temperature measurement of ions confined in a transparent Paul trap'. In: *Hyperfine Interactions* 199 (1 2011). 10.1007/s10751-011-0297-5, pp. 21–27. ISSN: 0304-3843.

[107] F. Pereira Dos Santos et al. 'Bose-Einstein Condensation of Metastable Helium'. In: *Phys. Rev. Lett.* 86 (16 2001), pp. 3459–3462. DOI: 10.1103/PhysRevLett.86.3459.

[108] URL: http://www.weizmann.ac.il/physics/nuc_exp/present/workshop/PMueller_Workshop%20on%20Traps.pdf.

[109] L.-B. Wang et al. 'Laser Spectroscopic Determination of the ^{6}He Nuclear Charge Radius'. In: *Phys. Rev. Lett.* 93 (14 2004), p. 142501. DOI: 10.1103/PhysRevLett.93.142501.

[110] P. Mueller et al. 'Nuclear Charge Radius of ^{8}He'. In: *Phys. Rev. Lett.* 99 (25 2007), p. 252501. DOI: 10.1103/PhysRevLett.99.252501.

[111] G. Konrad et al. 'Impact of Neutron Decay Experiments on non-Standard Model Physics'. In: (July 2010). eprint: 1007.3027.

[112] R. I. Steinberg et al. 'New Experimental Limit on T Invariance in Polarized-Neutron β Decay'. In: *Phys. Rev. Lett.* 33 (1 1974), pp. 41–44. DOI: 10.1103/PhysRevLett.33.41.

[113] Peng Wang. 'Neutrino Mass Implications for Physics Beyond the Standard Model'. PhD thesis. California Institute of Technology, 2007.

[114] Takeyasu M. Ito and Gary Prézeau. 'Neutrino Mass Constraints on β Decay'. In: *Phys. Rev. Lett.* 94 (16 2005), p. 161802. DOI: 10.1103/PhysRevLett.94.161802.

[115] KATRIN collaboration. *KATRIN: A next generation tritium beta decay experiment with sub-eV sensitivity for the electron neutrino mass*. 2001. eprint: arXiv:hep-ex/0109033.

[116] M. Drees and M. Rauch. 'Complete one-loop calculation of the T-violating D-parameter in neutron decay in the MSSM'. In: *The European Physical Journal C - Particles and Fields* 29 (4 2003). 10.1140/epjc/s2003-01247-8, pp. 573–585. ISSN: 1434-6044.

[117] Peter Herczeg. 'The T-Odd R and D Correlations in Beta Decay'. In: *Journal of Research of the National Institute of Standards and Technology* 110 (2005), pp. 453–459.

[118] John Ng and Sean Tulin. 'CP violation in beta decay and electric dipole moments'. In: *Phys. Rev. D* 85 (3 2012), p. 033001. DOI: 10.1103/PhysRevD.85.033001.

[119] O. Naviliat-Cuncic and N. Severijns. 'Test of the Conserved Vector Current Hypothesis in $T = 1/2$ Mirror Transitions and New Determination of $|V_{ud}|$'. In: *Phys. Rev. Lett.* 102 (14 2009), p. 142302. DOI: 10.1103/PhysRevLett.102.142302.

[120] Zheng-Tian Lu. 'Laser Trapping of ^{21}Na Atoms'. PhD thesis. University of California at Berkeley and Nuclear Science Division Lawrence Berkeley Laboratory University of California, 1994.

[121] Z-T. Lu et al. 'Laser trapping of short-lived radioactive isotopes'. In: *Phys. Rev. Lett.* 72.24 (1994), pp. 3791–3794. DOI: 10.1103/PhysRevLett.72.3791.

[122] N. D. Scielzo et al. 'Recoil-ion charge-state distribution following the β^+ decay of ^{21}Na'. In: *Phys. Rev. A* 68.2 (2003), p. 022716. DOI: 10.1103/PhysRevA.68.022716.

[123] M. Rowe et al. 'Ground-state hyperfine measurement in laser-trapped radioactive ^{21}Na'. In: *Physical Review A* 59.3 (Mar. 1999), pp. 1869–1873. ISSN: 1050-2947. DOI: 10.1103/PhysRevA.59.1869.

[124] N L Achouri et al. 'The β–γ decay of ^{21}Na'. In: *Journal of Physics G: Nuclear and Particle Physics* 37.4 (2010), p. 045103.

[125] E. Traykov et al. 'Production of radioactive nuclides in inverse reaction kinematics'. In: *Nuclear Instruments and Methods in Physics Research Section A: Accelerators, Spectrometers, Detectors and Associated Equipment* 572.2 (2007), pp. 580 –584. ISSN: 0168-9002. DOI: DOI:10.1016/j.nima.2006.11.053.

[126] G.P.A. Berg et al. 'Dual magnetic separator for TRIμP'. In: *Nuclear Instruments and Methods in Physics Research Section A: Accelerators, Spectrometers, Detectors and Associated Equipment* 560.2 (2006), pp. 169 –181. ISSN: 0168-9002. DOI: DOI:10.1016/j.nima.2005.12.214.

[127] G. P. A. Berg et al. 'TRIμP – A radioactive isotope trapping facility at KVI'. In: *Nuclear Physics A* 721 (2003), pp. C1107 –C1110. ISSN: 0375-9474. DOI: DOI:10.1016/S0375-9474(03)01296-X.

[128] E. Traykov et al. 'Development of a thermal ionizer as ion catcher'. In: *Nuclear Instruments and Methods in Physics Research Section B: Beam Interactions with Materials and Atoms* 266.19-20 (2008). Proceedings of the XVth International Conference on Electromagnetic Isotope Separators and Techniques Related to their Applications, pp. 4478 –4482. ISSN: 0168-583X. DOI: DOI:10.1016/j.nimb.2008.05.053.

[129] P.D. Shidling et al. 'Thermalization of different alkali and alkali-earth elements at the TRIμP facility'. In: *Nuclear Instruments and Methods in Physics Research Section A: Accelerators, Spectrometers, Detectors and Associated Equipment* 622.1 (2010), pp. 11 –16. ISSN: 0168-9002. DOI: DOI:10.1016/j.nima.2010.07.048.

[130] Curtis G. Callan and S. B. Treiman. 'Electromagnetic Simulation of T Violation in Beta Decay'. In: *Phys. Rev.* 162 (5 1967), pp. 1494–1496. DOI: 10.1103/PhysRev.162.1494.

[131] Shung ichi Ando, Judith A. McGovern and Toru Sato. 'The D coefficient in neutron beta decay in effective field theory'. In: *Physics Letters B* 677.1–2 (2009), pp. 109 –115. ISSN: 0370-2693. DOI: 10.1016/j.physletb.2009.04.088.

[132] Marc van Veenhuizen. 'Time-reversal violation in nuclear β-decay of ^{19}Ne and ^{21}Na'. MA thesis. University of Groningen, 2002.

[133] Steven Chu et al. 'Three-dimensional viscous confinement and cooling of atoms by resonance radiation pressure'. In: *Phys. Rev. Lett.* 55 (1 1985), pp. 48–51. DOI: 10.1103/PhysRevLett.55.48.

[134] Christopher J. Foot. *Atomic Physics (Oxford Master Series in Atomic, Optical and Laser Physics)*. Oxford University Press, USA, 2005. ISBN: 0198506961.

[135] O. Emile et al. 'Observation of a New Magneto-optical Trap'. In: *EPL (Europhysics Letters)* 20.8 (1992), p. 687.

[136] A. Höpe et al. 'Optical Trapping in a Cesium Cell with Linearly Polarized Light and at Zero Magnetic Field'. In: *EPL (Europhysics Letters)* 28.1 (1994), p. 7.

[137] R. Gaggl et al. 'Laser cooling of a sodium atomic beam using the Stark effect'. In: *Phys. Rev. A* 49 (2 1994), pp. 1119–1121. DOI: 10.1103/PhysRevA.49.1119.

[138] William D. Phillips and Harold Metcalf. 'Laser Deceleration of an Atomic Beam'. In: *Phys. Rev. Lett.* 48 (9 1982), pp. 596–599. DOI: 10.1103/PhysRevLett.48.596.

[139] C.-F. Cheng et al. 'An efficient magneto-optical trap of metastable krypton atoms'. In: *Review of Scientific Instruments* 81.12, 123106 (2010), p. 123106. DOI: 10.1063/1.3520133.

[140] T. Arpornthip, C. A. Sackett and K. J. Hughes. 'Vacuum-pressure measurement using a magneto-optical trap'. In: *Phys. Rev. A* 85 (3 2012), p. 033420. DOI: 10.1103/PhysRevA.85.033420.

[141] Arjen Amelink. 'Photoassociation of Ultracold Sodium Atoms'. PhD thesis. Universiteit Utrecht, 2000.

[142] M. H. Anderson et al. 'Reduction of light-assisted collisional loss rate from a low-pressure vapor-cell trap'. In: *Phys. Rev. A* 50 (5 1994), R3597–R3600. DOI: 10.1103/PhysRevA.50.R3597.

[143] D. Hoffmann et al. 'Excited-state collisions of trapped ^{85}Rb atoms'. In: *Phys. Rev. Lett.* 69 (5 1992), pp. 753–756. DOI: 10.1103/PhysRevLett.69.753.

[144] A. M. Steane, M. Chowdhury and C. J. Foot. 'Radiation force in the magneto-optical trap'. In: *J. Opt. Soc. Am. B* 9.12 (1992), pp. 2142–2158. DOI: 10.1364/JOSAB.9.002142.

[145] C. Monroe et al. 'Very cold trapped atoms in a vapor cell'. In: *Phys. Rev. Lett.* 65.13 (1990), pp. 1571–1574. DOI: 10.1103/PhysRevLett.65.1571.

[146] *James Booth, Private communication*. 2012.

[147] M. Prentiss et al. 'Atomic-density-dependent losses in an optical trap'. In: *Opt. Lett.* 13.6 (1988), pp. 452–454. DOI: 10.1364/OL.13.000452.

[148] Gene Lamm and Attila Szabo. 'Analytic Coulomb approximations for dynamic multipole polarizabilities and dispersion forces'. In: *The Journal of Chemical Physics* 72.5 (1980), pp. 3354–3377. DOI: 10.1063/1.439520.

[149] A. Cable, M. Prentiss and N. P. Bigelow. 'Observations of sodium atoms in a magnetic molasses trap loaded by a continuous uncooled source'. In: *Opt. Lett.* 15.9 (1990), pp. 507–509. DOI: 10.1364/OL.15.000507.

[150] Umakant D. Rapol, Ajay Wasan and Vasant Natarajan. 'Loading of a Rb magneto-optic trap from a getter source'. In: *Phys. Rev. A* 64 (2 2001), p. 023402. DOI: 10.1103/PhysRevA.64.023402.

[151] Daniel Adam Steck. 'Sodium D Line Data'. Revision 2.0.1, 2 May 2008.

[152] H. J. Lewandowski et al. 'Simplified System for Creating a Bose–Einstein Condensate'. In: *Journal of Low Temperature Physics* 132 (5 2003), pp. 309–367. ISSN: 0022-2291. DOI: 10.1023/A:1024800600621.

[153] M. H. Shah et al. 'Model-independent measurement of the excited fraction in a magneto-optical trap'. In: *Phys. Rev. A* 75 (5 2007), p. 053418. DOI: 10.1103/PhysRevA.75.053418.

[154] J. Van Dongen et al. 'Trap-depth determination from residual gas collisions'. In: *Phys. Rev. A* 84 (2 2011), p. 022708. DOI: 10.1103/PhysRevA.84.022708.

[155] Magnus Haw et al. 'Magneto-optical trap loading rate dependence on trap depth and vapor density'. In: *J. Opt. Soc. Am. B* 29.3 (2012), pp. 475–483.

[156] S. Bali, D. Hoffmann and T. Walker. 'Novel Intensity Dependence of Ultracold Collisions Involving Repulsive States'. In: *EPL (Europhysics Letters)* 27.4 (1994), p. 273.

[157] K. Lindquist, M. Stephens and C. Wieman. 'Experimental and theoretical study of the vapor-cell Zeeman optical trap'. In: *Phys. Rev. A* 46 (7 1992), pp. 4082–4090. DOI: 10.1103/PhysRevA.46.4082.

[158] Saptarishi Chaudhuri, Sanjukta Roy and C. S. Unnikrishnan. 'Realization of an intense cold Rb atomic beam based on a two-dimensional magneto-optical trap: Experiments and comparison with simulations'. In: *Phys. Rev. A* 74 (2 2006), p. 023406. DOI: 10.1103/PhysRevA.74.023406.

[159] G. D. Telles Ph. W. Courteille V. S. Bagnato K. M. F. Magalhães S. R. Muniz and L. G. Marcassa. 'The Escape Velocity in a Magneto-Optical Trap and Its Importance to Trap Loss Investigation'. In: *Laser Physics* 12 (2002), p. 145.

[160] V. S. Bagnato et al. 'Measuring the capture velocity of atoms in a magneto-optical trap as a function of laser intensity'. In: *Phys. Rev. A* 62 (1 2000), p. 013404. DOI: 10.1103/PhysRevA.62.013404.

[161] S. R. Muniz et al. 'Measurements of capture velocity in a magneto-optical trap for a broad range of light intensities'. In: *Phys. Rev. A* 65.1 (2001), p. 015402. DOI: 10.1103/PhysRevA.65.015402.

[162] Nathan Evetts. 'A Study of Excited State Atoms in Cold Atom Traps and a test of the Reif Model to Determine Trap Depth.' MA thesis. University of British Columbia, 2011.

[163] Kurt E. Gibble, Steven Kasapi and Steven Chu. 'Improved magneto-optic trapping in a vapor cell'. In: *Opt. Lett.* 17.7 (1992), pp. 526–528. DOI: 10.1364/OL.17.000526.

[164] Erik W. Streed et al. 'Large atom number Bose-Einstein condensate machines'. In: *Review of Scientific Instruments* 77.2, 023106 (2006), p. 023106. DOI: 10.1063/1.2163977.

[165] Robert Meppelink. 'Hydrodynamic excitations in a Bose-Einstein condensate'. PhD thesis. University of Utrecht, 2009.

[166] Emmanuel Mimoun et al. 'Fast production of ultracold sodium gases using light-induced desorption and optical trapping'. In: *Phys. Rev. A* 81.2 (2010), p. 023631. DOI: 10.1103/PhysRevA.81.023631.

[167] A. M. L. Oien et al. 'Cooling mechanisms in the sodium type-II magneto-optical trap'. In: *Phys. Rev. A* 55.6 (1997), pp. 4621–4624. DOI: 10.1103/PhysRevA.55.4621.

[168] Katsuki Furuta Yukihide Kato Susumu Tashiro Masayuki Abe Ryousuke Tajima Hideki Tanaka Hiromitsu Imaj and Atsuo Morinaga. 'Dual Magneto-Optical Trap of Sodium Atoms in Ground Hyperfine $F = 1$ and $F = 2$ States'. In: *Japanese Journal of Applied Physics* 46 (2007), pp. 492–494.

[169] W. Ertmer et al. 'Laser Manipulation of Atomic Beam Velocities: Demonstration of Stopped Atoms and Velocity Reversal'. In: *Phys. Rev. Lett.* 54 (10 1985), pp. 996–999. DOI: 10.1103/PhysRevLett.54.996.

[170] M. Zhu, C. W. Oates and J. L. Hall. 'Continuous high-flux monovelocity atomic beam based on a broadband laser-cooling technique'. In: *Phys. Rev. Lett.* 67 (1 1991), pp. 46–49. DOI: 10.1103/PhysRevLett.67.46.

[171] S. N. Atutov et al. '"White-light" Laser Cooling of a Fast Stored Ion Beam'. In: *Phys. Rev. Lett.* 80 (10 1998), pp. 2129–2132. DOI: 10.1103/PhysRevLett.80.2129.

[172] A. S. Parkins and P. Zoller. 'Laser cooling of atoms with broadband real Gaussian laser fields'. In: *Phys. Rev. A* 45 (9 1992), pp. 6522–6538. DOI: 10.1103/PhysRevA.45.6522.

[173] A. S. Parkins and P. Zoller. '$\sigma_+ - \sigma_-$ laser-cooling configuration with broadband laser fields: Instability at zero velocity'. In: *Phys. Rev. A* 45 (9 1992), R6161–R6164. DOI: 10.1103/PhysRevA.45.R6161.

[174] S.N. Atutov et al. 'Sodium MOT collection efficiency as a function of the trapping and repumping laser frequencies and intensities'. In: *The European Physical Journal D* 13.1 (Jan. 2001), pp. 71–82. ISSN: 14346060. DOI: 10.1007/s100530170289.

[175] Ying-Cheng Chen et al. 'Simple technique for directly and accurately measuring the number of atoms in a magneto-optical trap'. In: *Phys. Rev. A* 64 (3 2001), p. 031401. DOI: 10.1103/PhysRevA.64.031401.

[176] Keith Ladouceur et al. 'Compact laser cooling apparatus for simultaneous cooling of lithium and rubidium'. In: *J. Opt. Soc. Am. B* 26.2 (2009), pp. 210–217. DOI: 10.1364/JOSAB.26.000210.

[177] Brian P. Anderson and Mark A. Kasevich. 'Enhanced loading of a magneto-optic trap from an atomic beam'. In: *Phys. Rev. A* 50 (5 1994), R3581–R3584. DOI: 10.1103/PhysRevA.50.R3581.

[178] Gustavo Telles et al. 'Light-induced atomic desorption for loading a sodium magneto-optical trap'. In: *Phys. Rev. A* 81.3 (2010), p. 032710. DOI: 10.1103/PhysRevA.81.032710.

[179] M. Prevedelli et al. 'Trapping and cooling of potassium isotopes in a double-magneto-optical-trap apparatus'. In: *Physical Review A* 59.1 (Jan. 1999), pp. 886–888. ISSN: 1050-2947. DOI: 10.1103/PhysRevA.59.886.

[180] C. Klempt et al. 'Ultraviolet light-induced atom desorption for large rubidium and potassium magneto-optical traps'. In: *Phys. Rev. A* 73 (1 2006), p. 013410. DOI: 10.1103/PhysRevA.73.013410.

[181] D. C. McKay et al. 'Low-temperature high-density magneto-optical trapping of potassium using the open 4S→5P transition at 405 nm'. In: *Phys. Rev. A* 84 (6 2011), p. 063420. DOI: 10.1103/PhysRevA.84.063420.

[182] Stefan Schmid et al. 'An apparatus for immersing trapped ions into an ultracold gas of neutral atoms'. In: (Feb. 2012). eprint: 1202.2726.

[183] Han Yan-Xu et al. 'Realization of High Optical Density Rb Magneto-optical Trap'. In: *Chinese Physics Letters* 26.2 (2009), p. 023201.

[184] *Hai Wang, Private communication.* 2012.

[185] T. G. Tiecke et al. 'High-flux two-dimensional magneto-optical-trap source for cold lithium atoms'. In: *Phys. Rev. A* 80.1 (2009), p. 013409. DOI: 10.1103/PhysRevA.80.013409.

[186] Huidong Kim and D. Cho. 'A Double Magneto-optical Trap of ^{7}Li Loaded by a σ^--type Zeeman slower'. In: *Journal of the Korean Physical Society* 58 (2011), pp. 1110–1115.

[187] *D. Cho, Private communication*. 2012.

[188] G. Edward Marti et al. 'Two-element Zeeman slower for rubidium and lithium'. In: *Phys. Rev. A* 81 (4 2010), p. 043424. DOI: 10.1103/PhysRevA.81.043424.

[189] *Ed Marti, Private communication*. 2012.

[190] *Erik Streed, Private communication*. 2012.

[191] C.D.P. Levy et al. 'Polarized radioactive beam at ISAC'. In: *Nuclear Instruments and Methods in Physics Research Section B: Beam Interactions with Materials and Atoms* 204.0 (2003). 14th International Conference on Electromagnetic Isotope Separators and Techniques Related to their Applications, pp. 689 –693. ISSN: 0168-583X. DOI: 10.1016/S0168-583X(03)00485-3.

[192] S. Aubin et al. 'Francium developments at Stony Brook'. In: *Nuclear Physics A* 746 (2004). Proceedings of the Sixth International Conference on Radioactive Nuclear Beams (RNB6), pp. 459 –462. ISSN: 0375-9474. DOI: DOI:10.1016/j.nuclphysa.2004.09.135.

[193] J. F. Sell, K. Gulyuz and G. D. Sprouse. 'Collinear laser spectroscopy of francium using online rubidium vapor neutralization and amplitude modulated lasers'. In: *Review of Scientific Instruments* 80.12, 123108 (2009), p. 123108. DOI: 10.1063/1.3271037.

[194] J. F. Ziegler, U. Littmark and J. P. Biersack. *SRIM code: The stopping and range of ions in solids.* English. Pergamon, New York, 1985, 321 p. : ISBN: 008021603.

[195] Emil Traykov. 'Production of radioactive beams for atomic trapping'. PhD thesis. Groningen, 2006.

[196] Andrey Rochachevskiy. 'Production and trapping of Na isotopes for β-decay studies'. PhD thesis. Rijksuniversiteit Groningen, 2007.

[197] D Melconian et al. 'Release of ^{37}K from catcher foils'. In: *Nuclear Instruments and Methods in Physics Research Section A: Accelerators, Spectrometers, Detectors and Associated Equipment* 538.1-3 (Feb. 2005), pp. 93–99. ISSN: 01689002. DOI: 10.1016/j.nima.2004.08.135.

[198] T. Dinneen, A. Ghiorso and H. Gould. 'An orthotropic source of thermal atoms'. In: *Review of Scientific Instruments* 67 (Mar. 1996), pp. 752–755. DOI: 10.1063/1.1146804.

[199] M. Stephens, K. Lindquist and C. Wieman. 'Optimizing the capture process in optical traps'. In: *Hyperfine Interactions* 81 (1 1993). 10.1007/BF00567265, pp. 203–215. ISSN: 0304-3843.

[200] M. A. Bouchiat and J. Brossel. 'Relaxation of Optically Pumped Rb Atoms on Paraffin-Coated Walls'. In: *Phys. Rev.* 147.1 (1966), pp. 41–54. DOI: 10.1103/PhysRev.147.41.

[201] M. Stephens, R. Rhodes and C. Wieman. 'Study of wall coatings for vapor-cell laser traps'. In: *Journal of Applied Physics* 76.6 (1994), p. 3479. ISSN: 00218979. DOI: 10.1063/1.358502.

[202] S. Gozzini et al. 'Light-induced drift dynamics in an optically thin regime: Monochromatic and broadband laser excitations'. In: *Phys. Rev. A* 40 (11 1989), pp. 6349–6353. DOI: 10.1103/PhysRevA.40.6349.

[203] F. Buři č et al. 'Trap for polarized atoms based on light-induced drift'. In: *Phys. Rev. A* 54 (4 1996), pp. 3250–3253. DOI: 10.1103/PhysRevA.54.3250.

[204] AM. Bonch-Bruevich. Yu.M. Maksimov and V.V. Khromov. '() 1392 [Opt. Spectrosc. (USSR) 58 (1985)'. In: *Opt. Spektrosk.* 58 (1985), pp. 854,1392.

[205] H.G.C. Werij and J.P. Woerdman. 'Light-induced drift of Na atoms'. In: *Physics Reports* 169.3 (1988), pp. 145 –208. ISSN: 0370-1573. DOI: 10.1016/0370-1573(88)90172-X.

[206] S. Gozzini et al. 'Wall effects on light-induced drift'. In: *Optics Communications* 88.4–6 (1992), pp. 341 –346. ISSN: 0030-4018. DOI: 10.1016/0030-4018(92)90053-T.

[207] *Silvia Gozzini, Private communication.* 2012.

[208] J.H. Xu et al. 'Light induced drift of sodium atoms in absence of wall adsorption'. In: *Optics Communications* 63.1 (1987), pp. 43 –48. ISSN: 0030-4018. DOI: 10.1016/0030-4018(87)90219-7.

[209] D. Budker et al. 'Microwave transitions and nonlinear magneto-optical rotation in anti-relaxation-coated cells'. In: *Phys. Rev. A* 71 (1 2005), p. 012903. DOI: 10.1103/PhysRevA.71.012903.

[210] C. Rahman and H. Robinson. 'Rb O-O hyperfine transition in evacuated wall-coated cell at melting temperature'. In: *Quantum Electronics, IEEE Journal of* 23.4 (1987), pp. 452 –454. ISSN: 0018-9197. DOI: 10.1109/JQE.1987.1073365.

[211] ed David R. Lide, ed. *CRC Handbook of Chemistry and Physics, 89th Edition (Internet Version 2009)*. CRC Press/Taylor and Francis, Boca Raton, FL, 2009. ISBN: 0849304814.

[212] B. V. Yakshinskiy and T. E. Madey. 'Photon-stimulated desorption as a substantial source of sodium in the lunar atmosphere'. In: *Nature* 400 (1999), pp. 642–644. DOI: 10.1038/23204.

[213] J. H. Xu et al. 'Photoatomic effect: Light-induced ejection of Na and Na_2 from polydimethylsiloxane surfaces'. In: *Phys. Rev. A* 54 (4 1996), pp. 3146–3150. DOI: 10.1103/PhysRevA.54.3146.

[214] S. Gozzini and A. Lucchesini. 'Light-induced potassium desorption from polydimethylsiloxane film'. In: *The European Physical Journal D - Atomic, Molecular, Optical and Plasma Physics* 28 (2 2004). 10.1140/epjd/e2003-00300-9, pp. 157–162. ISSN: 1434-6060.

[215] A. Gozzini et al. 'Light-induced ejection of alkali atoms in polysiloxane coated cells'. In: *Il Nuovo Cimento D* 15 (5 1993). 10.1007/bf02482437, p. 709. ISSN: 0392-6737.

[216] S. N. Atutov et al. 'Fast and efficient loading of a Rb magneto-optical trap using light-induced atomic desorption'. In: *Phys. Rev. A* 67.5 (2003), p. 053401. DOI: 10.1103/PhysRevA.67.053401.

[217] S. N. Atutov et al. 'Light-induced diffusion and desorption of alkali metals in a siloxane film: Theory and experiment'. In: *Phys. Rev. A* 60.6 (1999), pp. 4693–4700. DOI: 10.1103/PhysRevA.60.4693.

[218] Krzysztof Rębilas and Marek J. Kasprowicz. 'Reexamination of the theory of light-induced atomic desorption'. In: *Phys. Rev. A* 79.4 (2009), p. 042903. DOI: 10.1103/PhysRevA.79.042903.

[219] Krzysztof R ębilas. 'Light-induced atomic desorption dynamics: Theory for a completely illuminated cell'. In: *Phys. Rev. A* 80 (1 2009), p. 014901. DOI: 10.1103/PhysRevA.80.014901.

[220] S. Atutov et al. 'Efficiency of photodesorption of Rb atoms collected on polymer organic film in vapor-cell'. In: *The European Physical Journal D - Atomic, Molecular, Optical and Plasma Physics* 62 (2 2011). 10.1140/epjd/e2011-10382-3, pp. 237–244. ISSN: 1434-6060.

[221] Ralf Guckert. 'Magneto-Optical Trapping of Radioactive Atoms'. PhD thesis. Giessen, 1998.

[222] S. J. Seltzer et al. 'Investigation of antirelaxation coatings for alkali-metal vapor cells using surface science techniques'. In: *The Journal of Chemical Physics* 133.14, 144703 (2010), p. 144703. DOI: 10.1063/1.3489922.

[223] T. Karaulanov et al. 'Controlling atomic vapor density in paraffin-coated cells using light-induced atomic desorption'. In: *Phys. Rev. A* 79 (1 2009), p. 012902. DOI: 10.1103/PhysRevA.79.012902.

[224] R. Guckert et al. 'Coupling an optical trap to a mass separator'. In: *Nuclear Instruments and Methods in Physics Research Section B: Beam Interactions with Materials and Atoms* 126.1–4 (1997). International Conference on Electromagnetic Isotope Separators and Techniques Related to Their Applications, pp. 383 –385. ISSN: 0168-583X. DOI: 10.1016/S0168-583X(97)01065-3.

[225] M. Klein et al. 'Slow light in narrow paraffin-coated vapor cells'. In: *Applied Physics Letters* 95.9, 091102 (2009), p. 091102. DOI: 10.1063/1.3207825.

[226] D.R. Swenson and L.W. Anderson. 'Relaxation rates for optically pumped Na vapor on silicone surfaces'. In: *Nuclear Instruments and Methods in Physics Research Section B: Beam Interactions with Materials and Atoms* 29.4 (1988), pp. 627 –642. ISSN: 0168-583X. DOI: DOI:10.1016/0168-583X(88)90470-3.

[227] D.R. Swenson and L.W. Anderson. 'Wall relaxation rates for an optically pumped Na vapor'. In: *Nuclear Instruments and Methods in Physics Research Section B: Beam Interactions with Materials and Atoms* 12.1 (1985), pp. 157 –160. ISSN: 0168-583X. DOI: DOI:10.1016/0168-583X(85)90711-6.

[228] D. Budker et al. 'Sensitive magnetometry based on nonlinear magneto-optical rotation'. In: *Phys. Rev. A* 62 (4 2000), p. 043403. DOI: 10.1103/PhysRevA.62.043403.

[229] E. B. Alexandrov et al. 'Light-induced desorption of alkali-metal atoms from paraffin coating'. In: *Phys. Rev. A* 66 (4 2002), p. 042903. DOI: 10.1103/PhysRevA.66.042903.

[230] *Michael Di Rosa, Private communication*. 2011.

[231] *Sergey Atutov, Private communication*. 2009,2010,2011.

[232] *Seth Aubin, Private communication*. 2009.

[233] S.N. Atutov et al. 'Experimental study of vapor-cell magneto-optical traps for efficient trapping of radioactive atoms'. In: *Eur. Phys. J. D* 53 (2009), pp. 89–96. DOI: 10.1140/epjd/e2009-00060-6.

[234] Y. Zhang and G. D. Alton. 'Modeling complex vapor-transport systems using Monte-Carlo techniques: Radioactive ion beam applications'. In: *Journal of Vacuum Science Technology A: Vacuum, Surfaces, and Films* 23.6 (2005), pp. 1558 –1567. ISSN: 0734-2101. DOI: 10.1116/1.2056553.

[235] M. H. Anderson et al. 'Observation of Bose-Einstein Condensation in a Dilute Atomic Vapor'. In: *Science* 269.5221 (1995), pp. 198–201. DOI: 10.1126/science.269.5221.198. eprint: http://www.sciencemag.org/content/269/5221/198.full.pdf.

[236] J. L. Roberts et al. 'Resonant Magnetic Field Control of Elastic Scattering in Cold ^{85}Rb'. In: *Phys. Rev. Lett.* 81 (23 1998), pp. 5109–5112. DOI: 10.1103/PhysRevLett.81.5109.

[237] Daniel Pertot et al. 'Versatile transporter apparatus for experiments with optically trapped Bose–Einstein condensates'. In: *Journal of Physics B: Atomic, Molecular and Optical Physics* 42.21 (2009), p. 215305.

[238] K. L. Corwin et al. 'Spin-Polarized Atoms in a Circularly Polarized Optical Dipole Trap'. In: *Phys. Rev. Lett.* 83.7 (1999), pp. 1311–1314. DOI: 10.1103/PhysRevLett.83.1311.

[239] T. L. Gustavson et al. 'Transport of Bose-Einstein Condensates with Optical Tweezers'. In: *Phys. Rev. Lett.* 88 (2 2001), p. 020401. DOI: 10.1103/PhysRevLett.88.020401.

[240] Erling Riis et al. 'Atom funnel for the production of a slow, high-density atomic beam'. In: *Phys. Rev. Lett.* 64.14 (1990), pp. 1658–1661. DOI: 10.1103/PhysRevLett.64.1658.

[241] E.J.D Vredenbregt, K.A.H van Leeuwen and H.C.W Beijerinck. 'Booster for ultra-fast loading of atom traps'. In: *Optics Communications* 147.4-6 (1998), pp. 375 –381. ISSN: 0030-4018. DOI: DOI:10.1016/S0030-4018(97)00604-4.

[242] Chang Yong Park, Myung Sim Jun and D. Cho. 'Magneto-optical trap loaded from a low-velocity intense source'. In: *Journal of the Optical Society of America B* 16.6 (June 1999), p. 994. ISSN: 0740-3224. DOI: 10.1364/JOSAB.16.000994.

[243] A. Steane et al. 'Phase Modulation of Atomic de Broglie Waves'. In: *Phys. Rev. Lett.* 74 (25 1995), pp. 4972–4975. DOI: 10.1103/PhysRevLett.74.4972.

[244] Markus Greiner et al. 'Magnetic transport of trapped cold atoms over a large distance'. In: *Phys. Rev. A* 63.3 (2001), p. 031401. DOI: 10.1103/PhysRevA.63.031401.

[245] Y. Song. 'Hollow beam atom funnel'. PhD thesis. University of Maryland, 1999.

[246] Dirk Müller et al. 'Guiding laser-cooled atoms in hollow-core fibers'. In: *Phys. Rev. A* 61 (3 2000), p. 033411. DOI: 10.1103/PhysRevA.61.033411.

[247] E. Dimova et al. 'Continuous transfer and laser guiding between two cold atom traps'. In: *The European Physical Journal D* 42.2 (Feb. 2007), pp. 299–308. ISSN: 1434-6060. DOI: 10.1140/epjd/e2007-00022-0.

[248] Junmin Wang et al. 'Transferring cold atoms in double magneto-optical trap by a continuous-wave transfer laser beam with large red detuning'. In: *Review of Scientific Instruments* 79.12, 123116 (2008), p. 123116. DOI: 10.1063/1.3058607.

[249] Braulio Gutiérrez-Medina. 'Quantum Transport and Control of Atomic Motion with Light'. PhD thesis. University of Texas at Austin, 2004.

[250] Ibrahim Archibald Sulai. 'Precision spectroscopy of laser trapped helium and radium atoms'. PhD thesis. Chicago, Illinois, 2011.

[251] Z. T. Lu et al. 'Low-Velocity Intense Source of Atoms from a Magneto-optical Trap'. In: *Phys. Rev. Lett.* 77 (16 1996), pp. 3331–3334. DOI: 10.1103/PhysRevLett.77.3331.

[252] L. Cacciapuoti et al. 'A continuous cold atomic beam from a magneto-optical trap'. In: *The European Physical Journal D - Atomic, Molecular, Optical and Plasma Physics* 15 (2 2001), pp. 245–249. ISSN: 1434-6060. DOI: 10.1007/s100530170172.

[253] Rob Williamson et al. 'A magneto-optical trap loaded from a pyramidal funnel'. In: *Opt. Express* 3.3 (1998), pp. 111–117. DOI: 10.1364/OE.3.000111.

[254] W. Wohlleben et al. 'An atom faucet'. In: *The European Physical Journal D - Atomic, Molecular, Optical and Plasma Physics* 15 (2 2001), pp. 237–244. ISSN: 1434-6060.

[255] Martin Christian Fischer. 'Atomic motion in optical potentials'. PhD thesis. University of Texas at Austin, 2001.

[256] De-Sheng Hong Tarek Ali Mohamed Lan-Sheng Yang Bai-Tzeng Han and D. J. Han. 'Loading and Compression of a Large Number of Rubidium Atoms Using a Semi-Dark Type Magneto-Optical Trap'. In: *Chinese Journal of Physics* 45 (2007), pp. 606–615.

[257] C. J. Myatt et al. 'Multiply loaded magneto-optical trap'. In: *Opt. Lett.* 21.4 (1996), pp. 290–292. DOI: 10.1364/OL.21.000290.

[258] Adrián Pérez Galván. 'Studies of atomic properties of francium and rubidium'. PhD thesis. University of Maryland, 2009.

[259] T. B. Swanson et al. 'Efficient transfer in a double magneto-optical trap system'. In: *Journal of the Optical Society of America B* 15.11 (Nov. 1998), p. 2641. ISSN: 0740-3224. DOI: 10.1364/JOSAB.15.002641.

[260] Christopher J Myatt. 'Bose-Einstein condensation experiments in a dilute vapor of rubidium'. PhD thesis. University of Colorado at Boulder, 1997.

[261] *Paul Vetter, Private communication*. 2012.

[262] J. W. Turkstra et al. 'Recoil Momentum Spectroscopy of Highly Charged Ion Collisions on Magneto-Optically Trapped Na'. In: *Phys. Rev. Lett.* 87.12 (2001), p. 123202. DOI: 10.1103/PhysRevLett.87.123202.

[263] S. Knoop et al. 'Multielectron removal processes in He^{2+}+Na collisions'. In: *Phys. Rev. A* 73.6 (2006), p. 062703. DOI: 10.1103/PhysRevA.73.062703.

[264] Robert Sylvester Williamson III. 'Magneto-optical trapping of potassium isotopes'. PhD thesis. University of Wisconsin, Madison, 1997.

[265] G. C. Bjorklund et al. 'Frequency modulation (FM) spectroscopy'. In: *Applied Physics B: Lasers and Optics* 32 (3 1983). 10.1007/BF00688820, pp. 145–152. ISSN: 0946-2171.

[266] R. H. L van Wooning. *Laser frequency offset Locking*. Tech. rep. Brede Bachelor of Engineering (BBoE) thesis, KVI and Hanzehogeschool, Groningen, 2008.

[267] Wolfgang Demtröder. *Laser Spectroscopy*. Springer, 2002. ISBN: 3540652256.

[268] *Datasheet Hamamatsu R7449, 28mm diameter, 11–stage, Bialkali Photocathode, Head–On Type, Low Dark Current, High Stability*.

[269] Nichia. 'Specifications for Nichia chip type UV model: NCSU034A (T) LED'. In: *Ceramics* 090605 ().

[270] J. A. Fedchak et al. 'The Argonne laser-driven D target: Recent developments and progress'. In: *American Institute of Physics Conference Series*. Vol. 421. American Institute of Physics Conference Series. Jan. 1998, pp. 129–138. DOI: 10.1063/1.55017.

[271] J. A. Fedchak et al. 'Silane coatings for laser-driven polarized hydrogen sources and targets'. In: *Nuclear Instruments and Methods in Physics Research Section A: Accelerators, Spectrometers, Detectors and Associated Equipment* 391.3 (1997), pp. 405 –416. ISSN: 0168-9002. DOI: DOI:10.1016/S0168-9002(97)00571-8.

[272] M. Pearson and J.M. revised by Grossman. 'Dri-film coating (July 21, 2001)'. 2001.

[273] Tobias Tiecke. 'Feshbach resonances in ultracold mixtures of the fermionic quantum gases ^{6}Li and ^{40}K'. PhD thesis. Universiteit van Amsterdam, 2009.

[274] Fred Zwarts. 'CADDIE'. https://www.kvi.nl/~itgroup/daq/caddie/UserManual.html.

[275] Rene Brun and Fons Rademakers. 'ROOT – An object oriented data analysis framework'. In: *Nuclear Instruments and Methods in Physics Research Section A: Accelerators, Spectrometers, Detectors and Associated Equipment* 389.1-2 (1997). New Computing Techniques in Physics Research V, pp. 81 –86. ISSN: 0168-9002. DOI: DOI:10.1016/S0168-9002(97)00048-X.

[276] H. Wilschut et al. 'Status of the TRIμP project'. In: *Hyperfine Interactions* 174 (1 2007). 10.1007/s10751-007-9570-z, pp. 97–102. ISSN: 0304-3843.

[277] P.D. Shidling et al. 'Production of short lived radioactive beams of radium'. In: *Nuclear Instruments and Methods in Physics Research Section A: Accelerators, Spectrometers, Detectors and Associated Equipment* 606.3 (2009), pp. 305 –309. ISSN: 0168-9002. DOI: DOI:10.1016/j.nima.2009.05.007.

[278] R. Hoekstra H.W. Wilschut M.N. Harakeh and R. Morgenstern. *TRIμP proposal NWO*. Tech. rep. KVI, 1999.

[279] *Hendrik Bekker, Private communication*. 2012.

[280] C. G. Townsend et al. 'Phase-space density in the magneto-optical trap'. In: *Phys. Rev. A* 52.2 (1995), pp. 1423–1440. DOI: 10.1103/PhysRevA.52.1423.

[281] K. M. R. van der Stam et al. 'Large atom number Bose-Einstein condensate of sodium'. In: *Review of Scientific Instruments* 78.1, 013102 (2007), p. 013102. DOI: 10.1063/1.2424439.

[282] *Otto Dermois, Private communication*. 2012.

[283] H. Katz. *Technologische Grundprozesse der Vakuumelektronik (German Edition)*. Springer, 1974. ISBN: 3540065326.

[284] F J Bradshaw. 'The Optical Emissivity of Titanium and Zirconium'. In: *Proceedings of the Physical Society. Section B* 63.8 (1950), p. 573.

[285] George Teodorescu. 'Radiative emissivity of metas and oxidized metals at high temperature'. PhD thesis. Auburn University, 2007.

[286] H.M. James P.D. Desal and C.Y. Ho. 'Electrical resistivity of vanadium and zirconium'. In: *J. Phys. Chem. Ref. Data.* 13.4 (1984).

[287] C. de Mauro et al. 'Measurement of diffusion coefficients of francium and rubidium in yttrium based on laser spectroscopy'. In: *Phys. Rev. A* 78.6 (2008), p. 063415. DOI: 10.1103/PhysRevA.78.063415.

[288] *TRIμP A-MOT logbook 2*. Page 67.

[289] Masahiro Yamamoto et al. 'Kinetics of oxygen absorption by α-zirconium'. In: *The Journal of Physical Chemistry* 93.13 (1989), pp. 5203–5209. DOI: 10.1021/j100350a035. eprint: http://pubs.acs.org/doi/pdf/10.1021/j100350a035.

[290] Z.-T. Lu et al. 'Efficient Collection of ^{221}Fr into a Vapor Cell Magneto-optical Trap'. In: *Physical Review Letters* 79.6 (Aug. 1997), pp. 994–997. ISSN: 0031-9007. DOI: 10.1103/PhysRevLett.79.994.

[291] M. D. Di Rosa et al. 'Magneto-optical trap and mass-separator system for the ultrasensitive detection of ^{135}Cs and ^{137}Cs'. In: *Applied Physics B: Lasers and Optics* 76 (2003), pp. 45–55. DOI: 10.1007/s00340-002-1063-9.

[292] A. Gorelov et al. 'Beta–neutrino correlation experiments on laser trapped ^{38m}K, ^{37}K'. In: *Hyperfine Interactions* 127 (1 2000). 10.1023/A:1012649229978, pp. 373–380. ISSN: 0304-3843.

[293] Daniel Grant Roberge. 'Polarization diagnostics for rubidium-80 in a spin-polarized beta decay experiment'. MA thesis. University of Victoria, 2006.

[294] Robert Andrew Pitcairn. 'The Search for Tensor Interactions in the β-decay of Polarized ^{80}Rb'. MA thesis. The University Of British Columbia, 2007.

[295] J. A. Behr et al. 'Magneto-optic Trapping of β-Decaying $^{38}K^m$, ^{37}K from an on-line Isotope Separator'. In: *Phys. Rev. Lett.* 79.3 (1997), pp. 375–378. DOI: 10.1103/PhysRevLett.79.375.

[296] Max Planck. *Vorträge, Reden, Erinnerungen*. Springer, 2001. ISBN: 3540412743.

[297] A.A. Radzig and B.M. Smirnov. *Reference Data on Atoms, Molecules, and Ions (Springer Series in Chemical Physics)*. Springer, 1985. ISBN: 3540124152.

[298] J. Mitroy and J.-Y. Zhang. 'Long-range dispersion interactions. II. Alkali-metal and rare-gas atoms'. In: *Phys. Rev. A* 76 (3 2007), p. 032706. DOI: 10.1103/PhysRevA.76.032706.

[299] David E. Fagnan et al. 'Observation of quantum diffractive collisions using shallow atomic traps'. In: *Phys. Rev. A* 80 (2 2009), p. 022712. DOI: 10.1103/PhysRevA.80.022712.

[300] M. Marinescu, H. R. Sadeghpour and A. Dalgarno. 'Dispersion coefficients for alkali-metal dimers'. In: *Phys. Rev. A* 49 (2 1994), pp. 982–988. DOI: 10.1103/PhysRevA.49.982.

[301] M. Marinescu and A. Dalgarno. 'Dispersion forces and long-range electronic transition dipole moments of alkali-metal dimer excited states'. In: *Phys. Rev. A* 52 (1 1995), pp. 311–328. DOI: 10.1103/PhysRevA.52.311.

[302] F. Reif. *Fundamentals of statistical and thermal physics*. McGraw-Hill Book Company, 1965.

[303] W.L. Kruithof. 'Comment on "Transferring cold atoms in double magneto-optical trap by a continuous-wave transfer laser beam with large red detuning" [Rev. Sci. Instr. 79, 123116 (2008)]'. In: *Review of Scientific Instruments* (2012). Submitted.